ALMA MATER STUDIORUM
UNIVERSITÀ DI BOLOGNA

DOTTORATO DI RICERCA IN
ASTROFISICA

Ciclo XXXV

Exploring the Internal Kinematics of Galactic Globular Cluster Cores

Presentata da: **Silvia Leanza**

Coordinatore Dottorato:

Prof. Andrea Miglio

Supervisore:

Prof. Francesco R. Ferraro

Co-supervisori:

Prof.ssa Barbara Lanzoni

Dott.ssa Cristina Pallanca

Esame finale anno 2023

Settore Concorsuale: 02/C1 – Astronomia, Astrofisica, Fisica della Terra e dei Pianeti
Settore Scientifico Disciplinare: FIS/05 – Astronomia e Astrofisica

Abstract

This thesis focuses on the study of the internal kinematics of Galactic Globular Clusters (GGCs) as part of the Multi-Instrument Kinematic Survey (MIKiS). The MIKiS survey aims to fully exploit the performance of different ESO Very Large Telescope (VLT) spectrographs to obtain comprehensive velocity dispersion and rotation profiles for a significant sample of GGCs.
Due to observational difficulties, the internal kinematics of GGCs has been poorly studied in the past, leading to the traditional view of globular clusters (GCs) as simple, quasi-relaxed non-rotating stellar systems, characterized by spherical symmetry and isotropy in velocity space. However, recent studies utilizing proper motions (PMs) based on high-precision astrometry from *Gaia* and *Hubble Space Telescope*, have revealed deviations from isotropic velocity distributions and significant internal rotation in many GCs. Additionally, dedicated ESO-VLT spectroscopic surveys have detected unambiguous rotation patterns in a growing number of GCs from line of sight (LOS) velocity measurements of individual stars. These findings definitely prove that the internal structure and kinematics of GCs are much more intricate than previously thought, and their understanding is crucial for clarifying their mechanism of formation, dynamical evolution and the interplay with the host galaxy.

In the context of the MIKiS survey, in this thesis work we present the kinematic investigation of three GGCs (NGC 1904, NGC 6440 and NGC 6569) from the LOS velocity of several hundreds of individual stars located over the entire radial extension of each system. Following the MIKiS approach, we employed the adaptive-optics (AO) assisted integral-field (IF) spectrograph SINFONI to resolve the stars in the central regions, the IF spectrograph KMOS to sample intermediate radii, and the multi-object spectrograph FLAMES/GIRAFFE to derive large samples of LOS velocities in the outer regions of the clusters. In addition, we took full advantage of the exceptional capabilities of the AO-assisted IF spectrograph MUSE/NFM to explore the internal kinematics of high-density GC cores at sub-arcsecond spatial resolution. MUSE/NFM is a powerful and unique instrument for measuring the radial velocity (RV) from the spectra of resolved stars in the overcrowded central regions, which are still largely unexplored.
Adopting this strategy, we obtained more than 1000 RV measurements from individual stars in each of the three clusters, sampling from the innermost to the outermost

regions. Therefore, we were able to construct the entire velocity dispersion profiles of the clusters. The large sample of RVs from MUSE spectra in the central regions allowed us to exclude the presence of an intermediate-mass black hole in the core of NGC 1904, at odds with previous findings obtained from integrated-light spectra. Our studies have also revealed signatures of internal rotation in each of the three GGCs we studied. In particular, a clear rotation curve was detected in both the LOS direction and in the plane of the sky for NGC 1904, with the latter being obtained from *Gaia* PMs. In addition, for a sub-sample of stars with both RV and PM measures, we derived the three-dimensional kinematic structure of NGC 1904. In the bulge GC NGC 6440 a peculiar core rotation has been found, which could indicate a very advanced dynamical stage, in agreement with theoretical predictions. These results, supported by those of N-body simulations, demonstrate that most of these systems were born with significant initial rotation that they gradually lost through internal two-body relaxation and angular momentum loss carried away by escaping stars. Furthermore, we characterized the structural properties and derived the structural parameters of the GCs NGC 6440 and NGC 6569, by using an approach based on resolved star counts. This allowed us to integrate the kinematic study with that of the structural characteristics and to verify that the same King model adequately reproduces both the kinematic and the structural properties of the studied GCs.

Contents

Chapter 1

Introduction

1.1 Globular Clusters

Globular clusters (GCs) are among the longest-studied stellar systems in which individual stars can be resolved. By definition, GCs are aggregates of $10^5 - 10^6$ gravitationally bound stars orbiting a common potential well under the effect of their mutual gravitational attraction, resulting in stellar systems with nearly spherical symmetry and compact, high-density central regions. The GCs hosted in the Milky Way (MW) are about 150 (Harris, 1996, 2010 edition) and are mainly located in the Galactic halo and bulge. Galactic GCs (GGCs) are considered ancient building blocks of our Galaxy dating back to the formation epoch of the MW. Indeed, they are known to be very old stellar systems with ages between 10 and 13 Gyr (see, e.g., Gratton et al., 1997; Chaboyer et al., 1998; Marín-Franch et al., 2009). Moreover, most GGCs are metal poor stellar systems ([Fe/H] $\lesssim -1$), essentially free of dust and gas.

For several decades, GCs have been considered the ideal example of Simple Stellar Populations (SSPs), i.e., systems composed of coeval stars with the same chemical composition. In recent years, this paradigm has been revised because several observational pieces of evidence have definitively proved that many GCs host multiple stellar populations showing significant chemical anomalies (see, e.g. Kraft, 1994; Gratton et al., 2004; Piotto et al., 2007; Gratton et al., 2012; Milone et al., 2017), for example the so-called "anticorrelations" among light-elements (e.g., Na, O, C, N, He, see, e.g. Carretta et al., 2009a,b). However, in general, these systems exhibit homogeneity in their iron abundance (see, e.g. Carretta et al., 2009b), although indications of iron spreads have recently been detected in a few GCs (Marino et al., 2019). Nevertheless, in most cases, GCs can still be considered as SSPs, at least as a first approximation. Therefore, GCs represent the best natural observational laboratories to address fundamental issues of present-day astrophysics, ranging from stellar evolution to the formation and evolutionary history of stellar systems and their interplay with the host galaxy, ending with the Galaxy formation process at early epochs of the Universe.

1.1.1 Internal dynamics and structure

GCs are multi-particle systems ideal to study most of the dynamical processes that take place in stellar systems. The internal dynamics of GCs is essentially driven by two-body encounters between the stars. Due to recurrent gravitational interactions, stars exchange energy with each others with the result that they progressively lose memory of their initial conditions. This process is known as *two-body relaxation* and occurs in a time scale called *two-body relaxation time* defined as:

$$t_{2b} = n_{2b}\, t_{cross}, \tag{1.1}$$

where t_{cross} is the crossing time of the system and n_{2b} is the number of crossing needed for a star to change its velocity by an amount equivalent to the velocity itself. In the approximation of a system of N particles with the same mass, t_{2b} can be expressed as (Binney & Tremaine, 1987):

$$t_{2b} \simeq \frac{0.1N}{\ln N} t_{cross}. \tag{1.2}$$

Typically, t_{2b} is compared with the age of the system (t_{age}), and clusters for which $t_{2b} > t_{age}$ are named *collisionless* systems, while those with $t_{2b} < t_{age}$ are defined *collisional* systems. In the case of GCs, for which $N \approx 10^5 - 10^6$ and $t_{cross} \approx 1\,\mathrm{Myr}$, the relaxation timescale is less than 1 Gyr, significantly shorter than their ages. Hence, they are collisional systems. On the contrary, galaxies have typical relaxation times much larger than their ages, which makes them examples of collisionless systems.

Being collisional systems, the internal dynamics and internal structure of GCs are strongly affected by the encounters occurring among the stars, and the velocity distribution of these systems is well-described by a Maxwellian function truncated at their escape velocity.
Traditionally, the so-called King models (King, 1966) are assumed to be the family of models that best reproduce the observed surface-brightness (SB) and density profile of GCs. This is why they are widely used to represent the GC structure. Indeed, taking into account the two-body relaxation, the Maxwellian distribution of stellar velocities, and the tidal truncation due to the gravitational potential of the host galaxy, they provide a proper representation of the physical structure of these star clusters. Briefly, the King models are described by the following distribution function:

$$f(E) = \begin{cases} C(e^{-\frac{E}{\sigma^2}} - 1) & \text{if } E < 0 \\ 0 & \text{if } E \geq 0 \end{cases} \tag{1.3}$$

where σ is the velocity dispersion and E the energy per unit mass in the mean potential $\Psi(r)$:

$$E = \frac{v^2}{2} + \Psi(r). \tag{1.4}$$

The distance from the cluster center at which the gravitational potential of the system becomes negligible with respect to that of the host galaxy, is called *tidal* (or *truncation*) *radius* (r_t), for which $\Psi(r_t) = 0$. Moreover, the King models are characterized by a scale length commonly called *King radius* and defined as:

$$r_0 = \sqrt{\frac{9\sigma^2}{4\pi G\rho_0}}, \tag{1.5}$$

where σ is the velocity dispersion, G is the gravitational constant and ρ_0 is the central density.

The King models represent a single-parameter family because the shape of each model (i.e., each density profile) is univocally determined by the dimensionless parameter W_0, which is proportional to the central gravitational potential according to: $W_0 \equiv \Psi(0)/\sigma^2$. These models are characterized by a constant surface density in the innermost region (representing to the so-called cluster *core*) followed by a rapid outwards decrease in the halo region. In particular, higher values of W_0 correspond to larger overall sizes of the system with respect to the core, which is usually quantified by the *concentration parameter* (c), defined as $c = \log(r_t/r_0)$. Figure 1.1 shows the projected density profiles of different King models for different values of W_0 or, equivalently, for different values of c: the number labelled beside each curve is the value of c (ranging from 0.5, to 2.5), while the arrows mark the position of r_t.
Other characteristic parameters are the *core radius* (r_c), i.e. the distance from the center at which the projected density (or SB) becomes equal to half its central value and indicating the size of the cluster core, the *half-mass* (r_h) and *half-light* (r_{hl}) *radii*, which represent the distances from the center including half the total mass and half the total projected luminosity, respectively.

1.1.2 Dynamical evolution

A brief overview about GC dynamical evolution is presented below.
The dynamical evolution of GCs is thought to start with an initial expansion phase, which is due to heavy mass loss from massive stars at the end of their main sequence evolution and to supernova explosions. The large amounts of irregular mass loss from the system may induce variations of the gravitational potential of the system during its early evolution. In this phase (which is called *violent relaxation*; Lynden-Bell, 1967, 1962; Hénon, 1964; King, 1966) the redistribution of energy is not due to gravitational encounters, but to the variations of the potential, which modify the orbits of the stars.

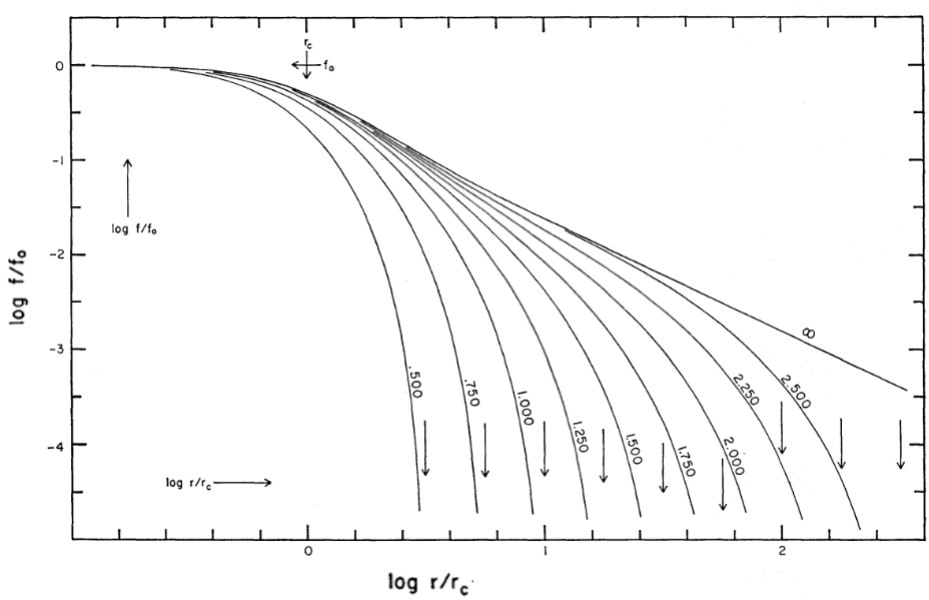

Figure 1.1: Examples of King models showing the surface density here named f and represented in logarithmic units, as a function of the distance from the center (r), f and r are normalized to the central density value (f_0) and the core radius (r_c), respectively. The curves are characterized by different values of W_0 and the corresponding values of the concentration parameter c are labeled. The vertical arrows shown on each curve mark the positions of the truncation radius for each model. Image taken from King (1966).

After this initial phase, the dynamical evolution is mainly dominated by the two-body relaxation process progressively leading to a quasi-Maxwellian velocity distribution, and the GC structure can be described by King profiles. The stars exchange energy through the mutual gravitational encounters that lead the system towards a state of energy equipartition. As a result, lighter stars gain velocity and if their velocity exceeds the escape velocity of the cluster, they can escape the potential of the system, generating a phenomenon known as *evaporation* (see, e.g., Meylan & Heggie, 1997; Vesperini & Heggie, 1997; Aarseth & Heggie, 1998; Takahashi & Portegies Zwart, 2000; Gieles et al., 2011; Madrid et al., 2017).

On the other hand, heavier stars lose kinetic energy and slow down due to dynamical friction, moving towards more internal orbits. The combination of these two phenomena results in a process called *mass segregation*: massive stars are preferentially located in the central regions, while low-mass stars move toward the outer regions. Therefore, the radial distribution of the heavy objects (e.g., Blue Straggler Stars) can be an excellent observational indicator of the stage of dynamical evolution of GCs (see, e.g., Ferraro et al., 2012).

Massive stars transfer kinetic energy to the light ones that moves toward the cluster periphery. Then, for the Virial Theorem, the core contracts and becomes hotter, thus needing to transfer even more energy to the envelope of the cluster. This results in a runaway process leading to the so-called *core-collapse* (CC, see

e.g., Hénon, 1961; Spitzer, 1987; Lynden-Bell & Wood, 1968; Meylan & Heggie, 1997). If unopposed, this process would lead to a divergent central density in a finite time. The contraction is stopped thanks to the energy provided by binary systems, which during the interaction with a third object shrink releasing energy to the cluster and contrasting the collapse. Observationally, the clusters that have experienced CC show a steep power-law cusp in the innermost $5'' - 10''$ portion of the density profile, rather than the typical flat-core behavior of the King models, because the central density significantly increases due to the core contraction.

The *post core collapse* (post-CC) phase can be characterized by the so-called *gravothermal oscillations* (e.g., Meylan & Heggie, 1997), i.e., several episodes of high central density, followed by stages during which the system rebounds toward a structure with lower central density and a more expanded core. However, the details of this process are still matter of debate (Breen & Heggie, 2012a,b).

In spite of their similar chronological ages ($\sim$ 12 Gyr), GGCs show different stages of internal dynamical evolution (*dynamical age*). For example, many GGCs present different levels of central segregation of massive stars (with high segregation levels indicating advanced dynamical age; see, e.g., Ferraro et al., 2020) and only 15-20% of GGCs show the central cusp in the density profile that classifies them as CC or post-CC systems (Djorgovski & King, 1984; Lugger et al., 1995). The dynamical evolution timescale (the relaxation time), hence the GC dynamical age, depends in a complex and largely unconstrained way on the intrinsic properties at formation (e.g., total mass, central mass density, binary content, etc.) and on the external effects of the environment (e.g., Galactic tides, disk shocks). Therefore, a proper characterization of GC dynamical age is crucial to get information on their evolutionary history and properties at formation.

1.2 Internal kinematics

As discussed in the previous Section, GGCs are the oldest collisional astrophysical systems in which the stars can be individually observed. Therefore, they are ideal laboratories where the complex interplay between stellar population properties, structural features, internal kinematics and dynamical evolution can be empirically investigated.

Over the last decades, kinematic and dynamical studies have been of fundamental importance to improve our understanding of these stellar systems. For example, radial velocity (RV) and proper motion (PM) measurements allowed to derive their velocity dispersion (e.g., Lane et al., 2010; Baumgardt & Hilker, 2018; Kamann et al., 2018a; Ferraro et al., 2018a) and detect signals of rotation (e.g., Bellazzini et al., 2012; Bianchini et al., 2013; Watkins et al., 2015; Bellini et al., 2017). From a theoretical point of view, the study of the internal dynamics of GCs is traditionally

based on simplified models involving spherical symmetry, absence of internal rotation and isotropy in the velocity space. These assumptions are mainly due to the roundish appearance of most GCs and observational difficulties in the determination of their internal kinematics. In fact, integrated-light spectra can be severely affected by the so-called *shot noise bias* (see Section 1.2.2), and a proper kinematical study therefore requires to measure the velocity of large samples of individual stars, either on the plane of the sky, or along the line-of-sight (LOS). The PMs analysis is very challenging because it requires high-precision photometry and astrometry on quite long time baselines, while the determination of the LOS velocity of resolved individual stars in these dense clusters requires sufficiently high spectral and spatial resolution, other than a lot of telescope time to acquire statistically large samples of spectra.

However, recent observational campaigns aimed at studying the morphological and kinematical properties of GCs have been performed, and revealed a much more complex scenario than the simplified traditional models, showing deviations from spherical symmetry (e.g., Chen & Chen, 2010), internal kinematics characterized by an anisotropic velocity distribution (see, e.g., Bianchini et al., 2013; Bellini et al., 2014; Watkins et al., 2015), and non-negligible internal rotation (see, e.g., Lane et al., 2009, 2010; Bellazzini et al., 2012; Bianchini et al., 2013; Fabricius et al., 2014; Kacharov et al., 2014; Bellini et al., 2017).
Similar findings are growing in number thanks to the advent of new facilities, which are providing new perspectives on GC internal dynamics and kinematics. The high-precision astrometry ensured by *Gaia* (e.g., Bianchini et al., 2018; Baumgardt et al., 2019; Vasiliev & Baumgardt, 2021) and by multi-epoch observations with the *Hubble Space Telescope* (*HST*, see e.g., Bellini et al., 2014, 2015; Watkins et al., 2015; Bellini et al., 2018; Libralato et al., 2022) have added crucial pieces to our exploration of GC internal kinematics in the plane of the sky (see Section 1.2.3). In addition, several studies mainly based on dedicated spectroscopic surveys (e.g., Ferraro et al., 2018b; Kamann et al., 2018a) have contributed to unveil kinematic properties from LOS velocity measurements (see Section 1.2.2), by efficiently exploiting the last generation of integral field (IF) spectrographs. Therefore high-performance facilities have given birth to an observational revolution, which is finally starting to unveil to us unexpected kinematic properties in many GGCs.

Also from a theoretical point of view, notable progress has been made recently. Realistic N-body models (e.g., Baumgardt & Makino, 2003; Tiongco et al., 2017) allowed us to better investigate the evolution and the internal properties of these systems, large parameter spaces have been explored through Monte Carlo simulations (Giersz et al., 2013) and analytical models were fundamental to improve our understanding of GCs dynamical evolution and kinematic properties (e.g., Varri & Bertin, 2012; Gieles & Zocchi, 2015).

Consequently, we are finally close to reach a proper understanding of the real internal dynamics and kinematics of GGCs.

1.2.1 Rotation in Globular Clusters

Distinct signals of internal rotation have been detected in more than 50% of the GCs surveyed so far (Bianchini et al., 2018; Kamann et al., 2018a; Ferraro et al., 2018b; Sollima et al., 2019). Moreover, indications of rotation have also been detected in different categories of stellar systems, as intermediate-age clusters (e.g., Mackey et al., 2013), young massive clusters (Hénault-Brunet et al., 2012), and nuclear star clusters (Feldmeier et al., 2014; Nguyen et al., 2018), pointing that rotation is a common and non-negligible factor in the evolution of dense stellar systems at different scales.

The present-day rotation in GCs is likely to be a relic of stronger primordial rotation in proto-GC, which originated for the initial conditions of these objects at the epoch of their formation and then dissipated by the effect of two-body relaxation (see, Mapelli, 2017; Tiongco et al., 2017). In particular, during the long-term evolution, the mass-loss experienced by the clusters (*escaping stars*) carry away angular momentum, which damps the rotation signal (Ernst et al., 2007; Kim et al., 2008; Hong et al., 2013; Tiongco et al., 2017). However, a fossil rotation, even if low, can still be observed today. The presence of internal rotation could, in addition, indicate a peculiar evolutionary interplay between the proto-GC and the external environment (Vesperini et al., 2014; Tiongco et al., 2018).

From a theoretical point of view, the presence of rotation is expected to have a significant impact on the formation and the long-term dynamical evolution of GCs. For example, many studies showed that rotation accelerates the dynamical evolution (e.g., Ernst et al., 2007; Kim et al., 2008; Hong et al., 2013), and severely shape the current observed morphology (van den Bergh, 2008; Bianchini et al., 2013). As regards the latter, internal rotation and pressure anisotropy are the main physical elements that could induce the observed flattening of GCs (Chen & Chen, 2010).

In most cases, observations in GCs showed rotation curves characterized by a shape that rises from the center of the cluster, reaches a peak and then decreases in the outer regions (e.g., Bianchini et al., 2013; Bellini et al., 2017; Kamann et al., 2018a; Lanzoni et al., 2018a). This trend is also in agreement with results of N-body simulations (Tiongco et al., 2017), which predict a peak at 1-2 half-mass radii. However, cases of significant rotation have recently been detected in the very central regions of few GCs (Usher et al., 2021; Dalessandro et al., 2021a, see also Section 4), whose origin is still unclear.
The ratio between the rotational velocity peak ($V_{\rm rot}^{\rm peak}$) and the cluster central velocity dispersions (σ_0) is commonly used to quantify the magnitude of ordered versus

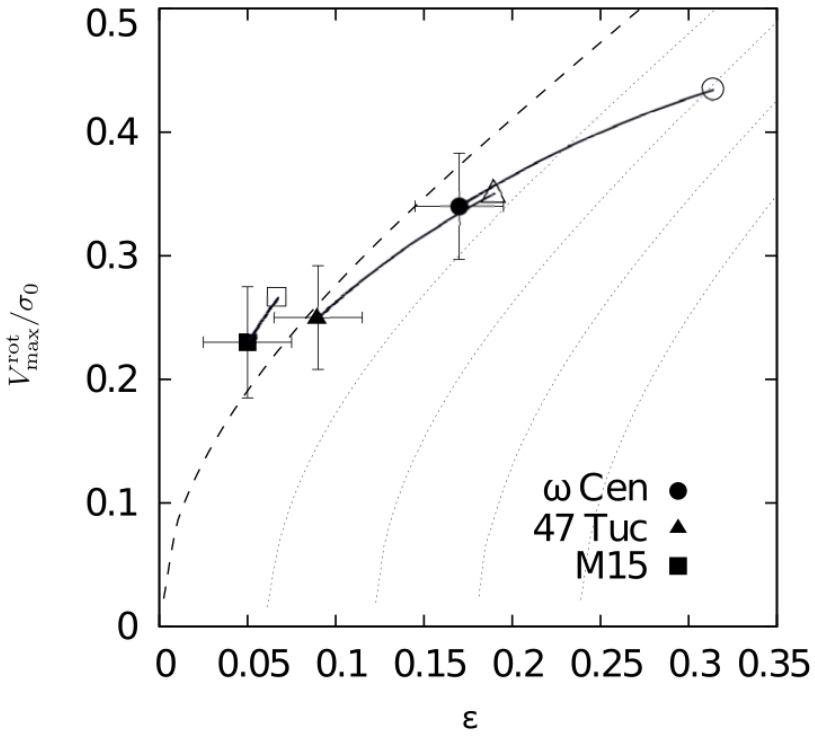

Figure 1.2: Example of V^{peak}_{rot}/σ_0 (here indicated as V^{rot}_{max}) vs. ϵ for ω Cen, 47 Tuc, and M15. The dashed line indicates the relation for isotropic oblate rotators viewed *edge-on* whereas the thin dotted lines indicate oblate rotators viewed *edge-on* with different global anisotropy parameters. Taken from Bianchini et al. (2013).

random motions, and to investigate the relevance of rotation in shaping the cluster. It typically ranges from about 0.05 to about 0.4 (see, e.g., Bellazzini et al., 2012; Fabricius et al., 2014; Bianchini et al., 2013; Kamann et al., 2018a; Lanzoni et al., 2018a). High values of V^{peak}_{rot}/σ_0 indicate that the rotation is a non-negligible component on the internal cluster dynamics.

As shown in Figure 1.2, where the dashed line represents the relation for isotropic oblate rigid rotators viewed *edge-on*, while the thin dotted lines indicate oblate rotators viewed *edge-on* with different global anisotropy (see Bianchini et al., 2013), GCs are mainly placed in the region of the diagram corresponding to small ellipticities, solid-body rotation and isotropy. While, a combination of inclination, differential rotation, and pressure anisotropy can be the cause of the deviations from the line of isotropic rotators. However, it is important to note that this tool gives only a baseline interpretation of the role played by rotation and pressure anisotropy in the dynamical evolution. In fact, this approach adopts global quantities that can be hard to measure in real cases. For example, the actual rotation peak is difficult to measure because it is strongly related to inclination effects, which are generally not easy to constrain observationally. In fact, LOS observations provide information on the rotation signal only if the measured RVs show a sinusoidal pattern as

a function of the azimuthal position of the stars, but the inclination angle of the rotation axis with respect the LOS remains unconstrained. Combining the three velocity components (LOS and PMs), as described in Chapter 3 (see also Bianchini et al., 2013; Bellini et al., 2017; Sollima et al., 2019), is the only way to determine the inclination angle of the rotation axis and address the projection effects. Hence, a three-dimensional study is necessary to reconstruct the actual three-dimensional kinematic structure of the system and determine the strength of the present-day rotation and anisotropy in the velocity distribution.

1.2.2 Line of sight velocity

The appropriate analysis of the LOS velocity (in this thesis also referred to as RV) provides the accurate determination of one of the three components of the *velocity dispersion* (VD) *profile* and possibly the *rotation curve* of GCs. If in principle, the LOS kinematics is easy to obtain (through spectroscopy), in practice, it is very challenging in GGCs. In fact, measuring the line broadening of integrated light spectra (see, e.g., Ibata et al., 2009; Lützgendorf et al., 2011, 2013; Fabricius et al., 2014) is prone to a severe *shot noise bias* (e.g., Dubath et al., 1997; Lanzoni et al., 2013) in the case of resolved stellar populations like GGCs. Indeed, the line broadening can be easily affected by the dominant contribution to the observed spectrum from the light of just a few bright stars, providing a measure of their RV scatter, instead of a measure of the cluster VD.
The alternative approach consists in deriving the VD from the RVs of a statistically significant sample of individual stars (e.g., Lane et al., 2010; Bellazzini et al., 2012; Bianchini et al., 2013; Kamann et al., 2018a; Baumgardt & Hilker, 2018): the RV of each star is measured from the Doppler shift of its spectral lines, and the cluster VD is then obtained from the dispersion of these values about the mean (systemic velocity). If on the one hand, this method is safe from obvious biases, on the other hand, obtaining a large samples of RVs from resolved stars over the entire cluster extension is a very difficult task from the observational point of view, especially in the highly crowded regions of GGCs, requiring both high spatial resolution and multi-object spectroscopic facilities.

In the last years, thanks to the new generations of ground-based multi-object spectrographs and IF spectrographs equipped with adaptive-optics (AO) facilities, it was possible to start overcoming these limitations.
For example, Ferraro et al. (2018b) present the Multi-Instrument Kinematic Survey (hereafter the MIKiS survey) of GGCs, which exploits the combination of different data sets acquired with appropriate spectrographs at the ESO Very Large Telescope (VLT), to determine the VD and rotation profiles along the entire radial extension of a large sample of GGCs. Since the MIKiS survey is the mother project of this thesis, more details about it, and some notable results obtained in its context, are

described in the following Chapter 2.

Part of the fundamental improvements recently obtained in the context of GC internal kinematics (and largely contributed by this thesis work) have been achieved thanks to spectroscopic surveys based on the IF spectrograph MUSE (see, e.g., Husser et al., 2016; Kamann et al., 2016, 2018a; Kamann et al., 2018b). In Husser et al. (2016) and Kamann et al. (2018a), the authors describe and show the unique performances of MUSE in the study of the internal kinematics in crowded stellar fields. Combining good spatial resolution and a large spectral range in the optical band, MUSE opens up the possibility to acquire the spectra of thousand individual stars simultaneously. Indeed, to date it appears to be the ideal instrument for this kind of studies.
In this context, Kamann et al. (2018a) present the kinematic analysis of 22 GGCs. Using multiple MUSE pointings to cover the areas inside the half-light radius of each system, they obtain huge samples of spectra of individual stars and perform a detailed analysis of the rotation and VD profiles of each cluster. Significant rotation has been detected in the majority of the targets (in agreement with the previous findings of Fabricius et al., 2014). In addition, they investigate the link between rotation and ellipticity (see the left panel of Figure 1.3), and find a mild correlation between the strength of internal rotation and the relaxation time of the clusters (see right panel in Figure 1.3). The latter, suggests that the observed signals are the relics of a stronger rotation at the epoch of the cluster formation gradually dissipated via two-body relaxation, in agreement with other observational results (e.g., Bianchini et al., 2018; Sollima et al., 2019), and N-body simulations (Tiongco et al., 2017).

Recently, the large data sets provided by MUSE opened the possibility to search for differences in the kinematics of the multiple populations hosted by GCs (e.g., Kamann et al., 2020; Dalessandro et al., 2021a). The origin of these populations is still unknown, but it is clear that their kinematics still contain clues about their formation and evolution processes (e.g., Hénault-Brunet et al., 2015).
Overall, these results strengthen the growing empirical evidence of the kinematic complexity of GGCs, motivating the need for deeper understanding.

1.2.3 Motions in the plane of the sky

Although studies based on LOS velocity have significantly improved our knowledge of GC internal kinematics, the PM measures provide advantages over some limitations of LOS velocities. LOS measurements require spectroscopy and are therefore limited to only the brightest (more massive) stars. Conversely, PMs are obtained from photometry and typically allow the observation of much fainter stars. In turn, this implies that PM studies provide larger statistics and measures for stars of different masses. Moreover, through the LOS measurements it is possible to derive a single velocity component, while PMs provide two velocity components. This is a

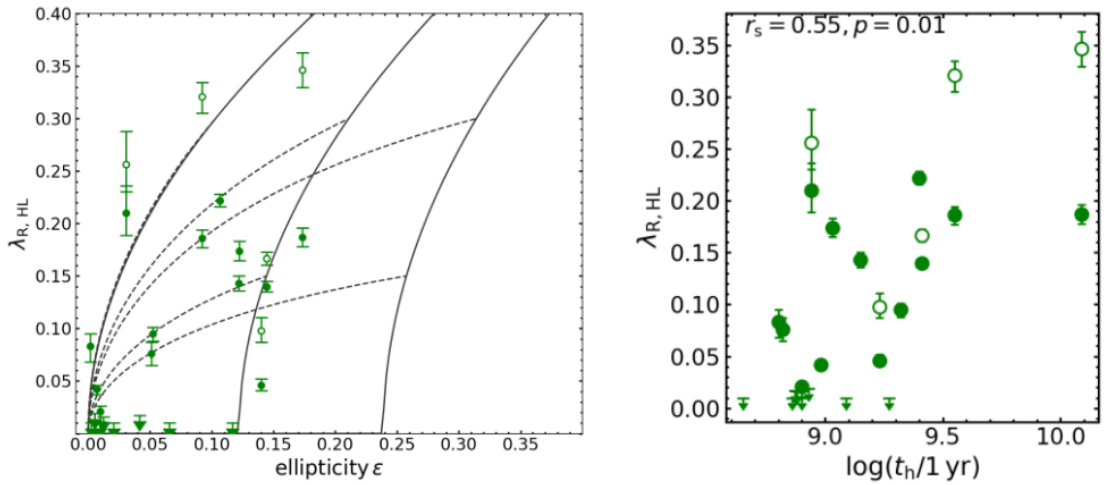

Figure 1.3: Rotation strengths (quantified by the parameters $\lambda_{\mathrm{R,HL}}$, similar to $V_{\mathrm{rot}}^{\mathrm{peak}}/\sigma_0$) as a function of the global ellipticities of the clusters (left panel), and of the logarithm of the relaxation time at the half-light radius logt_h (right panel). The values of $\lambda_{\mathrm{R,HL}}$ have been calculated at the half-light radius where possible, otherwise at the maximum radius covered by the MUSE data. In the latter cases, the authors show the values obtained by linear extrapolation to the half-light radius as open symbols. The solid lines in the left panel show the prediction for *edge-on* rotators in the isotropic case and for different values of anisotropy. While the dashed lines indicate the behaviour expected when varying the inclination. Figures taken from Kamann et al. (2018a).

great advantage because it allows to determine the velocity anisotropy of the cluster on the plane of the sky, as the ratio between the velocity dispersion of the tangential and radial components ($\sigma_{\mathrm{tan}}/\sigma_{\mathrm{rad}}$), thus leading to break the mass-anisotropy degeneracy (Binney & Mamon, 1982).
On the other side, obtaining accurate PM measurements can be very challenging, because it requires high-precision photometry and astrometry on quite long time baselines. Moreover, it is difficult to achieve fairly accurate photometric and astrometric measurements with ground-based telescopes, especially for faint stars in high-crowded regions (see, e.g., van Leeuwen et al., 2000; Bellini et al., 2009).

In the recent years, we have witnessed a breakthrough in PM-based studies mainly dues to the combination of multi-epoch HST observations on time baselines of more than 10 years and the launch of the Gaia mission.
Thanks to multi-epoch observations and high spatial resolution, HST is an excellent facility to measure the position of stars in GCs with high precision, even in the very crowded central regions. Moreover, improved techniques of data analysis (see Bellini et al. 2014, and the series of subsequent works, e.g., Watkins et al. 2015; Bellini et al. 2017, 2018; Libralato et al. 2018, 2022) have contributed to obtaining a growing number of increasingly accurate PM measurements.

Recently, Libralato et al. (2022) have presented a collection of PMs measures for 56 GCs, and the relative analysis of the internal kinematic properties of the clusters by computing the velocity dispersion and anisotropy profiles of their member stars

(see Figure 1.4). The anisotropy profiles show that the clusters generally have mildly

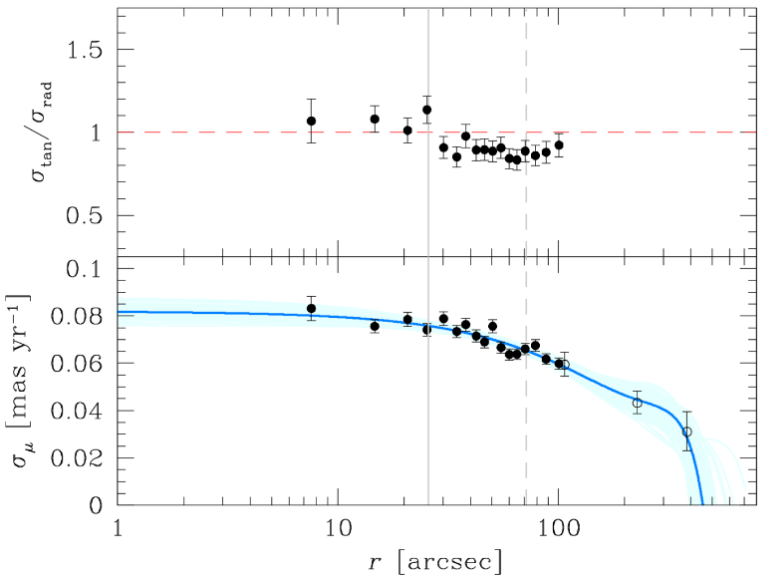

Figure 1.4: Velocity dispersion (bottom panel) and anisotropy radial profiles (top panel) obtained for NGC 5024 from PM measurements. The solid and dashed vertical lines mark the core and the half-light radius, respectively. Taken from Libralato et al. (2022).

radially anisotropic velocity distributions near the half-mass–radius, in agreement with previous findings (Watkins et al., 2015). Moreover, their results suggest that dynamically young clusters present a radially anisotropic velocity distribution at the half-light radius, while an isotropic distribution is characteristic of older systems, even at the half-light radius (see Figure 1.5). These results are consistent with theoretical predictions (see, e.g., Vesperini et al., 2014; Tiongco et al., 2016b; Bianchini et al., 2017) and previous observational works (Watkins et al., 2015), and confirm one more time the close link between kinematic and dynamical evolution.

The real revolution for the astrometry occurred with the Gaia mission, which by spanning the entire sky and providing high-precision PMs has ensured numerous improvements in many fields (Gaia Collaboration et al., 2018; Ibata et al., 2019, 2021). As for the study of the internal kinematics of GCs, dedicated studies have provided detailed characterization of the VD profiles, rotation curves, and anisotropy profiles of many GGCs (see, e.g., Bianchini et al., 2013; Jindal et al., 2019; Vasiliev & Baumgardt, 2021). However, Gaia-PM based studies are typically limited to bright stars outside the innermost high-density cluster regions. In fact, over-crowded environments, like GC cores, are challenging hurdles to overcome for the Gaia capabilities (Pancino et al., 2017).

Therefore, while Gaia observations are ideal to investigate the outermost regions, HST-PMs are required to explore the GC cores and their fainter stars, which are necessary to properly characterize GC internal kinematics. HST and Gaia are currently

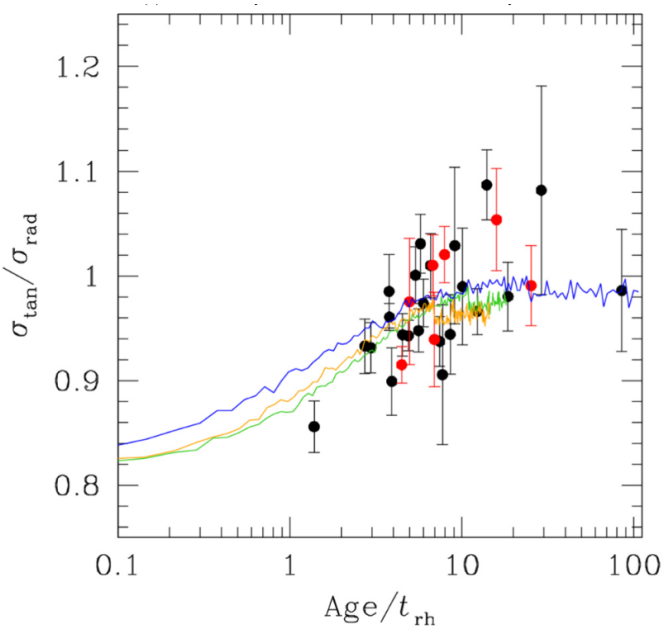

Figure 1.5: Anisotropy at the half-light radius as a function of the ratio between the cluster age and the half-mass relaxation time. The red points mark CC GCs. The three solid lines show the time evolution of $\sigma_{tan}/\sigma_{rad}$ from three Monte Carlo simulations with different initial W_0 and filling factors (defined as the ratio between the half-mass and tidal radius). Taken from Libralato et al. (2022).

the most suitable space missions for accurate, yet complementary, investigations of GGC kinematics on the plane of the sky.

1.3 Internal kinematics in Globular Cluster cores

In the previous Sections, we have extensively discussed the crucial importance of obtaining a full characterization of GCs internal kinematics to improve our understanding of the formation and evolutionary history of star clusters. It has been shown as well, that over the last decade, our abilities to study the internal kinematics of these systems have drastically increased, and that the advent of IF spectrographs has enabled us to perform spectroscopic analysis of individual stars even in crowded fields, like GCs.
However, most of the results so far, especially those based on LOS velocity, have been obtained by sampling the external and intermediate regions of GCs, while the exploration of the innermost cluster areas ($r < 10''$) is still limited by observational difficulties.

Being the most affected by dynamic processes, it is reasonable to expect remarkable and crucial kinematic features from the proper exploration of GC cores. For example, these high-density regions offer the ideal environment for the occurrence of stellar interactions able to generate exotic objects, like interacting binaries, blue

stragglers, millisecond pulsars (Bailyn, 1995; Ferraro et al., 1997, 2003; Pooley et al., 2003; Ransom et al., 2005), and even the long-sought class of intermediate-mass black holes (IMBHs; e.g., Giersz et al., 2015, see also Section 1.3.1). In addition, signatures of rotation or orbital anisotropy may also be expected. Therefore, a systematic exploration of the internal kinematic properties of the cores of these systems is an essential piece of information to reach a comprehensive view of the internal kinematics and dynamics of stellar clusters.
A few recent studies have started to reveal some of these interesting features, for instance: the central region of the GC NGC 3201 has been found to be the ideal environment to host a population of compact objects (Vitral et al., 2022), a complex counter rotating core has been observed in M15 (Usher et al., 2021), while Göttgens et al. (2021) have searched for an IMBH in the center of M80.

The studies presented in the following Chapters pose particular attention to the detailed exploration of the LOS kinematics in the cores of three GGCs (NGC 1904, NGC 6440 and NGC 6569). For this purpose we adopted the *multi-instruments approach* used in the MIKiS survey (Ferraro et al., 2018b, see also Chapter 2), complementing SINFONI, KMOS and FLAMES observations with data obtained from the AO-assisted IF spectrograph MUSE in the Narrow Field Mode (NFM) configuration, which provides the highest spatial resolution available. As clearly demonstrated by the results presented in the following Chapters (see also Göttgens et al., 2021; Usher et al., 2021), the MUSE/NFM performances have a breakthrough impact on the study of GC cores, allowing us to finally obtain the still missing characterization of their kinematic properties. The very efficient AO facilities of the MUSE/NFM configuration provide a really high spatial resolution ($0.025''$ pixel^{-1}), comparable to that of HST (see Figure 1.6). These unique capabilities allow to resolve hundreds of individual stars even in the first arcseconds from the cluster center, ensuring remarkable improvements over the capabilities of the wide field mode (WFM) configuration (e.g., Kamann et al., 2018a). Therefore, MUSE/NFM represents an unrivaled resource for exploring the kinematics in GC cores, enabling a much finer radial sampling of the innermost VD and rotation profiles, which are critical to properly quantifying the breadth and extent of kinematic features and possibly obtaining the first convincing detection of an IMBH.

1.3.1 IMBHs in Globular Cluster cores

Intermediate-mass black holes (IMBHs) are defined as black holes (BHs) with a mass in the range of $10^2 - 10^5\,M_\odot$, covering the empty gap between the upper boundary of stellar-mass BHs and the lower boundary of super-massive BHs (SMBHs). However, the IMBHs existence is still under debate.
Confirming their existence could be of fundamental importance for several astrophysical open issues: they would naturally bridge the gap between the two observed

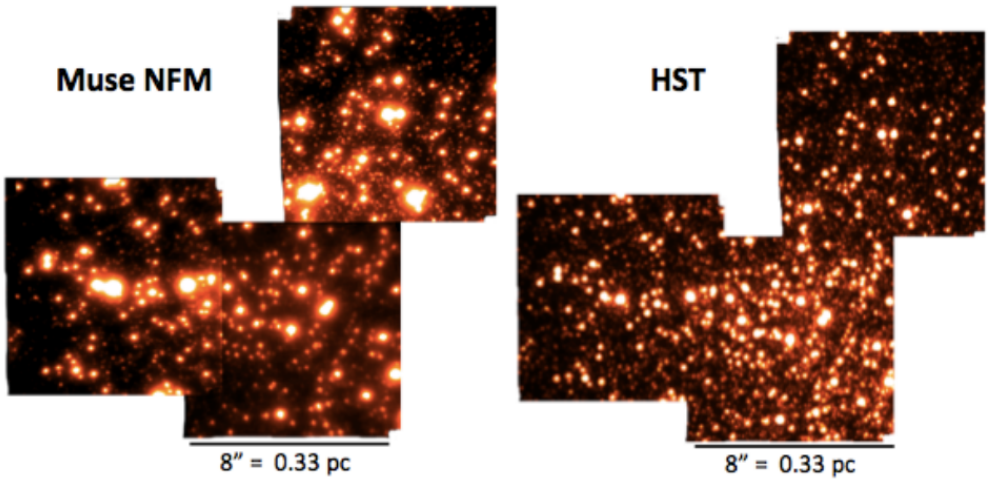

Figure 1.6: Comparison between the mosaic of three MUSE/NFM reconstructed images acquired during the Science Verification run in the centre of NGC 6440, and the corresponding HST/WFC3 images of the same fields. The high angular resolution of the MUSE/NFM observations, comparable to that of HST, appears evident. Note that this image was published in Leibundgut et al. (2019) as one of the major highlight of the MUSE/NFM Science Verification, to illustrate to the scientific community the revolutionary capability in terms of spatial resolution of this new MUSE mode.

BH mass limits (e.g., Reines & Volonteri, 2015), would help explaining the formation of SMBHs, which are observed even at redshift $z > 6$, when the Universe was just 1 Gyr old (e.g., Ebisuzaki et al., 2001; Tanaka & Haiman, 2009), would be among the best targets for gravitational wave detection, particularly in the core of dense stellar systems where they could easily capture other compact objects.
Several formation scenarios have been proposed for IMBHs. These objects could be the remnants of Population III stars (Madau & Rees, 2001), while according to Portegies Zwart et al. (2004), they could be originated from a runaway collision between highly massive main sequence stars located in the central regions of star systems. A recent scenario (Giersz et al., 2015) suggests that IMBHs form in star clusters as a result of aggregation of BH mass due to mergers during dynamical interactions and mass transfers in binaries. Therefore, considering that the extrapolation of the *Magorrian relation* (Magorrian et al., 1998) down to the IMBH masses leads to the GC mass regime (see Figure 1.7), and that most of the proposed formation scenarios require extreme stellar densities, GC cores are the best place where we can expect to find IMBHs. Up to now, the most promising observational hints of IMBH candidates are obtained from phenomena of mass accretion detected in massive clusters in distant galaxies (see, e.g., Ulvestad et al., 2007; Lin et al., 2020). While direct detection of an IMBH from radio or X-ray emissions in GCs are extremely challenging and often inconclusive since these stellar systems are almost gas free (e.g., Strader et al., 2012; Tremou et al., 2018; Kains et al., 2016).

The effects of the presence of an IMBH are also expected to be imprinted in the

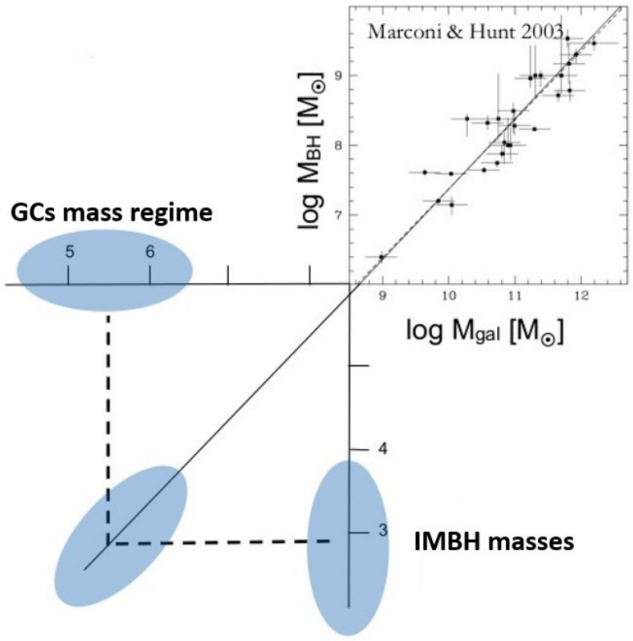

Figure 1.7: Extrapolation of the *Magorrian relation* (BH mass vs. bulge mass in logarithmic scale) to small masses. Following this relation, the mass of star systems that could host IMBHs matches that of GCs. Credits to Marconi & Hunt (2003).

phase-space distribution of stars in its vicinity (Bahcall & Wolf, 1976), impacting the structural and kinematic properties of the innermost regions of the host star cluster (Baumgardt et al., 2005; Miocchi, 2007). In particular, the best signatures of these elusive objects in GGCs are: the detection of a shallow cusp in the surface brightness or projected density profile (e.g., Noyola et al., 2008) and the presence of a Keplerian rise in the projected VD profile towards the centre (e.g., Noyola et al., 2008; Anderson & van der Marel, 2010; Lützgendorf et al., 2013).
However, other processes can also cause similar features, e.g., core collapse, mass segregation, or a population of dark remnants (black hole and neutron stars) hidden in the centre also produce a cusp in the density profile. In addition, an artificial central cusp in the VD profile can be observed in case of studies based on integrated light spectroscopy, as evidenced by the controversial case of NGC 6388. The latter is an explanatory case because Lützgendorf et al. (2011) using integrated light spectroscopy find a central cusp in the VD profile concluding that an IMBH is hidden in this cluster, while Lanzoni et al. (2013) deriving the VD profile from RV of individual stars refute this result because they find a constant inner plateau in the VD profile (a similar case is discussed in Chapter 3 for the GC NGC 1904). The discrepancy is likely ascribable to the presence of two bright stars with opposite RV that dominate the integrated-light spectra, thus bringing to an overestimate of the central VD of the system and of the central mass (see Lanzoni et al., 2013).

Hence, VD profiles from measurements of resolved individual stars are needed for the reliable detection of IMBHs in GGC cores, and consequently very high spatial resolution is requested as well. In fact, the radius of influence ($r_{\rm BH}$) for an IMBH of mass $M_{\rm BH} = 10^3\,{\rm M}_\odot$ in a GC with typical central velocity dispersion ($\sigma_0 \sim 10$ km s^{-1}) is only $\sim$0.04 pc, corresponding to less than $1''$ in the plane of the sky at the typical distance of a GGC, and this is the region where the cusp in the VD profile must be unveiled to prove the presence of an IMBH.

Therefore, the detection of IMBHs in GGCs is really challenging and it requires a very high spatial resolution to resolve stars in the very central regions of the clusters. At the moment, only HST PMs in the plane of the sky and MUSE/NFM data for the LOS velocities provide us with a chance to finally determine if IMBHs are hiding in the cores of GGCs.

Chapter 2

The MIKiS survey

2.1 The project

The MIKiS survey (Ferraro et al., 2018b) is an ongoing project aimed to provide the entire VD and rotation profiles of a large sample of GGCs, by exploiting a *multi-instruments approach* based on the combination of spectroscopic data sets acquired with different ESO-VLT instruments, with appropriate multi-object capabilities and different angular resolution powers.
The strategy adopted in the MIKiS survey is to explore the kinematics over the entire radial extension of a sample of representative GGCs exploiting the exceptional performances and the complementary capabilities of the current generation of spectrographs available at the ESO-VLT: (1) the diffraction-limited AO-assisted IF spectrograph SINFONI (operating in the NIR) to resolve the stars in the innermost regions, (2) the seeing-limited IF spectrograph KMOS to sample the intermediate radial range, and (3) the wide-field multi-object fiber-fed spectrograph FLAMES/GIRAFFE to cover the outermost cluster regions through more than 100 fibers simultaneously. This initial configuration has been recently complemented with observations acquired with the AO-assisted IF spectrograph MUSE/NFM under an ongoing large program (ID: 106.21N5, PI: Ferraro) and a series of other specific observational programs.

The sample of clusters selected for the MIKiS survey consists of 30 GGCs having properties representative of the overall Galactic population (see Figure 2.1), including a large range of central densities (as parameterized by the King concentration), different dynamical evolution stages (as measured by the value of the core relaxation time) and different environmental conditions (as traced by different heights on the Galactic plane). This variety of targets allows to explore possible correlations between kinematic properties and other fundamental features that affect the dynamical evolution of GCs.

Thanks to the adopted strategy, the MIKiS survey is expected to allow a comprehensive investigation of the LOS internal kinematics from the innermost to the outermost regions of each cluster, with crucial impact on different aspects of GC physics. First, the project aims to unveil the presence of systemic rotation and the

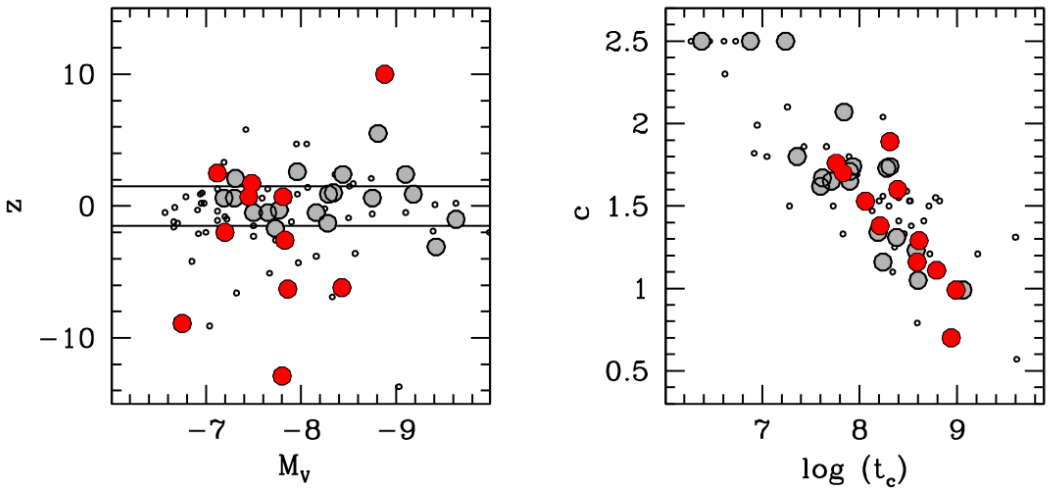

Figure 2.1: Distribution of the GGCs observed in the MIKiS survey (large circles) in the planes of height on the Galactic plane (z) vs. absolute integrated V-band magnitude (M_V, left panel) and concentration parameter (c) vs. core relaxation time (t_c, right panel). The red large circles mark the 11 GCs discussed in Ferraro et al. (2018b), while the small dots represent the entire GGC population plotted for reference. Taken from Ferraro et al. (2018b).

long-sought IMBHs (see Section 1.3.1), improving the constraints on the physics and formation processes of both GCs and these elusive compact objects (see, e.g., Baumgardt et al., 2005; Miocchi, 2007; Varri & Bertin, 2012; Zocchi et al., 2017; Tiongco et al., 2017). Then, from the values of the central velocity dispersion it is possible to derive an estimate of the total mass of the system. Moreover, the study of the kinematic properties of multiple populations with different light-element content is another goal of the survey, in order to improve the constraints to GC formation scenarios (e.g., Vesperini et al., 2013; Richer et al., 2013; Bellini et al., 2015; Hénault-Brunet et al., 2015). Finally, by combining the LOS velocity measurements of the MIKiS survey with appropriate PM measures (based on HST and/or Gaia observations), it is possible to obtain the full three-dimensional characterization of the internal kinematics of GGCs (see, e.g., Sollima et al., 2019, and the scientic case discussed in Chapter 3).

At the same time, it is of crucial importance to combine the kinematic results of the MIKiS survey with those obtained from complementary studies, such as the accurate characterization of GC structural parameters from resolved star density profiles (e.g., Lanzoni et al., 2007a, 2019; Miocchi et al., 2013, see also Chapter 4 and 5), the investigation of the population of stellar exotica (e.g., Ferraro et al., 2003, 2015, 2016; Pallanca et al., 2010, 2013, 2017; Cadelano et al., 2017, 2018, 2020a), and the determination of GC dynamical ages from fully empirical methods (e.g., Ferraro et al., 2012, 2018a, 2019; Lanzoni et al., 2016; Bhat et al., 2022, 2023). The combination of these complementary aspects provides a comprehensive overview of the internal kinematics and structure of GCs, which is necessary to

properly reconstruct the evolutionary history of these systems and understand how dynamical processes impact their evolution and the formation of stellar exotica.

2.2 The MIKiS data sets and reduction

The spectroscopic data sets adopted in the MIKiS survey were acquired mainly under three dedicated ESO large programs: 193.D-0232 (PI: Ferraro) for FLAMES and KMOS observations, 195.D-0750 (PI: Ferraro) for SINFONI observations, and the ongoing program 106.21N5 (PI: Ferraro) for the complementary MUSE/NFM data set, plus additional individual programs.
The kinematic studies presented in this thesis are primarily based on data sets acquired as part of the MIKiS survey. For this reason, in this Section, we present a description of the main characteristics and key capabilities of each instrument exploited by the MIKiS survey and adopted in this thesis work, along with a brief description of the related data reduction. In addition, Appendix A is specifically dedicated to the preliminary validation tests performed on the MUSE data.

2.2.1 MUSE

The innermost cluster regions are excellently sampled with the spectrograph MUSE in the narrow field mode (NFM) configuration. MUSE (Bacon et al., 2010) is mounted on the Yepun, the VLT-UT4 telescope at the ESO Paranal Observatory. It has a modular structure composed of 24 identical Integral Field Units (IFUs), and it is available in two configurations, wide field mode (WFM) and NFM, the latter providing a higher spatial resolution. MUSE/WFM provides a $1' \times 1'$ field of view, with a spatial sampling of $0.2''$ pixel^{-1}. The WFM configuration is available with no AO-correction or equipped with the Adaptive Optics Facility (AOF) of the VLT in combination with GALACSI (the Ground Atmospheric Layer Adaptive Corrector for Spectroscopic Imaging, Arsenault et al., 2008; Ströbele et al., 2012). MUSE in the NFM configuration covers a $7.5'' \times 7.5''$ field of view with a spatial sampling of $0.025''$ pixel^{-1}. It is available only in the AO mode and, compared with the WFM, additionally takes advantage of the Laser Tomography AO correction. MUSE/WFM offers two different wavelength coverages, nominal and extended mode, which correspond to $4800 - 9300$ Å and $4650 - 9300$ Å, respectively, with a spectral resolution R ~ 3000 at $\lambda \sim 8700$. Conversely, MUSE/NFM is available only in nominal mode providing the same resolving power.

The MUSE/NFM targets acquired as part of the MIKiS survey consist of mosaics of multiple pointings located in the center region of the clusters. As typically adopted in the MIKiS observing campaign, for each MUSE pointing, multiple exposures, typically three, were acquired with a small dithering pattern and a rotation offset

of 90° between consecutive exposures, in order to remove possible systematic effects and resolution differences between the individual IFUs. The MUSE data of the MIKiS survey was reduced by using the standard MUSE pipeline (Weilbacher et al., 2020). In a first step, the pipeline applies the bias subtraction, flat fielding, and wavelength calibration for each individual IFU. In a second step, it uses these pre-processed data to perform the sky subtraction and flux and astrometric calibration. In addition, all the data are corrected for the heliocentric velocity. Then, the data from all 24 IFUs are combined into a single datacube. As the last step, the pipeline provides a final datacube by combining the datacubes of the multiple exposures of each pointing, taking into account the offsets and rotations among the different exposures.

2.2.2 SINFONI

The cluster central regions have been also investigated by using the spectrograph SINFONI (Eisenhauer et al., 2003), which is a near-infrared ($1.1 - 2.45\mu$m) IF spectrograph fed by an AO module. SINFONI operates with 4 gratings (J, H, K, H+K). In particular, the MIKiS program exploits the $K-$band grating, providing a spectral resolution R $\sim$ 4000 and sampling the $1.95 - 2.45$ μm wavelength range. SINFONI provides a spatial scale of $0.25''$/spaxel corresponding to a field of view of $8'' \times 8''$ (hereafter named "LR" for low resolution), and a spatial scale of $0.1''$/spaxel and a $3'' \times 3''$ field of view (hereafter, "HR" for high resolution). During the acquisition, multiple exposures were performed on the target and, for background subtraction purposes, on a sky position, following the target-sky sky-target sequence. The data reduction was performed by using esorex (3.13.6) following the workflow 3.3.2 under the EsoReflex environment (Freudling et al., 2013). The pipeline first corrects all target and sky exposures for darks, flats, geometrical distortions, and differential atmospheric refraction. Then, the sky background is subtracted by using the sky exposures, the wavelength calibration is performed through the observations of a Th-Ar reference arc lamp, and, the datacubes are built for each exposure by combining the corrected target frames.

2.2.3 KMOS

The intermediate distances from the center are sampled by using the spectrograph KMOS (Sharples et al., 2013) at ESO-VLT. It is equipped with 24 IFUs that can be allocated within a $7.2'$ diameter field of view. Each IFU covers a projected area on the sky of about $2.8'' \times 2.8''$, with a spatial sampling of $0.2''$/pixel. The observation included in the MIKiS survey were performed using the YJ grating covering the 1.025-1.344 μm spectral range at a resolution R $\sim$ 3400, corresponding to a spectral sampling of $\sim$ 1.75 Å/pixel. Typically, each IFU is centered on one star, while the

targets stars are selected along the red giant branch (RGB) of the cluster from an appropriate photometric catalogs, usually using the near-infrared SOFI catalogs available at the web site http://www.bo.astro.it/∼GC/ir_archive/ (Valenti et al., 2004, 2007), and 2MASS catalogs in the J, H, and Ks filters to sample the outer regions. The KMOS data reduction has been performed by using the dedicated pipeline* executing background subtraction, flat field correction, and wavelength calibration.

2.2.4 FLAMES

The outermost cluster regions are sampled by using the fiber-fed multi-object spectrograph FLAMES (Pasquini et al., 2002) in the GIRAFFE/MEDUSA mode. This configuration consists of 132 fibers, each one with an aperture of 1.2″ on the sky, that can be allocated over a field of view of 25′ in diameter. Within the MIKiS survey the FLAMES spectra were acquired with the HR21 grating setup, which provides a resolving power $R \sim 18000$ between 8484 and 9001 Å. As for KMOS the targets were selected from the same photometric SOFI catalogs (Valenti et al., 2004, 2007)†, and from the 2MASS catalogs. The data set has been reduced with the dedicated ESO pipelines*, including bias subtraction, flat-fielding correction, wavelength calibration, and extraction of one-dimensional spectra. For each spectrum, the sky background has been subtracted, using a master sky spectrum obtained from the sky exposures acquired with 15-20 dedicated fibers in each pointing.

2.3 Some remarkable results

Notable results obtained as part of the ESO-VLT MIKiS survey are presented in Ferraro et al. (2018b), Lanzoni et al. (2018a) and Lanzoni et al. (2018b).
In Ferraro et al. (2018b), the authors explore the potentiality of the multi-instrument approach by investigating the internal kinematics of 11 GCs using RV from spectra of individual stars acquired from FLAMES and KMOS observations. They provide the VD profile of all the surveyed systems (see Figure 2.2), finding that they decline at increasing radii, in agreement with the expectation from the King models that best fit the density/luminosity profiles. In the majority of the analyzed GCs, Ferraro et al. (2018b) detect signatures of rotation within a few half-mass radii from the center. These results are in general agreement with the predictions of theoretical studies (e.g., Fiestas et al., 2006; Ernst et al., 2007; Hong et al., 2013; Tiongco et al., 2017), suggesting that the observed signals could be the relic of significant internal rotation set at the epoch of the cluster's formation.

* http://www.eso.org/sci/software/pipelines/
†The catalogs are available at the web site http://www.bo.astro.it/∼GC/ir_archive/

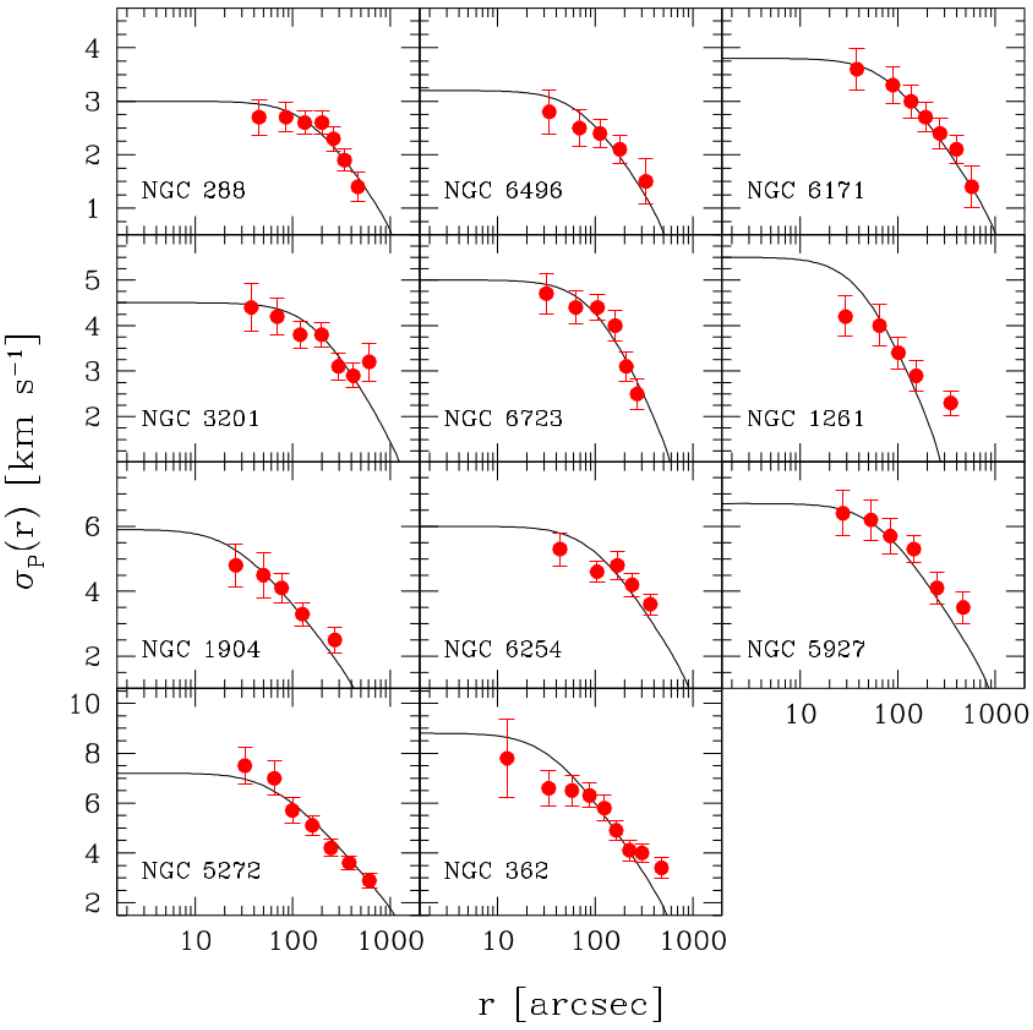

Figure 2.2: Projected velocity dispersion profiles of the 11 GGCs surveyed in Ferraro et al. (2018b) determined from the RV of individual stars (red filled circles). The solid lines correspond to the projected VD profiles of the King models that best fit the observed density/surface brightness distributions. Taken from Ferraro et al. (2018b).

Lanzoni et al. (2018a) derive the LOS rotation curve of the GC M5 (NGC 5904) finding one of the cleanest and strongest signal of rotation observed in GGCs (only a few other similar cases are known, e.g., NGC 4372 in Kacharov et al. 2014 and 47 Tucanae in Bellini et al. 2017), with a very stable rotation axis over the entire cluster extension. The exceptional rotation curve shown in Figure 2.3 is well reproduced by the analytical relation for a cylindrical rotation (red line in the figure), which is inspired by the structure of the velocity space of stellar systems resulting from the process of violent relaxation (Lynden-Bell, 1967; Gott, 1973). Lanzoni et al. (2018a) find a rotation velocity peak of ~ 3 km s^{-1} at ~ 0.6 half-mass radii, while the ratio between the rotation peak and the central velocity dispersion, commonly used to determine the relative importance of ordered versus random motions (see Section

1.2.1, and also, e.g., Bianchini et al. 2013; Kacharov et al. 2014; Fabricius et al. 2014; Boberg et al. 2017), is $V_{\rm rot}^{\rm peak}/\sigma_0 \sim 0.4$ suggesting that the ordered motions play a non-negligible role in the dynamical evolution of the cluster. The study reveals also the expected flattening of the system in the direction perpendicular to the rotation axis.
These results, together with the other rotation signatures found in Ferraro et al. (2018b), provide further confirmation that most of these systems were born with significant amounts of ordered motions, implying that the angular momentum has a significant role in the dynamical evolution of collisional systems, like GCs.

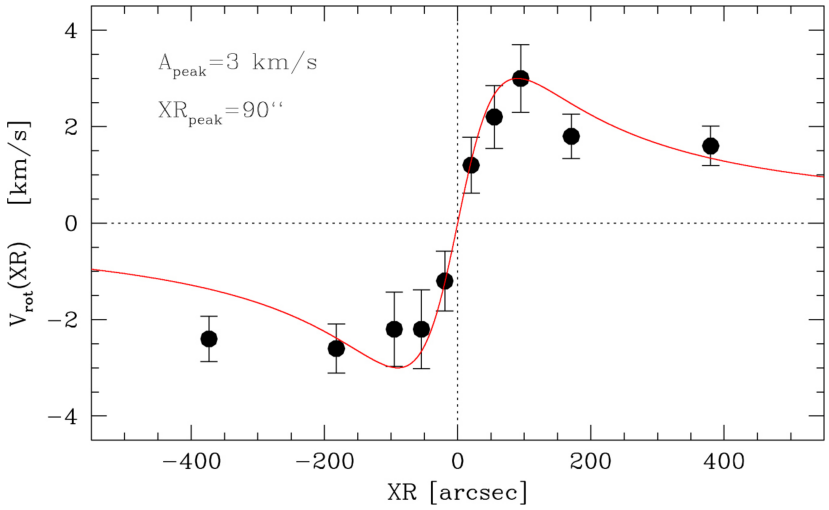

Figure 2.3: Rotation curve of M5. The red line is the analytical model for a cylindrical rotation (Lynden-Bell, 1967), which well reproduces the observed curve (black circles). Taken from Lanzoni et al. (2018a).

The other interesting result concerns the internal kinematics of NGC 5986 investigated in Lanzoni et al. (2018b). The authors reveal the presence of a solid-body rotation extending from the cluster center to the outermost regions (see the left panel of Figure 2.4), and a VD profile showing a significant deviation from the commonly expected King model. In fact, the profile initially decreases with the distance from the cluster center, but then stays flat with a constant behavior at ~ 5 km s^{-1} for distances larger than about one half-mass radius (see the right panel of Figure 2.4). From the comparison with theoretical models (Tiongco et al., 2016a,b; Tiongco et al., 2017), Lanzoni et al. (2018b) find that the co-existence of these two kinematic features may be due to the evolutionary interplay between the system and the MW tidal field, which has a strong impact on the dynamical evolution of GGCs. In particular, this result proves that the current kinematic properties of these systems are the consequence of their long-term dynamical evolution, which is strongly affected by the internal relaxation, star escape, angular momentum transport and loss, and the interaction with the Galaxy tidal field.

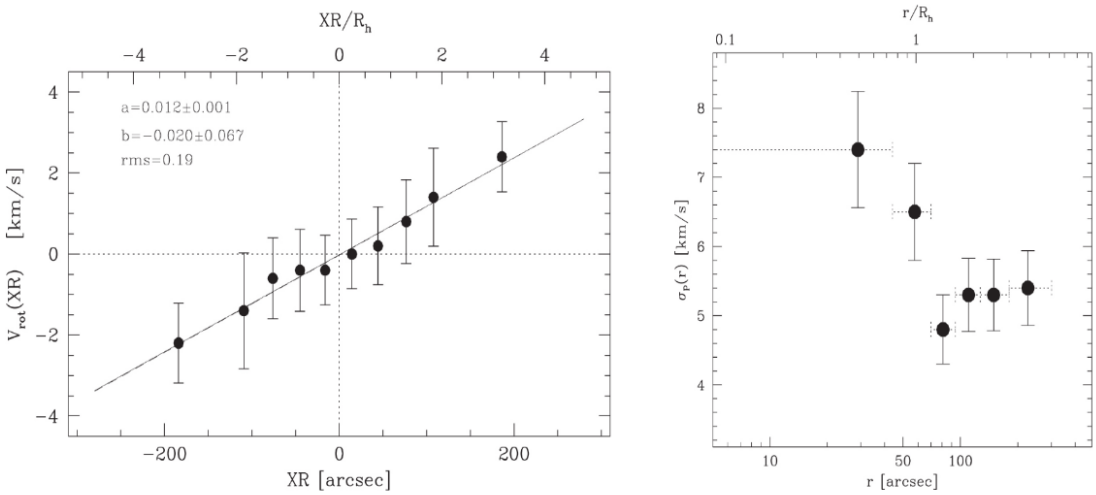

Figure 2.4: Rotation curve (left panel) and projected velocity dispersion profile (right panel) of NGC 5986. In the left panel, the slope (a), intercept (b), and rms scatter (rms) of the best-fit line (solid black line) to the observed behavior are labelled. Figures taken from Lanzoni et al. (2018b).

2.3.1 Thesis work in the context of the MIKiS Survey

As stated above, this thesis was developed as part of the ESO-VLT MIKiS survey, and Chapters 3, 4, and 5 are reserved for the detailed description of the latest results obtained in this context. Comprehensive studies combining internal kinematic and structural properties of these three GGCs are discussed in the following. In particular, the analyzed targets have different values of concentration (c), located two in the Galactic bulge (NGC 6440 and NGC 6569) and one in the halo (NGC 1904), and among them, NGC 1904 is a possible candidate to host an IMBH (see, Lützgendorf et al., 2013). Moreover, this thesis work has the particular goal of unraveling the core kinematics of these GCs, including, for the first time in the MIKiS survey, the analysis of MUSE/NFM data sets.

Chapter 3

Velocity dispersion profile and rotation curve of NGC 1904

Mainly based on:
Leanza et al. (2022), ApJ, 929, 186

3.1 Introduction

In this Chapter, we present the detailed investigation of the internal kinematic properties of M79 (NGC 1904). The target is a well-known metal-intermediate and low-extinction GGC, with [Fe/H]$= -1.6$ dex, E$(B-V) = 0.01$ (Harris, 1996, 2010 edition; Ferraro et al., 1999b), and a blue extended Horizontal Branch (Ferraro et al., 1992; Lanzoni et al., 2007b; Dalessandro et al., 2013). According to the King model that best fits the star count density profile presented in Miocchi et al. (2013), the internal structure of NGC 1904 is characterized by a dimensionless central potential $W_0 = 7.75$, which corresponds to a concentration parameter $c = 1.76$, while the core, three-dimensional half-mass, projected half-mass and tidal radius are $r_c = 9.4''$, $r_h = 56.7''$, $R_h = 41.7''$ and $r_t = 9.32'$, respectively.
This cluster is particularly intriguing since it was indicated as the possible host of an IMBH of $\sim 3000\,M_\odot$ on the basis of the central rise in the VD profile obtained from integrated-light spectra in the innermost regions of the system (see, Lützgendorf et al., 2013).

The kinematic study presented in this Chapter is based on RVs of individual stars obtained from the MIKiS survey (see Chapter 2) by complementing the KMOS and FLAMES measurements in the external regions (see, Ferraro et al., 2018b), with recent MUSE observations of the innermost $\sim 15''$ in the highest available spatial resolution configuration. In addition, archive MUSE data at lower spatial resolution have also been used extending the data set to radial distances of $\sim 67''$ from the center.
Combining the mentioned data sets, we derived the VD profile and rotation curve of NGC 1904 from a sample of more than 1700 RV measures of individual stars distributed over the entire cluster extension, between $\sim 0.3''$ and $770''$ ($\sim 14 \times r_h$)

from the center. We investigated the rotation also in the plane of the sky by using the PMs provided by the Gaia EDR3, and then we obtained the three-dimensional kinematic characterization of the cluster by combining PMs and LOS measurements for a sub-sample of stars. As a final result, the comparison of the observed rotation curves with the results of a representative *N*-body simulation of a rotating star cluster confirmed what was discussed in the previous Chapter (see Section 1.2.1), showing that the present-day kinematic properties of NGC 1904 are consistent with those of a dynamically old system that has lost a significant fraction of its initial angular momentum.

3.2 Data sets

As discussed above, to construct the VD profile of NGC 1904 we complemented the catalog presented in Ferraro et al. (2018b) with a new set of spectroscopic data at high spatial resolution. To acquire spectra of individual stars in the innermost regions of NGC 1904, we took advantage of the superb spatial resolution capabilities of the AO-assisted IF spectrograph MUSE/NFM (Bacon et al., 2010, see also Chapter 2, Section 2.2.1). The MUSE/NFM data set acquired in NGC 1904 consists of a mosaic of seven MUSE/NFM pointings covering the innermost $\sim 15''$ from the cluster centre (Lanzoni et al., 2007b). The observations have been collected on 2019, November 1-5 and December 2-6 (ESO proposal ID: 0104.D-0636(A), PI: Ferraro, see Table 3.1). A series of 835 s long exposures were secured under good seeing conditions: the average DIMM seeing during the observations was always better than $\sim 0.7''$.

The NFM data set has been complemented with archive observations (ESO program ID: 098.D-0148(A), PI: Dreizler) acquired with MUSE/WFM, providing velocity measures at intermediate distances from the cluster center and allowing a proper overlap with the data presented in Ferraro et al. (2018b). A mosaic of four WFM pointings has been included in the analysis, each pointing having an exposure time of 120 s. This data set covers a cluster region up to $\sim 67''$ from the center, including the area sampled by the high-resolution NFM observations.

Figure 3.1 (left panel) shows the reconstructed data cube image of the NFM observations for the 7 available pointings named according to their position with respect to the cluster center: *Center* (C), *South* (S), *East* (E), *West* (W), *North* (N1), *North* (N2) *South-East* (SE). Note that only two exposures were acquired in fields N2 and E because of technical problems. The reconstructed image of the four WFM pointings is shown in the right panel of the same figure.

Indeed, already from a first visual inspection, the NFM observations immediately appears of superb quality, well comparable to the quality of HST images. This can be even better appreciate in Figure 3.2, where the reconstructed NFM image of

the W pointing (central panel) is compared with an image of same region as seen from the Planetary Camera of the HST/WFPC2 (right panel), and as sampled by the WFM observations (left panel). From this comparison, it is clear that NFM observations are mandatory to obtain a large number of RV measurements from individual stars in the core of the cluster.

Table 3.1: MUSE/NFM data set.

Name	RA	Dec	Date	N_{exp}
C	81.045674	−24.52522	2019-11-05	3
S	81.044944	−24.52612	2019-12-03	3
SE	81.046915	−24.52657	2019-12-04 2019-12-06	3 3
E	81.049125	−24.52575	2019-12-03	2
W	81.043994	−24.52513	2019-12-04	3
N1	81.046829	−24.52267	2019-12-06	3
N2	81.046788	−24.52191	2019-11-02	2

NOTE– Name, coordinates (in degree), observation date and number of exposures (N_{exp}) for each NFM pointing analyzed.

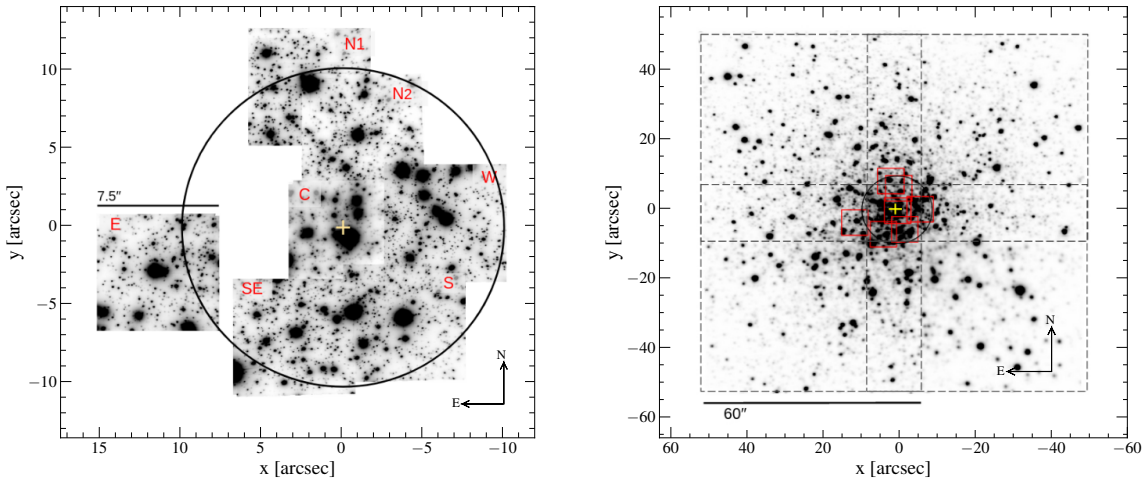

Figure 3.1: *Left:* Reconstructed I-band images of the seven MUSE/NFM pointings. The x and y axes represent the projected positions of the stars with respect to the cluster center (yellow cross, from Lanzoni et al., 2007b). The circle is centered on the center and has a radius of 10″. *Right:* Reconstructed I-band image of the four MUSE/WFM pointings (each sampling 60″ × 60″ on the sky; dashed squares), with the location of the seven NFM pointings overplotted in red. The yellow cross and the circle are as in the left panel.

3.3 Analysis

3.3.1 Photometric analysis and selection of target stars

The photometric analysis has been performed on the two-dimensional image extracted from each data cube from the stacking of MUSE slices in the wavelength range $8540 - 8550$Å (which is the region of the Calcium triplet, providing the highest signal-to-noise ratio, S/N). To determine the position of the centroid of individual sources and identify possible blends in the MUSE data, we took advantage of catalogs obtained from HST observations, which guarantee the necessary angular resolution to properly resolve stars in the highly crowded central regions of the system. For the innermost area we used a catalog obtained from images acquired with the HST/WFPC2 Planetary Camera (having a pixel-scale of $0.046''$ pixel^{-1}), in the filters F439W (hereafter B) and F555W (hereafter V). The catalog has been placed on the absolute astrometric system through cross-correlation with the photometric catalog of Stetson et al. (2019)*, and the instrumental magnitudes were then calibrated using the catalog discussed in Lanzoni et al. (2007b).

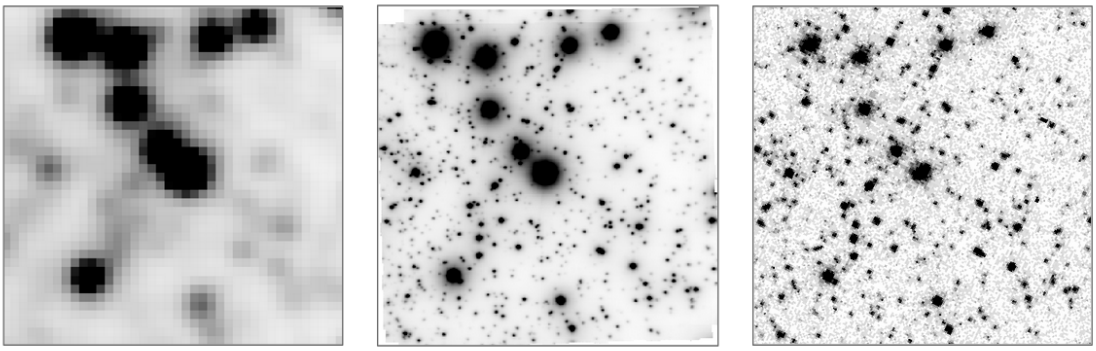

Figure 3.2: Reconstructed MUSE/NFM image of the W pointing (central panel), compared with that obtained with the Planetary Camera of the HST/WFPC2 (right panel) and the MUSE/WFM observations (left panel). In all cases the field of view samples an area of $\sim 8'' \times 8''$ on the sky.

A quick photometric analysis of the NFM images provided us with the preliminary position of the brightest sources. Then, the cross-correlation with the HST catalog allowed us to assign to every star observed with HST an (X,Y) position in the coordinate system of the NFM images. The best-fit PSF model has been determined by analyzing the brightest ~ 10 stars in each pointing with daophot/psf (Stetson, 1987). Finally, we ran daophot/allstar (Stetson, 1987) to perform the PSF fitting photometry at the (X,Y) centroid position of all the HST sources with $V < 21$.†

*For the photometric catalog, see https://www.canfar.net/storage/list/STETSON/homogeneous/MNRAS_Photometry_for_48_Clusters/.

†This magnitude cut has been set after the preliminary photometric analysis revealed that sources fainter than this limit are not reliably detected by the available NFM observations.

As a result, the PSF fitting analysis yields, for each image, the accurate position of the centroid and the instrumental magnitudes of each stellar source. As a double check, we verified that the position of the stellar centroids obtained from the PSF fitting procedure was not significantly altered by the procedure (this could happen, in principle, for the effect of a bright neighbor, or in the case of blending). Stars with centroid deviations larger than δX and $\delta Y > 0.5''$, with respect the HST position, have been excluded from the analysis. As final result of the entire procedure, for each star identified in each MUSE pointing, we obtain the X and Y positions in the datacube, the RA, Dec absolute coordinates, and the B and V magnitudes.

A similar analysis has been performed for the WFM data set. In this case, the HST reference catalog used to identify the stellar centroids has been obtained from the combination of the two WFPC2 data sets presented in Lanzoni et al. (2007b) and different magnitude cuts have been adopted: $V < 17$ for $r < 20''$, and $V < 19$ in the region between $20''$ and $80''$ from the center. The adopted limits are brighter than those used in the analysis of the NFM data because of the brighter magnitude level reached by the WFM observations, which is clearly apparent from the comparison shown in Figure 3.2 and is due to shorter exposure times. Moreover, these limits depend on the radial distance from the center because, due to the low spatial resolution of the WFM observations, only brighter stars can be resolved in the higher density regions.

The $(V, B-V)$ color-magnitude diagrams (CMDs) of all the stars identified in the MUSE NFM and WFM images are overplotted to the CMD of NGC 1904 (from Lanzoni et al., 2007b) in the left and right panels of Figure 3.3, respectively.

3.3.2 Stellar radial velocities

As mentioned in the Introduction, our approach to determine the internal kinematics of GGCs consists in measuring the RVs of resolved sources from individual stellar spectra. The procedure adopted for each MUSE data cube can be summarized as follows:

- *step (1): extraction of the spectra.* The spectra have been extracted at the coordinates of the stellar centroids identified during the photometric procedure (see Section 3.3.1). Since the targets are located in highly crowded regions, in order to limit the possible contamination from close sources, we made the conservative choice of extracting only the spectrum of the centroid spaxel of the target star and the 4 adjacent ones along the X and Y directions (hence, the 5 spaxels drawing a cross centered on the centroid of the source).

- *step (2): normalization of the spectra.* The spectra have been normalized to the continuum estimated by a spline fitting of the portion of the spectrum in the wavelength range $6700 - 9300$ Å. The S/N has been estimated for each

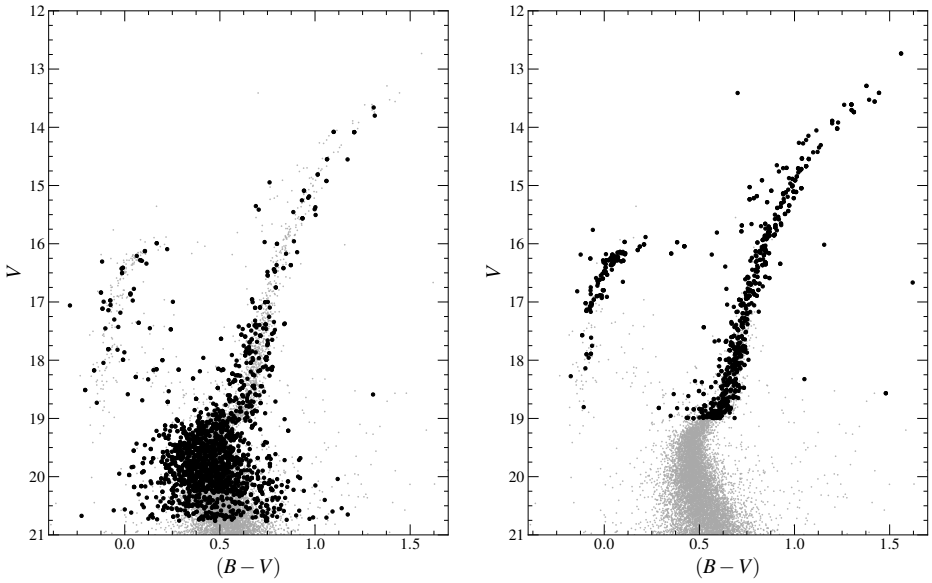

Figure 3.3: CMD of NGC 1904 (gray dots) obtained from the WFPC2 catalogs presented in Lanzoni et al. (2007b), with all the stars identified in the photometric analysis of the MUSE NFM and WFM images highlighted as large black dots (left and right panels, respectively).

spectrum as the ratio between the average of the counts and its standard deviation in the wavelength range $8000 - 9000$ Å.

- *step (3): selection of template spectra.* A library of template synthetic spectra has been computed with the SYNTHE code (Sbordone et al., 2004; Kurucz, 2005), adopting the cluster metallicity (Harris 1996, 2010 edition) and appropriate atmospheric parameters (effective temperature and gravity) according to the target evolutionary stage derived from the CMD.

- *step (4): measurement of RVs.* The RV of almost all the selected stars has been measured from the Doppler shift of the Calcium Triplet lines in the normalized spectra, in the wavelength range 8450 - 8740 Å. In the case of horizontal branch (HB) stars, because of the blending between the Calcium triplet lines and the hydrogen Paschen lines, we used the hydrogen lines in the spectral range 8500 - 8930 Å. The adopted method consists in the analysis of the residuals between the observed spectrum and a set of reference spectra shifted in wavelength by quantities corresponding to different velocities, testing all the values in the range $0 - 400$ km s^{-1}, at 0.1 km s^{-1} steps. The adopted RV is obtained from the wavelength shift that minimizes the standard deviation of the residuals.

Figure 3.4 shows an example of the output of this procedure. The observed spectra, with different S/N and corresponding to stars with different temperatures, are shown

in black. For each of them, the figure also shows the best-fit template shifted by the adopted value of RV. As discussed above, while the Calcium triplet has been used to measure RV of the two colder stars ($T < 5000$ K, two top spectra), the hydrogen Paschen lines have been exploited for the hottest source ($T = 8500$ K, bottom spectrum). The RV values obtained from the adopted method have been compared with the results of the "standard" cross-correlation approach (Tonry & Davis 1979a) implemented in IRAF, always showing good agreement independently of the spectrum S/N.

The final value of RV for each star and its uncertainty have been then computed, respectively, as the weighted mean and the weighted standard deviation of the measures obtained from the 5 extracted spaxels, after a 3σ-rejection procedure aimed at removing clearly discrepant values generated by spurious effects. The relative weights of the five measures have been defined according to the fraction of the star light sampled by each spaxel, estimated from the adopted PSF model: we assumed weight = 1 for the central and most exposed spaxel, while weight = 0.4 and 0.5 for the 4 adjacent spaxels in the NFM and WFM samples, respectively. We used the sub-samples of stars having multiple measures to check for the reliability of the RV uncertainties. By applying the method described in Section 4.1 of Kamann et al. (2016), we found that the adopted errors could be slightly overestimated (by ~ 0.4 km s^{-1}). However, by taking into account that the sample of repeated measures is poor ($\sim 80 - 100$ stars) and the impact on the results of the study is negligible, we decided to introduce no corrective factors. The final S/N associated to each star is the weighted average of the S/N values of the considered spectra. For the following analysis, we finally selected only those stars for which the RV value was determined from at least 3 spaxels over 5, and with S/N≥ 10. The typical uncertainties are < 5.0 km s^{-1} for the brightest stars ($V < 16$), while they increase for fainter magnitudes according to the corresponding decrease in S/N (see Figure 3.5). To produce a homogeneous final catalog, we first checked for possible systematic offsets in RV among the different MUSE pointings. To this purpose, we compared the RV values of the stars in common between two overlapping fields, always finding good agreement within the errors (only the E pointing has no objects in common with the other fields). In the cases of multiple exposures for the same star, we determined its final RV as the weighted mean of all the measures, by using the individual errors as weights.

To sample the entire radial extension of NGC 1904, we then needed to combine the MUSE RVs thus measured, with the catalog obtained by Ferraro et al. (2018b) from FLAMES and KMOS observations. We assumed as "reference" RV values those measured from the FLAMES data set, because the spectral resolution of this instrument is the highest and thus provides the most accurate and reliable measures. By using the stars in common between the MUSE/WFM and the FLAMES samples,

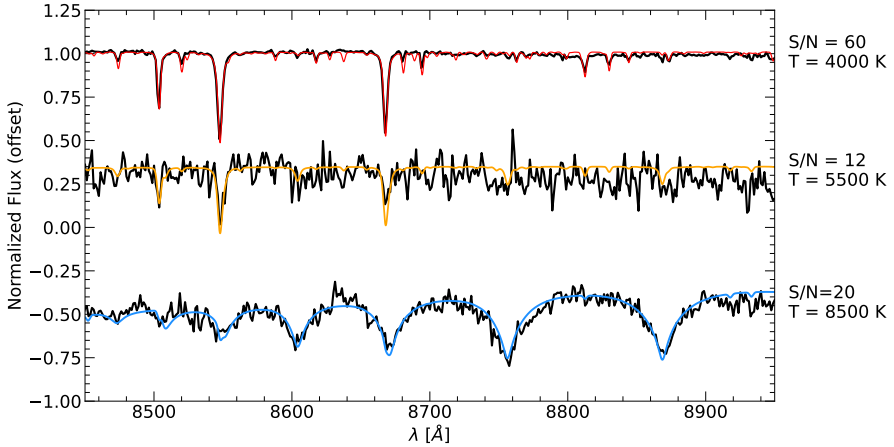

Figure 3.4: Examples of spectra acquired with MUSE/NFM in the region of the Calcium triplet lines (in black) for different S/N values and for stars with different atmospheric parameters (see labels). The best-fit template spectra, shifted by the adopted RV value, are overplotted as colored lines. In the bottom spectrum, corresponding to an HB star with effective temperature $T = 8500$ K, the Calcium triplet lines is strongly blended with the hydrogen Paschen lines. The examples shown are a good representation also of the spectra acquired with MUSE/WFM.

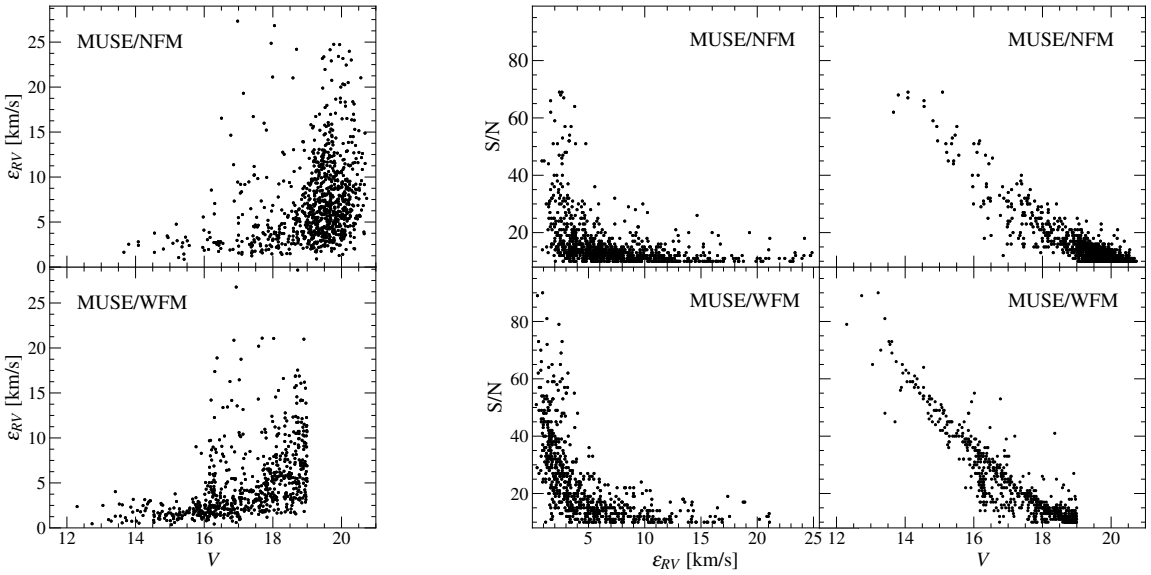

Figure 3.5: *Left panel:* RV uncertainty (ϵ_{RV}) as a function of the star magnitude for the targets of the MUSE/NFM and MUSE/WFM samples (top and bottom panel, respectively). *Central and right panels*: S/N as a function of velocity error and star magnitude, for the NFM targets (top panels) and the WFM sample (bottom panels).

we found just a very small average offset (-1.0 km s^{-1}), which was then applied to the WFM sample for realigning it with the reference catalog. A residual -0.5 km s^{-1} offset was then identified between the RV values measured for the stars in common

between the NFM and the (realigned) WFM data sets. After applying this small offset to the NFM data, we finally obtained three homogeneous samples of RVs. To create the final catalog, where every star is assigned with a single RV value, we adopted the following criteria aimed at adopting the best available measure in each case: for the stars in common between FLAMES and MUSE/WFM, we selected the RV measurements obtained with FLAMES, for the stars in common between KMOS and MUSE, we used the MUSE measures, and in case of common targets between MUSE/WFM and MUSE/NFM, we used the NFM values.

The final catalog lists 1726 individual stars with measured RV, each data set contributing as follows:

(1) The MUSE/NFM catalog consists of 946 measures for sources located between 0.3″ and 15.7″ from the cluster center (Figure 3.6, left panel). They sample the magnitude range $13.5 < V < 21$, and their position in the $(V, B-V)$ CMD is shown in left panel of Figure 3.7 (black dots).

(2) The MUSE/WFM data set consists of 587 stars located between 2.3″ and 66.5″ from the cluster center (black dots in the right panel of Figure 3.6) and with magnitudes $12 < V < 19$ (green circles in the left panel of Figure 3.7).

(3) The FLAMES/KMOS sample consists of 193 stars, sampling the radial region beyond $\sim 20''$, out to 774″ from the cluster center (see Ferraro et al., 2018b).

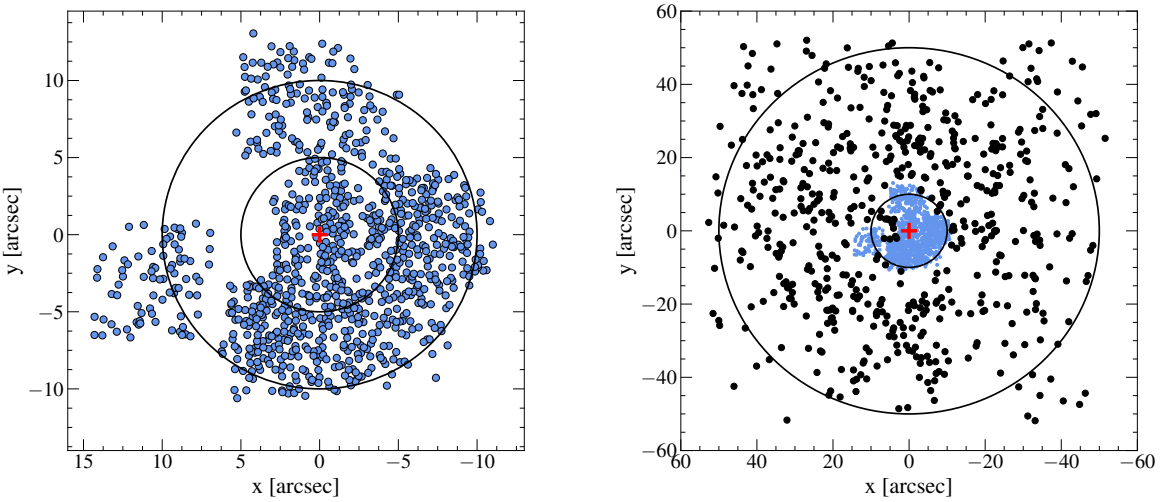

Figure 3.6: *Left panel:* map on the plane of the sky, with respect to the adopted cluster center (red cross), for all the stars with RVs measured from MUSE/NFM data. The two circles mark distances of 5″ and 10″ from the center. *Right panel:* the same, but for the stars with RVs obtained from the MUSE/WFM observations (black dots). The MUSE/NFM sample is also shown in blue and the two circles mark distances of 10″ and 50″ from the center (red cross).

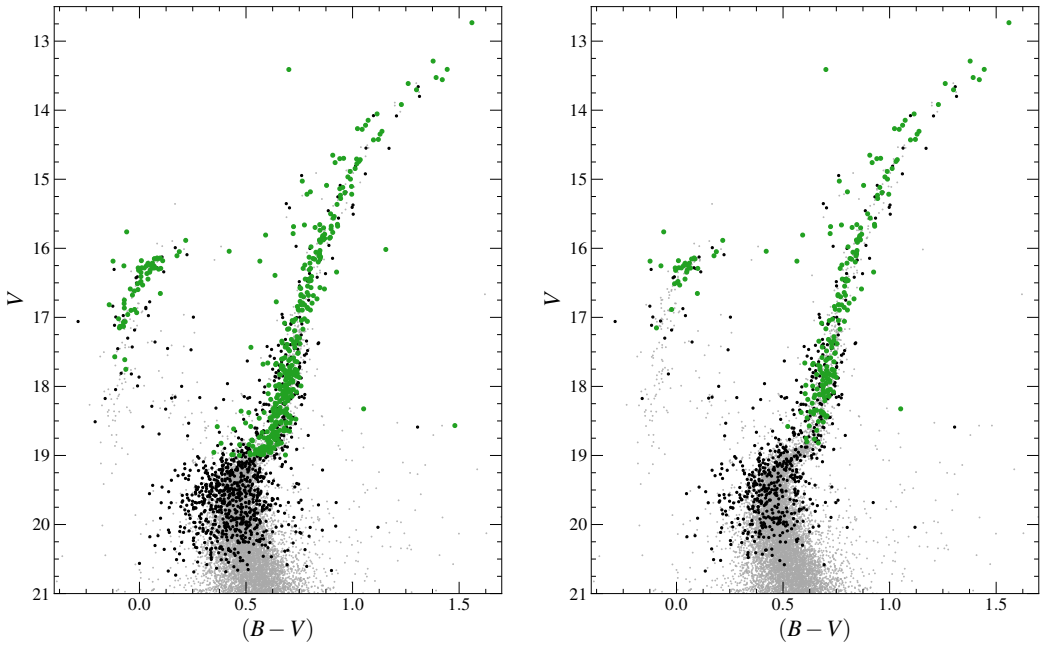

Figure 3.7: *Left panel:* CMD of NGC 1904 obtained from the photometric catalog discussed in Lanzoni et al. (2007b) (gray dots), with the stars having RVs measured from the MUSE observations marked as black circles (NFM sample) and green circles (WFM data set). *Right panel:* the same, but only for the stars used to determine the internal kinematics of NGC 1904, i.e., stars with RV uncertainty $\epsilon_{RV} < 10$ km s^{-1}, S/N> 10 and contamination ratio $C \leq 0.05$.

3.3.3 Contamination estimate of the MUSE targets

Although in NGC 1904 we do not expect significant contamination from the foreground Galactic field sources, the MUSE observations presented in this Chapter sample the core of the cluster, where stellar crowding is critical. Hence, the RV value measured for a given star might be affected by the presence of bright neighboring sources. In turn, this can impact the final results, in terms of velocity dispersion and systemic rotation of the cluster. To quantify this effect and select the spectra contributed by the light of individual stars only, we implemented a procedure aimed at estimating the level of contamination suffered by each MUSE target.

We considered all the sources listed in the HST catalogs used for the photometric analysis and we modelled each of them with the adopted MUSE PSF function (see Section 3.3.1). For every MUSE target, this allowed us to estimate the amount of light in the central spaxel contributed by the star under analysis and the surrounding objects. Using the entire HST catalogs (instead of only the MUSE targets with measured RV) guarantees that we are taking into account a complete list of sources, including stars that are not identified (because they are too faint) or are blended in

the MUSE observations, as well as stars that are located just beyond the edges of the MUSE fields. From this analysis we then quantify the level of contamination of each MUSE target through the contamination parameter (C) defined as the ratio between the fraction of light contributed by the first contaminant and that of the target under analysis, where the first contaminant is the neighbouring source providing the largest contribution to the central spaxel light after the target itself.

Figure 3.8 shows the parameter C estimated for all the MUSE targets as a function of the magnitude, with the color code illustrating the dependence on the distance from the cluster center. As expected, the most contaminated stars (large values of C) are the faint ones. Moreover, the contamination from neighbouring stars is more severe for the observations acquired at lower spatial resolution (WFM, right panel), with respect to those performed with AO correction (NFM, left panel). The figure also illustrates that, to discriminate isolated from contaminated targets, it is more efficient to select a threshold in C, instead of a cut in magnitude; indeed, this allows us to keep in the sample faint but isolated stars, as well as to reject targets that, in spite of being relatively bright, are contaminated by neighbors. For the following analysis, we made the conservative choice of keeping in the sample only the MUSE targets with contamination parameter smaller than 5% ($C \leq 0.05$), for which we estimate that neighboring stars have a negligible impact on the measured RV. The final sample includes 857 stars in the NFM data set, and 351 stars observed with MUSE/WFM.

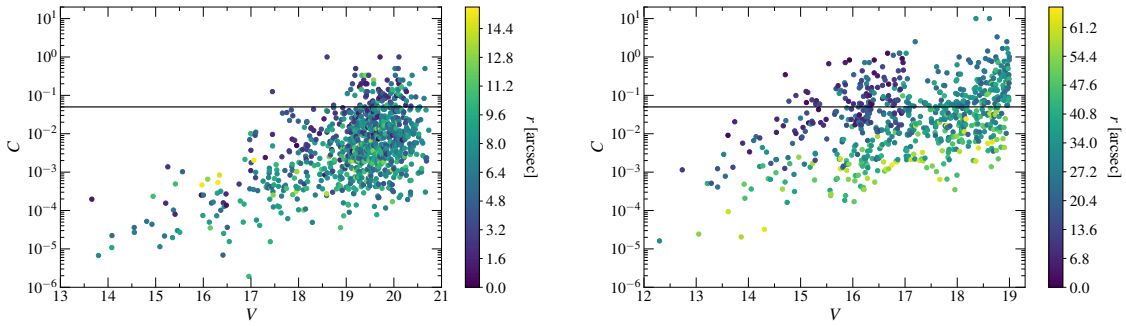

Figure 3.8: Contamination parameter (C, see Section 3.3.3) as a function of magnitude, for the MUSE/NFM targets (left panel) and the MUSE/WFM sources (right panel). The color scale indicates the distance of the targets from the cluster center (see color bars). The black line flags the adopted contamination threshold: only targets with $C \leq 0.05$ have been used to determine the internal cluster kinematics.

3.4 Results and discussion

To properly determine the internal kinematics (systemic velocity, VD profile and rotation curve) of NGC 1904 from the available data set, we further selected the

sample by considering only stars with RV uncertainty smaller than 10 km s^{-1} and S/N higher than 10. This brought the final sample to a total of 1078 RV measures, for individual stars located in a large range of radial distances, from 0.3″ out to $\sim$ 774″ (about 14 $\times$ r_h) from the cluster center. The CMD distribution of the selected MUSE target is shown in the right panel of Figure 3.7.

3.4.1 Systemic velocity

Figure 3.9 shows the distribution of the 1078 RVs measured in NGC 1904 as a function of the distance from the cluster center. The population of cluster members is clearly distinguishable as a narrow, strongly peaked component, which dominates the sample at RV $\sim$ 200 km s^{-1}. To carefully determine the value of the cluster systemic velocity ($V_{\rm sys}$), we rejected obvious outliers, selecting only the targets with RV in the range 190 km s^{-1} $<$ RV $<$ 220 km s^{-1}. Under the assumption that the RV distribution is Gaussian, we used a Maximum-Likelihood approach (e.g., Walker et al. 2006) to estimate the cluster systemic velocity and its uncertainty. By applying the selection criteria described above and a 3σ-clipping procedure, a sample of 998 RV measures has been used for the estimate of $V_{\rm sys}$. These are marked as black solid circles in the left panel of Figure 3.9 and their distribution is shown in grey in the right panel of the same figure. The resulting value is $V_{\rm sys}$ 205.4 $\pm$ 0.2 km s^{-1}, in good agreement with previous determinations, e.g., 205.8 $\pm$ 0.4 km s^{-1} (Harris, 1996, 2010 edition), 205.78 $\pm$ 0.54 km s^{-1} (D'Orazi et al., 2015), 205.4 $\pm$ 0.6 km s^{-1} (Ferraro et al., 2018b) and 205.6$\pm$0.2 km s^{-1} (Baumgardt & Hilker, 2018). Different, but still reasonable, assumptions about the cuts in RV, error and contamination parameter produce no significant variations in this result. We also verified that using only the MUSE/NFM and MUSE/WFM catalogs individually provides perfectly consistent values of $V_{\rm sys}$, as illustrated in Table 3.2. In the following, we will use V_r = RV $-$ $V_{\rm sys}$ to indicate the RV values referred to the cluster systemic velocity.

3.4.2 Second velocity moment profile

The dispersion of the measured RVs about the cluster systemic velocity, determined at different radial distances from the center, provides the second velocity moment profile of the system, $\sigma_{II}(r)$. Under the assumption of no relevant rotation, this is a good approximation of the projected VD profile, $\sigma_P^2(r)$. In fact:

$$\sigma_P^2(r) = \sigma_{II}^2(r) - A_{\rm rot}^2(r), \tag{3.1}$$

where $A_{\rm rot}$ is the rotation curve amplitude. Indeed, preliminary evidence of rotation was recently detected in the external region of NGC 1904 (Ferraro et al., 2018b), and it is confirmed in the present study, as discussed in the next section. Hence, the

Table 3.2: Systemic velocity of NGC 1904.

Catalog	r_{min}	r_{max}	N	N_V	V_{sys}
MUSE/NFM	0.3	15.7	599	553	205.2 ± 0.3
MUSE/WFM	4.2	64.1	286	276	205.7 ± 0.4
MUSE + FLAMES/KMOS	0.3	773.7	1078	998	205.4 ± 0.2

NOTE– For the catalog including only MUSE/NFM targets, that of MUSE/WFM stars, and the global catalog obtained after the combination of the previous two with the catalog discussed in Ferraro et al. (2018b), the table lists the minimum and maximum distances from the cluster center sampled by the observed stars ($r_{\rm min}$ and $r_{\rm max}$, respectively), total number of stars after all selections (i.e., RV uncertainty $\epsilon_{RV} < 10$ km s^{-1}, S/N > 10 and $C \leq 0.05$), the number of stars used for the determination of the systemic velocity (N_V), and the resulting value of $V_{\rm sys}$ with its 1σ uncertainty.

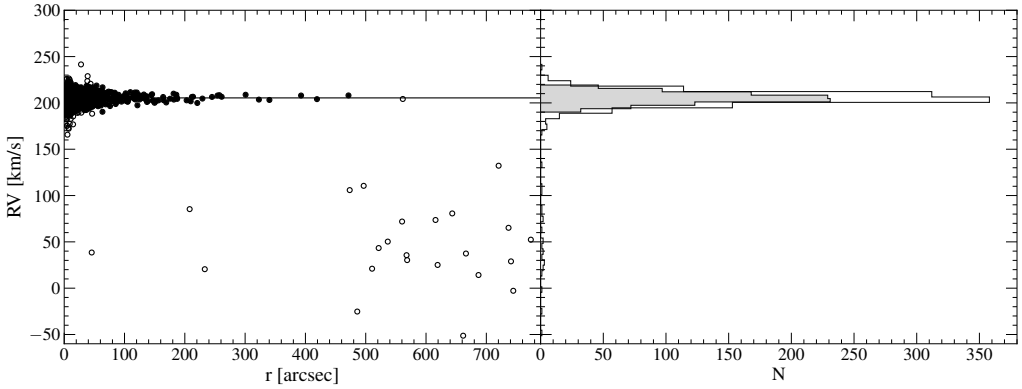

Figure 3.9: *Left panel:* Radial velocities of the final sample of (1078) selected stars as a function of their distance from the cluster center. The solid circles flag those used to determine the cluster systemic velocity (black solid line), while the empty circles mark those rejected by the 3σ-clipping algorithm. The number distribution of the targets used for the systemic velocity is plotted as a filled gray histogram and compared to that of the entire sample (empty histogram) in the right panel.

correct determination of the VD profile of this system requires the evaluation of the strength of rotation and its radial variation. However, the second velocity moment profile is still worth to be determined since it offers the opportunity of a first-order comparison with previous results in literature that ignored the effects of the cluster rotation.

As usual, the radial profile has been obtained by splitting the surveyed area into a set of concentric annuli, at increasing distance from the cluster center, chosen as

a compromise between a good radial sampling and a statistically significant number of stars (at least 20 - 30). In each radial bin, obvious outliers (like field stars, having RVs in clear disagreement with the cluster distribution in that radial interval) have been excluded from the analysis and a 3σ-clipping algorithm about the cluster systemic velocity has been applied to further clean the sample. Then, $\sigma_{II}(r)$ has been computed from the dispersion of the values of V_r measured for all the remaining stars in each annulus, by following the Maximum-Likelihood method described in Walker et al. (2006, see also Martin et al. 2007; Sollima et al. 2009). The error is estimated following the procedure outlined in Pryor & Meylan (1993a).

For the sake of illustration, the left panel of Figure 3.10 shows the second velocity moment profiles obtained from the three considered catalogs, separately: MUSE/NFM and MUSE/WFM discussed in this study (black triangles and gray squares, respectively) and the FLAMES-KMOS catalog of Ferraro et al. (2018b, empty circles). Table 3.3 lists the values obtained. The figure illustrates how the three catalogs provide complementary coverages of different radial portions of the cluster, and that the resulting kinematic profiles are in very good agreement each other. The final second velocity moment profile of NGC 1904, as obtained from the combined catalog, is shown in the right panel of Figure 3.10 (solid circles) and listed in Table 3.3. Its stays flat in the central regions ($r \lesssim 10''$) with a central value of ~ 6.0 km s^{-1}, then decreases in the outer regions, as usually observed.

In the right panel of Figure 3.10, this profile is compared with that published in Lützgendorf et al. (2013, empty triangles), which was obtained by measuring the line broadening of integrated-light spectra at $r < 10''$, and with that obtained in Scarpa et al. (2011, empty squares) from individual RVs in the outer cluster region. As can be seen, while the profiles agree quite well at large distances from the center, the value measured in the innermost core is significantly larger than that presented here, and it was interpreted as the signature of a $\sim 3000 M_\odot$ IMBH. This discrepancy is qualitatively similar, although significantly less pronounced, to that found in the case of NGC 6388, where it was ascribed to the presence of two bright central stars with opposite RVs provoking a spurious broadening of the (integrated-light) spectral lines and, in turn, an over-estimate of the velocity dispersion in the cluster innermost region (see Lanzoni et al., 2013). In the innermost $10''$ of NGC 1904 we measured the RV for almost 530 stars. Hence, we conclude that the result presented in the right panel of Figure 3.10 is solid. It indicates a central value of the second velocity moment $\sim 25\%$ smaller than that quoted in Lützgendorf et al. (2013, $\sigma_0 = 6$ km s^{-1} instead 8 km s^{-1}), and it excludes the presence of a central IMBH, at least an IMBH massive enough to produce a detectable perturbation in the second velocity moment profile. We also note that, in spite of having adopted the results of Lützgendorf et al. (2013), the best-fitting N-body model to the surface density and VD profiles of NGC 1904 determined by Baumgardt & Hilker (2018)

suggests a central value of $\sim$ 6.5 km s^{-1} (see their Figure E1), which is in good agreement with our analysis.

Table 3.3: Second velocity moment profiles obtained from the MUSE/NFM and MUSE/WFM data sets, separately, and using the combined catalog of MUSE/NFM, MUSE/WFM and FLAMES data.

r_i [arcsec]	r_e [arcsec]	r_m [arcsec]	N	σ_{II} km s^{-1}	$\epsilon_{\sigma_{II}}$ km s^{-1}
MUSE/NFM					
0.01	2.00	1.28	31	6.00	0.99
2.00	5.00	3.69	121	5.90	0.58
5.00	9.00	7.05	294	5.90	0.37
9.00	15.00	10.43	125	5.90	0.62
MUSE/WFM					
0.01	15.00	8.54	35	5.70	0.73
15.00	30.00	23.74	88	5.30	0.51
30.00	66.00	44.00	187	4.30	0.32
Combined Catalog					
0.01	2.00	1.28	31	6.00	0.99
2.00	7.00	4.96	269	5.90	0.40
7.00	11.00	8.69	259	5.90	0.39
11.00	35.00	22.58	203	5.30	0.36
35.00	55.00	43.84	138	4.90	0.40
55.00	100.00	69.37	73	4.10	0.39
100.00	170.00	125.57	43	3.30	0.35
170.00	600.00	270.13	23	2.50	0.38

NOTE– The first three columns list the internal, external, and mean radii of each adopted radial bin (r_i, r_e and r_m, respectively), with the mean radius computed as the average distance from the center of all the stars in the bin (N, fourth column). The last two columns list the second velocity moment and its uncertainty in each bin, respectively.

3.4.3 Systemic rotation

A significant signature of rotation has been found in the outer regions of NGC 1904, from the analysis of individual RVs by Ferraro et al. (2018b). This is consistent with the findings presented in Scarpa et al. (2011), who measured a cluster rotational

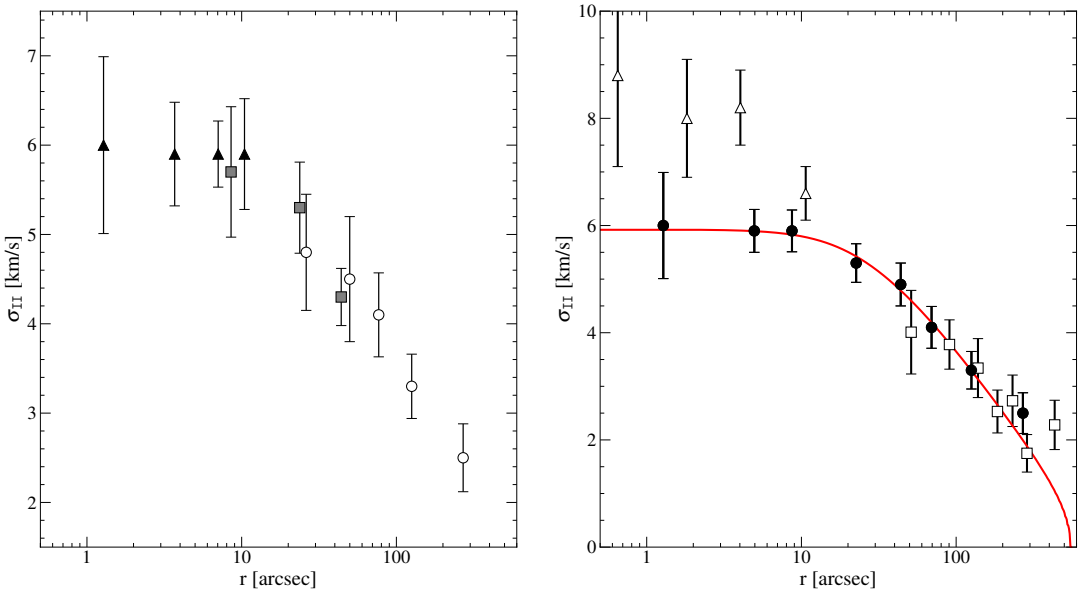

Figure 3.10: *Left panel:* Second velocity moment profiles obtained from the three considered catalogs separately: MUSE/NFM data (black triangles), MUSE/WFM data (gray squares) and the catalog presented in Ferraro et al. (2018b, empty circles). *Right panel:* Second velocity moment profile of NGC 1904 obtained from the individual RVs of all the stars included in the combined MUSE/NFM, MUSE/WFM and FLAMES data set (solid circles). The empty triangles represent the profile derived by Lützgendorf et al. (2013), from the line broadening of integrated-light spectra in the inner regions, while the empty squares have been obtained from individual RVs by Scarpa et al. (2011) in the outskirts. The red solid line shows the King model that best fits the star density profile of NGC 1904, as obtained in Miocchi et al. (2013).

velocity of 1.1 km s^{-1} within 3′ from the center, with respect to an axis with position angle PA= 85° (as measured from North toward East), from a total sample of ∼ 150 RVs. Signatures of rotation in the plane of the sky, as determined from the analysis of PMs, appears more controversial. A signal of rotation has been presented in the recent compilation of Vasiliev & Baumgardt (2021), while Sollima et al. (2019) classified the cluster rotation as uncertain, because, although a signal was detected at more than 3σ significance level, the GC failed one of the tests performed to check for spurious rotation effects. Thanks to the large sample of MUSE individual RVs presented in this Chapter, we are now able to explore the rotational properties of NGC 1904 over its entire radial extension. On the other hand the analysis of the Gaia EDR3 offers the opportunity to study the kinematics also in the plane of the sky, thus providing a comprehensive analysis of the cluster rotation.

For the LOS direction, we adopted the same approach followed in Ferraro et al. (2018b); Lanzoni et al. (2018a); Lanzoni et al. (2018b) and described, e.g., in Bellazzini et al. (2012, see also Lanzoni et al., 2013). The method consists in splitting the RV data set in two sub-samples by means of a separation line passing through

the cluster center and with position angle (PA) varying between 0° (North direction) and 180° (South direction), in steps of 10°, with PA= 90° corresponding to the East. For each value of PA, the difference between the mean velocities of two groups of stars ($\Delta V_{\rm mean}$) is measured and recorded. By construction, the method requires a sample of RVs symmetrically distributed on the plane of the sky, while it cannot be applied if large areas remain unsampled by the available data set. The presence of rotation along the LOS is expected to produce the following set of observable properties:

(1) By progressively rotating the separating line from North to South, $\Delta V_{\rm mean}$ is expected to draw a coherent sinusoidal dependence on PA. The maximum/minimum of this curve provides the position angle of the rotation axis ($\rm PA_0$), since it corresponds to the strongest separation in an approaching and a receding sub-samples. The absolute value of the maximum/minimum of this curve corresponds to twice the rotation amplitude ($A_{\rm rot}$).

(2) The projected spatial distribution is expected to be flattened in the direction of the rotation axis.

(3) The sub-samples of stars on each side of the rotation axis are expected to show, not only different mean velocities (as quantified by $\Delta V_{\rm mean}(\rm PA_0)$), but also different cumulative V_r distributions. To quantify the statistical significance of such difference we used three estimators: the probability that the RV distributions of the two sub-samples are extracted from the same parent family is evaluated by means of a Kolmogorov-Smirnov (KS) test, while the statistical significance of the difference between the two sample means is estimated with both the Student's t-test and a Maximum-Likelihood approach.

We applied this procedure to our RVs sample, in three concentric annuli around the cluster center with sufficiently symmetric spatial sampling (we thus excluded the innermost 10″: see the left panel of Figure 3.6). The results are plotted in Figure 3.11. In all the considered annuli, we find well-defined sinusoidal behaviors of $\Delta V_{\rm mean}$ as a function of PA (left-hand panels), asymmetric distributions of V_r as a function of the projected distance from the rotation axis XR (central panels), and well-separated cumulative V_r distributions for the two samples on either side of the rotation axis (right-hand panels). The reliability of these systemic rotation signatures is also confirmed by the values of the KS and t-Student probabilities and by the significance level of different sample means obtained from the Maximum-Likelihood approach (see the three last columns in Table 3.4), thus providing a solid confirmation of a coherent global rotation of the system. Averaging values of $\rm PA_0$ weighted by the number of stars in each radial bin, we obtained $\rm PA_0 = 98°$, which is adopted as global position angle for the cluster rotation axis. This locates the rotation axis essentially

aligned to the East-West direction, dividing the observed data set into a northern sub-sample with positive mean V_r, and a southern approaching sub-sample (with negative mean V_r). By fixing PA_0 to this value, we applied the described procedure to all stars measured at $r > 5''$ (for the reason discussed in the next paragraph), finally obtaining the diagnostic plots shown in the three bottom panels of Figure 3.11 and the results listed in the bottom line of Table 3.4.

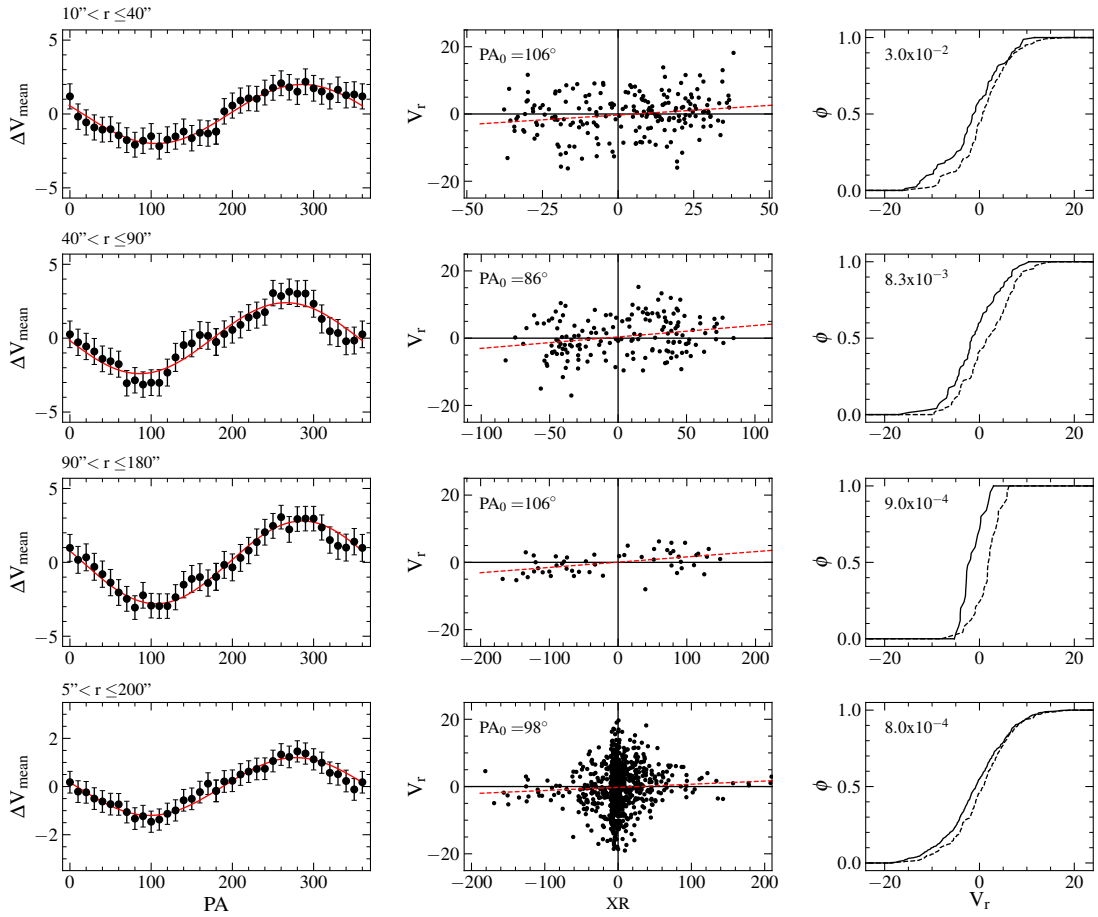

Figure 3.11: Diagnostic diagrams of the rotation signature detected in three concentric annuli at different distances from the cluster center (three top panels; see labels in their top-left corner), and considering the entire sample with $r > 5''$ (bottom panels). For each bin the *left panels* show the difference between the mean RV on each side of a line passing through the center with a given position angle (PA), as a function of PA itself. The continuous line is the sine function that best fits the observed patterns. The *central panels* show the distribution of the radial velocities V_r as a function of the projected distances from the rotation axis (XR) in arcseconds. The position angle of the rotation axis (PA_0) is labeled in each panel. The red dashed lines are the least square fits to the data. The *right panels* show the cumulative RV distributions for the sample of stars with XR< 0 (solid line) and for that with XR> 0 (dotted line). The KS probability that the two samples on each side of the rotation axis are drawn from the same parent distribution is also labelled.

Table 3.4: Rotation signatures detected in circular annuli around the cluster center and global rotation found in NGC 1904 using the entire sample with $r > 5''$ (bottom line).

r_i	r_e	r_m	N	PA_0	A_{rot}	P_{KS}	P_{Stud}	n-σ_{ML}
10	40	27.3	206	106	1.0	3.0×10^{-2}	> 95.0	2.2
40	90	54.7	165	86	1.2	8.3×10^{-3}	> 99.8	3.1
90	180	122.2	51	106	1.4	9.0×10^{-4}	> 99.8	4.0
5	800	34.6	881	98	0.6	8.0×10^{-4}	> 99.0	2.9

NOTE– For each radial bin the table lists: the inner and outer radius (r_i and r_e) in arcseconds, the mean radius and the number of stars in the bin (r_m and N, respectively), the position angle of the rotation axis (PA_0), the rotation amplitude (A_{rot}), the KS probability that the two samples on each side of the rotation axis are drawn from the same parent distribution (P_{KS}), the t-Student probability that the two RV samples have different means (P_{Stud}), and the significance level (in units of n-σ) that the two means are different following a Maximum-Likelihood approach (n-σ_{ML}).

The peculiar behaviour of the innermost core - In performing the analysis of the rotation curve, we discovered a peculiar feature that needs to be further investigated. Since the sampling of the innermost $3''$ is sufficiently symmetric (see the left panel of Figure 3.6), we applied the described procedure also in this region, leaving the position angle free to vary between 0° and 180°. We found evidence of a rotation signal for $PA_0 = 93°$, but the rotation pattern is just opposite to that found for $r > 10''$: the northern sub-sample has negative mean V_r (it is approaching), while the the stars observed in the southern hemisphere are preferentially receding from the observer (positive mean V_r). Admittedly the detection of this effect is based on a just limited number of stars ($\sim$ 60) and the statistical significance is not high (e.g., t-Student probability that the two RV samples have different means is $P_{Stud} \sim 90\%$, only). Figure 3.12 shows a MUSE/NFM image zoomed in the innermost $3''$ from the center with the considered stars flagged with two different colors: in red those receding from the observer, in green the approaching ones. The difference in the mean RV of the two samples is apparent also by eye. If confirmed, this could represent the detection of a kinematically decoupled core. A similar kinematic feature has been detected so far only in M15 (van den Bosch et al., 2006; Bianchini et al., 2013; Kamann et al., 2018a; Usher et al., 2021). It has been suggested that stellar interactions with a massive binary black holes (Mapelli et al., 2005) may produce this feature but the viability of this scenario in M15 is unclear and further investigations of other dynamical scenarios and the possible role of core collapse are necessary. In any case, the statistics is admittedly too poor to draw any firm conclusion. We therefore avoid any further discussion of this feature and

we exclude the stars located at $r < 3''$ from the following analysis.

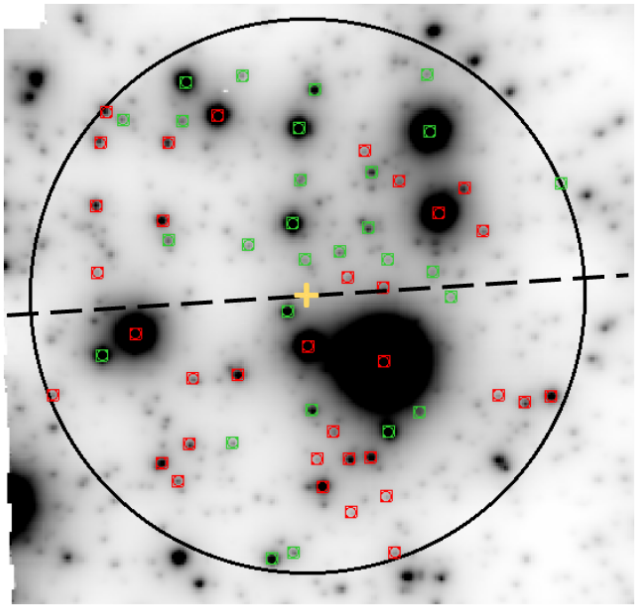

Figure 3.12: Zoomed portion of the reconstructed MUSE/NFM image in the innermost region of NGC 1904. The black circle is center on the cluster center (yellow cross) and has a radius of $3''$. North is up, East is left. Red symbols mark stars with RV larger than the cluster systemic velocity (receding stars), while green symbols mark the stars approaching the observer. The orientation ($PA_0 = 93°$) of the axis that maximizes the difference between the mean RVs of the two subsamples is also shown as a dashed line.

3.4.4 Line of sight rotation curve

We built the rotation curve of NGC 1904 by splitting the RV sample in four intervals sampling increasing values of XR on both sides of the rotation axis. Following Walker et al. (2006); Sollima et al. (2009); Lanzoni et al. (2018a), we used a Maximum-Likelihood method to determine the mean velocity of all the stars belonging to each XR bin. The errors have been estimated following Pryor & Meylan (1993b). The resulting rotation curve is shown in Figure 3.13 and presented in Table 3.5. It clearly shows the expected shape, with a steep increasing trend in the innermost regions, and a maximum value followed by a soft decreasing behavior outward. The observed trend is well reproduced by an analytic function (Lynden-Bell, 1967) appropriate for cylindrical rotation:

$$V_{\rm rot} = \frac{2A_{\rm peak}}{{\rm XR}_{\rm peak}} \quad \frac{\rm XR}{1 + ({\rm XR}/{\rm XR}_{\rm peak})^2}, \tag{3.2}$$

where $A_{\rm peak}$ and ${\rm XR}_{\rm peak}$ are the maximum rotation amplitude and its distance from the rotation axis, respectively. The red solid line in Figure 3.13 shows the model

computed for a maximum amplitude of $\sim$ 1.5 km s^{-1} at XR$_{\rm peak}$ $\sim$ 70″ from the rotation axis, approximately corresponding to r_h (or $\sim$ 2R$_h$). The evidence of systemic rotation of NGC 1904 along the LOS is apparent. As discussed in Chapter 1, rotation patterns as clear as that found here are now detected in a growing number of cases (NGC 4372 in Kacharov et al. 2014, 47 Tucanae in Bellini et al. 2017, M5 by Lanzoni et al. 2018a, NGC 5986 by Lanzoni et al. 2018b, NGC 6362 by Dalessandro et al. 2021a, see also Bianchini et al. 2013; Vasiliev & Baumgardt 2021).

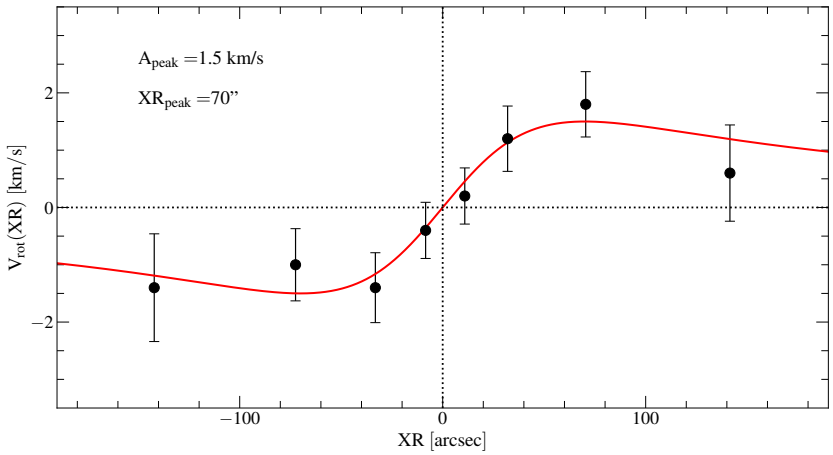

Figure 3.13: Rotation curve of NGC 1904. The black circles mark the stellar mean velocity as a function of the projected distance on either side of the rotation axis (XR) for the intervals listed in Table 3.5. The red line, which well reproduces the observed curve, is the model shown in equation (3.2), with $A_{\rm peak}$ = 1.5 km s^{-1} and XR$_{\rm peak}$ = 70″.

Table 3.5: Line of sight rotation curve of NGC 1904

XR$_i$	XR$_e$	XR$_m$+	N+	$V_{\rm rot}$−	ϵ_{V+}	XR$_m$−	N−	$V_{\rm rot}$−	ϵ_{V-}
5	20	10.88	139	0.20	0.49	−8.41	212	−0.40	0.49
20	50	31.99	102	1.20	0.57	−33.17	78	−1.40	0.61
50	110	70.46	36	1.80	0.57	−72.49	28	−1.00	0.63
110	200	141.51	9	0.60	0.84	−142.11	11	−1.40	0.94

NOTE– For four intervals of projected distances from the rotation axis (XR), the table lists: the inner and outer absolute limits of each bin (XR$_i$ and XR$_e$) in arcseconds, the mean distance, number of stars, average velocity and its error (in km s^{-1}) on the positive side of the XR axis (columns 3–6), and on its negative side (columns 7–10).

3.4.5 Velocity dispersion profile

Once the LOS rotation curve is determined, the projected VD profile, $\sigma_P(r)$, can be finally obtained from the dispersion of the measured RVs after subtraction of the

ordered motion contribution. We thus assigned to each star the mean rotational velocity of the XR shell to which it belongs, and subtracted this value from the measured RV. Then, we repeated the Maximum-Likelihood procedure described in Section 3.4.2 to determine the projected VD profile of NGC 1904 in circular concentric shells. The result is shown in Figure 3.14 (red circles) and listed in Table 3.6. For the sake of comparison we also show the radial profile of second velocity moment (black circles) determined in Section 3.4.2 and listed in Table 3.3.

By construction the VD is systematically smaller than the second velocity moment in every bin. However, the differences are small and always within the errors, as expected in the case of a pressure-supported system. Indeed, in spite of a clean rotation signal, the rotational velocity is small and it is smaller than the velocity dispersion in all radial bins, confirming that the kinematics of NGC 1904 is dominated by non-ordered motions.

Table 3.6: Velocity dispersion profile of NGC 1904.

r_i [arcsec]	r_e [arcsec]	r_m [arcsec]	N	σ_{II} km s^{-1}	$\epsilon_{\sigma_{II}}$ km s^{-1}
0.01	2.00	1.28	31	6.00	0.99
2.00	7.00	4.96	269	5.90	0.40
7.00	11.00	8.69	259	5.90	0.39
11.00	35.00	22.58	203	5.20	0.35
35.00	55.00	43.84	138	4.80	0.39
55.00	100.00	69.37	73	3.90	0.38
100.00	170.00	125.57	43	3.10	0.34
170.00	600.00	270.13	23	2.50	0.38

NOTE– The first four columns list the internal, external, mean radii and number of stars of each adopted radial bin (r_i, r_e, r_m and N, respectively). The last two columns list the VD and its uncertainty in each bin, respectively.

Adopting the values obtained in (Miocchi et al., 2013, see also Section 3.1 and Table 3.8) as representative of the structure of the cluster, we compared the projected VD profile of this model to the observations (see Figure 3.14). By performing a χ^2 test, we found the value of σ_0 that minimizes the residuals between the observed VD profile and the adopted King model. From the solutions providing $\chi^2 = \chi^2_{min} \pm 1$, we then obtained the 1σ uncertainty on the best fit value. The resulting central velocity dispersion is $\sigma_0 = 5.9 \pm 0.3$ km s^{-1}, and the comparison with the observed profile clearly shows that the adopted King model is able to nicely reproduce both the observed structure and the observed kinematics of NGC 1904. This value is

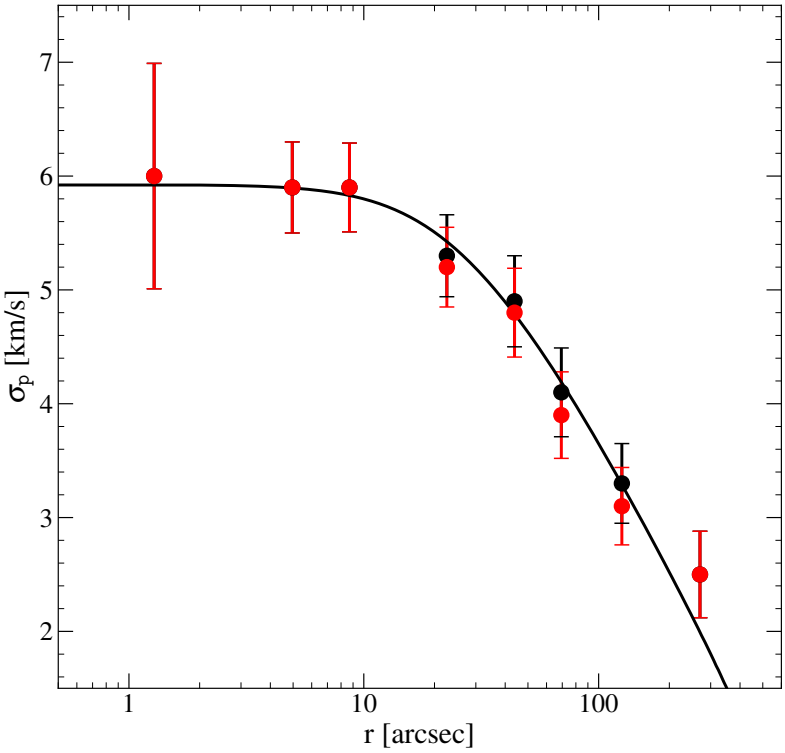

Figure 3.14: Velocity dispersion profile of NGC 1904 (red circles) obtained after subtracting the contribution of rotation in all radial bins. The second velocity moment profile (the same as in Figure 3.10), which includes the effects of both rotation and velocity dispersion in each circular shell, is also shown for comparison (black circles). The sold line shows the King model that best fits the projected density distribution of NGC 1904 by Miocchi et al. (2013).

in good agreement with previous determinations: it is only slightly larger than the value listed in the Harris (1996, 2010 edition) catalog ($\sigma_0 = 5.3$ km s^{-1}), and slightly smaller than that found by Baumgardt & Hilker (2018), who quote $\sigma_0 = 6.5$ km s^{-1}, in spite of the fact that they adopt the VD profile by Lützgendorf et al. (2013) who, conversely obtain a significantly larger value of the central velocity dispersion ($\sigma_0 > 8$ km s^{-1}).

3.4.6 Rotation in the plane of the sky

In order to study the rotation of the cluster in the plane of the sky we used the most recent data release (EDR3) of the Gaia mission (Gaia Collaboration et al., 2021). Using this data set Vasiliev & Baumgardt (2021) have detected a signal of rotation in NGC 1904 at more than 3σ confidence level and with a maximum amplitude of ~ 2.0 km s^{-1} at $\sim 2'$. In a previous analysis using both LOS velocities and PMs from Gaia DR2, Sollima et al. (2019) quoted a rotation velocity amplitude of 2.24 ± 0.46 km s^{-1}, but classified the rotation signal as uncertain, because the cluster failed one of the tests performed against random or systematic effects (see their

Table 1). Here we independently analyzed the Gaia EDR3 data searching for signature of rotation in the plane of the sky. We first applied the following selection criteria on the astrometric and photometric quality indicators (given in the Gaia archive and discussed in Lindegren et al., 2021; Riello et al., 2021; Fabricius et al., 2021), in order to use the stars with the most reliable astrometric measures: (*i*) RUWE[‡] < 2.4; (*ii*) astrometric_excess_noise[§] < 2; (*iii*) phot_bp_rp_excess_factor[¶] $< 2.6 + 0.12(\mathrm{BP} - \mathrm{RP})^2$, where BP and RP are the magnitude in the BP and RP bands, respectively; (*iv*) G < 19; (*v*) PM errors < 0.06 mas yr^{-1} for stars with G < 16, while for G > 16 we have divided the sample into bins of distance (0″- 50″, 50″- 100″, 100″- 150″and distance $> 150''$) and bins of magnitude 0.5 G magnitude wide, and we have excluded the stars with PM errors larger than 1σ of the local mean error in each bin. Finally, we selected stars within 0.2 mas yr^{-1} (corresponding to about $2 \times \sigma_0$ at the distance of NGC 1904) from the absolute motion (Vasiliev & Baumgardt, 2021, see also Table 3.8) in the vector-point diagram (VPD, see the left panel of Figure 3.15). The final sample includes 437 stars located between 7″

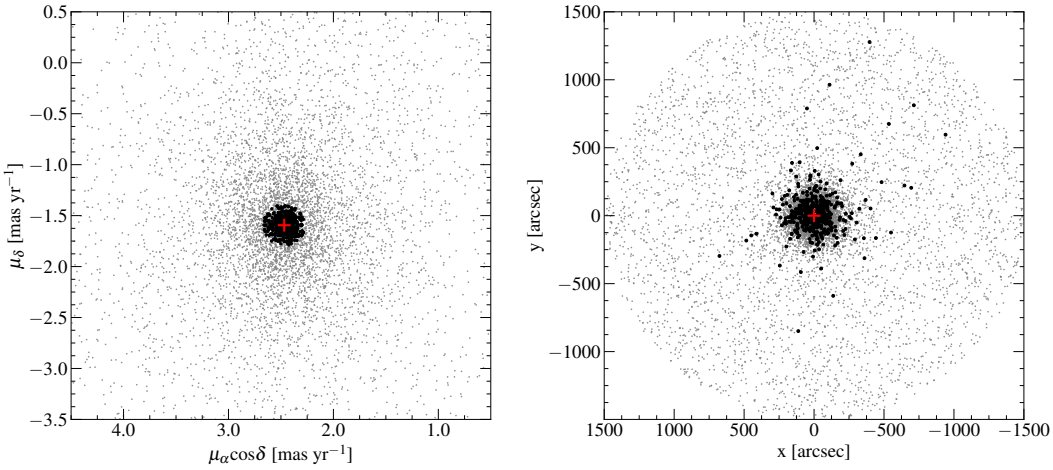

Figure 3.15: *Left panel*: VPD of the stars of the selected sample (black circles) and of the original Gaia EDR3 data set (gray points), with the red cross marking the absolute motion (Vasiliev & Baumgardt, 2021). *Right panel*: Map on the plane of the sky, with respect to the adopted cluster center (red cross), of the selected star sample (black circles) and of the original Gaia EDR3 one (gray points).

and 1338″ from the center. Their $\mu_\alpha cos\delta$ and μ_δ PMs are shown (black dots) in the VPD in the left panel of Figure 3.15, while their distribution on the plane of

[‡]RUWE is the renormalised unit weight error (for astrometry) discussed in Lindegren et al. (2021).

[§]it is the excess noise of the source and it measures the disagreement, expressed as an angle, between the observations of a source and the best-fitting standard astrometric model.

[¶]it is the sum of the integrated BP and RP fluxes divided by the G flux. It gives an indication of the consistency between the three fluxes (for more details see Riello et al., 2021).

the sky is plotted in the right panel of the same figure. The PMs measured for the selected stars and their corresponding uncertainties have been converted into a Cartesian reference frame centered on the cluster center using eq. 2 of Gaia Collaboration et al. (2018) and corrected for perspective effect using eq. 6 of van de Ven et al. (2005) and assuming a cluster distance of 13.2 kpc (Ferraro et al., 1999b, consistent with the more recent estimate by Baumgardt & Vasiliev, 2021). PMs are then decomposed into projected tangential μ_{TAN} and radial μ_{RAD} components and converted into units of km s^{-1} using eq. 4 of van de Ven et al. (2005).

Similarly to what has been done for the LOS component, we derived the VD in both the tangential (σ_{TAN}) and radial (σ_{RAD}) components by dividing the sample in radial bins and using a Maximum-Likelihood approach. The results are listed in Table 3.7 and shown in Figure 3.16 (top and central panels). For comparison purposes, we also show the PM dispersion profile obtained by Vasiliev & Baumgardt (2021) using the Gaia EDR3 data set (blue solid line in the top panel of Figure 3.16). Within the errors, their results are in agreement with the profile obtained in our analysis (black circles), except for a couple of points at $r \sim 100''$. It is interesting to note that the radial profile of $\sigma_{TAN}/\sigma_{RAD}$ shown in the bottom panel of Figure 3.16 indicates that this cluster is characterized by an isotropic velocity distribution, although the large uncertainties do not allow to rule out the possible presence of anisotropy. As shown in Tiongco et al. (2016a) an isotropic velocity distribution would suggest that this cluster is in an advanced dynamical stage and lost any velocity anisotropy developed during its early or long-term phases of evolution (see Section 3.4.9 below for further discussion). We also derived the rotation curve in the plane of the sky by computing, again with a Maximum-Likelihood method, the average value of μ_{TAN} in each radial bin. We assumed negative μ_{TAN} values in the case of a clockwise rotation in the plane of the sky (from North to West). The obtained rotation profile is shown in Figure 3.17 (black circles) and listed in Table 3.7 (last two columns). In Figure 3.17, the rotation curve is compared with that published in Vasiliev & Baumgardt (2021, blue solid line), showing a quite good agreement. In agreement with what derived from LOS measurements, we find a signature of clockwise rotation even in the plane of the sky, with a maximum amplitude of ~ -2.0 km s^{-1} at $\sim 80''$ ($2R_h$ or $\sim 1.5 \times r_h$) from the cluster center. As a final result, the rotation profile both in the plane of the sky and in the LOS direction will be compared with rotation curve models with different inclination angles in Section 3.4.9.

Since for a sub-sample of 130 stars we have the three velocity components (i.e. RV, $\mu_\alpha cos\delta$ and μ_δ), as sanity check, we applied the method described in Sollima et al. (2019) to verify that the values of PA_0 and rotation amplitude estimated separately along the line of sight and the plane of the sky directions are able to properly reproduce also the three-dimensional velocity space of the system as traced

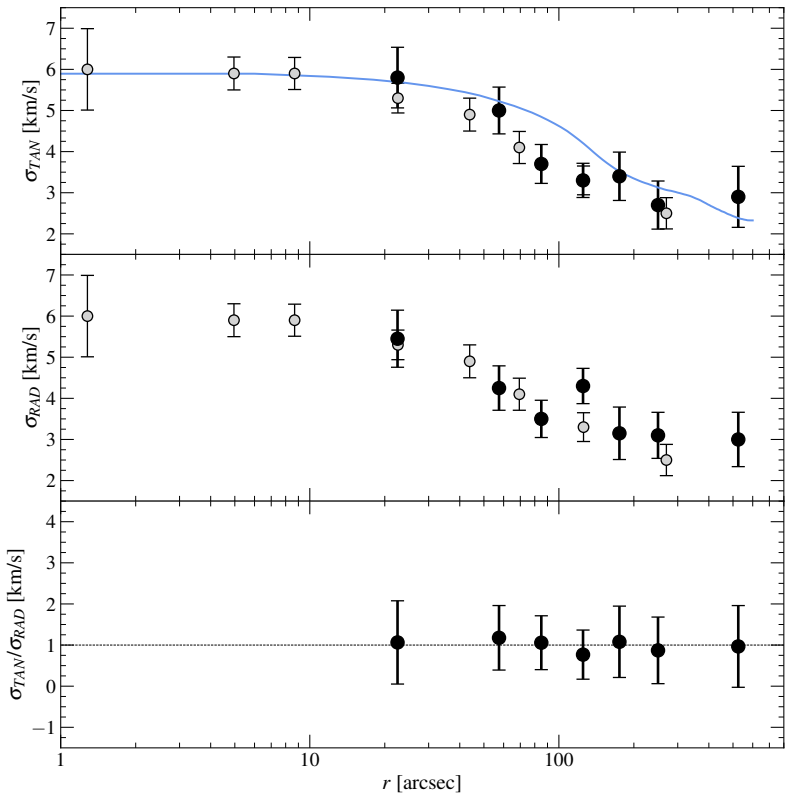

Figure 3.16: *From top to bottom*: Tangential and radial velocity dispersion profiles, and anisotropy profile. The black circles mark the results obtained with the sample selected from the Gaia EDR3 data set, while the grey circles correspond to the second velocity moment profile obtained from individual RVs (the same as in Figure 3.10). The PM dispersion profile presented in Vasiliev & Baumgardt (2021) is marked for comparison by the blue solid line in the top panel, with shaded area representing its 68% confidence interval.

by this sub-sample. Following Sollima et al. (2019), in case of rotation, a modulation of the mean velocity in the three components as a function of the angular position of the stars is detected. According to their eq. (2), for a solid-body rotation the three velocity components are:

$$\begin{aligned} \mathrm{RV} &= \omega\ R\ sin\ (\theta - \mathrm{PA}_0)\ sin\ i \\ v_{\parallel} &= \omega\ R\ sin\ (\theta - \mathrm{PA}_0)\ cos\ i \\ v_{\perp} &= \omega\ R\ cos\ (\theta - \mathrm{PA}_0)\ cos\ i \end{aligned} \tag{3.3}$$

where ω is the angular velocity, R is the projected distance from the cluster center, $0° < \theta < 360°$ is the angular position of the stars (growing anti-clockwise from North to Est), $0° < i < 90°$ is the inclination angle of the rotation axis with respect to the LOS, PA_0 is the position angle of the rotation axis defined as above, RV is the velocity component along the LOS and $v_{\parallel}$ and $v_{\perp}$ are the components in the

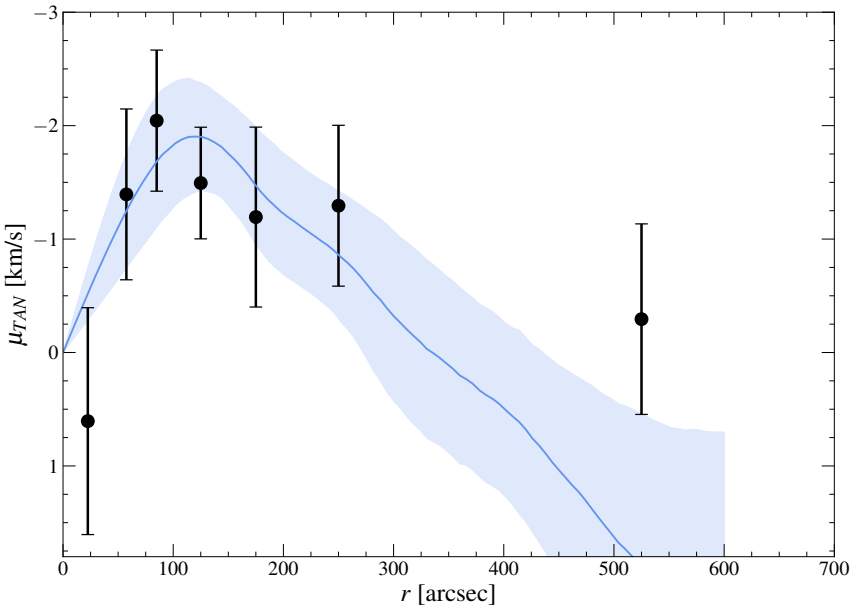

Figure 3.17: Rotation profile of NGC 1904 in the plane of the sky obtained with the star sample selected from the Gaia EDR3 data (black circles). The solid blue line and shaded area show the PM rotation profile presented in Vasiliev & Baumgardt (2021) and its 68% confidence interval, respectively.

Table 3.7: Radial and tangential velocity dispersion profile and rotation curve in the plane of the sky of NGC 1904.

r_i [arcsec]	r_e [arcsec]	N	σ_{RAD} km s^{-1}	$\epsilon_{\sigma_{RAD}}$ km s^{-1}	σ_{TAN} km s^{-1}	$\epsilon_{\sigma_{TAN}}$ km s^{-1}	μ_{TAN} km s^{-1}	$\epsilon_{\mu_{TAN}}$ km s^{-1}
5	45	38	5.45	0.69	5.80	0.74	0.61	1.00
45	70	65	4.25	0.54	5.00	0.57	−1.39	0.75
70	100	79	3.50	0.45	3.70	0.47	−2.04	0.62
100	150	104	4.30	0.43	3.30	0.42	−1.49	0.49
150	200	52	3.15	0.64	3.40	0.59	−1.19	0.79
200	300	59	3.10	0.56	2.70	0.59	−1.29	0.71
300	750	33	3.00	0.66	2.90	0.74	−0.29	0.84

NOTE– The table lists: the internal and external radii of each adopted radial bin (r_i and r_e, respectively), the number of stars in each bin (N), the velocity dispersion and its uncertainty in the radial and tangential component (columns 4–7) and the average μ_{TAN} and its uncertainty in each radial bin (columns 8–9).

directions parallel and perpendicular to the rotation axis, respectively (for more details see Appendix A of Sollima et al., 2019). We then defined $A = \langle \omega \ R \rangle$ as the average projected rotation velocity amplitude and we assumed it negative for

clockwise rotation in the plane of the sky. In our analysis, we have fixed PA_0 to the value obtained above from the LOS velocities ($PA_0 = 98°$, see Section 3.4.3 and Table 3.8) and we then used a Maximum-Likelihood algorithm to determine the best-fit values of i ($i = 37°$) and A ($A = -2.05$ km s^{-1}). The latter is in very good agreement with the estimates obtained from the previous analyses along the LOS and on the plane of the sky, separately. The result of this analysis is plotted in Figure 3.18.

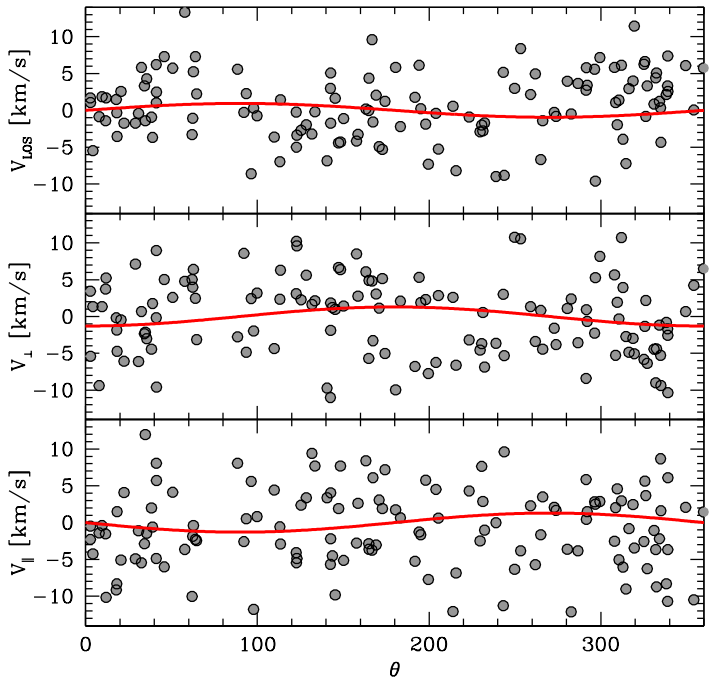

Figure 3.18: Distribution of the three velocity components for the 130 stars in NGC 1904, for which the three-dimensional kinematic information is available, as a function of their angular position in degree. The red solid lines show the curves obtained for $PA_0 = 98°$ and for the best-fit values of the rotation amplitude $A = -2.05$ km s^{-1} and inclination angle $i = 37°$, as discussed in the text (see Section 3.4.6).

3.4.7 Determination of the total mass of the cluster

From the derived value of the central velocity dispersion (see Table 3.8) we estimated the total mass of the system. To this end, we used equation (3) in Majewski et al. (2003), where the parameters μ and β have been determined, respectively, by following Djorgovski (1993) and by assuming $\beta = 1/\sigma_0^2$ (as appropriate for models with $W_0 > 5$; see the discussion in Richstone & Tremaine 1986). The resulting total mass is $M = 1.28^{+0.15}_{-0.14} \times 10^5 M_\odot$. The uncertainties have been estimated through a Monte Carlo simulation, performing 1000 random extractions of the values of c, r_0 and σ_0 from normal distributions centered in their best fit values and with disper-

sions equal to the estimated uncertainties of the respective parameters (these values are listed in the summary Table 3.8). This mass estimate is in perfect agreement with the value obtained in Ferraro et al. (2018b, $1.29 \times 10^5 M_\odot$), and slightly smaller than the values quoted in McLaughlin & van der Marel (2005, $1.58^{+0.15}_{-0.14} \times 10^5 M_\odot$), Lützgendorf et al. (2013, $1.44 \pm 0.10 \times 10^5 M_\odot$), and Baumgardt & Hilker (2018, $1.69 \pm 0.11 \times 10^5 M_\odot$). These differences can be justified taking into account all the uncertainties and the fact that the estimates have been obtained through different methods.

3.4.8 Ellipticity

A rotating system is also expected to be flattened in the direction perpendicular to the rotation axis (Chandrasekhar, 1969a). As discussed in Chapter 1, this flattening is also predicted in case of rotation in GCs (see, e.g., Chen & Chen, 2010; van den Bergh, 2008; Bianchini et al., 2013).
Although the cluster rotation measured along the LOS direction has a maximum amplitude of just ~ 1.5 km s^{-1}, we investigated the morphology of NGC 1904 by using the catalog discussed in Lanzoni et al. (2007b) to build the two-dimensional (2D) stellar density map of the system. The analysis was limited to an area of $\sim 400'' \times 400''$ and only stars with $V < 21$ have been used to avoid incompleteness effects. The distribution of star positions was transformed into a smoothed 2D surface density function through the use of a kernel with a width of $1'$ (see Dalessandro et al., 2015). The resulting 2D density map is shown in Figure 3.19, where the black solid lines represent the isodensity curves, the white lines correspond to their best-fit ellipses and the dashed line marks the position of the rotation axis estimated from the star RVs ($PA_0 = 98°$). As is clear from the figure, the stellar density distribution has spherical symmetry in the center and becomes slightly more flattened for increasing radius. The ellipticity $\epsilon = 1 - b/a$ where a and b are the major and minor axis, respectively, reaches its maximum in the external region (at $r \sim 220''$) where we measured a value of 0.04 ± 0.02, qualitatively consistent with what found previously by Harris (1996, 2010 edition, 0.01) and in line with the small measured rotation. Although the ellipticity is small, ellipses major axis tend to have an orientation of $\sim 10°$ in the North-East direction, implying that the stellar density distribution is flattened in the direction perpendicular to the rotation axis in agreement with what is expected for a rotating system and qualitatively consistent with that predicted, for example, by the models introduced by Varri & Bertin (2012) and found in other observational studies (e.g., Dalessandro et al., 2021a; see also Bianchini et al., 2013; Bellini et al., 2017; Lanzoni et al., 2018a).

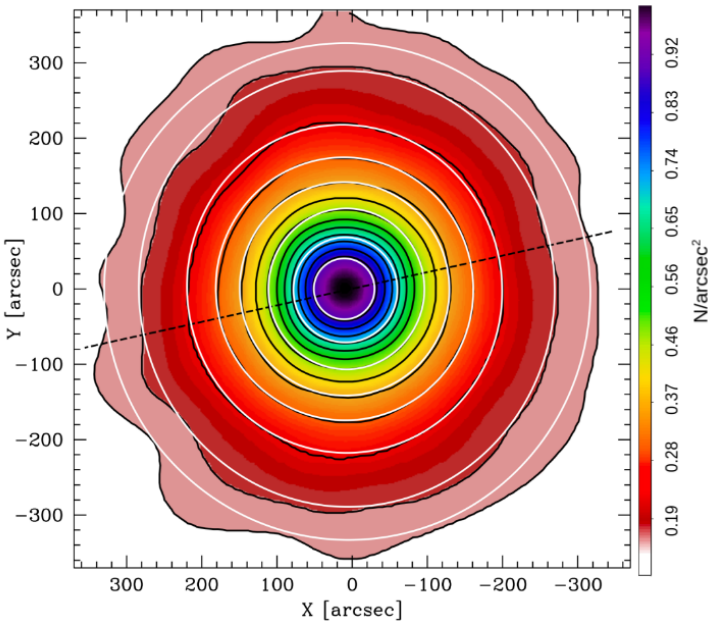

Figure 3.19: Smoothed stellar density map of the inner $400'' \times 400''$ of NGC 1904, obtained from the photometric catalog discussed in Lanzoni et al. (2007b). The solid black lines are isodensity contours, while the white curves mark their best-fit ellipses. The black dashed line marks the direction of the global rotation axis (with position angle of 98°, see Section 3.4.4).

3.4.9 Comparison with theoretical models

As introduced in Chapter 1, theoretical studies (e.g., Fiestas et al., 2006; Ernst et al., 2007; Hong et al., 2013; Tiongco et al., 2017) have shown that star clusters gradually lose their initial rotation as a result of the effects of internal two-body relaxation and angular momentum loss carried away by escaping stars. Hence, the extent of the present-day rotation detected in many GGCs (see, e.g., Bianchini et al., 2013; Fabricius et al., 2014; Bellini et al., 2017; Ferraro et al., 2018b; Kamann et al., 2018a; Lanzoni et al., 2018a; Sollima et al., 2019; Dalessandro et al., 2021a) represents only a lower limit to the primordial rotation of these systems and suggests that the initial cluster kinematics might be characterized by a stronger rotation (Hénault-Brunet et al., 2012; Mackey et al., 2012; Kamann et al., 2018b; Dalessandro et al., 2021b). To address this issue for the case of NGC 1904, in Figure 3.20 we compare the observed rotation (black squares) with the results (colored lines) of a representative N-body simulation of a rotating star cluster from the survey of models presented in Tiongco et al. (2016a). The results reported here are those from the VBrotF04 model (see Tiongco et al. 2016a for further details), a system initially set up with phase space properties following those of the rotating models introduced by Varri & Bertin (2012). We emphasize that a study specifically aimed at identifying the best evolutionary model for NGC 1904 would require an extensive investigation following the evolution of systems with a broad range of different initial conditions.

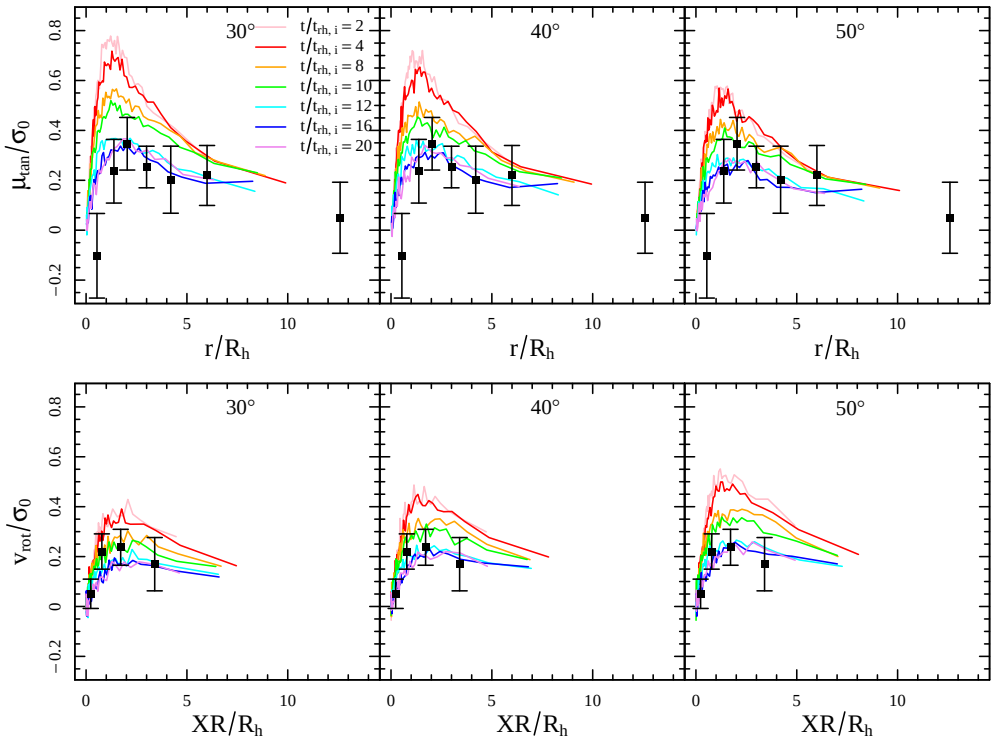

Figure 3.20: Comparison between the observed rotation curves normalized to the central velocity dispersion (black squares) and the results from the *N*-body simulations of Tiongco et al. (2016a, VBrotF04 model, see their Table 1), obtained at different evolutionary times (curves of different colors; see labels in the top-left panel, where $t_{hr,i}$ is the cluster's initial half-mass relaxation time). The top and bottom panels show, respectively, the rotation in the plane of the sky and that in the LOS direction. From left to right, the results obtained for different inclination angles between the LOS and the rotation axis of the simulated cluster are shown: $i = 30°$, $i = 40°$, $i = 50°$, as labelled. The distance from the cluster center (top panel) and the distance from the rotation axis (bottom panel) are normalized to the projected half-mass radius (R_h).

The purpose of our comparison here is just to illustrate a general dynamical path leading to the observed rotational properties of NGC 1904. Figure 3.20 shows the rotation curves in the plane-of-the-sky (upper panels), and in the LOS direction (lower panels). From left to right, the inclination angle of the simulated cluster rotation axis with respect to the LOS direction varies from $i = 30°$, to $i = 40°$, to $i = 50°$ (see labels), which are values close to that determined by the analysis presented in Section 3.4.6 ($i = 37°$). Curves of different colors correspond to simulated rotation curves obtained at different evolutionary times, as labelled in the top-left panel. The comparison with the observations shows a general good agreement, both on the plane of the sky and along the LOS direction, with the rotation curves obtained in advanced evolutionary phases of the *N*-body model, when the system has lost a significant fraction of its initial angular momentum. Hence, the cluster rotational properties suggest an old dynamical age for NGC 1904, in agreement with what inferred from the radial distribution of blue straggler stars (see Ferraro et al., 2012, 2018b, 2020; Lanzoni et al., 2016). This study shows the importance of a complete

three-dimensional kinematic characterization of stellar systems. Indeed, it allows not only a proper determination of the actual strength of the cluster internal rotation, but also to constrain the dynamical phase of the system.

Table 3.8: Summary of the parameters used and the main results obtained for the GGC NGC 1904.

Parameter	Estimated Value	Reference
Cluster center [deg]	RA= 81.0462112 Dec= −24.5247211	Lanzoni et al. (2007b)
Color excess	$E(B-V) = 0.01$	Ferraro et al. (1999b)
Metallicity	$[Fe/H] = -1.6$	Harris (1996, 2010 edition)
Cluster distance	$d = 13.2$ kpc	Ferraro et al. (1999b)
3D half-mass radius	$r_h = 56.7^{+0}_{-0.005}$	Miocchi et al. (2013)
2D Projected half-mass radius	$R_h = 41.68^{+0.08}_{-0.03}$	Miocchi et al. (2013)
Dimensionless central potential	$W_0 = 7.75^{+0.05}_{-0.1}$	Miocchi et al. (2013)
Concentration parameter	$c = 1.76^{+0.02}_{-0.03}$	Miocchi et al. (2013)
Core radius	$r_c = 9.4^{+0.6}_{-0.3}$	Miocchi et al. (2013)
Tidal radius	$r_t = 9.32^{+0.04}_{-0.09}$	Miocchi et al. (2013)
Systemic velocity	$V_{sys} = 205.4 \pm 0.2$ km s^{-1}	this work
Central velocity dispersion	$\sigma_0 = 5.9 \pm 0.3$ km s^{-1}	this work
Line-of-sight rotation peak	$A_{peak} = 1.5$ km s^{-1}	this work
Plane-of-the-sky rotation peak	$A = -2.0$ km s^{-1}	this work
Rotation axis position angle	PA $= 98°$	this work
Inclination angle of the rotation axis	$i = 37°$	this work
Absolute Proper Motions	$\mu_\alpha cos\delta = 2.469 \pm 0.025$ mas yr^{-1} $\mu_\delta = -1.594 \pm 0.025$ mas yr^{-1}	Vasiliev & Baumgardt (2021)
Ellipticity	$\epsilon = 0.04 \pm 0.02$	this work
Total Mass	$M = 1.28^{+0.15}_{-0.14} \times 10^5 M_\odot$	this work

NOTE– All radii are in units of arcseconds, with the exception of r_t, which is in arcminutes.

Chapter 4

Structural parameters and internal kinematics of NGC 6440

Mainly based on:
Pallanca, Lanzoni, [...], Leanza, et al. (2021a), ApJ, 913, 137
Leanza et al. (2023), ApJ, 944, 162

4.1 Introduction

In Chapter 1, we extensively discuss the crucial importance of the accurate characterization of GCs in terms of structural properties, dynamical status, and internal kinematics to properly understand how dynamical processes affect their evolutionary history. To this aim, in this Chapter, we present a comprehensive study of the structural and kinematic properties of the GGC NGC 6440. This cluster is a massive, metal-rich ([Fe/H]~ -0.56 dex, Origlia et al. 1997, 2008) GC located in the MW bulge, $\sim$1.3 kpc away from the center of the Galaxy (Harris, 1996, 2010 edition). This target is relatively poorly investigated because of the strong and differential extinction ($E(B-V) = 1.15$, Valenti et al., 2004, 2007, see also Pallanca et al. 2019) along its line of sight. An in-depth study of this cluster is attractive because it was quoted (Mauro et al., 2012) to have properties similar to those detected in Terzan 5 and Liller 1, two massive clusters in the bulge direction that are suspected to be the relics of the primordial assembling process of the Galactic bulge and define a new class of stellar systems named *Bulge Fossil Fragments* (BFFs, see Ferraro et al., 2009, 2016, 2021; Origlia et al., 2011; Massari et al., 2014). The BFFs are systems that, in spite of their appearance as genuine GCs, host multi-age stellar populations and could be the remnants of massive clumps that contributed to form the bulge at the epoch of the Galaxy assembly.

The investigation of the properties of NGC 6440 was started with the determination of a high-resolution extinction map (see Pallanca et al., 2019), which was adopted to correct the effects of the strong differential reddening in the direction of the cluster. This allowed to derive a high-precision, differential reddening-corrected, proper motion-selected CMD. Starting from this data set, in this Chapter, we present

a new determination of the center of gravity and the cluster age, and the construction of an accurate star density profile, from which new structural parameters and characteristic relaxation times have been derived. Then, following the approach of the MIKiS survey, we present the kinematic study of the cluster based on the combination of different data sets acquired with four appropriate spectrographs: the AO-assisted IF spectrographs SINFONI and MUSE/NFM sample the innermost regions, while we use the IF spectrograph KMOS and the multi-object fiber-fed spectrograph FLAMES/GIRAFFE to cover at intermediate and large radii, respectively. In the Chapter, the VD profile and the detection of internal rotation of the cluster are also shown. Therefore, we are able to present a full and accurate characterization of the internal structure and the kinematics view of NGC 6440.

4.2 Determination of the structural properties of NGC 6440

The systematic use of HST and, more recently, AO-assisted observations has opened the possibility of deriving structural parameters from projected density profiles obtained directly from star counts even for the innermost regions of high-density stellar systems, not only in the Galactic halo and bulge (e.g., Ferraro et al. 2009; Saracino et al. 2015; Ferraro et al. 2021), but also beyond the MW (Lanzoni et al., 2019). In spite of this, the vast majority of GC structural and morphological parameters currently available in largely used catalogs (e.g., Harris, 1996, 2010 edition; McLaughlin & van der Marel, 2005) are still derived from surface brightness (SB) profiles. The advantages of determining the cluster structural parameters from individual star counts instead of SB are several. By construction, SB profiles directly depend on the luminosity of the surveyed stars and can therefore be artificially distorted by the sparse presence of luminous sources (see, e.g., Noyola & Gebhardt, 2006, for the discussion of methods trying to correct for this problem) and/or reddening bubbles within the field of view (FOV). Instead, this has no impact on the density distribution obtained from resolved star counts since every object has the same weight independently of its luminosity. In addition, if PMs can be measured, field stars (that may be particularly bright and substantially contribute to SB) can be explicitly excluded from the determination of the number count density profile. Hence, although SB can be helpful in cases of severe photometric incompleteness of the catalogs (e.g., Santos et al., 2020), it should be always used with caution, and number counts generally represent the most robust way for determining the cluster structural parameters (e.g. Lugger et al., 1995; Ferraro et al., 1999a). Moreover, once the cluster core is full resolved into individual stars, the determination of the center of gravity of the system becomes possible by simply averaging the coordinates of the detected stars, hence using the center of gravity, instead of the center of luminosity, as optimal proxy of the cluster center (Montegriffo et al. 1995, see also Calzetti et al.

1993). However, apart from a few studies regarding individual or very small sets of clusters (e.g. Salinas et al., 2012), these techniques have not be fully exploited in the literature yet, because constructing complete samples of stars in the highly crowded central regions of GCs is not an easy task (Ferraro et al., 1997; Raso et al., 2017).

In this Section, we address the study of the structural properties of NGC 6440 from resolved star counts, by using a combination of high-resolution HST images, wide-field ground-based observations performed with the ESO-FORS2, and the public survey catalog Pan-STARRS. In the following, we present the accurate determination of the gravitational center, projected density profile and structural parameters of this globular from resolved star counts. In addition, by taking advantage of high-quality optical and near-infrared CMDs, we also estimated the cluster age, distance and reddening.

4.2.1 Observations and Data Analysis

To properly sample the entire radial extension of NGC 6440, in the present work we used a combination of high-resolution and wide-field images, complemented with catalogs from public surveys.

The highly crowded central regions of the system have been investigated by means of HST data, consisting in a series of deep images acquired with the Wide Field Camera 3 (WFC3) through different filters (especially, F606W and F814W) and in various epochs (see Table 4.1). This is essentially the same data set used in Pallanca et al. (2019) to construct the extinction map in the direction of the cluster. Hence more details can be found there. Here we just remind that this data set provides us with two different samples: (a) the *HST-PM sample* including all the stars with measured PM, thus allowing the decontamination from possible non-cluster members (Galactic field stars), and (b) the *HST-noPM sample* including also the stars observed in only one epoch (hence, with no PM measure) and covering a larger area on the plane of the sky.

For the intermediate cluster region, we used ground-based data acquired with the FOcal Reducer/low dispersion Spectrograph 2 (FORS2) mounted at the ESO-VLT at Paranal Observatory (Chile) and retrieved from the ESO Science Archive. The FORS2 imaging detector consists of a mosaic of two 2000x4000 pixel MIT CCDs (15 μm/pixel) that combines a relatively large FOV ($6.8' \times 6.8'$) and reasonably high-resolution capabilities (pixel size of $\sim 0.25''$) for the standard resolution set up. The core of the cluster is roughly located at the center of the FORS2 FOV. Only one image in the $V_{\rm BESS}$ and one in the $I_{\rm BESS}$ filters were available for NGC 6440.

To properly sample the cluster outskirts and beyond, we retrieved (from `https://catalogs.mast.stsci.edu/panstarrs/`) the Pan-STARRS catalog for a circular region of $700''$ radius centered on NGC 6440. The Panoramic Survey Tele-

scope and Rapid Response System (Pan-STARRS) is a wide-field photometric survey operated by the Institute for Astronomy at the University of Hawaii, performed with a 1.4 Gigapixel camera (GPC1) mounted at a 1.8 meter telescope, in five broad-band filters (g, r, i, z, y). For the present analysis we used only i and r data.

The detailed description of the data analysis procedure for the HST data set can be found in Pallanca et al. (2019). Here we just summarize the main steps. The photometric analysis has been carried out by using the DAOPHOT package (Stetson, 1987). The point spread function (PSF) for each image has been modelled on several bright and isolated stars, by using the DAOPHOTII/PSF routine. Then PSF-fitting photometry has been performed independently on all the images by imposing a source detection threshold more than 5-σ above the background level and, a master list has been produced considering as reliable sources all the objects measured in more than half of the images in at least one filter. We then run the ALLFRAME package (Stetson, 1987, 1994) that simultaneously determines the brightness of the stars in all the frames, while enforcing one set of centroids and one transformation between all the images. Finally, the magnitudes obtained for each star have been normalized to a reference frame and averaged. The photometric error was derived from the standard deviation of the repeated measures. The instrumental magnitudes have been calibrated to the VEGAMAG system by using the photometric zero points reported on the WFC3 web page*. Geometric distortions have been corrected following the prescription of Bellini et al. (2011) and then reported to the absolute coordinate system (α, δ) as defined by the World Coordinate System by using a sample of stars in common with the publicly available Gaia DR2 catalog (Gaia Collaboration et al., 2016a,b). The resulting astrometric accuracy turns out to be $< 0.1''$.

A similar procedure was adopted in the analysis of the FORS2 wide-field data set. In summary, per each exposure we modelled the PSF by using dozens of bright, isolated and non saturated stars and we applied such model to all the sources detected at 3-σ above the background level. In a second step we created a master list containing all the detected sources and for each object we forced the fit in both filters. The further step consisted in the creation of the catalog listing all the magnitudes measured in both filters. Finally, the instrumental positions have been reported to the absolute coordinate system by using a sample of stars in common with the Gaia DR2 catalog. In order to make the three catalogs homogeneous in magnitude, we calibrated the V_{BESS} and I_{BESS} magnitudes of FORS2 onto the HST F606W and F814W magnitudes, respectively, by using color equations obtained from a large number of stars in common between the two data sets. Then, we used the stars in common between Pan-STARRS and FORS2 to homogenize the r and i magnitudes of the former with the FORS2 magnitudes previously calibrated onto HST. Hence,

*http://www.stsci.edu/hst/wfc3/phot_zp_lbn.

at the end of the procedure, the magnitudes measured in the three data sets are all homogeneous and calibrated in the same (HST) system. From now on, we use the symbols V_{606} and I_{814} to indicate both the HST magnitudes, and the magnitudes of the other two data sets calibrated onto the F606W and the F814W bands, respectively.

Table 4.1: Summary of the used data set.

Instrument Survey	Program ID	PI	Filter	$N_{exp} \times T_{exp}$
WFC3 [1]	GO 11685	Van Kerkwijk	F606W	1×392 s + 1×348 s
			F814W	1×348 s + 1×261 s
WFC3 [1]	GO 12517	Ferraro	F606W	27×392 s
			F814W	27×348 s
WFC3 [1]	GO 13410	Pallanca	F606W	5×382 s
			F814W	5×222 s
			F656N	10×934 s
WFC3 [1]			F606W	5×382 s
			F814W	5×222 s
			F656N	10×934 s
WFC3 [1]			F606W	5×382 s
			F814W	4×222 s + 1×221 s
			F656N	6×934 s + 2×864 s +2×860 s
WFC3 [1]	GO/DD 15403	Pallanca	F606W	2×382 s
			F814W	1×223 s + 1×222 s
			F656N	2×969 s + 2×914 s
FORS2	077.D-0775(B)	Saviane	V_BESS	1×30 s
			I_BESS	1×30 s
GPC1 [2]			r	
			i	

NOTE– [1]=Pallanca et al. (2019), [2]=Pan-STARRS.

Four catalogs have been obtained from the available data sets. The *HST-PM* catalog includes all the stars measured in the portion of the cluster where multi-epoch WFC3 images have been acquired. It has been corrected for differential reddening (see Pallanca et al., 2019) and decontaminated from Galactic field stars via PM analysis. It counts 137194 stars. The *HST-noPM* catalog is made of all the stars detected in the portion of the cluster surveyed by all the available WFC3 observations. It reports the observed magnitudes (with no correction for differential reddening) for a total of 174418 objects. The *FORS2* catalog contains 27487 stars measured in a roughly square region of 200″ size around the cluster center. The

Pan-STARRS catalog lists 40419 stars within a circle of 700″ radius.

Figure 4.1 shows the spatial distribution of all the stars included in each of the four catalogs (blue dots), with respect to the cluster center. The corresponding

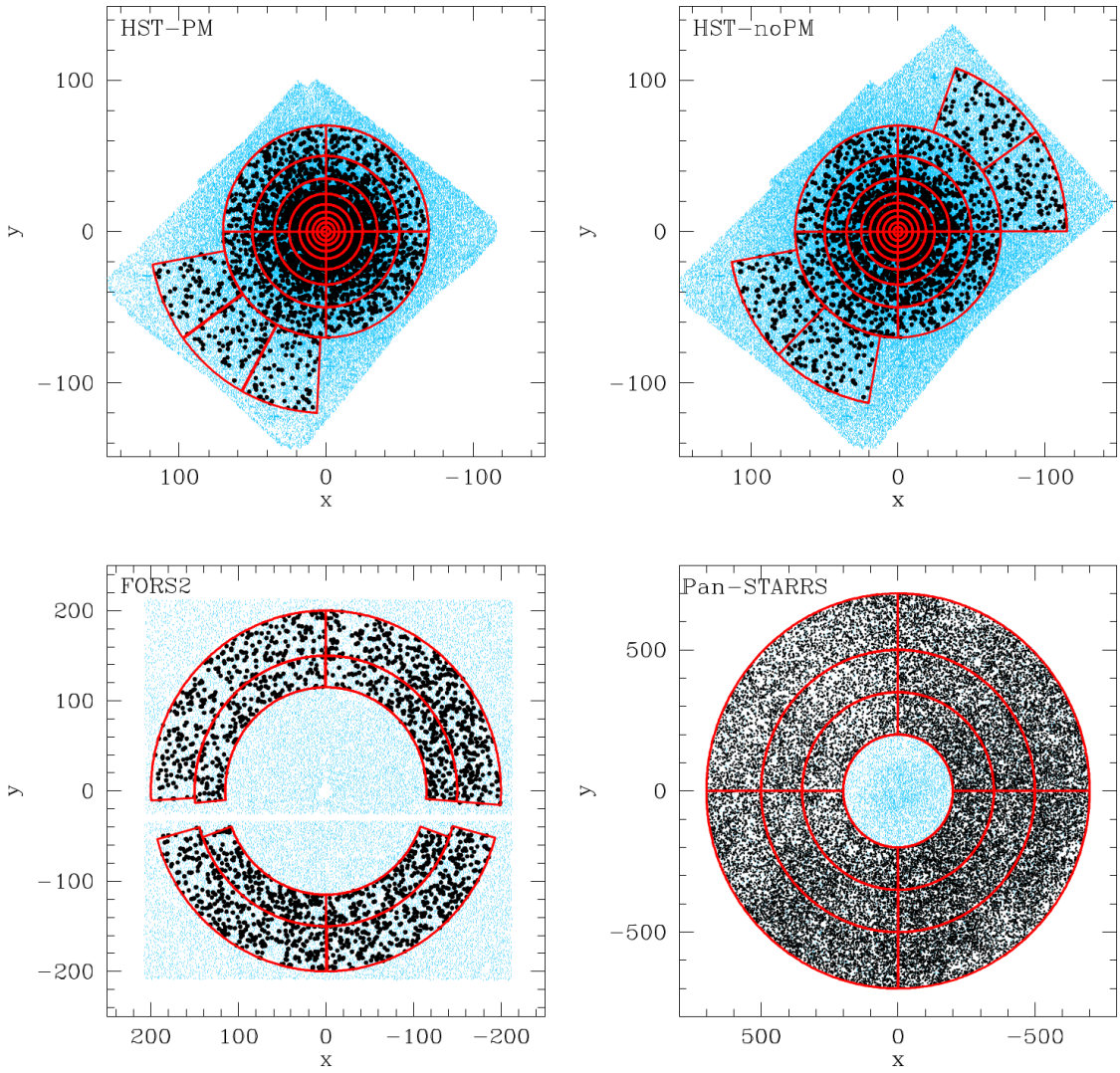

Figure 4.1: Spatial distribution of all the observed stars in each catalog (blue dots), with respect to the newly determined cluster center (see Table 4.6). The black dots correspond to the objects used to determined the cluster density profile: stars with $I_{814} < 19$ belonging to the HST-PM catalog (used to build the density profile shown in red in Figure 4.4) and stars with $I_{814} < 18.5$ in the other three data sets (used for the density profile shown in black in Figure 4.4). The red lines delineate the annuli and sub-sectors used to construct the density profile.

CMDs, which are plotted in Figures 4.2 and 4.3, are deep enough to trace the (cluster and field) stellar populations down to 3-4 magnitudes below the cluster Red Clump. Of course, an increasing population of field stars appears and becomes dominant with respect to cluster members for increasing distances from the cluster center, i.e., from the HST, to the FORS2, to the Pan-STARRS data set.

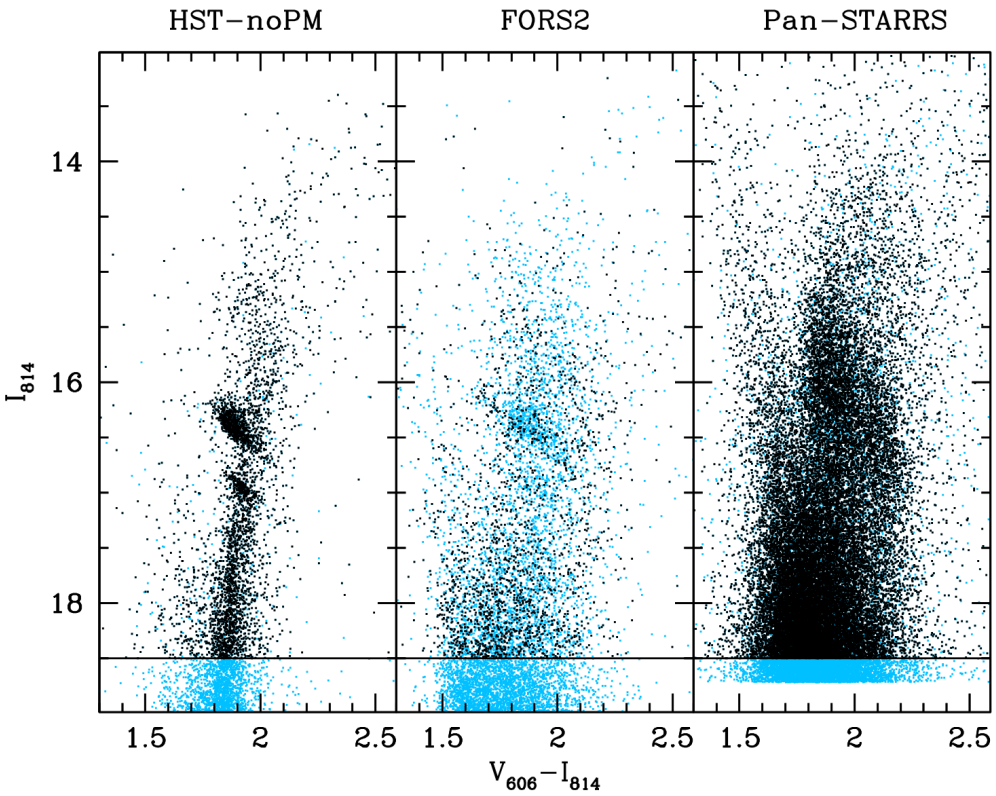

Figure 4.2: CMDs of NGC 6440 obtained from the *HST-noPM*, *FORS2* and *Pan-STARRS* catalogs discussed in the text (left, central, and right panel, respectively). The entire samples of surveyed stars are plotted in light blue, while the black dots highlight the stars used for the construction of the density profile.

4.2.2 Determination of the center of gravity

As discussed in many previous works (see, e.g., Montegriffo et al., 1995; Ferraro et al., 1997, 1999a), dealing with resolved stars for the determination of the cluster center avoids introducing the bias induced by the possible presence of a few bright stars, which can generate a SB peak in an off-set position with respect to the true gravitational center. Here we thus took advantage of the *HST-PM* catalog, which properly samples the central region of the cluster, is corrected for the effects of differential reddening, and has been decontaminated from field star interlopers (see Figure 4.3). We used the same iterative procedure already adopted, e.g., in Lanzoni et al. (2007a, 2010, 2019), where the gravitational center ($C_{\rm grav}$) is determined by averaging the (x, y) coordinates on the plane of the sky of all the stars observed in a selected range of magnitude and within a circle of radius r centered on a first-guess value (typically, the center quoted in the literature). We always adopt different values for the magnitude-cut and radius r, both to check the occurrence of possible dependencies of the result on these assumptions, and to estimate the uncertainty on the final position of $C_{\rm grav}$. As discussed in Miocchi et al. (2013), the adopted values

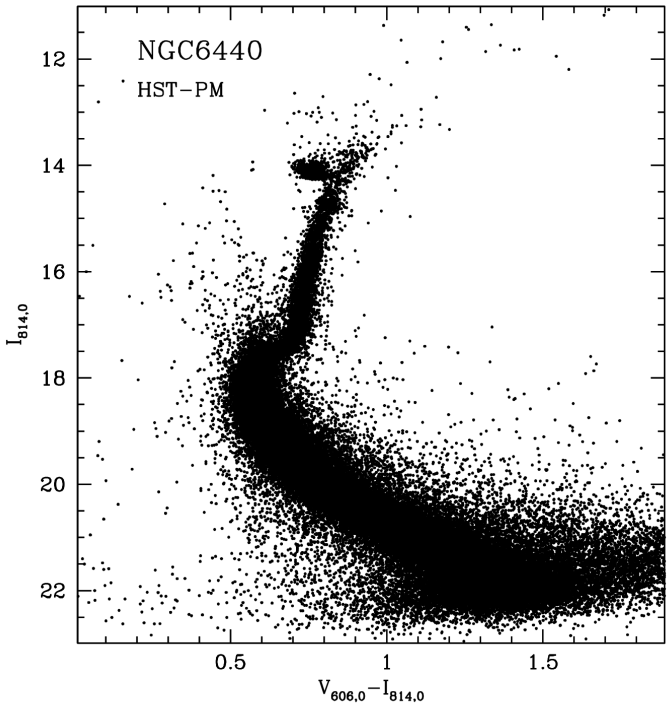

Figure 4.3: CMD of NGC 6440 from the *HST-PM* catalog. Only high-quality stars are plotted. Non-member stars (as determined from the proper motion analysis) have been removed. The magnitudes are corrected for the effect of reddening (Pallanca et al., 2019).

of r always exceed the core radius (r_c) quoted in the literature, to guarantee that the averaging procedure acts in a region where the density profile decreases with radius, i.e., is no more uniform (as it is, instead, in the innermost region). Taking into account that the literature values of r_c vary from $\sim 5''$ to $\sim 8''$ (see Table 2), we adopted $r = 15''$, $20''$, $30''$. As magnitude-cuts, we used reddening corrected $I_{814,0} < 18, 18.2, 18.5$, thus selecting approximately equal-mass samples, since the difference in mass between the stars at the main-sequence turnoff level and those in evolved evolutionary phases is quite small (within a few 0.01 $M_\odot$). For every pair of magnitude-cut and r values, $C_{\rm grav}$ has been determined iteratively starting from the center quoted in the Harris (1996, 2010 edition) catalog and assuming that convergence is reached when ten consecutive iterations yield values of the cluster center that differ by less than $0.01''$ among them. As gravitational center of NGC 6440, we finally adopted the average of the values of $C_{\rm grav}$ obtained from this procedure, namely: $\alpha = 17^{\rm h}48^{\rm m}52.84^{\rm s}$ and $\delta = -20°21'37.5''$, with an uncertainty of $\sim 0.3''$. This is $\sim 2''$ east and $\sim 0.6''$ south from the center quoted in the Harris (1996, 2010 edition) catalog. Such a difference can have a non negligible impact on the derived shape of the star density profile and, more in general, on the study of the radial behavior of any stellar population within the cluster potential well.

4.2.3 Star count density profile

In order to build the projected star density profile, $\Sigma_*(r)$, along the entire cluster radial extension, we combined the available photometric data-sets as follows: the *HST-noPM catalog* covers the innermost cluster regions ($\leq 115''$), the *FORS2 catalog*, where the center remains unresolved because of stellar crowding, is used to sample the intermediate regions ($115'' < r \leq 200''$), and the *Pan-STARRS catalog* refers to the outermost cluster regions ($200'' < r \leq 700''$). We considered only stars brighter than $I_{814} < 18.5$ (i.e., ~ 2 mag above the main-sequence turnoff; black dots in the top-right and bottom panels of Figure 4.1 and in Figure 4.2), because this limit ensures comparable levels of (high) photometric completeness, in combination with high enough statistics (thousands of stars) in all the catalogs. Following the standard procedure already adopted in several previous works (see Lanzoni et al., 2019 and references therein), we divided each photometric sample in several concentric annuli centered on $C_{\rm grav}$ (see Figure 4.1), and split each annulus into an adequate number of sub-sectors (typically four). The number of stars lying in each sub-sector was counted, and the star surface density was obtained by dividing these values by the corresponding sub-sector area. The stellar density in each annulus was then obtained as the average of the sub-sector densities, and the standard deviation was adopted as the uncertainty.

The observed stellar density profile is shown in Figure 4.4 (upper panel), where different symbols refer to different catalogs (empty circles for HST, triangles for FORS2 and squares for Pan-STARRS) and the radius associated with each annulus is the midpoint of the radial bin. As can be seen, the contribution of the Galactic field starts to be evident for distances from the cluster center larger than $r > 100''$ (i.e. in the FORS2 data-set) and becomes dominant for $r > 200''$ (Pan-STARRS catalog). As expected, the spatial distribution of field stars is approximately uniform on the considered radial scale, thus producing a well defined plateau in the outermost portion of the density profile. Hence, the level of Galactic field contamination has been estimated by averaging the data-points aligned in the plateau (see the dashed line in Figure 4.4) and the (decontaminated) cluster profile, obtained after subtraction of the Galaxy background level, is finally shown in Figure 4.4 (top panel; filled symbols). As apparent, after the field subtraction, the profile remains almost unchanged at small radii, which are in fact dominated by the cluster population, while it significantly decreases in the most external regions, where it turns out to be significantly below the Galactic background. This clearly indicates that an accurate measure of the field level is crucial for the reliable determination of the outermost portion of the density profile. The background subtraction has a well-perceivable effect also in the region sampled by HST data. We thus took advantage of the *HST-PM* catalog, which is already cleaned from Galactic field interlopers, to double check the reliability of the adopted decontamination procedure. Thanks to

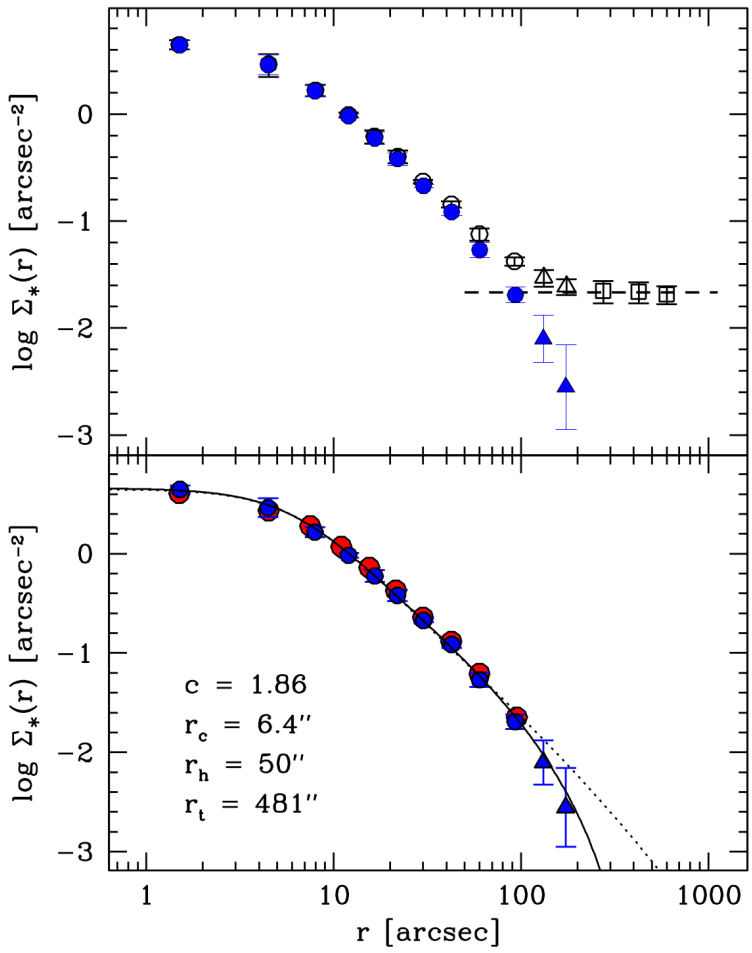

Figure 4.4: *Top:* Observed star density profile of NGC 6440 obtained from resolved star counts by combining three different catalogs: *HST-noPM* (empty circles), *FORS2* (empty triangles) and *Pan-STARRS* (empty squares). The filled blue symbols correspond to the cluster density profile obtained after subtraction of the Galaxy field contribution (dashed line). *Bottom:* Cluster density profile shown in the top panel (blue symbols) compared to that obtained from the *HST-PM* catalog (red circles). As can be seen the agreement is very good, thus guaranteeing the reliability of the applied background subtraction (see text). The black line shows the best-fit King model profile. The corresponding values of the concentration parameter (c) and a few characteristic scale-lengths (in arcseconds) are also labelled. The dotted line shows the best-fit Wilson model.

the high level of completeness of the HST observations, we constructed the cluster density profile by using stars down to the sub-giant branch (i.e., 0.5 magnitudes deeper than the sample used in the previous procedure; black dots in the top-left panel of Figure 4.1), thus benefitting from a much larger statistics. Figure 4.4 (bottom panel) shows the density profile obtained from the *HST-PM* catalog (in red), vertically shifted to match the one obtained with the procedure described above (in blue): as can be seen, the two profiles are essentially identical in the common region, thus confirming the solidity of the adopted field decontamination approach.

In order to derive the physical parameters of the program cluster, we fit the observed star density profile with the family of King (1966) models in the isotropic,

spherical and single-mass approximation. As discussed in Chapter 1, Section 1.1.1, they constitute a *single*-parameter family, since their shape is uniquely determined by the dimensionless parameter W_0, or, alternatively, to the concentration parameter c ($c \equiv \log(r_t/r_0)$, where r_t and r_0 are the tidal and the King radii of the cluster, respectively).

The best-fit King model has been determined by exploring a grid of W_0 values varying between 0.4 and 12 in steps of 0.05, and selecting the solution that minimizes the χ^2 residuals between the observed and the theoretical density profiles (see Miocchi et al., 2013 and Lanzoni et al., 2019 for a detailed description of the adopted procedure and the method used to estimate the uncertainties). The resulting values of W_0, concentration parameter, core, half-mass and tidal radii are: $W_0 = 8.10$, $c = 1.86$, $r_c = 6.4''$, $r_h = 50.2''$, $r_t = 481.4''$, respectively, with the uncertainties quoted in Table 4.6. The effective radius, defined as the radial distance including half the total number counts in projection (and corresponding to the projected half-light radius if SB, instead of resolved star density, is considered) is $r_e = 36.8''$. The comparison with previous determinations in the literature shows significant discrepancies for all the parameters. In particular, the Harris catalog reports the values estimated by McLaughlin & van der Marel (2005), who found $c = 1.62$, $r_c = 8.1''$, $r_h = 44.8''$, $r_{\rm eff} = 28.8''$, and $r_t = 354.9''$ (the values originally quoted in pc have been converted into arcseconds by using the cluster distance provided in that work: $d = 8.4$ kpc). Hence, we find that NGC 6440 is more centrally concentrated than previously thought, with a smaller core radius and larger truncation radius, translating in a larger concentration parameter. The comparison with the values quoted by Baumgardt & Hilker (2018) is less straightforward because N-body simulations, instead of King models, are used there to fit the observation, and no uncertainties are provided. However, the provided values of core, half-mass and effective radii are consistent with ours within 10-20%. We also stress that SB (instead of number count) profiles and an offset position of the cluster centre are used in those studies, thus likely accounting for the different results. The density profile of some GCs is found to be best reproduced by Wilson (1975), instead of King (1966), models (see, e.g., McLaughlin & van der Marel, 2005; Miocchi et al., 2013). We thus compared the observations also with the Wilson (1975) model family, finding the best solution for $c = 3.30$, $r_c = 6.6''$ and $r_t \sim 230'$ (see the dotted line in the bottom panel Figure 4.4). Although the core radius is very similar to that obtained from the King fit, the Wilson model (that, by construction, provides a smoother cutoff at the limiting radius) severely overestimate the observed stellar density in the external portion of the profile. This is in agreement with the fact that NGC 6440 is orbiting the Bulge of our galaxy, where tidal truncation is expected to be more relevant than for faraway halo GCs.

4.2.4 The distance modulus and the age of NGC 6440

The distance modulus and the age of resolved stellar populations (as Galactic GCs) can be estimated through the comparison between the observed CMD and theoretical stellar isochrones, the main obstacle being the well known degeneracy of these parameters with the metallicity and the reddening.

In the case of NGC 6440, the metallicity is relatively well known since the first low-resolution spectroscopic measures (see Armandroff & Zinn 1988; Origlia et al. 1997; Frogel et al. 2001), indicating an overall iron abundance of the order of 1/3 - half solar. More recent high-resolution spectroscopy of small samples of giants measured in the IR (Origlia et al., 2008) and in the optical band (Muñoz et al., 2017) confirmed a considerable iron content ([Fe/H]$= -0.5, -0.6$ dex) with some $\alpha-$enhancement ($[\alpha/Fe] = +0.3$ dex), corresponding to a global metallicity[†] [M/H]~ -0.4 dex.

The accurate estimate of the reddening, instead, is complicated by the fact that NGC 6440 is located close to the Galactic plane and toward the bulge, where the extinction law likely deviates from the canonical and commonly assumed behavior. An extensive discussion about extinction and reddening is presented in McCall (2004). Particular attention, however, has to be given to the extinction toward the inner Galaxy, where the R_V value is not constant and can significantly vary along different directions (e.g., Popowski, 2000; Udalski, 2003; Nataf et al., 2013a; Alonso-García et al., 2017, and references therein). Indeed, as discussed in Nataf et al. (2013a); Casagrande & VandenBerg (2014), and recently confirmed by Ferraro et al. (2021) and Pallanca et al. (2021b), the region toward the Galactic center seems to be better described by an extinction law with a significantly smaller value of R_V (even down to $R_V = 2.5$). Conversely some other authors found larger R_V values ($R_V = 3.2$) to be more appropriate (e.g., Bica et al., 2016; Kerber et al., 2019). Hence, as already discussed by Udalski (2003), the proper dereddening of a particular field in the Galactic bulge might be difficult without prior determination of R_V along its line of sight.

The best way to constrain R_V in a specific direction is by simultaneously investigating the IR and the optical CMDs, which are, respectively, weakly and strongly sensitive to the true extinction law. To this purpose we used a combination of optical and IR catalogs of NGC 6440.

The adopted HST optical catalog was presented in Pallanca et al. (2019), while the IR one is based on deep J and K_s observations obtained with GeMS/GSAOI (S. Saracino et al., 2023, in preparation). For a proper comparison with stellar isochrones, we first corrected the CMDs obtained from these catalogs for the

[†]The global metallicity has been calculated trough the relation reported by Ferraro et al. (1999b) and assuming $[Fe/H] = -0.56$ dex (Origlia et al., 2008)

effect of differential reddening, which broadens and distorts the evolutionary sequences. To this end, we applied the procedure fully described in Pallanca et al. (2019) to the HST data set. Briefly, we determined the reference mean ridge line of NGC 6440 using a sample of well-measured stars. Then, for every star in the HST catalog we selected a sample of close sources, thus defining a "local-CDM". Finally, we estimated the value δE(B−V) necessary to superpose the reference mean ridge line onto the local-CMD and assigned this value to the corresponding investigated star. By construction, the δE(B−V) values thus obtained express the differential component of the reddening within the sampled FOV and can be positive or negative. This quantity, multiplied by the coefficient appropriate for the considered filter, is added to the observed magnitudes to get differential reddening corrected (DRC) magnitudes: $I_{814,DRC}$, $V_{606,DRC}$ (see Figure 4.5). Finally, for all the stars in common with the GeMS/GSAOI sample, the estimated values of δE(B−V) have been used to correct also the IR magnitudes and build the corresponding differential reddening corrected CMD: K_{DRC}, $(J-K)_{DRC}$ (Figure 4.5).

To estimate the distance modulus and the age of NGC 6440, while constraining R_V, we then compared the differential reddening corrected CMDs with a set of PARSEC (Bressan et al., 2012) and Dartmouth (Dotter et al., 2008) isochrones of different ages computed for [M/H]= −0.4 dex in the four photometric bands of interest, namely, the WFC3 V_{606} ad I_{814} filters, and the 2MASS J and Ks filters. To place the isochrones in the differential reddening corrected CMDs, we determined the values of the (temperature- and gravity-dependent) extinction coefficients in the four bands (namely, $R_{V_{606},i}$, $R_{I_{814},i}$, $R_{J,i}$ and $R_{Ks,i}$) for each i^{th} combination of effective temperature and surface gravity along every isochrone (Casagrande & VandenBerg, 2014). This has been done by interpolating the values calculated for the MARCS grid (Gustafsson et al., 2008) under the assumption of the cluster metallicity and the Cardelli et al. (1989) extinction law with $R_V = 2.5$ and $R_V = 3.1$. A linear interpolation between these two limits then allowed us to determine the temperature- and gravity-dependent coefficients for intermediate values of R_V (between 2.5 and 3.1, stepped by 0.1).

We found that, under the assumption of $R_V = 3.1$, no combination of parameters is able to reproduce the optical and the IR CMDs simultaneously. In particular, a combination that well fits the optical CMD corresponds to an excessively bright and red isochrone in the IR, for both the considered models (see the black dashed lines in Figure 4.5). The problem becomes progressively milder for decreasing values of R_V, and the best solution is found for $R_V = 2.7$. Interestingly, similarly small values are needed to properly reproduce the observations of other GCs in the Galactic bulge (Ferraro et al., 2021; Pallanca et al., 2021b). The red lines shown in Figure 4.5 correspond to PARSEC and Dartmouth isochrones (upper and lower panels, respectively) computed under the assumption of $R_V = 2.7$, for an age of 13 Gyr,

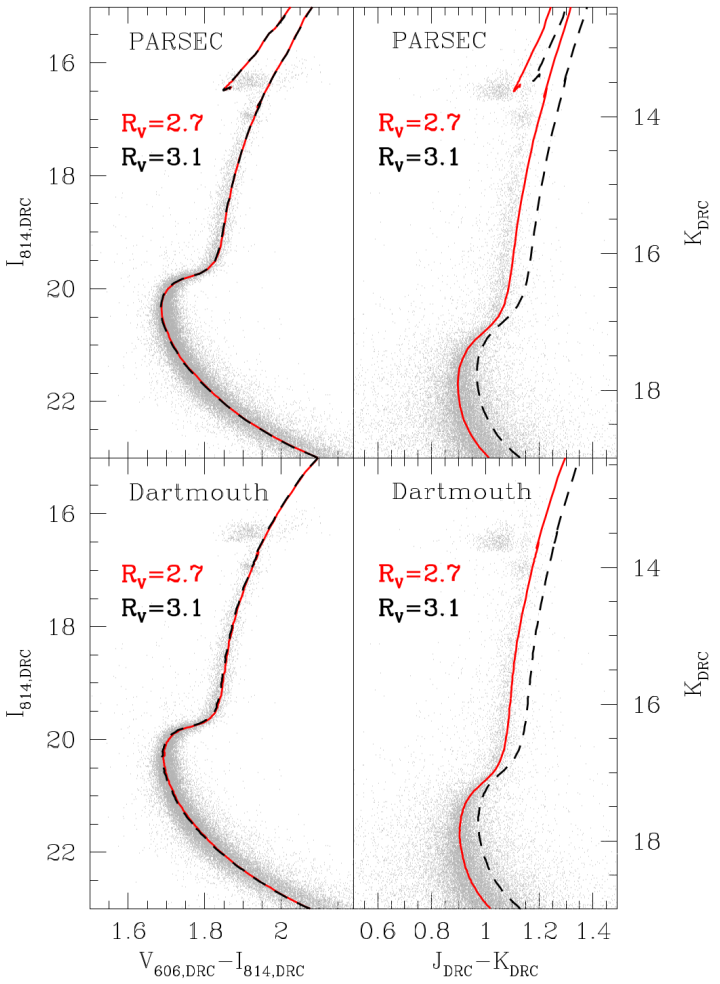

Figure 4.5: Comparison between the differential-reddening corrected CMD of NGC 6440 (grey dots) and theoretical isochrones computed for $R_V = 3.1$ (black dashed lines) and for $R_V = 2.7$ (red lines). The left and right panels show, respectively, the optical and the IR CMDs. The top panels refer to PARSEC isochrones, while the bottom panels show Dartmouth models. No solution able to properly fit the optical and the IR CMDs simultaneously is found for $R_V = 3.1$, while if $R_V = 2.7$ is assumed, both models well reproduce the observations for an age of 13 Gyr, a distance modulus of 14.60 and $E(B-V) = 1.26$-1.28. The fact that the RGB looks steeper than the model in the IR CMDs may be due to non-linearity effects of the GeMS/GSAOI photometry (see Saracino et al., 2016).

a distance modulus $\mu_0 = 14.60$ and an absolute color excess that is just slightly different between the two models: $E(B-V) = 1.28$ and 1.26, respectively. In particular, this combination of parameters not only well reproduces the horizontal branch magnitude level (see the PARSEC isochrones in the figure), but also best-fits the SGB/MS-TO region, which is the most sensitive to age variations. The best-fit solution has been evaluated through a χ^2 analysis, by determining, for each SGB/MS-TO star, the difference between its observed color and the color at the same magnitude level along the isochrones of 11, 12, 13 and 14 Gyr. As already done in previous works (Ferraro et al., 2021; see also Saracino et al., 2016) the χ^2

parameter has been computed as the ratio between the square of this difference and the color along the isochrone, summed over all the selected stars. The best-fit model to the optical CMD and the χ^2 values as a function of the investigated ages are plotted, respectively, in the top and bottom panels of Figure 4.6. Taking into account the various uncertainties and degeneracies entering the fitting procedures, conservative estimates of the errors on the distance modulus and age are 0.1 mag and 1.5 Gyr, respectively. Several previous works in the literature have been devoted

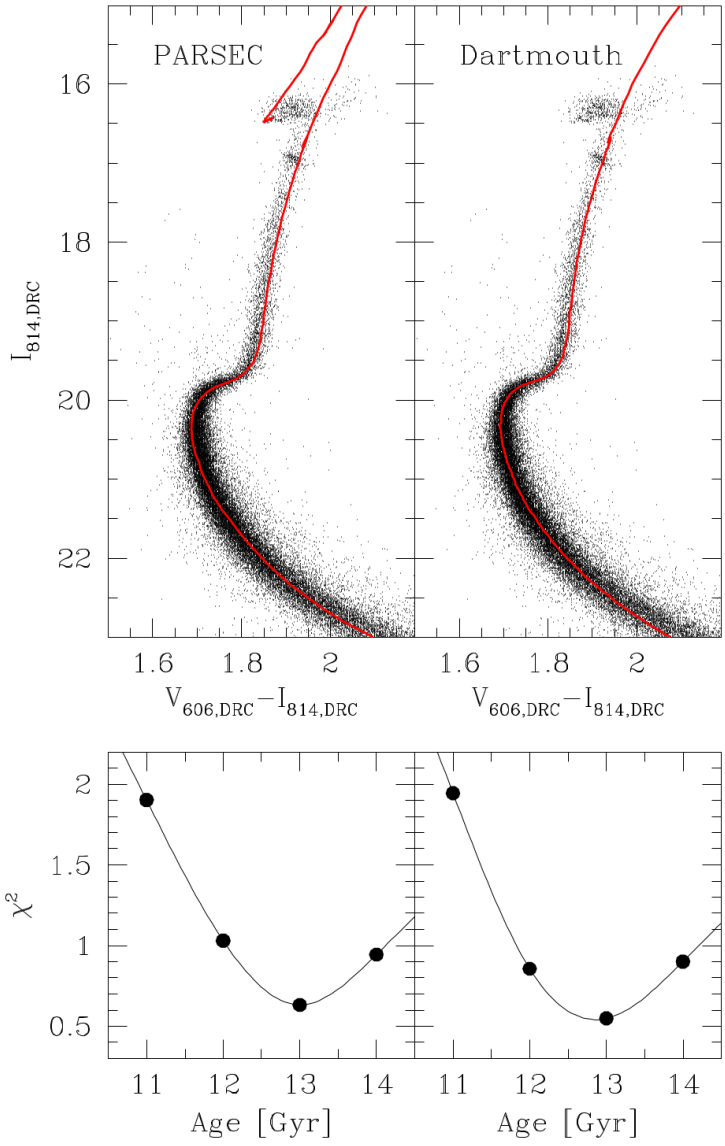

Figure 4.6: *Top panels:* differential-reddening corrected CMD of NGC 6440 with the best-fit isochrone from the PARSEC (left) and the Dartmouth (right) models superimposed as red lines (the same as in Figure 4.5). *Bottom panels:* value of the χ^2 parameter (see text) obtained from the fit of the SGB/MS-TO region through PARSEC (left) and Dartmouth (right) isochrones of 11, 12, 13, and 14 Gyr, as a function of the model age. The minimum of the χ^2 parameter is found for an age of 13 Gyr.

to the determination of these parameters for NGC 6440. The study by Ortolani et al. (1994) is based on optical photometry, while the others have been performed in the IR, and in all cases the standard reddening law has been assumed. The only exception is the investigation of Kuchinski & Frogel (1995), who combined IR data with V band photometry and suggested that the anomalous colors observed for this cluster might require a non-standard reddening law. This is in agreement with our finding, although a detailed comparison between the proposed reddening laws in not obvious. Given the different R_V adoption, the comparison among various reddening determinations in the literature has to be done in terms of the extinction coefficient A_V, instead of the color excess E(B − V), which is linked to the former by the following relation: $A_V = R_V \times$ E(B − V). Minniti (1995) quote E(J − K) = 0.57 and comment that this value is in good agreement with that of Ortolani et al. (1994), who found E(B − V) = 1 and adopt $R_V = 3$, corresponding to $A_V = 3$. Valenti et al. (2004) quote E(B − V) = 1.15 and adopt $R_V = 3.1$, thus providing $A_V = 3.56$. From the Harris compilation, $A_V = 3.32$ is obtained for the standard value of R_V. The value estimated in the present study ($A_V = 2.7 \times 1.27 = 3.43$) therefore is within the range spanned by the results of previous works, which however do not correct for differential reddening, nor take into account the optical and IR CMDs simultaneously. Also the distance modulus here determined is in reasonable agreement with previous determinations and included between them: $\mu_0 = 14.64$ and 14.58 in Ortolani et al. (1994) and Valenti et al. (2004), respectively. Finally, an age of 11^{+3}_{-2} Gyr was estimated by Origlia et al. (2008) from pioneering adaptive optics photometry, and 13 Gyr is the value adopted by Muñoz et al. (2017) to fit the observed CMD with theoretical isochrones. These are both consistent with our determination of 13 ± 1.5 Gyr.

4.2.5 The RGB-bump

The high-quality of the CMDs obtained allows us to easily identify a well known evolutionary feature along the RGB: the so-called RGB bump. This feature appears in the CMD as a well defined clump of stars along the RGB. This evolutionary feature flags the moment when the H-burning shell reaches the H discontinuity left by the inner penetration of the convective envelope (see the seminal works by Fusi Pecci et al. 1990, Ferraro et al. 1992 and Ferraro et al. 1999b, 2000; see also the compilation by Zoccali et al. 1999, Riello et al. 2003 and Valenti et al. 2004b, and more recently by Nataf et al. 2013b). Figure 4.7 shows the differential luminosity function of the bright RGB stars in the differentially-corrected V_{606}, J, K bands. The well-defined peaks at $V_{606,DRC} = 18.84 \pm 0.05$, $J_{DRC} = 15.16 \pm 0.05$, $K_{DRC} = 14.04 \pm 0.05$ correspond to the RGB bump. Adopting the extinction and the distance reported in Table 4.6, we transformed the above values into absolute magnitudes obtaining $M^{Bump}_{V_{606}} = 1.12 \pm 0.12$, $M^{Bump}_{J} = -0.37 \pm 0.12$ and $M^{Bump}_{K} = -0.94 \pm 0.12$. In

Figure 4.8 we show the comparison among these measures and previous determinations in the literature. In particular in the bottom and central panels of Figure 4.8 we show the nice agreement of the RGB bump magnitude in the IR bands with the estimates and the relations quoted in Valenti et al. (2004b). The situation appears to be much more complex in the optical V_{606} band, since the magnitude level found in the present study appears significantly brighter than that obtained by Nataf et al. (2013b), who quote $M_{V_{606}}^{Bump} = 1.48$. While the adopted extinction law and distance modulus are just slightly different between the two studies, most of the discrepancy is due to the observed RGB bump magnitude: $V_{606} = 19.431 \pm 0.021$ in Nataf et al. (2013b), $V_{606} = 18.9$ in our study. In addition, a metallicity as high as [M/H] = +0.03 has been assumed in that work. Nevertheless, we note that the

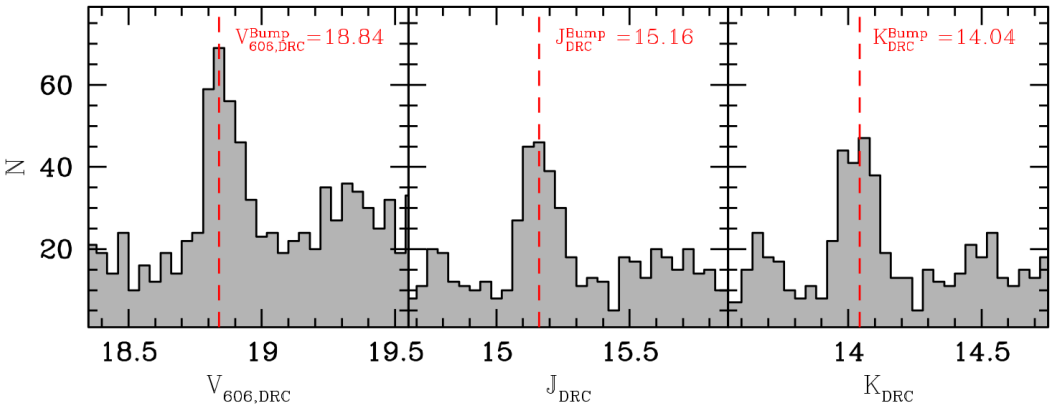

Figure 4.7: Differential luminosity function of RGB stars classified as cluster members and photometrically well measured. The detected peaks (marked by the dashed red lines) correspond to the RGB-bump magnitude in the three photometric bands (see labels).

new determination of the RGB bump combined with the adopted metallicity well follows the trend of the GC distribution reported by Nataf et al. (2013b).

4.2.6 Central relaxation time and half-mass relaxation time

The new determinations of the cluster structural parameters, distance and reddening allow us to also update the value of relaxation time of NGC 6440, which characterizes the dynamical evolutionary stage of the system. It quantifies the timescale needed by two-body interactions (causing kinetic-energy exchanges among stars) to bring the cluster toward a thermodynamically relaxed state. Primarily depending on the local density, the value of the relaxation time changes with the radial distance from the cluster center. To estimate the central relaxation time (t_{rc}) we used equation (10) of Djorgovski (1993). For the half-mass relaxation time (t_{rh}) we followed equation (8-72) of Binney & Tremaine (1987). The latter parameter can be estimated also from eq. (11) of Djorgovski (1993) once the first coefficient

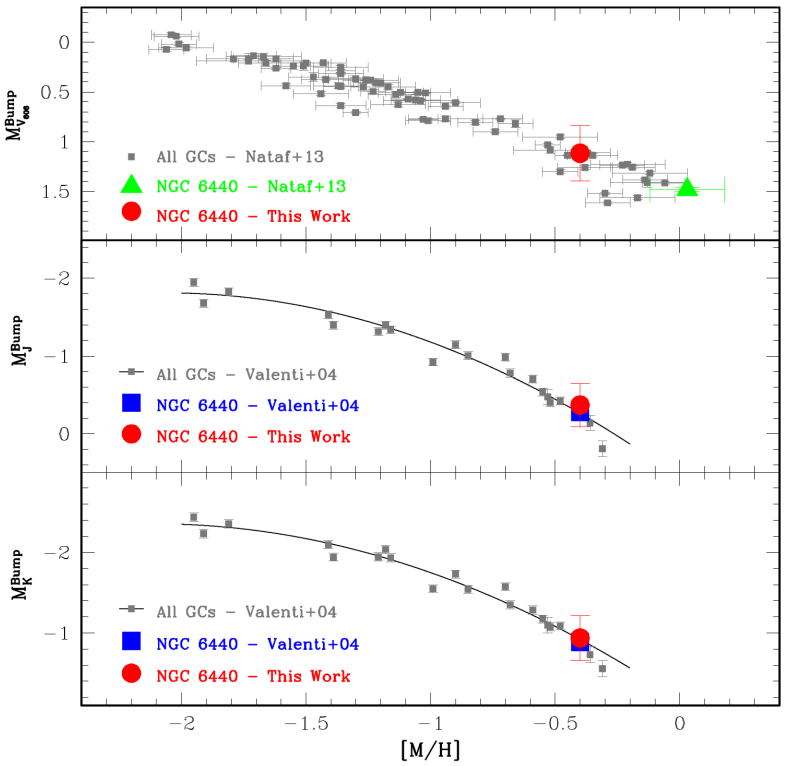

Figure 4.8: Absolute magnitude of the RGB-bump in the V_{606}, J and K bands (from top to bottom) as a function of the GC global metallicity [M/H]. The gray symbols are from the literature (see labels). The blue squares and the green triangle mark the location of NGC 6440 according to literature (Nataf et al., 2013b; Valenti et al., 2004b) while the red circle mark the values determined in this work.

(8.993×10^5 in the equation) is substituted by its proper value (2.055×10^6; see Binney & Tremaine, 1987; McLaughlin & van der Marel, 2005). We also emphasize that the projected half-light radius r_e (instead of the three-dimensional half-mass radius r_h) is often used in this estimate (see, e.g., Harris, 1996, 2010 edition; McLaughlin & van der Marel, 2005), under the implicit assumption that these radial scales are equal. However, depending on the value of the concentration parameter, the ratio between the effective and the half-mass radii varies between 0.73 and 0.76. As a consequence, since t_{rh} scales with half-mass radius at the power of 3/2, the relaxation time obtained by adopting r_e (t_{re}) is $\sim 35\%$ shorter than that calculated by using r_h. Assuming the absolute $V-$band magnitude and central SB quoted for NGC 6440 in the Harris (1996, 2010 edition) catalog, and the same values adopted there for the average stellar mass ($0.3 M_\odot$) and V-band mass-to-light ratio ($M/L_V = 2$), the new determinations of the structural parameters, distance, and extinction quoted in Table 4.6, bring to $\log(t_{rc}) = 7.4$ and $\log(t_{rh}) = 9.0$ (in units of year). If the effective radius is used in place of r_h (as it is done, e.g., in the Harris catalog and in McLaughlin & van der Marel, 2005), the relaxation time becomes smaller than 1 Gyr: we find $\log(t_{re}) = 8.8$, which is 37% shorter than t_{rh}. For comparison, the central relaxation

time quoted in the Harris (1996, 2010 edition) catalog is $\log(t_{rc}) = 7.6$, i.e., a factor of ~ 1.6 longer than our determination, and the median relaxation time (8.62 in logarithmic units) is a factor of ~ 1.5 shorter than our value of t_{re}, mainly reflecting the scale-length differences discussed above, while the assumption of different extinction law and color excess has a negligible impact on the result. Anyway, these values suggest that NGC 6440 is in a dynamically evolved stage, since its age being much longer than the relaxation times.

4.3 Internal kinematics of NGC 6440

In the context of the ESO-VLT MIKiS of GGCs, in this Section, we exploit the results obtained in the previous Section 4.2 to complement the study of the internal structure of NGC 6440 with the LOS-based characterization of its kinematic properties. By combining the data acquired with four different spectrographs, we obtained the RV of a sample of ~ 1800 individual stars distributed across all the cluster extension, from $\sim 0.1''$ to $778''$ from the center. Our data set allowed us to properly derive the VD profile of the cluster, and to detect a non-negligible rotation in the core region. As for NGC 1904 (see Chapter 3), also in this case the exceptional capabilities of MUSE/NFM in the exploration of GC cores are pointed out.

4.3.1 Data sets

As done in the Chapter for 3 NGC 1904, we adopted a multi-instrument approach to characterize the internal kinematics of NGC 6440, by measuring the RVs of resolved, individual stars located over the entire radial extension of the system.

- *MUSE* - The spectra of the stars in the innermost cluster regions were acquired with the AO-assisted IF spectrograph MUSE/NFM (Bacon et al., 2010, see Chapter 2, Section 2.2.1 for a more detailed description of the instrument), as part of the NFM science verification run (program ID: 60.A-9489(A), PI: Ferraro, see Table 4.2). Our MUSE/NFM data set consists of a mosaic of four pointings centered within $15''$ from the cluster center (see Section 4.2.2, and Table 4.6). Each exposure, usually three for each pointing, has been acquired with an exposure time of 850 s, and the DIMM seeing during the observations ranged from $0.45''$ to $0.8''$. The mosaic of the reconstructed I-band images from the stacking of MUSE datacubes is shown in the left panel of Figure 4.9. Each pointing is labeled with a name according to its position with respect to the cluster center ("C", "S", "E", and "N" standing for central, southern, eastern, and northern pointing, respectively).

- *SINFONI* - The MUSE/NFM data analysis in the innermost cluster regions has been complemented using additional AO-assisted IF observations, per-

formed with the spectrograph SINFONI (Eisenhauer et al., 2003) at the ESO-VLT (see Chapter 2, Section 2.2.2). The observations were conducted under ESO proposals 093.D-0319(A), PI: Lanzoni, and ID:195.D-0750(A), PI: Ferraro (see Table 4.2), and consist of 7 LR pointings and 3 HR pointings (see Section 2.2.2 for more details) covering a region within $\sim 16''$ from the cluster center. Multiple exposures of 20-30 s each were performed on the target and on a sky position located $\sim 165''$ from the center. The observations have been executed under an average DIMM seeing of $\sim 0.8''$, leading to a Strehl ratio between 10 and 40. The right panel of Figure 4.9 shows the reconstructed image of the SINFONI pointings obtained by stacking the datacubes in the wavelength range $2.15 - 2.18\mu$m. Clearly, some stars are in common with the MUSE data set, but the SINFONI pointings, in spite of a worse angular resolution, also sample the west and south-west regions around the cluster center that remained uncovered by MUSE (see Figure 4.10). In Figure 4.11 we compare the same cluster region as seen in the reconstructed MUSE and SINFONI images (central and right panels, respectively) and in the HST observations (left panels). This well illustrates the exceptional resolving capabilities of the AO systems used in the SINFONI (especially in the HR set put) and, even more, in the MUSE observations, which are mandatory to obtain large samples of RVs of individual stars in the high-density core of dense stellar systems like NGC 6440.

- KMOS - To investigate the cluster kinematics at intermediate distances from the center, we have used the IF spectrograph KMOS (Sharples et al., 2013) at ESO-VLT (see Chapter 2, Section 2.2.3). The data have been collected as part of the ESO Large Program ID: 193.D-0232(A). These consist in 12 pointings within $\sim 6'$ from center, each one obtained with three sub-exposures 30 s long. Every IFU is typically centered on one star, selected at $J < 14$ along the red giant branch (RGB) of the cluster from the near-infrared SOFI (Valenti et al., 2004, 2007)[‡] and a J, H, and Ks bands 2MASS catalog sampling the outer regions.

- FLAMES - The external regions of NGC 6440 have been sampled out to $\sim 12'$ from the center by using the fiber-fed multi-object spectrograph FLAMES (Pasquini et al., 2002) in the GIRAFFE/MEDUSA mode (see Chapter 2, Section 2.2.4 for more details about the instrument). As for KMOS, also the FLAMES observations have been performed within the MIKiS survey under the ESO Large Program 193.D-0232(B). Five pointings have been performed, each one securing two exposures of 2700 s. The targets are RGB stars brighter than $J = 14$ selected from the same photometric SOFI catalog used for the

[‡]http://www.bo.astro.it/∼GC/ir_archive/

KMOS targets and from the 2MASS catalog.

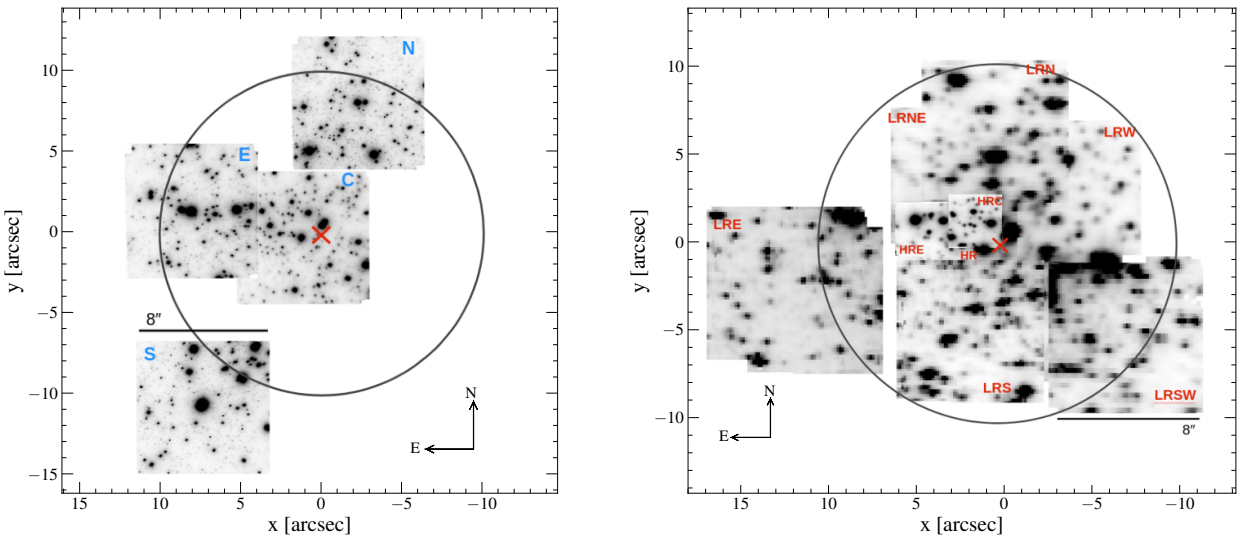

Figure 4.9: *Left:* Reconstructed I-band images of the MUSE/NFM pointings. The circle is centered on the cluster center (red cross, as derived in Section 4.2.2, see also Table 4.6) and has a radius of 10″. *Right:* Reconstructed mosaic of the SINFONI/LR fields (each sampling 8″ × 8″ on the sky) and SINFONI/HR pointings (with a 3″ × 3″ field of view). The red cross and the circle are as in the left panel. In both panels the names of the pointings are labelled.

4.3.2 Analysis

To properly analyze the four data sets, each one acquired with a different instrument, we have performed specific analyses, which are briefly summarized below.

4.3.2.1 MUSE/NFM data set

For the extraction of the spectra from the MUSE/NFM datacubes we used the code PampelMuse presented in Kamann et al. (2013). This is a software dedicated to the extraction of individual stellar spectra from MUSE data in crowded regions of the sky, such as GC cores, by performing a source deblending via wavelength-dependent point spread function (PSF) fitting. While all the details can be found in Kamann et al. (2013), in the following we briefly describe the main steps of the procedure.

Besides the spectroscopic datacube, PamelMuse needs in input a photometric reference catalog providing the coordinates and magnitudes of all the stars across the field of view. To ensure high photometric completeness and astrometric accuracy, we have used the *HST-PM* catalog described in the previous Section 4.2 and, to properly include also, the brightest stars ($I < 16$), which are saturated in those long-exposures used to build the catalog above, we analyzed the HST/WFC3 images

Table 4.2: Spectroscopic data sets for NGC 6440.

Name	Date	N_{exp}	t_{exp} [s]
	MUSE/NFM		
C	2018-09-14	3	850
E	2018-09-14	3	850
N	2018-09-12	3	850
S	2018-09-13	2	850
	SINFONI		
HR	2014-08-16	5	20
LRNE	2014-08-14	5	20
LRSE	2014-08-14	4	20
HRC	2015-06-24	6	30
	2016-07-21	6	30
HRE	2015-06-25	6	20
	2016-07-29	6	20
LRE	2016-07-30	6	30
LRN	2016-06-30	6	30
LRS	2016-07-30	6	30
LRSW	2015-07-17	6	30
LRW	2016-07-29	6	30
	KMOS		
kmos_1	2014-05-10	3	30
kmos_2	2014-07-13	3	30
kmos_3	2014-07-04	3	30
kmos_4	2014-07-13	3	30
kmos_5	2014-07-13	3	30
kmos_6	2014-07-13	3	30
kmos_7	2014-07-13	3	30
kmos_8	2014-07-13	3	30
kmos_9	2014-07-13	3	30
kmos_10	2014-07-13	3	30
kmos_external_1	2014-07-20	3	30
kmos_external_2	2014-07-20	3	30
	FLAMES		
flames_1	2014-06-19	2	2700
flames_2	2014-06-20/23	2	2700
flames_3	2014-06-23/2014-07-08	2	2700
flames_alt_1	2014-07-08	2	2700
flames_alt_2	2014-07-08	2	2700

NOTE– Name, observation date, number of exposures (N_{exp}), and exposure time (t_{exp}, in seconds) of each exposure for the MUSE/NFM, SINFONI, KMOS and FLAMES pointings analyzed. In the name of the SINFONI pointings, LR and HR indicate the two different instrument configurations used here (low and high resolution, respectively).

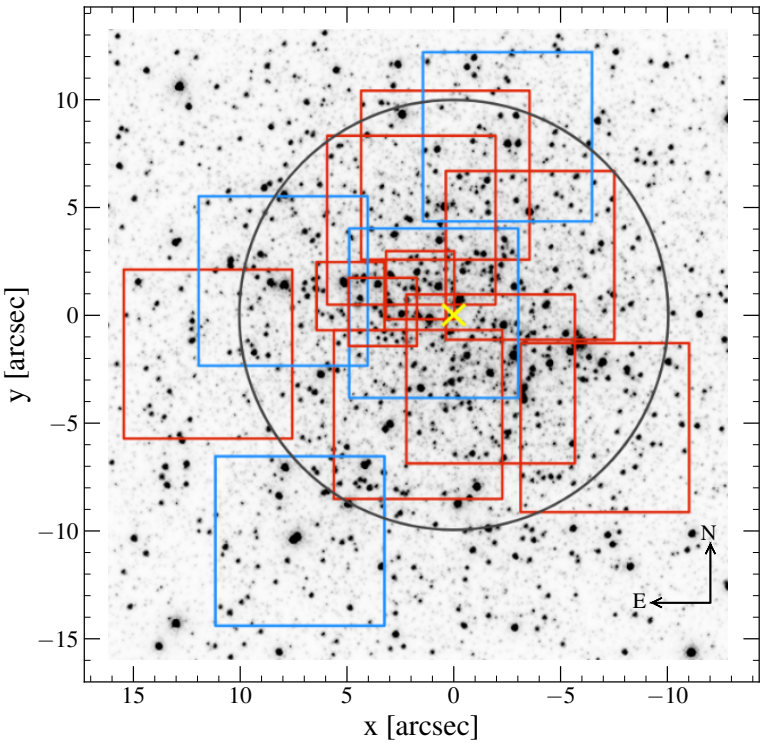

Figure 4.10: HST/WFC3 image of the central region of NGC 6440 with the areas sampled by the spectroscopic observations overplotted: the blue squares show the fields of the four MUSE/NFM pointings ($\sim 8'' \times 8''$ on the sky), the red large squares are the SINFONI/LR fields ($\sim 8'' \times 8''$), and the small red squares are the SINFONI/HR pointings ($\sim 3'' \times 3''$). The black circle has a radius of $10''$ and is centered on the cluster center (yellow cross, see Table 4.6).

acquired under the proposal GO15232 in the F555W and F814W filters (hereafter, V and I, respectively). The photometric analysis of this data set has been performed following the procedures described in Anderson & King (2006), using the publicly available program img2xym_WFC.09x10. To place the instrumental coordinates onto the absolute astrometric system, and to calibrate the instrumental magnitudes we have used the stars in common with the first HST catalog obtained in Section 4.2. For source deblending purposes, PampelMuse also needs in input an analytical PSF model. We thus selected the MAOPPY function (Fétick et al., 2019), which is already implemented in the code (see Göttgens et al., 2021) and is designed to accurately reproduce the typical double-component (core and halo) shape of the AO-corrected PSF in MUSE/NFM observations. Once setting the inputs, the spectra are extracted from the observed datacubes through subsequent steps. First, a sub-sample of isolated stars, on which the PSF will be modelled, is selected according to several criteria, including: signal-to-noise ratio higher than a certain threshold (S/N$>$ 5), relative contribution from neighboring sources negligible in region where the PSF is modelled, and no bright stars within a distance equal to 1.5 $\times$ the PSF

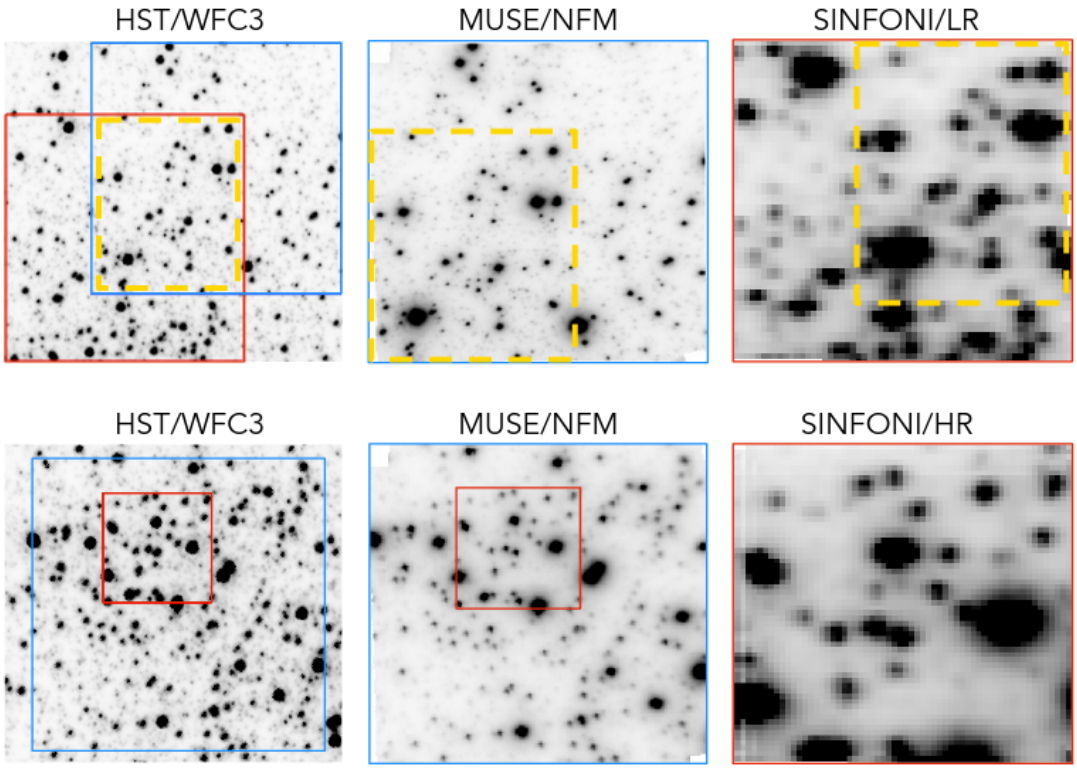

Figure 4.11: *Upper panels*: comparison among the HST/WFC3 image (left panel), the reconstructed I-band image of a MUSE/NFM pointing (central panel) and the stack image of a SINFONI/LR pointing (right panel), of a central area of NGC 6440. In the left panel, the blue square marks the MUSE/NFM field of view ($\sim 8'' \times 8''$ on the sky), as in the central panel, and the red region indicates the SINFONI/LR pointing ($\sim 8'' \times 8''$) shown in the left panel, while, in all the panels, the yellow dashed lines mark the common area among the three images. *Bottom panels*: comparison among the images of the same area of the cluster (bounded by the red square, $\sim 3'' \times 3''$ on the sky) obtained using HST/WFC3 (left), MUSE/NFM (central), and the stack image of a SINFONI/HR pointing (right). The blue square in the left panel marks the area of MUSE/NFM field ($\sim 8'' \times 8''$ on the sky) shown in the central panel.

definition radius. The S/N is mainly estimated from the magnitudes in the input catalog and an initial guess on the PSF parameters. In the second step, the PSF fitting procedure is applied to the selected sub-sample of stars in each individual slice of the datacube, providing, as output, the wavelength dependencies of the PSF parameters and of the source coordinates. Finally, these wavelength dependencies are adopted in the PSF-fitting procedure that is performed through the slices of the datacube, to extract the spectra of all the sources present in the MUSE field of view. Among all the extracted spectra, we selected only those marked as "good" by PampelMuse, which correspond to individual stars with S/N ≥ 10.

The RVs of the target stars have been measured from the Doppler shifts of the Calcium Triplet lines in the wavelength range $8450 - 8750$ Å. To this end, the extracted spectra have been normalized to the continuum (estimated through a spline fitting in the $7300 - 9300$ Å range). Then, a library of template synthetic

spectra has been computed with the SYNTHE code (Sbordone et al. 2004 and Kurucz 2005), assuming an $\alpha-$enhanced chemical mixture and the cluster metallicity ([α/Fe]= 0.34 dex and [Fe/H]= -0.56 dex; Origlia et al. 2008), and adopting a set of atmospheric parameters (effective temperature and gravity) appropriate for the evolutionary stage of the target stars, as derived from the CMD. The template spectra have been convolved with a Gaussian profile to reproduce the spectral resolution of MUSE, and re-sampled at the same pixel size of the observed spectra. The procedure adopted to measure the target RV computes the residuals between the observation and each template spectrum of the library shifted in velocity in steps of 0.1 km s^{-1}. The distribution of the residuals showing the smallest standard deviation ($\sigma_{\rm min}$) provides the best-fit synthetic spectrum (hence, the best estimate of the stellar atmospheric parameters), and from the minimum of this distribution the RV of the target is derived. A value of S/N independent of that obtained by PampelMuse has been computed for each spectrum as the ratio between the average of the counts and their standard deviation in the wavelength range $8000 - 9000$ Å. We will use this S/N estimate in the following analysis.
The uncertainties on the RV measures have been estimated by means of Monte Carlo simulations. By adding different amounts of Poisson noise to the adopted synthetic templates, we simulated ~ 9000 observed spectra with S/N ratios ranging from 10 to 90, in step of 10, running 100 simulations for every considered value of S/N. Then, this sample has been analyzed as for real observations, computing the residuals between the simulations and each synthetic spectrum of the library progressively shifted in velocity, as described above. For each synthetic spectrum we selected the distribution of residuals showing the smallest standard deviation ($\sigma_{\rm min}$) and we adopted the corresponding value of RV. This allowed us to plot the difference between the output and the input RVs (ΔRV) as a function of $\sigma_{\rm min}$, from which a polynomial relation between the two parameters has been obtained, with the values of ΔRV increasing for increasing $\sigma_{\rm min}$ (hence, for decreasing S/N ratios). Finally, knowing the value of $\sigma_{\rm min}$ of the observed spectra, we used this relation to determine the corresponding value of ΔRV, which has been adopted as RV uncertainty. The typical RV errors are ~ 2 km s^{-1} for the brightest stars ($I < 16$), and they increase up to ~ 8 km s^{-1} for the faintest targets, as shown in the top-left panel of Figure 4.12. To check that the measured RVs were homogeneous among the different MUSE pointings, we compared the values obtained for the stars in common between the two overlapping fields (the central and the east ones), and the average RV value obtained in each pointing, always finding a good agreement within the errors. In the case of multiple exposures for the same star, we adopted as the final RV the weighted mean of all the measures, by using the individual errors as weights.

The final MUSE catalog consists of 1128 individual RV measures for stars located between $\sim 0.1''$ and $\sim 18''$ from the cluster center, in the magnitude range

$13 < I < 22$ (see Table 4.3). The position of the stars on the plane of the sky is shown in the right panel of Figure 4.13 (blue triangles), while the first panel on the left of Figure 4.14 shows the corresponding CMD.

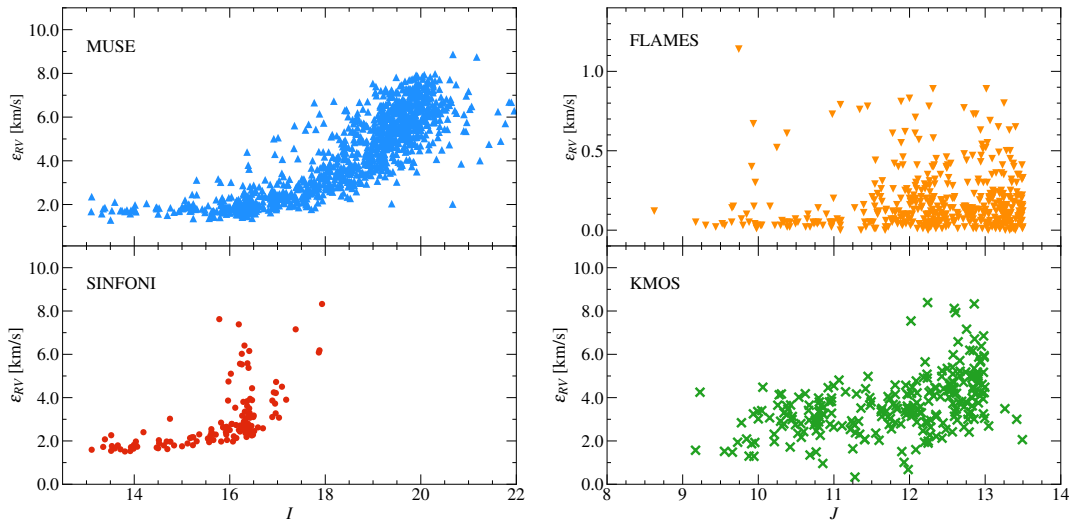

Figure 4.12: RV uncertainty ($\epsilon_{\rm RV}$) as a function of the star magnitude for the observed targets in the MUSE/NFM, SINFONI, FLAMES, and KMOS samples (top-left, bottom-left, top-right, and bottom-right panels, respectively, see labels).

4.3.2.2 SINFONI data set

A forthcoming paper (C. Pallanca et al., 2023, in preparation) will be specifically devoted to the detailed description of the procedure adopted for the analysis of the SINFONI spectra. Here we just summarize the main key points.

First of all, in each observed datacube, we selected all the spaxels with photon counts above a threshold of 10σ the background level. Setting the threshold level to such a high value guantantees the selection of only the spaxels acquired at the largest S/N ratio. A value of RV has been measured from the 1D spectrum extracted from each selected spaxel, applying a procedure analogous to that adopted for the MUSE/NFM data, using the Doppler shift of the $^{12}C^{16}O$ band-heads, instead of the Calcium Triplet lines. More specifically, the observed spectra have been compared with synthetic templates progressively shifted in velocity, computed with the SYNTHE code (Sbordone et al., 2004; Kurucz, 2005) in the appropriate NIR wavelength range and at the SINFONI spectral resolution. We used synthetic spectra computed for 10 pairs of effective temperature and surface gravity properly sampling the entire RGB of the cluster, with iron and $\alpha-$element abundances measured by Origlia et al. (2008), plus 7 additional models with appropriate carbon-depletion [C/Fe]$= -0.36$ dex (Origlia et al., 2008) for stars above the RGB bump. This is to take into account

the fact that the deepness of the CO band-heads depends on both the temperature and the chemical abundance, and the stars above the RGB bump could be depleted in carbon. The best estimates of the RV and its uncertainty have been evaluated as in the case of the MUSE data, from the distribution of the residuals between the observed and the synthetic spectra showing the smallest standard deviation, and from Monte Carlo simulations, respectively. The RV errors are of the order of 2 km s^{-1} and their trend as a function of the star magnitude is shown in the bottom-left panel of Figure 4.12.

From the cross-correlation with the HST catalog described above we finally identified the resolved stars in each SINFONI datacube. To enhance the quality of the data set, for each source we used only the RV measured from the central spaxel (with the largest S/N ratio). By comparing the values obtained from repeated observations of the same stars (which are available especially in the HR fields), and the average RVs of each field, we verified that no relevant offsets in the RV zero points are present, the average differences being about 2 km s^{-1}, which is consistent with the value of the standard deviation. Hence, the final RV catalog has been generated by averaging the values measured in different datacubes in case of multiple exposures of the same star, using the estimated errors as weights. If a star was sampled both in an HR and in a LR pointing, we kept the value measured in the former for the higher spatial resolution of this instrumental setup.

As discussed below, to reliably investigate the internal kinematics of NGC 6440 we restricted the sample of RVs to the safest measures only. The SINFONI data sample the cluster core where stellar crowding is critical, but the procedure used to extract the spectra includes no source deblending algorithms. Hence, the derived RVs might be affected by the presence of brighter neighboring stars, and this can impact the final results in terms of the cluster velocity dispersion and systemic rotation. To address this issue and select only the spectra contributed by the light of individual stars, as in the case of NGC 1904 (see Chapter 3), we applied the same procedure described in Section 3.3.3, which is briefly summarized here. Using as inputs the list of detected stars from the HST catalog and the PSF model adopted in the SINFONI data reduction, the procedure computes the contamination parameter (C) as the ratio between the fraction of light contributed by the first contaminant and that of the target under analysis, where the first contaminant is the neighboring source providing the second largest contribution of light to the central spaxel, after the target itself.

For the final SINFONI sample we selected only the safest targets, with negligible contamination from neighboring sources, by including only the stars with contamination parameter lower than 3% ($C < 0.03$). The final catalog consists of 138 RVs for individual stars located between 1.1″ and 15.0″ from the cluster center (red circles in the right panel of Figure 4.13), in the magnitude range $13 < I < 18$ (see

Table 4.3). The CMD of the targets is shown in the second panel from the left of Figure 4.14.

Table 4.3: Summary of the different data sets used in this work.

Data set	Number of stars	Radial region in arcsec	Magnitude range
MUSE/NFM	1128	$0.1 - 18.0$	$13.0 < I < 22.0$
SINFONI	138	$1.1 - 15.0$	$13.0 < I < 18.0$
KMOS	258	$1.1 - 407.3$	$9.2 < J < 13.5$
FLAMES	448	$22.0 - 778.5$	$8.6 < J < 13.5$

NOTE– For each data set, the columns list the name of the instrument, the number of stars with RV measured, the sampled radial region expressed as the distance from the center in arcsec, and the magnitude range of the target stars.

4.3.2.3 KMOS and FLAMES data sets

The procedures adopted to measure the RVs of the KMOS and FLAMES targets are fully described in Ferraro et al. (2018a,b), where the MIKis survey is presented. Briefly, for the KMOS observations, the 1D spectra have been extracted manually by visually inspecting each IFU and selecting the most exposed spaxel, which corresponds to the stellar centroid. Then, after correction for heliocentric velocity, both KMOS and FLAMES spectra have been cross-correlated with template spectra following the procedure described in Tonry & Davis (1979b), which is implemented in the FXCOR task under the software IRAF. To verify that using two different methods does not introduce systematic effects in the RV measurements, we applied the cross correlation of IRAF to the MUSE spectra, obtaining results in perfect agreement with those obtained with the method described in Section 4.3.2.1. As in the cases of the other data sets, the template spectra have been computed with the SYNTHE code (Sbordone et al., 2004; Kurucz, 2005) in the appropriate wavelength range, adopting the cluster metallicity and RGB atmospheric parameters, and applying a convolution with a Gaussian profile to reproduce the instrument spectral resolutions. For KMOS observations, the RV has been obtained from the cross-correlation with individual near-IR features in the sampled wavelength range, and the RV uncertainties have been derived using Monte Carlo simulations similar to those used for MUSE and SINFONI. For the FLAMES targets, the RV has been measured in three different regions of the spectrum, each including a large number of atomic lines, and the final value and its uncertainty have been obtained, respectively, as the average of the three measures, and their dispersion divided by the square root of 3. The typical RV errors are of the order of 1-5 km s^{-1} for the KMOS targets, while they decrease to $\sim$ 0.1-0.3 km s^{-1} for the FLAMES measures (bottom-

right and the top-right panels of Figure 4.12, respectively). The final KMOS and FLAMES samples consist of 258 and 448 RV measures, respectively (see Table 4.3). The left panel of Figure 4.13 shows the position of the stars on the plane of the sky with orange triangles and green crosses for the FLAMES and KMOS samples, respectively, while the corresponding CMDs are shown in the third (KMOS) and fourth panels (FLAMES) from the left of Figure 4.14.

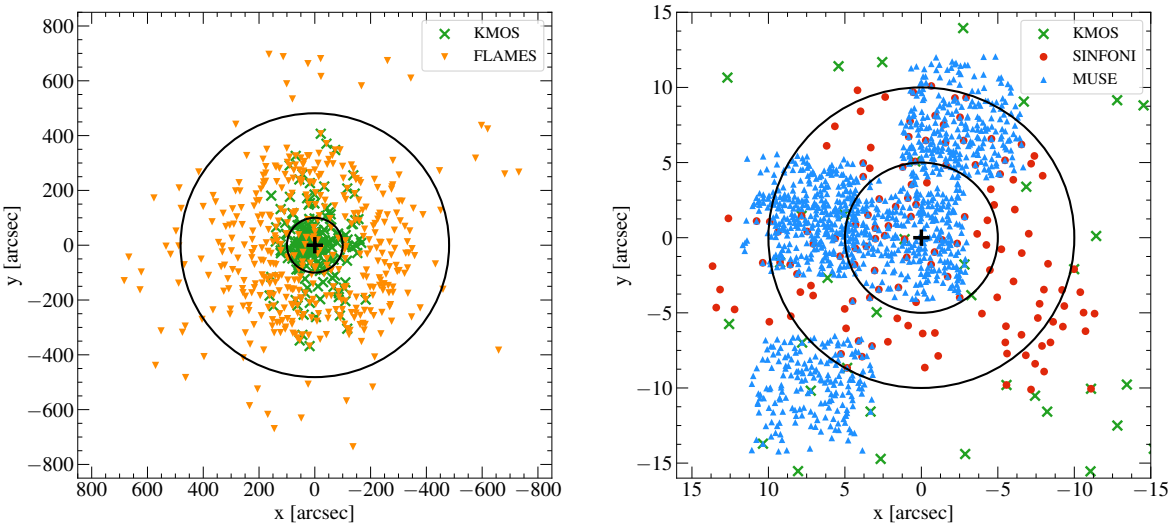

Figure 4.13: Maps on the plane of the sky, with respect to the adopted cluster center (black cross), of the stars with measured RV for each data set. The left panel shows the external portion of the cluster sampled by the FLAMES (orange triangles) and the KMOS (green crosses) data sets. The two circles mark distances of 100″ and 481.4″ (corresponding to the truncation radius of the cluster, see Section 4.2.3) from the center. The right panel is focused on the central region covered by the MUSE (blue triangles) and SINFONI (red circles) samples. A few KMOS targets are also visible (green cross). The two circles mark distances of 5″ and 10″ from the .

4.3.2.4 Final combined catalog

Before combining all the RV measurements in a single final catalog, we have checked for possible systematic offsets among the different catalogs. These could be due to the different instrumental setups, including the wavelength range used to derive the RVs, and also the different spectral resolution of each spectrograph.

To this aim, we compared the RVs of the stars in common between two data sets, using only reliable RV measures (i.e., high S/N and small RV uncertainty) and adopting the values obtained from the FLAMES observations as reference, due to the highest spectral resolution of this instrument. From the stars in common between FLAMES and KMOS, we found an average offset of -5.2 km s^{-1}, which was then applied to the KMOS measures for realigning this sample with the reference one. Unfortunately, no stars are in common between the FLAMES data set and the

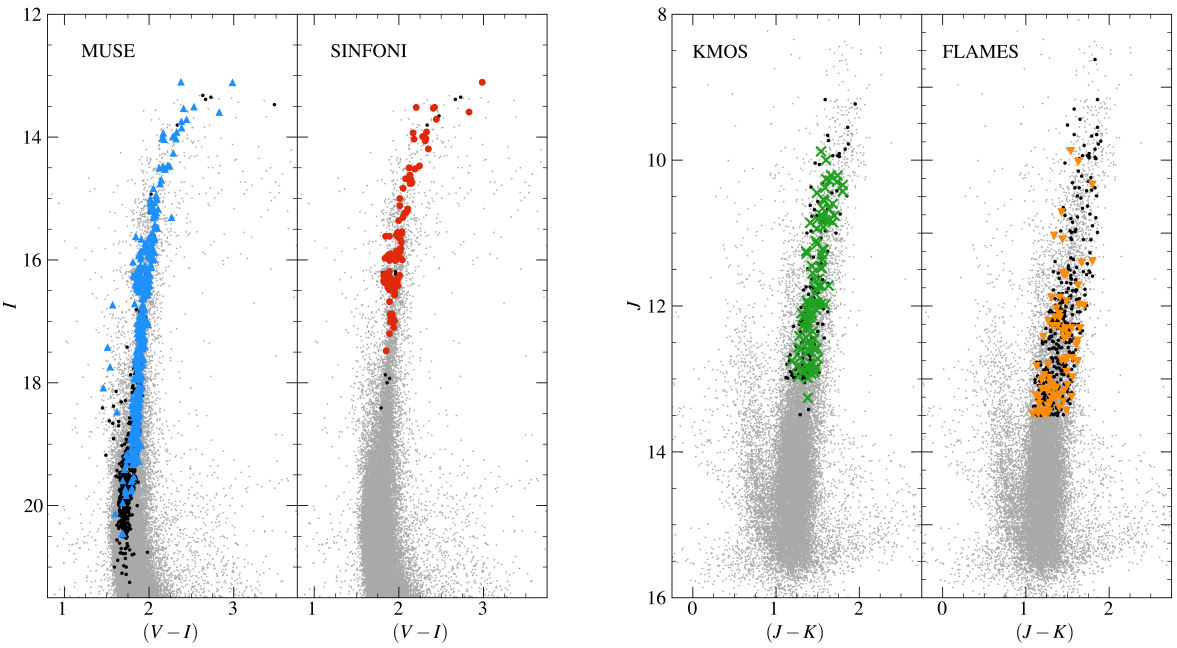

Figure 4.14: CMDs of NGC 6440 with the star having measured RV highlighted. *Left panels*: the gray dots show the $(I, V-I)$ CMD obtained from the photometric HST-PM catalog discussed in 4.2, with overplotted the MUSE (left) and SINFONI (right) samples. The blue triangles on the left and the red circles on the right mark, respectively, the MUSE and SINFONI targets after all the membership and quality selections described in Sections 4.3.3 and 4.3.4, respectively, while the black dots are the rejected targets. *Right panels*: $(J, J-K)$ CMD obtained from the reference SOFI/2MASS catalog (gray dots in both the panels; see Section 4.3.1), with the KMOS and FLAMES data sets highlighted on the left and on the right, respectively. The green crosses on the left and the orange triangles on the right correspond to the KMOS and FLAMES samples selected for the kinematic analysis, respectively (see Section 4.3.3 and 4.3.4). The black dots indicate the rejected stars. Note that in each panel, the targets observed by two or more instruments are also included.

MUSE and SINFONI ones, since they sample very different regions of the cluster. Moreover, no reliably enough RV measures from the KMOS observations have been found in common with the MUSE and SINFONI data sets. Therefore, to realign the innermost samples with the reference catalog, we compared, after excluding the obvious outliers, the average velocities obtained from the FLAMES and the MUSE catalogs finding a good agreement within the errors (-67.5 ± 1.1 km s^{-1} and -67.7 ± 0.5 km s^{-1}, respectively). As last step, a very small residual offset of -1.0 km s^{-1} was detected between the RVs of the stars in common between the MUSE and the SINFONI data sets. Hence, this offset was applied to the SINFONI RVs to realign this sample with all other catalogs.

To create the final catalog, we combined the four data sets (summarize in Table 4.3) by performing a weighted mean of the RV measures by using the individual errors as weights, for the targets observed by more than one instrument.

The final catalog consists of 1831 RV measurements of individual stars [§] sampling the entire radial extension of the cluster, from 0.1″, out to 778″ (corresponding to ~ 1.6 times the truncation radius $r_t = 481.4''$, and ~ 15 times the three-dimensional half-mass radius $r_h = 50.2''$; see Section 4.2.3) from the cluster center, as shown in Figure 4.13, and covering a wide magnitude range ($13 < I < 22$, see Figure 4.14).

4.3.3 Cluster membership

Being a GC in the bulge direction, the contamination from field stars of the population of NGC 6440 is not negligible. For this reason, a thoughtful and accurate analysis was performed to properly address the issue of cluster membership of the measured stars. For the external sample (FLAMES and KMOS), we took advantage of the PMs provided in the Gaia EDR3 (Gaia Collaboration et al., 2018): we selected as cluster members the stars with PMs within 0.9 mas yr^{-1} from the absolute motion of NGC 6440 (Vasiliev & Baumgardt, 2021) in the vector-point diagram (VPD, see the top-left panel of Figure 4.15), this value corresponding to ~ 3 times the central velocity dispersion of NGC 6440 (see Section 4.3.4.2), assuming a distance of 8.3 kpc obtained in Section 4.2.4. The same could not be done for the internal sample (mostly MUSE and SINFONI) because they either have no measured PM, or the measures are not reliable, due to the limited capabilities of Gaia in the very central regions of dense GCs like NGC 6440. Therefore, to identify the cluster members in the innermost samples, we used the same criteria based on the relative HST PMs presented in Pallanca et al. (2019). The VPD and the member selection of the internal sample are shown in the top-right panel of Figure 4.15. The bottom panel of the figure shows the measured RVs as a function of the distance from the center, with the PM-selected member stars highlighted as large, colored circles. As apparent, the RVs of the bulk of cluster members are centered at about -67 km s^{-1}, while field stars have significantly different (especially, larger) RVs and become dominant in the most external regions. The residual field contamination that appears to be still present in the PM-selected sample, especially at large distances from the center, will be easily removed in the following analysis by means of a σ-clipping procedure aimed at excluding the obvious outliers (see Section 4.3.4).

4.3.4 Results

To properly explore the internal kinematics of NGC 6440, in the following analysis we have used only stars with the most reliable RV measures, selected by adopting the following criteria. Among the PM-selected cluster members, only the targets

[§]The final catalog including the identification number, right ascension, declination, RV measure and its error for each star is available for free download at: http://www.cosmic-lab.eu/Cosmic-Lab/MIKiS_Survey.html

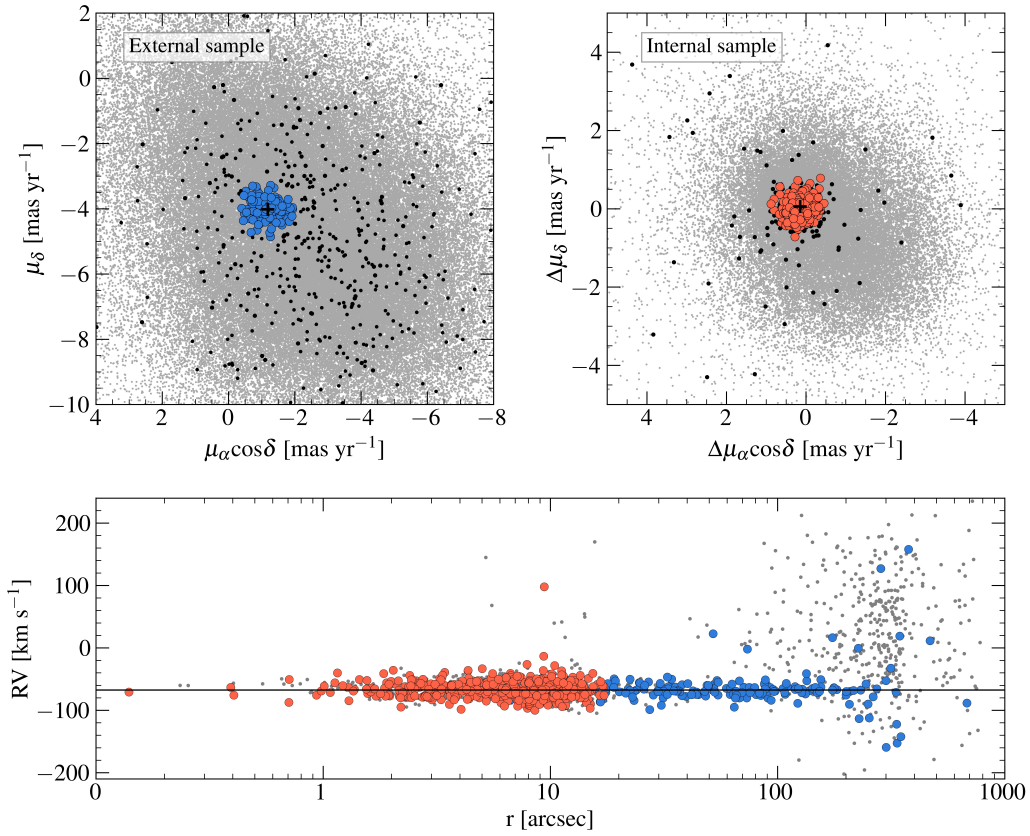

Figure 4.15: *Top-left panel*: VPD of the Gaia EDR3 data set (gray dots) with the targets of the external sample selected as member stars marked with blue circles. The black dots show the targets rejected as field stars. The black cross marks the absolute motion of NGC 6440 (Vasiliev & Baumgardt, 2021). *Top-right panel*: VPD of the relative HST PMs obtained in Pallanca et al. (2019, gray dots). The red circles mark the member stars selected from the internal sample, while the black circles are the targets considered as non-member stars. *Bottom panel*: RVs of the final catalog as a function of the distance from the cluster center. The large circles show the targets selected as cluster members, color-coded as in the top panels. The targets rejected as field stars are marked with gray circles.

with S/N $>$ 15 and RV error $<$ 5 km s^{-1} have been considered. After applying these selections to the targets of the combined catalog (see Section 4.3.2.4), we obtained a total sample of 704 targets. Figure 4.14 shows the positions of the selected targets in the appropriate CMDs. This is the sample of RV measurements that we used to determine the systemic velocity and the VD profile, and to detect possible signatures of rotation.

4.3.4.1 Systemic velocity

The measured RVs as a function of the distance from the center are plotted in the left panel of Figure 4.16, and the corresponding RV distribution is shown in the right panel. The gray dots and empty histogram refer to the entire final catalog (1831 RV measures), and the apparent well defined peak indicates the cluster systemic

velocity ($V_{\rm sys}$). For the measure of $V_{\rm sys}$ only, in order to minimize the risk of a residual contamination from field stars, from the confident sample of stars selected as described above, we considered only those with distances within 200″ ($\sim 4 \times r_h$) from the center and with RVs in the range -92 km s^{-1} <RV< -42 km s^{-1}, and we applied a 3σ-clipping procedure to remove the obvious outliers. The resulting sample of 625 RVs is shown in the left panel of Figure 4.16 as black circles, while its distribution is plotted as a gray histogram in the right panel. Hence, under the assumption that the RV distribution of the selected stars is Gaussian, the value of $V_{\rm sys}$ and its uncertainty have been computed through a Maximum-Likelihood method (Walker et al., 2006). We obtained $V_{\rm sys} = -67.5 \pm 0.4$ km s^{-1}. This estimate is in good agreement with the previous result published in Baumgardt & Hilker (2018, -67.8 ± 1.0 km s^{-1}), while it disagrees with the value quoted in Harris (1996, 2010 edition, -76.6 ± 2.7 km s^{-1}). In the following, we will indicate as $V_r = {\rm RV} - V_{\rm sys}$ the RVs referred to the cluster systemic velocity.

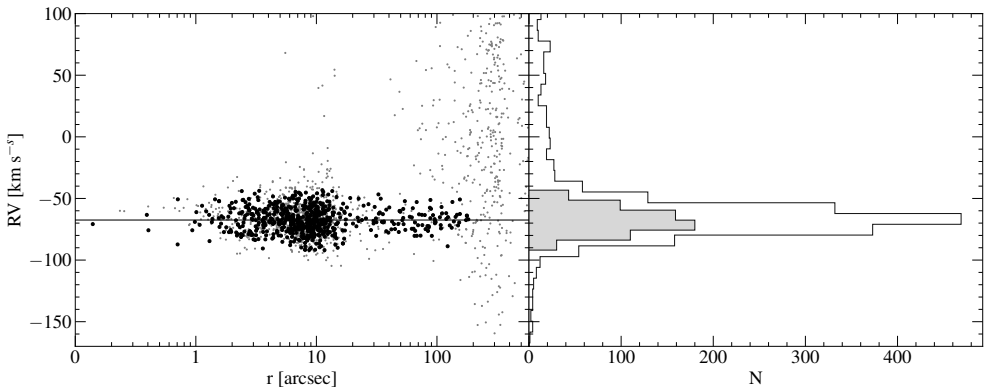

Figure 4.16: *Left panel:* RVs of the final catalog (gray dots) as a function of the distance from the cluster center, with the 625 RVs used to determine the cluster systemic velocity (solid line) highlighted as black circles. *Right panel:* Number distributions of the final catalog (empty histogram) and of the targets used for the determination of $V_{\rm sys}$ (gray histogram).

4.3.4.2 Second velocity moment profile

As discussed in Chapter 3 (see also, e.g., Lanzoni et al., 2018a), the second velocity moment profile ($\sigma_{II}(r)$) derived from the measured RVs represents a very good approximation of the projected velocity dispersion profile $\sigma_P(r)$, in the case of no or negligible systemic rotation, according to the relation represented in equation 3.1 (Chapter 3, Section 3.4.2). For this cluster no evident signatures of rotation have been clearly detected in previous works. Therefore, we first compute the second velocity moment profile to compare it with the previous results, and then, in Section 4.3.4.3, we complete the kinematic analysis of the cluster investigating the possible presence of internal rotation.

To determine the second velocity moment profile, starting from the RVs sample selected as described is Section 4.3.4, we have adopted the standard approach already used in Chapter 3 (see also, Ferraro et al., 2018a; Lanzoni et al., 2018a; Lanzoni et al., 2018b): the RV sample is divided into radial bins using a set of concentric annuli, which are selected at increasing distance from the cluster center and provide a good compromise between fine radial sampling and statistically significant numbers of stars (at least 25) in each bin. A $3\sigma-$clipping procedure is performed on the RVs in each radial bin to exclude the obvious outliers from the analysis. Then, we applied a Maximum-Likelihood method (Walker et al., 2006, see also Martin et al., 2007; Sollima et al. 2009) to compute the dispersion of the V_r values of the selected stars in each bin. The uncertainties are estimated following the procedure described in Pryor & Meylan (1993b).

The resulting $\sigma_{II}(r)$ profile of NGC 6440 is shown in Figure 4.17 (black circles) and listed in Table 4.4. It nicely follows the King model (red line) that best fits the observed star density profile of the cluster (see Section 4.2.3). We have estimated the central velocity dispersion as the value that minimizes the residuals between the observed VD profile and the adopted King model finding $\sigma_0 = 12.0 \pm 0.4$ km s $^{-1}$. The 1σ uncertainty has been obtained from the solutions of the χ^2 test for which $\chi^2 = \chi^2_{min} \pm 1$.

In Figure 4.17 we also compare our result with the observed profile obtained by Baumgardt & Hilker (2018, empty triangles) from RV measures at intermediate and large radii from the center. Formally, the two outermost points of Baumgardt & Hilker (2018) are larger than ours, possibly due to a different membership selection applied in the two works, or an effect of residual field star contamination in the former. The difference, however, is not significant (the error bars are just 1σ), but we verified that the King model that best fits the observed density distribution would be unable to reproduce a velocity dispersion profile obtained by combining our innermost four points and the three measures by Baumgardt & Hilker (2018), while it is well consistent with the determination provided in this work (solid circles and red line in Figure 4.17).

4.3.4.3 Systemic rotation

In previous kinematics analysis (e.g., Sollima et al., 2019; Vasiliev & Baumgardt, 2021) no unambiguous signals of rotation have been detected in the external regions of NGC 6440. However, thanks to the large sample of MUSE and SINFONI data presented here, we have the opportunity to perform the very first exploration of the central region of the cluster searching for evidence of systemic rotation.

To this purpose, we used the same method adopted in Chapter 3, Section 3.4.3, for NGC 1904, and fully described in previous works (e.g., see Cote et al., 1995; Lane

Table 4.4: Second velocity moment profiles obtained for NGC 6440.

r_i [arcsec]	r_e [arcsec]	r_m [arcsec]	N	σ_{II} km s^{-1}	$\epsilon_{\sigma_{II}}$ km s^{-1}
0.01	2.50	1.75	58	12.20	1.19
2.50	4.50	3.47	96	11.20	0.86
4.50	7.50	6.05	130	11.50	0.76
7.50	13.00	9.79	228	11.80	0.59
13.00	50.00	24.49	79	11.00	0.94
50.00	100.00	74.23	37	7.30	1.01
100.00	250.00	157.22	30	5.60	0.82

NOTE– The first three columns list the internal, external, and mean radii of each adopted radial bin (r_i, r_e and r_m, respectively), with the mean radius computed as the average distance from the center of all the stars in the bin (N, fourth column). The last two columns list the second velocity moment and its uncertainty in each bin, respectively.

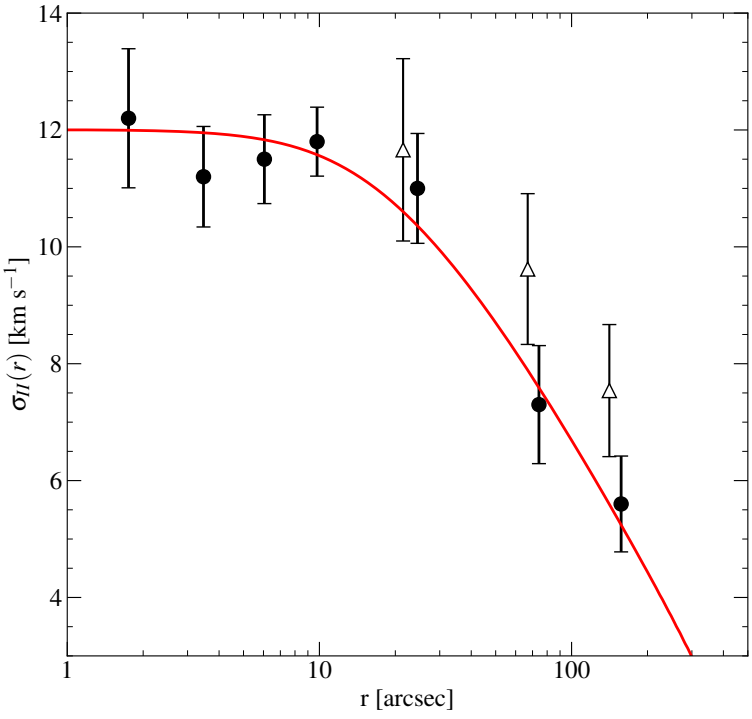

Figure 4.17: Second velocity moment profile of NGC 6440 obtained from the measured individual RVs (solid circles). The empty triangles show the profile derived by Baumgardt & Hilker (2018). The red solid line represents the King model that best fits the star density profile of the cluster as determined in Chapter 4.2.3.

et al., 2009; Bellazzini et al., 2012; Lanzoni et al., 2013). Following this method, the RV sample is split into two sub-samples by a line passing through the cluster center, varying the position angle (PA) of the line from 0° (North direction) to 180° (South direction), by steps of 10° and with PA = 90° corresponding to the East direction. For each value of PA, the difference between the mean velocity of the two RV sub-samples ($\Delta V_{\rm mean}$) is computed. In the presence of systemic rotation, $\Delta V_{\rm mean}$ would show a coherent sinusoidal variation as a function of PA. The maximum/minimum absolute value of this curve provides twice the rotation amplitude ($A_{\rm rot}$) and the position angle of the rotation axis ($\rm PA_0$). In addition, if the cluster is rotating, the stellar distribution in a diagram showing the velocity V_r as a function of the projected distances from the rotation axis (XR) shows an asymmetry, with two diagonally opposite quadrants being more populated than the other two. Moreover, the sub-samples of stars on each side of the rotation axis are expected to also show different cumulative V_r distributions. Three estimators have been used to quantify the statistical significance of the detected differences: the probability that the RV distributions of the two sub-samples are extracted from the same parent family is estimated by means of a KS test, while the statistical significance of the difference between the two sample means are evaluated with both the Student's t-test and a Maximum-Likelihood approach.

Of course, by construction, the method can be used only in the case of a RV sampling symmetrically distributed in the plane of the sky. Thus in order to avoid some heavy under-sampled regions, we were forced to limit our analysis to the innermost 5″ portion (approximately covering the core radius of the cluster $r_c = 6.4''$), where the combination of the MUSE and SINFONI samples offers a reasonably symmetric coverage of the cluster (see Figure 4.13). We thus performed the analysis over the entire region ($r < 5''$) and in two radial annuli around the cluster center ($r < 3''$ and $< 3'' < r < 5''$).

The results are plotted in Figure 4.18 and listed in Table 4.5. The diagnostic plots show the characteristics of systemic rotation in the considered regions: a sinusoidal behavior of $\Delta V_{\rm mean}$ as a function of PA (left-hand panels), asymmetric distributions of V_r as a function of XR (central panels), and well distinct cumulative V_r distributions for the two samples on either side of the rotation axis (right-hand panels). Hence, we can reasonably (at $\sim 2\sigma$ statistical significance) conclude that the core region within 5″ of NGC 6440 is rotating, with an average position angle of the rotation axis $\rm PA_0 \sim 132 \pm 2°$, and an amplitude of $\sim 2.8 \pm 0.2$ km s^{-1}. Unfortunately, the non-uniform coverage of the intermediate region of the cluster does not allow us to assess of the exact radial extension of the rotation signal. Moreover, we have searched for signatures of systemic rotation in outermost part of the cluster by applying the same procedure to the regions covered by KMOS and FLAMES. In this case, no significant evidence of rotation was found, in agreement with previous

studies (Sollima et al., 2019; Vasiliev & Baumgardt, 2021).

Table 4.5: Rotation signature detected in the core of NGC 6440 in three circular annuli around the cluster center.

r_i	r_e	r_m	N	PA_0	A_{rot}	P_{KS}	P_{Stud}	n-σ_{ML}
0.01	3.00	2.10	85	131 ± 4	2.2 ± 0.3	3.2×10^{-1}	< 90.0	2.2
3.00	5.00	3.90	86	134 ± 2	3.4 ± 0.3	7.8×10^{-2}	> 95.0	3.3
0.01	5.00	3.00	171	132 ± 2	2.8 ± 0.2	4.9×10^{-2}	> 95.0	3.6

NOTE– The table lists: inner (r_i), outer (r_e) and mean radius (r_m) in arcseconds, the number of stars in the bin (N), the position angle of the rotation axis (PA_0) and its 1σ error in degree, the rotation amplitude ($\mathrm{A}_{\mathrm{rot}}$) and its error in km s^{-1}, the KS probability that the two samples on each side of the rotation axis are drawn from the same parent distribution (P_{KS}), the t-Student probability that the two RV samples have different means (P_{Stud}), and the significance level (in units of n-σ) that the two means are different following a Maximum-Likelihood approach (n-σ_{ML}).

4.3.5 Ellipticity

From previous analyses, NGC 6440 shows a low global ellipticity (see Harris, 1996, 2010 edition, 0.01), as expected for a non-rotating system. However, because of the rotation signal detected in the core, we have explored the morphology of the innermost region of the cluster to check for a possible flattening of the system in the direction perpendicular to the rotation axis, as expected from theoretical models (e.g., Chandrasekhar, 1969b; Varri & Bertin, 2012). We thus determined the 2D stellar density map of the inner $\sim 50'' \times 50''$ area, by using the stars with $I < 20.5$ (to avoid incompleteness effects) in the photometric catalog obtained as described in Section 4.2. By applying a Gaussian kernel to the stellar distribution (see Dalessandro et al., 2015), we obtained the smoothed 2D surface density map shown in Figure 4.19. The gray solid lines represent the best-fit ellipses to the isodensity contours, and show that the system is slightly flattened in the center, and it acquirers a more spherical symmetric for increasing radii. Indeed, the resulting ellipticity (defined as $\epsilon = 1 - b/a$ with a and b being the major and minor axes, respectively) achieves its maximum value (0.18 ± 0.02) at $r \sim 3''$ and gradually decreases at larger radii ($\epsilon = 0.04 \pm 0.02$ at $r \sim 45''$). Where the ellipticity is maximum, the ellipses major axis has an orientation of $\sim 15°$ from North to East. Although the direction of the major axis is not exactly perpendicular to the rotation axis ($\mathrm{PA}_0 \sim 132 \pm 2°$), the presence and the orientation of the detected flattening are qualitatively consistent with the systemic rotation signal found in the inner $5''$ of the system.

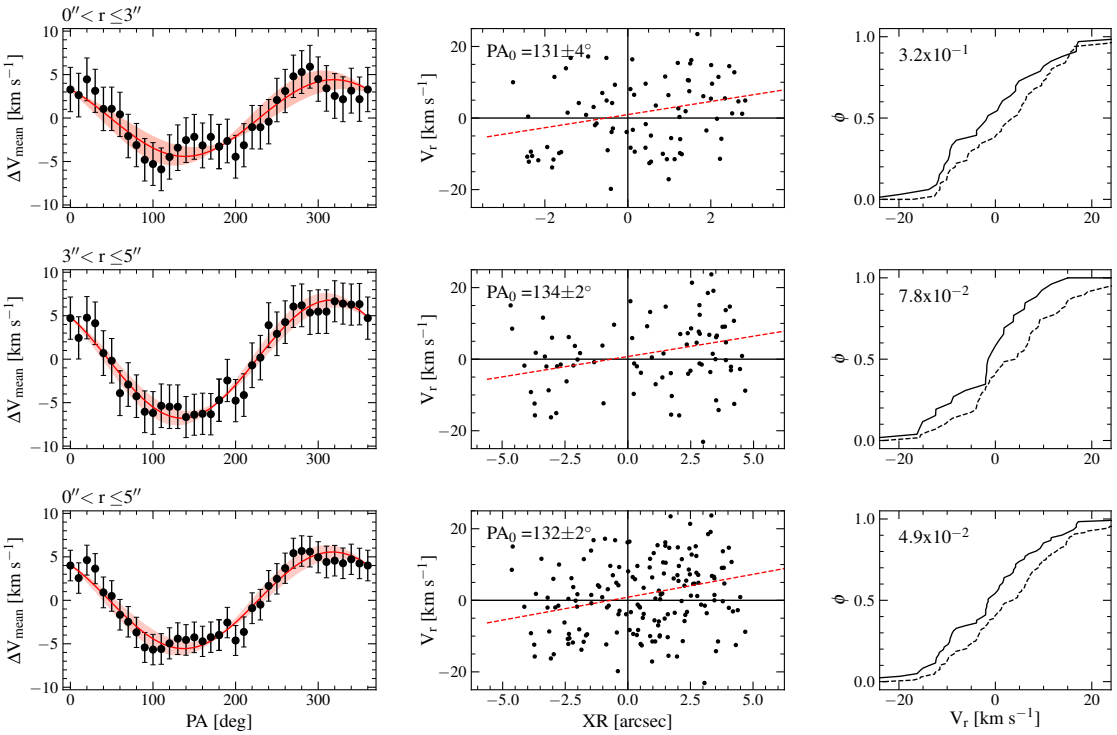

Figure 4.18: Diagnostic diagrams of the rotation signature detected in three concentric radial bins in the core of the cluster at different distances from the center (see labels in the top-left corner of each row). For each bin, the *left panels* show the difference between the mean RV on each side of a line passing through the center with a given PA, as a function of PA itself. The continuous line is the sine function that best fits the observed patterns and the red shaded region marks the confidence level at 3σ. The *central panels* show the distribution of the velocities V_r as a function of the projected distances from the rotation axis (XR) in arcseconds. The value of PA_0 is labeled in each panel. The red dashed lines are the least square fits the data. The *right panels* show the cumulative V_r distributions for the stars with XR<0 (solid line) and for those with XR>0 (dotted line). The KS probability that the two samples are extracted from the same parent distribution is also labelled.

4.4 Discussion

In this Chapter, using a combination of the high-precision photometric analysis and an accurate kinematic study, we provide a comprehensive view of internal structure and kinematics of the bulge GC NGC 6440. Using the improved estimation of the gravitational center from the positions of PM-selected member stars, we built the most radially extended surface density profile so far from resolved star counts, and derived the entire VD profile from the RVs of resolved member stars by sampling from core to the outermost regions. Moreover, we detected a non-negligible signal of a core rotation.

From the King model that best fits the density distribution, we derived the structural parameters of the cluster, finding significantly larger concentration parameter, a smaller core radius, and a larger overall extension (truncation radius) on the plane

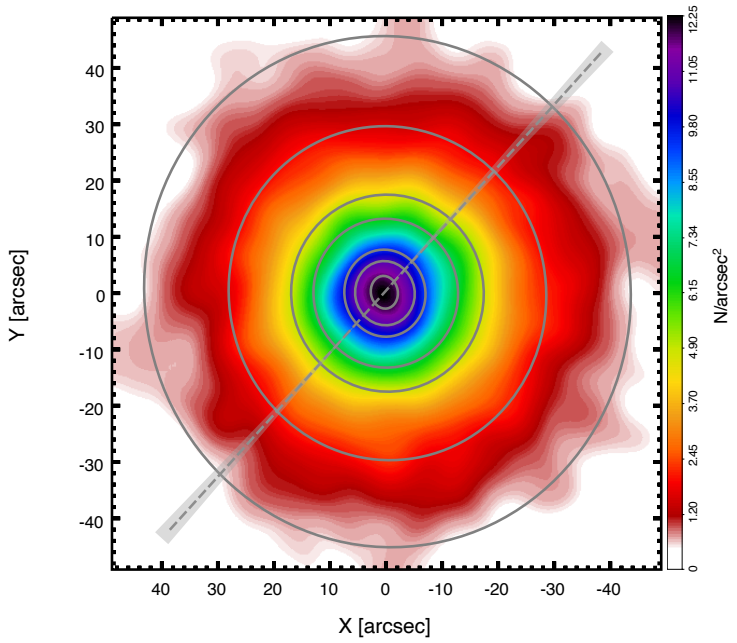

Figure 4.19: Projected stellar density map of the central region of NGC 6440. The solid gray lines are the best-fit ellipses to the isodensity curves and the gray dashed line marks the estimated direction of the rotation axis ($PA_0 \sim 132 \pm 2°$; see Section 4.3.4.3) with the 1σ error shown by the shaded area.

of the sky, with respect the values quoted in the literature (see, Harris, 1996, 2010 edition; McLaughlin & van der Marel, 2005). Moreover, the high-quality CMDs provided us also with the cluster age, distance modulus and the corresponding cluster distance, and absolute color excess (see Table 4.6). In particular, the age estimate here obtained for NGC 6440 is the most accurate so far (although the uncertainty is still quite large: 1.5 Gyr). Figure 4.20 shows the age-metallicity distribution for the bulge GCs with available age estimate, where NGC 6440 is marked as a large red square. The data for the other clusters are mainly from Saracino et al. (2019, see their Figure 16) and Oliveira et al. (2020, see their Figure 12) with the addition of the recent age determination of NGC 6256 (Cadelano et al., 2020a). We also mark the age-metallicity of the oldest stellar population in the two BFFs (namely Terzan5 and Liller1) so far discovered into the bulge (Ferraro et al., 2009, 2016, 2021). The updated values of the cluster center, and all the derived parameters are listed in Table 4.6.

The accurate determination of the structural parameters and the velocity dispersion profile of the cluster, allow us to prove that the adopted King model is able to well reproduce both the internal structure and kinematics of the cluster (see Figure 4.17). Compared to Baumgardt & Hilker (2018), our VD profile samples a much inner region of the cluster, and our estimate of σ_0 is significantly smaller (12 km s $^{-1}$, in place of 15.8 km s $^{-1}$). This difference could be ascribed to an effect of energy equipartition and mass segregation, which implies a lower velocity

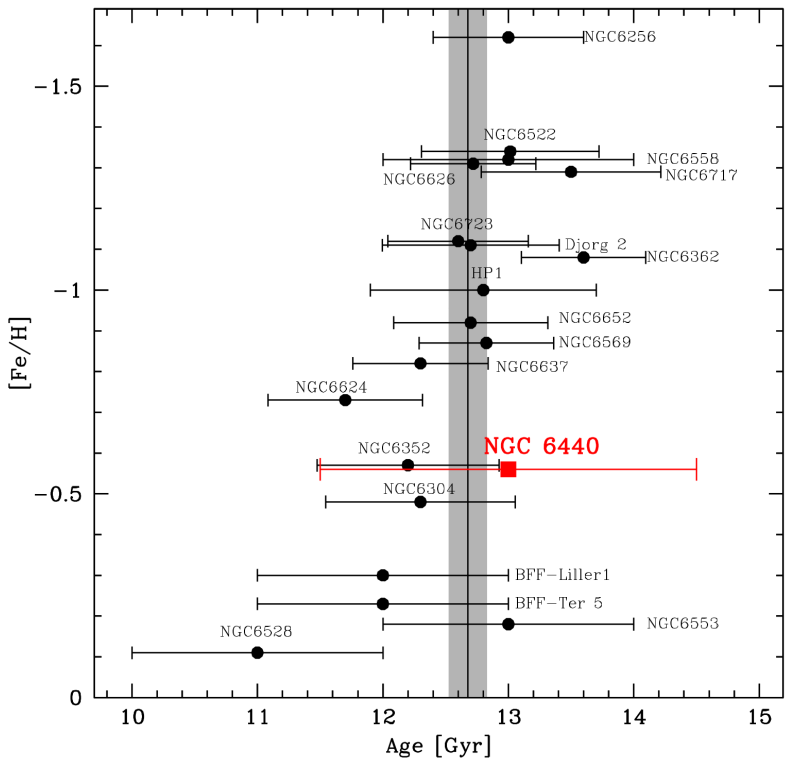

Figure 4.20: Age-metallicity distribution for the bulge GCs with age estimate available. NGC 6440 is marked as a large red square. Data for the other clusters are mainly from Saracino et al. (2019, see their Figure 16) and Oliveira et al. (2020, see their Figure 12) with the addition of the recent age determination of NGC 6256 (Cadelano et al., 2020a). We also plotted the age-metallicity of the oldest stellar population in the two BFFs (Terzan5 and Liller1) so far discovered into the bulge (Ferraro et al., 2009, 2016, 2021). The grey vertical strip marks the weighted average and 1σ uncertainty (12.7 ± 0.2 Gyr) of the entire sample.

dispersion for RGB stars, compared to the average, less massive, cluster members. Indeed, based on our estimations of age and half-mass relaxation time ($t = 13$ Gyr and $t_{rh} = 1$ Gyr, respectively; see also Baumgardt & Hilker, 2018) NGC 6440 has undergone about 13 relaxations so far, and likely is mass-segregated. Consistently, the value of σ_0 estimated in this work (which has been obtained mainly from giant stars) is smaller than the mass-weighted central velocity dispersion determined by Baumgardt & Hilker (2018) from the comparison with N-body simulations.

According to equation 3.1, in the presence of rotation, the velocity dispersion is expected to be smaller than the second velocity moment. However, in the case of NGC 6440 the contribution of the detected rotation signal is small compared to the measured second velocity moment, thus we can conclude that the cluster is, with a reasonable approximation, a pressure-supported system, dominated by non-ordered motions. These considerations make the approximation that the cluster is well represented by single-mass, spherical, isotropic, and non-rotating (King, 1966) models well acceptable. Hence, we can use the derived value of σ_0 to estimate the total mass of the system. To this end, we used equation (3) of Majewski et al.

(2003), deriving μ as in Djorgovski (1993) and assuming $\beta = 1/\sigma_0^2$ (see Richstone & Tremaine, 1986). We then estimated the total mass uncertainty by running 1000 Monte Carlo simulations, extracting the values of c, r_0 and σ_0 from a appropriate normal distributions for each parameter, as described in Chapter 3. The result obtained for NGC 6440 is $M = 2.66^{+0.27}_{-0.24} \times 10^5 M_\odot$. We emphasize, however, that this value likely underestimates the true total mass of the system, because the adopted central velocity dispersion has been measured from giant stars (see above). This is qualitatively in agreement with the larger mass ($4.42 \pm 0.64 \times 10^5$ $M_\odot$) estimated by Baumgardt & Hilker (2018) from the mass-weighted value of σ_0.

Although no evidence of systemic rotation have been detected in previous analyses (see Sollima et al., 2019; Vasiliev & Baumgardt, 2021), and although in the present study we could not derive a rotation curve for reasons of non-uniform sampling, a not negligible signal of ordered rotation has been found in the core of NGC 6440 (see Section 4.3.4.3). By assuming that the maximum peak of the rotation is the found value of $\sim 3.4 \pm 0.3$ km s^{-1} between $3''$ and $5''$ from the center, we can derive the value of $V_{\rm rot}^{\rm peak}/\sigma_0 = 0.3$, similarly to what has been done in other works (Bianchini et al., 2013; Fabricius et al., 2014; Boberg et al., 2017; Dalessandro et al., 2021a). Nevertheless, since the non-uniform sampling prevents the exploration of the rotation signal at larger radii, we cannot exclude that the rotation peak is higher for $r > 5''$. Despite this, it is interesting to note that such a central rotation is a rare feature in GCs and only two similar cases are known to date in the literature, namely M 15 (van den Bosch et al., 2006; Usher et al., 2021) and NGC 6362 (Dalessandro et al., 2021a). Interestingly, N-body simulations (Tiongco et al., 2017) show that such central ($< r_h$) velocity signals are expected only in very dynamically evolved systems that lost a significant amount of their mass because of both two-body relaxation effects and interactions with the host galaxy potential. This prediction is also in agreement with our estimation of the half-mass relaxation time of the cluster, which suggests an advanced dynamical age.

This study demonstrates the need to perform a complementary investigations of the structural and kinematic properties of GCs, and at the same time to improve the available theoretical models, to unveil their dynamical evolution history and their mechanisms of formations.

Table 4.6: Identity card of NGC 6440: summary of the new determinations of its basic structural and kinematic parameters.

Parameter	Estimated value
Center of gravity	$\alpha_{\rm J2000} = 17^{\rm h}48^{\rm m}52.84^{\rm s}$
	$\delta_{\rm J2000} = -20°21'37.5''$
Reddening law	$R_V = 2.7$
Color excess	$E(B-V) = 1.26 - 1.28$
Distance modulus	$\mu_0 = 14.6 \pm 0.1$
Distance	$d = 8.3 \pm 0.4$ kpc
Age	$t = 13 \pm 1.5$ Gyr
RGB bump	$M_{\rm V_{606}}^{Bump} = 1.12 \pm 0.12$
	$M_J^{Bump} = -0.37 \pm 0.12$
	$M_K^{Bump} = -0.94 \pm 0.12$
Dimensionless central potential	$W_0 = 8.10^{+0.20}_{-0.20}$
Concentration parameter	$c = 1.86^{+0.06}_{-0.06}$
Core radius	$r_c = 6.4^{+0.3}_{-0.3}$ arcsec $= 0.26^{+0.01}_{-0.01}$ pc
Half-mass radius	$r_h = 50.2^{+5.2}_{-4.5}$ arcsec $= 2.02^{+0.21}_{-0.18}$ pc
Effective radius	$r_e = 36.8^{+3.7}_{-3.2}$ arcsec $= 1.48^{+0.15}_{-0.13}$ pc
Truncation radius	$r_t = 481.4^{+43.9}_{-42.3}$ arcsec $= 19.4^{+1.8}_{-1.7}$ pc
Central relaxation time	$\log(t_{rc}/{\rm yr}) = 7.4$
Half-mass relaxation time	$\log(t_{rh}/{\rm yr}) = 9.0$
Systemic velocity	$V_{sys} = -67.5 \pm 0.4$ km s^{-1}
Central velocity dispersion	$\sigma_0 = 12.0 \pm 0.4$ km s^{-1}
Central rotation peak	$V_{\rm rot}^{\rm peak} = 3.4 \pm 0.3$ km s^{-1}
Strength of rotation	$V_{\rm rot}^{\rm peak}/\sigma_0 = 0.3$
Total Mass	$M = 1.28^{+0.15}_{-0.14} \times 10^5 M_\odot$

Chapter 5

Internal kinematics and structure of the bulge GC NGC 6569

Mainly based on:
Pallanca, Leanza et al. (2023), ApJ, in press

5.1 Introduction

The Galactic bulge is the sole spheroid where individual stars can be observed and for this reason is a formidable laboratory to study the processes that drive the formation of galaxy bulges. Unfortunately, because of observational limitations mainly related to the large extinction and stellar density in this direction of the sky, it still remains one of the most inaccessible regions of the MW and its structure, formation, and evolution are still subjects of intense debate in the literature (see, for example, Richer et al. 2013; Ness et al. 2013; Origlia et al. 2014; Zoccali & Valenti 2016; Johnson et al. 2022; Marchetti et al. 2022). In this respect, the investigation of the GCs orbiting the bulge is a key tool to trace the bulge properties in terms of kinematics, chemical abundances, and age (Bica et al., 2006; Valenti et al., 2007, 2010; Barbuy et al., 2018). In addition, the discovery that Terzan5 and Liller1 are not genuine GCs but host multi-iron and multi-age stellar populations has opened a new line of investigation, providing the first detection of *Bulge Fossil Fragments*, the possible remnants of primordial giant clumps that contributed to the bulge formation, surviving the violent phase of its assembling (Ferraro et al., 2009, 2016, 2021; Lanzoni et al., 2010; Origlia et al., 2011, 2013; Massari et al., 2014; Dalessandro et al., 2022).

In the framework of a complete kinematical, chemical and photometric characterization of bulge GCs, in this Chapter, we present the VD profile and the determination of the structural parameters of NGC 6569, a massive GC (with absolute total magnitude $M_V = -8.3$) located in the Sagittarius region ($l = 0°.48$, $b = 6°.68$ Harris, 1996, 2010 edition) of the Galactic bulge, at a distance of ~ 3 kpc from the Galactic center (Harris, 1996, 2010 edition). The cluster is projected toward the dark nebula Barnard 305 (Barnard et al., 1927) and it is therefore highly red-

dened, with an average color excess $E(B-V) = 0.53$ (Ortolani et al., 2001). It is an intermediate-high metal rich cluster, with a quoted metallicity ranging from [Fe/H]$= -0.79 \pm 0.02$ dex (Valenti et al., 2011) to [Fe/H]$= -0.87$ dex (Johnson et al., 2018), and with an $\alpha-$element enhancement of $[\alpha/\mathrm{Fe}] = +0.4$ dex (Valenti et al., 2011). This system has been subject to a detailed photometric analysis (see Saracino et al. 2019) by using a combination of optical HST/WFC3 data, and multi-conjugate AO assisted near-infrared (NIR) GEMINI observations. This allowed an accurate measure of PMs, which provided a robust selection of cluster member stars. A differential reddening map has been also derived. The PM-selected and differential reddening CMD then has allowed an accurate measure of the cluster distance and age: the distance modulus is $(m-M)_0 = 15.03 \pm 0.08$, corresponding to 10.1 ± 0.2 kpc from the Sun, while the age amounts to about 12.8 Gyr, with an uncertainty of $0.8 - 1.0$ Gyr (Saracino et al., 2019).

5.2 Data sets

As in the previous Chapters, to build the VD profile of NGC 6569 we used a multi-instrument approach combining the RV measurements obtained from four different spectroscopic data sets.

MUSE/NFM - The innermost cluster regions were sampled mainly by using MUSE in the NFM configuration (Bacon et al., 2010, see also Chapter 2, Section 2.2.1). Our data set has been collected as part of the ESO Large Program 106.21N5.003 (PI: Ferraro, see Table 5.1) and consists of a mosaic of seven MUSE/NFM pointings located within $\sim 15''$ from the center. Three 750 s long exposures were acquired for each pointing, always with an average DIMM seeing during the observations better than $\sim 0.7''$. The data reduction was performed with the dedicated MUSE ESO pipeline (Weilbacher et al., 2020).

SINFONI - To sample the innermost regions, we used also an additional spectroscopic data set acquired with the AO-assisted IF spectrograph SINFONI (Eisenhauer et al., 2003, see also Chapter 2, Section 2.2.2). The data set (ESO Large program 195.D-0750(A), PI: Ferraro) is listed in Table 5.1 and includes eight pointings covering a region within $\sim 15''$ from the cluster center. For each pointing, multiple exposures (usually six) were acquired on target and on a sky region following a typical target-sky sky-target sequence, in order to allow an adequate subtraction of the background. The observations have been executed adopting an exposure time of 30 s and under an average DIMM seeing of $\sim 0.8''$.

KMOS - The cluster region at intermediate distances from the center has been sampled by using the spectrograph KMOS (Sharples et al., 2013). Nine pointings (see Table 5.1) were acquired under the ESO Large Program 193.D-0232 (PI: Ferraro),

covering an area of $\sim 3'$ from center. Four pointings consist of a sequence of three repeated sub-exposures each one 60 s long, while for the other five pointings a set of three repeated longer (100s-long) sub-exposures was acquired in order to sample fainter stars. The spectroscopic targets have been selected adopting the NIR catalog described in Valenti et al. (2005, 2007)* complemented, in the outermost regions of the clusters, with data from the 2MASS catalog (Skrutskie et al., 2006).

FLAMES - To investigate the cluster kinematics in the outermost cluster regions we used the fiber-fed multi-object spectrograph FLAMES (Pasquini et al., 2002) in the GIRAFFE/MEDUSA mode (see Chapter 2, Section 2.2.4 for more details). The observations have been executed adopting the HR21 and HR13 grating setups (ESO Large Program ID: 193.D-0232(F), PI: Ferraro, and ID: 093.D-0286(A), PI: Villanova, respectively, see Table 5.1). The HR13 grating samples the spectral range $6120-6405$ Å with a resolving power $R \sim 26400$, and consists of two repeated exposures (each 2775 s long) of the same targets. The HR21 grating provides a resolving power $R \sim 18000$ sampling the wavelength range between 8484 and 9001 Å. The HR21 targets have been selected to sample the full extension in the luminosity of the RGB. Thus, six pointings were planned to optimize the observations of targets with different luminosities: the brightest portion of the RGB has been sampled through three pointings (each with a 1800 s long exposure), while two pointings with an exposure time of 2700 s were devoted to observe intermediate-luminosity RGB stars, and finally an additional pointing of 5400 s was dedicated to sample the fainter portion of the RGB. As for the KMOS data set, the targets have been selected from the SOFI/2MASS photometric catalogs by sampling the full extension along the cluster RGB.

5.3 Determination of the center of gravity

For a proper analysis of the density and RV distributions of stars in NGC 6569, the first step is the determination of the center of gravity of the cluster. To this aim, we used the photometric catalog described in Saracino et al. (2019). This is based on F555W and F814W images obtained from high-resolution HST/WFC3 observations and a set of J- and K_s-band images acquired with the Gemini multi-conjugate adaptive optic system (GeMS). The field of view of the GeMS observations is almost entirely included within that of the HST/WFC3 images, which extend out to $\sim 150''$ from the center (see Figure 2 of Saracino et al., 2019). As in Chapter 4, we have determined the position of the gravitational center ($C_{\rm grav}$) from the position of resolved stars (in the HST data set), rather than the surface brightness peak. This is done to avoid possible biases induced by the presence of a few bright stars, which

* The catalog is available at the web site http://www.bo.astro.it/~GC/ir_archive/

Table 5.1: Spectroscopic data sets for NGC 6569.

Name	Date	N_{exp}	t_{exp} [s]
	MUSE/NFM		
C	2021-08-16	3	750
E	2021-08-16	3	750
N	2021-08-16	3	750
NE	2021-08-21	3	750
W	2021-08-21	3	750
SW	2021-08-21	3	750
S	2022-09-27	3	750
	SINFONI		
LR_SW	2015-08-02	6	30
LR_W	2015-08-03	6	30
LR_N	2015-07-18	6	30
LR_NE	2016-07-22/2016-08-04	7	30
LR_S	2016-06-23	6	30
LR_NN	2016-07-15	6	30
LR_C	2015-08-23	6	30
LR_E	2016-07-21	12	30
	KMOS		
kmos_1	2015-04-30	3	60
kmos_2	2015-05-02	3	60
kmos_3	2015-05-02	3	60
kmos_4	2015-05-02	3	60
kmos_faint_1	2015-05-02	3	100
kmos_faint_2	2015-05-02	3	100
kmos_faint_3	2015-05-02	3	100
kmos_faint_4	2015-05-03	3	100
kmos_faint_5	2015-05-02	3	100
	FLAMES		
flames_HR13	2014-06-19/2014-08-01	2	2775
flames_HR21_faint_1	2015-06-22	1	1800
flames_HR21_faint_2	2015-07-26	1	1800
flames_HR21_faint_3	2015-07-26	1	1800
flames_HR21_veryfaint_1	2015-06-27	1	2700
flames_HR21_veryfaint_2	2015-06-27	1	2700
flames_HR21_VVfaint_2	2015-06-28/2015-07-26	2	2700

NOTE—For each of the data sets analyzed in this work (MUSE/NFM, SINFONI, KMOS and FLAMES), and for each individual pointing, the table lists the name, execution date, number of exposures (N_{exp}) and exposure time of each frame (t_{exp}, in seconds).

could significantly offset the location of the surface brightness peak, with respect to the real $C_{\rm grav}$.

To identify the position of $C_{\rm grav}$, we adopted the iterative procedure described in Montegriffo et al. (1995) and used in Chapter 4, Section 4.2.2, (see also, Lanzoni et al., 2010, 2019; Miocchi et al., 2013). This method computes the position of $C_{\rm grav}$ by averaging the projected coordinates (x, y) on the plane of the sky of a sample of resolved stars selected in an appropriate range of magnitude and within a given radial distance (r) from the center, starting from a first-guess value of the latter. Among the targets of the photometric catalog described in Saracino et al. (2019), we considered only the stars brighter than $m_{\rm F814W} = 20.0,\ 20.3,\ 20.6$, which are reasonable selections to obtain statistically large samples while avoiding incompleteness effects. For each magnitude cut, we considered the stars included within circles of different radii ($r = 30''$, $r = 34''$, $r = 38''$) from the adopted center. These values are larger than the cluster core radius quoted in the literature ($r_c = 21''$; Harris, 1996, 2010 edition) to ensure that the procedure is applied in a region where the density profile starts to decrease (see Miocchi et al., 2013). As first-guess center we adopted the value quoted in Harris (1996, 2010 edition). Then, from each sub-sample of selected stars we computed a new guess value of the cluster center by averaging the stellar coordinates projected on the plane of the sky. The procedure is repeated iteratively by using each time the center value computed in the previous iteration, until convergence. The convergence is reached when ten consecutive iterations provide values of the center that differ by less than $0.01''$ from each other. We determined the final position of $C_{\rm grav}$ of NGC 6569 as the average of the values obtained from each sub-sample, finding $\alpha = 18^{\rm h}13^{\rm m}38.70^{\rm s}$, $\delta = -31°49'37.13''$, with an uncertainty of $\sim 0.3''$. This is located at $\sim 0.1''$ west and $\sim 0.3''$ south from the previous estimate reported in Harris (1996, 2010 edition). In the next analysis, we always adopted the position of the cluster center obtained in this work.

5.4 Radial velocity measurements

To properly derive the RV of individual stars from the spectra acquired with the four different spectrographs used in this study, we have performed a specific analysis for each data set following a procedure similar to that described in Chapter 4. Below we summarize only the main steps.

MUSE - The MUSE spectra have been extracted by using the software PampelMuse (Kamann et al., 2013), which allows us to obtain deblended source spectra of individual stars even in crowded regions of stellar systems, by performing a wavelength-dependent point spread function (PSF) fitting. PampelMuse uses as input a reference catalog with the magnitudes and the coordinates of all the stars

present in the field of view of the datacube. For this purpose we adopted the photometric catalog obtained by Saracino et al. (2019). As PSF model we selected the MAOPPY function (Fétick et al., 2019), which was developed to properly reproduce both the core and the halo of the AO-corrected PSF in MUSE/NFM observations (for more details, see Göttgens et al., 2021). Briefly, for each slice of the MUSE datacube, PampelMuse fits the PSF and a coordinate transformation from the reference catalog to the data and uses these quantities to extract the spectra of all the stars in the datacube optimizing the deblending of the sources. The RV measures have been derived from the Doppler shifts of the Calcium Triplet lines in the wavelength range $8450 - 8750$ Å by following the same procedure described in the previous Chapter 4, Section 4.3.2. To this aim, a library of synthetic spectra computed with the SYNTHE code has been used. The template spectra have been produced in the wavelength range covered by MUSE, adopting the cluster metallicity with an α-enhanced chemical mixture ([Fe/H]$= -0.79$ dex and [α/Fe]$= 0.4$ dex, respectively; Valenti et al. 2011), appropriate atmospheric parameters (effective temperature and gravity), according to the evolutionary phase of the targets, and applying a convolution with a Gaussian profile to obtain the MUSE spectral resolution. Briefly, the procedure first normalizes the spectra corrected for heliocentric velocity to the continuum, which is estimated by a spline fitting of the spectrum in an appropriate wavelength range. Then, it computes the residuals between the normalized observed spectra and each template of the library, shifted in RV by steps of 0.1 km s^{-1} in an appropriate velocity range. By determining the smallest standard deviation in the distribution of the residuals, the procedure then provides, as a result, the best-fit synthetic spectrum (hence, the best estimates of temperature and gravity), and the RV of the target. An estimate of the S/N of the spectrum is also computed as the ratio between the average of the counts and their standard deviation in the wavelength range $8000 - 9000$ Å. The top-left panel of figure 5.1 shows an example of the output of this procedure. For stars with different atmospheric parameters (the estimated effective temperature is labeled), and in the wavelength range used to estimate the RV, each panel shows the observed spectrum (in black) and the best-fit synthetic spectrum shifted by the estimated RV (in a color code). The RV uncertainties have been determined by running 9000 Monte Carlo simulations of spectra with S/N between 10 and 90 and applying to these simulated spectra the same procedure used for the observed ones (see also Chapter 4, Section 4.3.2). The typical RV errors are lower than 2 km s^{-1} for the brightest stars and increase as function of the magnitude up to ~ 8 km s^{-1}, as shown in Figure 5.2 (top left panel). In the case of overlapping MUSE pointings, the stars in common have been used to search for possible systematic offsets in the RV measures, always finding a good agreement within the errors. In the case of stars with multiple exposures, we performed a weighted mean of all the RV measures by using the individual errors as weights. In

total we obtained RV measures for a sample of 475 targets. The position of these targets in the plane of the sky is plotted in Figure 5.3, while the color scale shows the magnitude range covered by the sample.

SINFONI - The method adopted for the extraction and the analysis of the SINFONI spectra has been shortly presented in Chapter 4 (Section 4.3.2) and will be extensively described in a forthcoming paper (C. Pallanca et al., 2023, in preparation). SINFONI spectra have been extracted from all the spaxels showing photon counts above a fixed threshold that was assumed at 10σ from the background level. RVs were then computed by following a procedure analogous to that applied for the MUSE spectra. In the case of SINFONI, we used the $^{12}C^{16}O$ band-heads as reference lines to determine the Doppler shift. The set of synthetic spectra has been computed with the SYNTHE code (Sbordone et al., 2004; Kurucz, 2005) adopting temperature and surface gravity typical of RGB stars, metallicity and $\alpha-$element abundances of the cluster (Valenti et al., 2011). The synthetic spectra have been computed to cover the same NIR wavelength range covered by the SINFONI observations with the same spectral resolution (by means of a convolution with a Gaussian profile). Moreover, since the deepness of the CO band-heads severely depends on both the chemical abundance and the temperature, as shown by the example in the top-right panel of Figure 5.1, and stars above the RGB bump could be depleted in carbon, we computed seven additional synthetic spectra with appropriate carbon-depletion [C/Fe]$= -0.27$ dex (Valenti et al., 2011) and different values of the atmospheric parameters to properly reproduce the brightest portion of the RGB, above the RGB-bump. As mentioned above, to obtain the RVs we applied the same procedure used for the MUSE data and also the RV uncertainties have been estimated from similar Monte Carlo simulations. The errors obtained are of the order of 2 km s^{-1} and also in this case they display a trend with the magnitude (see the bottom-left panel of Figure 5.2). No significant offsets have been detected by comparing the RV measures of stars in common between different overlapping pointings. At the end of this procedure we merged the measures obtained from all the pointings by adopting as final value of RV for each star the weighted average of all the multiple measures using the estimated errors as weights. Since the SINFONI data set covers the overcrowded innermost regions of the cluster and no deblending procedures similar to those implemented in PampelMuse are available in this case, it is important to evaluate the effect on the RV measures of the possible contamination of the spectra from the light coming from bright neighboring stars. For this reason, for each target we first estimate the contamination parameter (C, see the description in Chapter 3, Section 3.3.3). This is defined as the ratio between the fraction of "contaminating light" with respect to the contribution of the target itself in the central spaxel. The "contaminating light" is estimated as the expected photon counts from the neighbouring sources providing the largest contribution to the cen-

tral spaxel and it is estimated on the basis of the PSF model that best reproduces the SINFONI data and the list of stellar sources from the HST/GeMS catalog. In order to select only the safest targets with negligible contamination from the light of neighboring sources, we selected only the SINFONI targets with $C < 0.03$. The final sample consists of 51 targets, which are all bright stars.

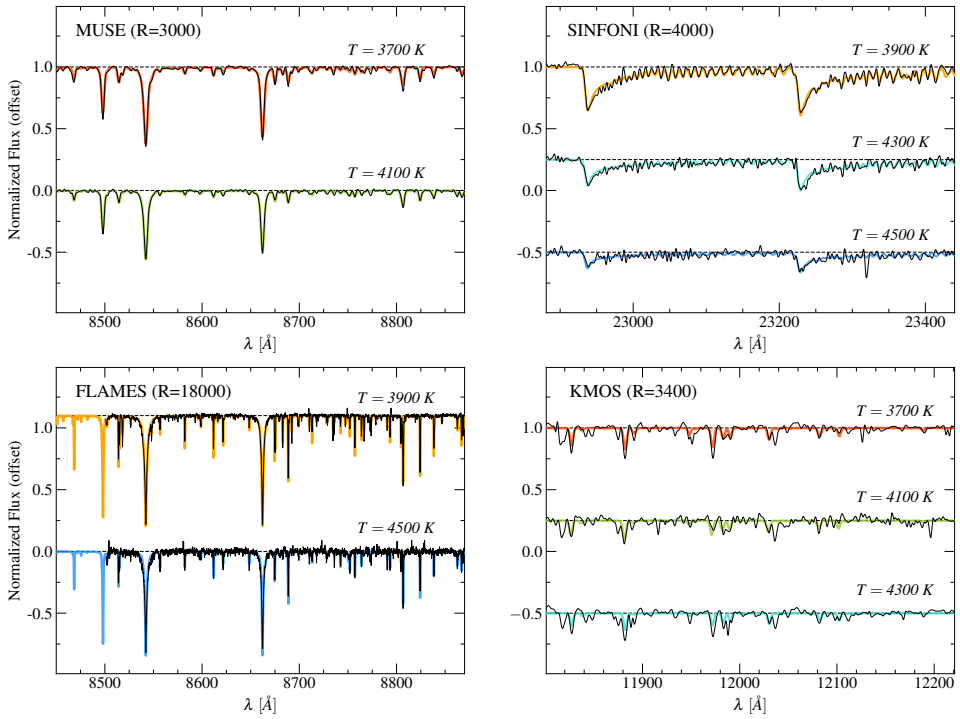

Figure 5.1: Examples of normalized observed spectra (in black) of stars with different atmospheric parameters, acquired with MUSE/NFM (top-left), SINFONI (top-right), FLAMES in the HR21 setup (bottom-left) and KMOS (bottom-right). For each observed spectrum, the best-fit synthetic spectrum obtained from the procedures described in Section 5.4 and shifted by the derived RV value is overplotted in color, according to the effective temperature (labeled for each spectrum) associated to the best-fit template. The difference in the spectral resolution (labeled in each panel) of the various instruments is evident, as it is also the temperature dependence of the CO band-head deepness in the SINFONI spectra.

FLAMES - For the FLAMES spectra, we determined the RVs from the Doppler shift of atomic lines in the wavelength ranges $6200 - 6350$ Å and $8520 - 8870$ Å for the HR13 and HR21 data sets, respectively. Also in this case, the library of template spectra has been computed with the SYNTHE code (Sbordone et al., 2004; Kurucz, 2005) in the appropriate wavelength range adopting the cluster metallicity and different atmospheric parameters sampling the entire RGB extension. The RV uncertainties have been derived as in the previous cases, by means of Monte Carlo simulations, obtaining typical errors of the order of 0.5 km s^{-1} thanks to the higher spectral resolution. The top-right panel of Figure 5.2 shows that the RV errors have a roughly constant trend as a function of the magnitude of the stars in place of the typical increasing trend seen for the other data sets. This is because faint

stars have been observed with longer exposure times, thus keeping the S/N (and the uncertainties) almost constant at all magnitudes. We obtained a final FLAMES sample of 680 RV measures. The position of the target stars in the plane of the sky is shown in the bottom-right panel of Figure 5.3, in which the color scale represents the magnitude.

KMOS - For the KMOS data set, the RVs have been measured by adopting the procedure described in Lapenna et al. (2015) and Ferraro et al. (2018a,b). The spectra have been extracted from the central and most exposed spaxel of each target star identified in the field of view of each IFU. Then, by using the FXCOR task under the software IRAF, the spectra corrected for heliocentric velocity have been cross-correlated with appropriate synthetic spectra, according to the method described in Tonry & Davis (1979b). As for the other data sets, the synthetic spectra have been obtained with the SYNTHE code (Sbordone et al., 2004; Kurucz, 2005) using the wavelength range and the spectral resolution adequate for KMOS, and the uncertainties have been computed using similar Monte Carlo simulations. The derived errors are of about 3 km s^{-1} and they show the trend with magnitude plotted in the bottom-right panel of Figure 5.2. As described above, consistent methods have been used to measure the RVs of the MUSE, SINFONI and FLAMES targets, while a cross-correlation technique has been adopted in the case of KMOS spectra. Hence, to ensure that this introduced no systematics, we redetermined the RVs of a sub-sample of control stars observed with MUSE, SINFONI and FLAMES by using the cross-correlation implemented in IRAF. In all cases, we obtained RV values in excellent agreement with the previous determinations. The final KMOS catalog consists of 220 RV measures. The bottom-left panel of Figure 5.3 shows the targets position on the plane of the sky with respect the cluster center and the sampled magnitude range.

5.4.1 Final catalog

To produce a homogeneous final catalog, we checked for possible systematic offsets in RV among the different spectroscopic data sets. Adopting the FLAMES RVs as reference, because of the highest spectra resolution of this instrument, we compared the RV values of the stars in common between each pair of data sets using only the most reliable measures. We detected and applied the following offsets to realign all the measures on the FLAMES values: shift of -2.4 km s^{-1} has been applied to all the KMOS RVs, 1.9 km s^{-1} to the MUSE values, and -0.5 km s^{-1} to the SINFONI measures. Moreover, to check whether the RV uncertainties are properly estimated, we used the velocity measures (v_1 and v_2) of the targets observed in multiple data

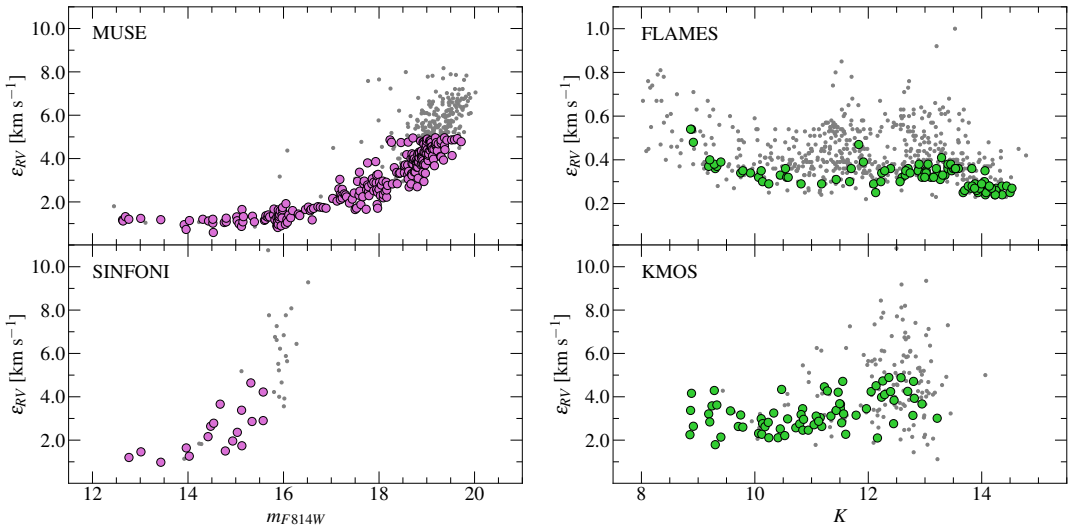

Figure 5.2: RV uncertainty ($\epsilon_{\rm RV}$) as a function of the star magnitude for the stars observed in the MUSE/NFM, SINFONI, FLAMES, and KMOS data sets (top-left, bottom-left, top-right, and bottom-right panels, respectively; see labels). In all panels, the colored circles correspond to the targets surviving the membership and the quality selections (see Section 5.5), while the gray dots are the stars rejected from the analysis.

sets and their associated errors (ϵ_1 and ϵ_2) to derive the quantity

$$\delta v_{1,2} = \frac{v_1 - v_2}{\sqrt{{\epsilon_1}^2 + {\epsilon_2}^2}}, \tag{5.1}$$

which should return a normal distribution with a standard deviation of 1 in the case of correct uncertainties (see also Kamann et al., 2016). To have a large enough sample of repeated measures, we used the stars in common between FLAMES and KMOS, and between MUSE and SINFONI, obtaining in both cases distributions consistent with a normal function with a standard deviation of ~ 1, thus guaranteeing that the errors are correctly estimated.

Then, to create the final catalog, we combined the four data sets previously homogenized by averaging the RV values of the targets with multiple measures using the estimated errors as weights. We obtained a final sample of 1292 RVs of individual stars distributed from 0.8″ to 723.7″ from the cluster center (corresponding to ~ 1.2 times the truncation radius $r_t = 589.7''$; see Section 5.7). Figure 5.4 shows the position of the targets in the optical and NIR CMDs for the internal (MUSE and SINFONI) and external (FLAMES and KMOS) samples, respectively.

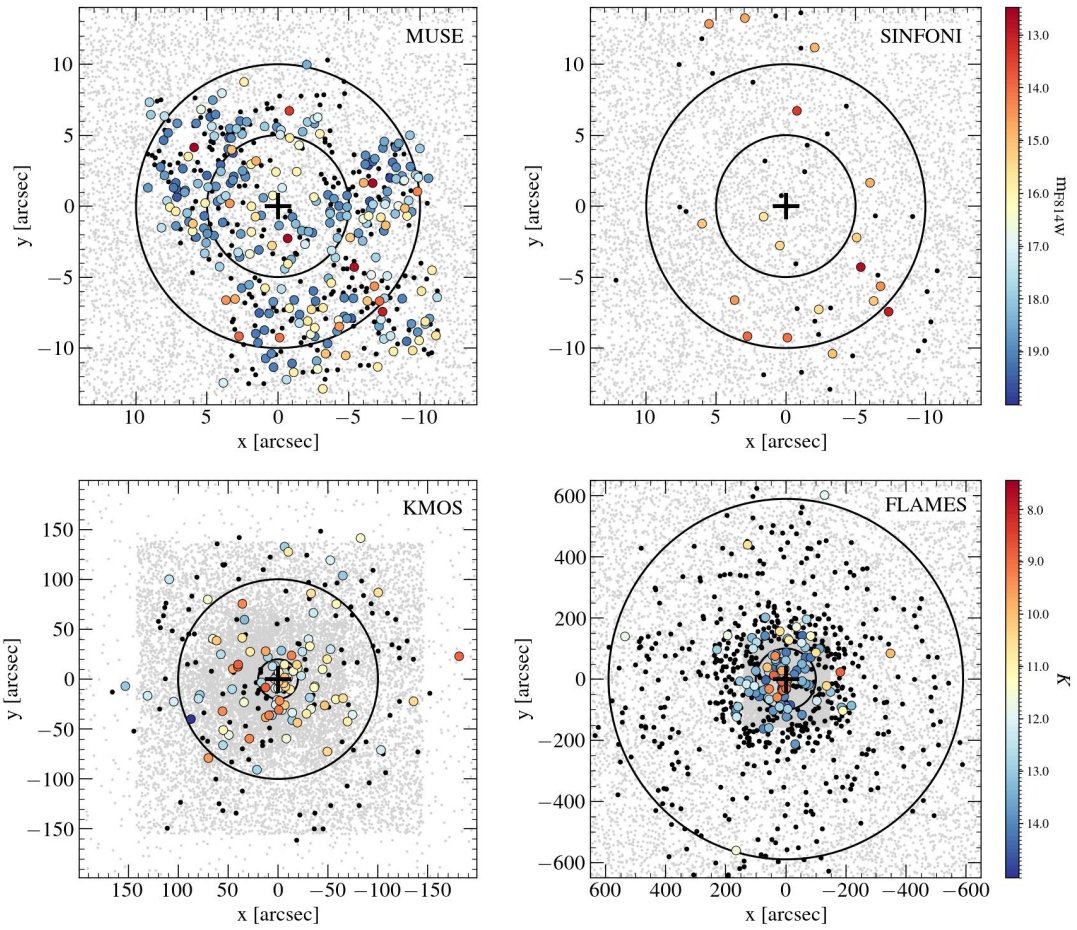

Figure 5.3: Maps in the plane of the sky, with respect to the adopted cluster center (black cross, determined in Section 5.3), of the stars with measured RV in each data set. In all panels, the colored large circles mark the targets that survived the membership and quality selections and have been used for the kinematic analysis (see Section 5.5), while the black dots are the rejected stars. The color scales indicate the m_{F814W} and K-band magnitudes for the inner sample (MUSE and SINFONI, top panels) and for the external data sets (KMOS and FLAMES, bottom panels), respectively. *Top-left*: focus on the central region sampled by MUSE. The gray dots are the stars of the HST/GeMS photometric catalog (Saracino et al., 2019). The two circles mark distances of 5″ and 10″ from the center. *Top-right*: as in the top-left panel but relating to the SINFONI data set. *Bottom-left*: map relative to the position of the KMOS targets. The gray dots in the background mark the stars in the SOFI/2MASS catalog. The two circles are centered in the cluster center and have radii of 19.9″ (equal to the core radius of the cluster; see Section 5.7) and 100″. *Bottom-right*: external portion of the cluster sampled by the FLAMES targets. The gray dots are as in the bottom-left panel, while the two circles mark distances of 100″ and 589.7″ (corresponding to the truncation radius of the cluster; see Section 5.7) from the center.

5.5 Internal kinematics

5.5.1 Cluster membership

In order to properly study the internal kinematics of the cluster, we have performed an accurate selection of member stars among the targets of our final catalog. To

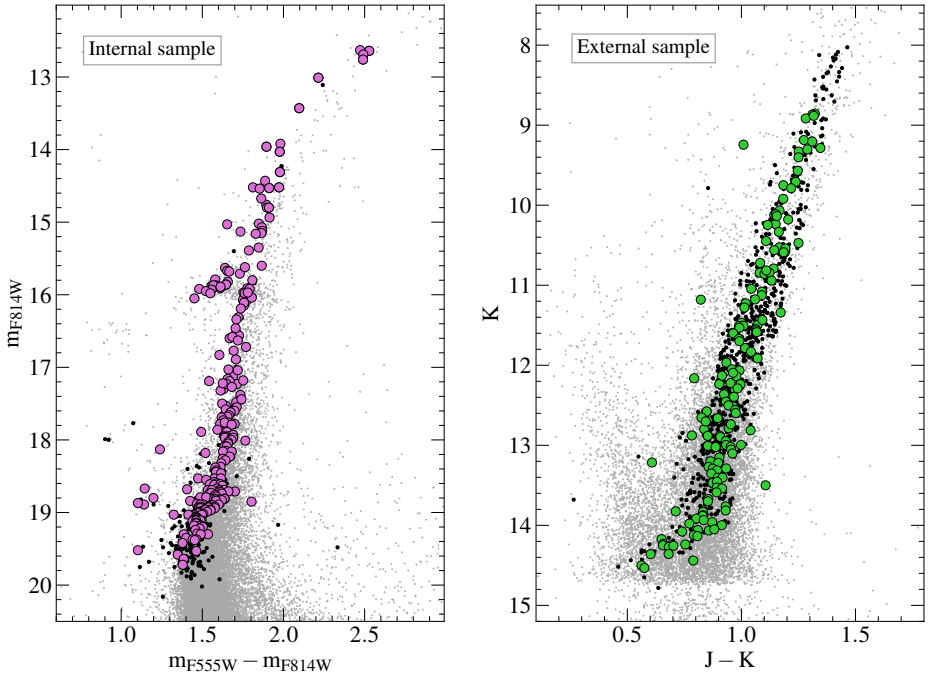

Figure 5.4: CMDs of NGC 6569 showing the targets of the final kinematic catalog. *Left panel*: HST optical CMD (gray dots, from Saracino et al., 2019) with the targets of the internal sample (MUSE and SINFONI) highlighted. The large magenta circles mark the targets after all the membership and quality selections described in Sections 5.5, while the black dots are the rejected targets. *Right panel*: the gray dots show the $(K, J-K)$ CMD obtained from the SOFI/2MASS catalog. The large green circles and black dots are, respectively, the targets of the external sample (KMOS and FLAMES) selected for the kinematic analysis and rejected on the basis of the adopted membership and quality selections.

obtain the most reliable cluster membership selection, we used a combination of PMs provided by the Gaia EDR3 (Gaia Collaboration et al., 2018) and the relative PMs measured by Saracino et al. (2019). In particular, for the external sample (FLAMES and KMOS), we adopted the Gaia PMs by selecting as cluster members the targets with magnitude $G < 19$ and PMs within 0.5 mas yr^{-1} from the absolute PM of the cluster (Vasiliev & Baumgardt, 2021) in the vector-point diagram (VPD). The Gaia VPD and the member selection of the external sample are shown in the top-right panel of Figure 5.5. Most of the targets of the inner sample (MUSE and SINFONI), instead, are located in regions too crowded to allow reliable Gaia PM measures. We thus used the relative PMs obtained by Saracino et al. (2019) from the combination of HST and GeMS observations secured at two different epochs. In selecting member stars for this sample we followed the prescriptions described in Saracino et al. (2019): the targets of the internal sample selected as member stars are shown with large magenta circles in the VPD of the relative PMs in the top-left panel of Figure 5.5. The efficiency of the adopted PM selection in excluding field stars is evident from the bottom panel of Figure 5.5, which shows the target

RVs as a function of the distance from the center, with the stars selected as cluster members marked with colored large circles. After this selection, the bulk of cluster members is centered at about -48 km s^{-1}, while the number of contaminating field stars (gray dots in the figure) is significant at larger radii and become dominant in the outermost regions. The remaining obvious outliers have been removed in the following analysis, according to their RV. With the purpose to perform a precise kinematic analysis, we also adopted additional criteria to select the targets with the most reliable RV measurements[†] Therefore, for the following analysis, we used only the cluster member targets with S/N$>$ 15 and RV error $<$ 5 km s^{-1} (see their position on the plane of the sky and in the CMDs in Figure 5.3 and 5.4, respectively).

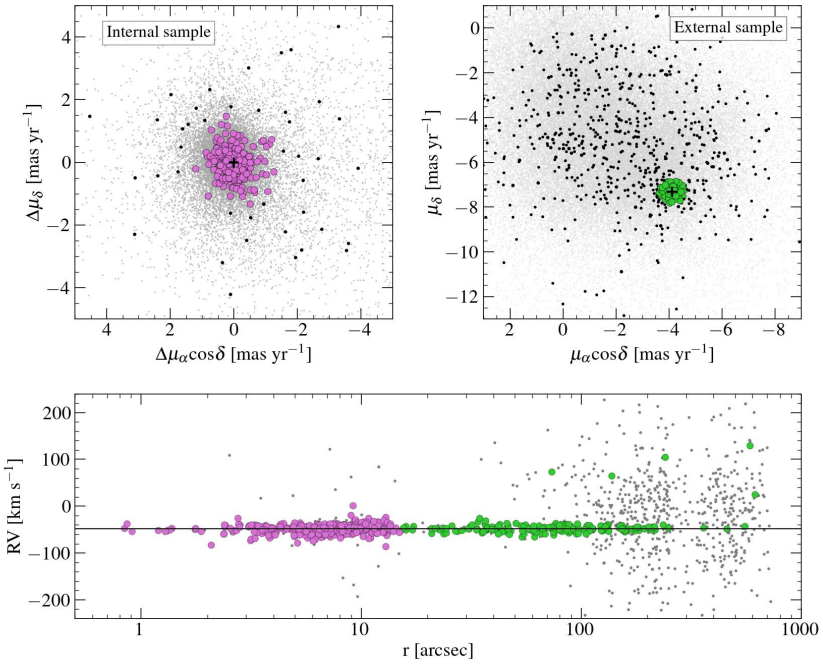

Figure 5.5: *Top-left panel*: VPD of the relative PMs obtained in Saracino et al. (2019, gray dots). The member stars selected from the internal sample for the kinematic analysis of the cluster are marked with large magenta circles, while the black dots are the targets rejected as non-members. The black cross is centered on (0,0), thus marking the bulk motion of the cluster. *Top-right panel*: VPD of the Gaia EDR3 data set (gray dots; only stars with $g < 18$ are plotted for visualization purposes). The green circles show the targets of the external sample selected as member stars, while those considered as field stars are indicated with black dots. The black cross marks the absolute PM of NGC 6569 (Vasiliev & Baumgardt, 2021). *Bottom panel*: RVs of the 1292 targets of the final catalog as a function of the distance from the cluster center. The large circles mark the targets selected as cluster members on the basis of the measured PMs, color-coded as in the top panels, while the gray dots are the targets rejected as field stars.

[†]The RV sample with the corresponding errors is available for free download at: `http://www.cosmic-lab.eu/Cosmic-Lab/MIKiS_Survey.html`

5.5.2 Systemic velocity

For the determination of $V_{\rm sys}$ of NGC 6569, among the targets selected with the criteria described above, we conservatively adopted additional cuts in RVs (-80 km s^{-1} <RV< -20 km s^{-1}) and applied a 3σ-clipping algorithm to the remaining distribution, thus minimizing the risk of residual field contamination. The RVs of the resulting sample (made of 393 stars) are plotted as black circles as a function of the distance from the center in the left panel of Figure 5.6, while their distribution is drawn as a filled gray histogram in the right panel, with the peak indicating the systemic velocity of the cluster. Assuming a Gaussian RV distribution, we determined the value of $V_{\rm sys}$ and its uncertainty by means of a Maximum-Likelihood procedure (Walker et al., 2006), obtaining $V_{\rm sys} = -48.5 \pm 0.3$ km s^{-1}. Our estimate is in agreement with the value derived in Valenti et al. (2011, -47 ± 4 km s^{-1}) and, marginally, with that obtained by Baumgardt & Hilker (2018, -49.9 ± 0.4 km s^{-1}), while it strongly disagrees with that listed in Harris (1996, 2010 edition, -28.1 ± 5.6 km s^{-1}).

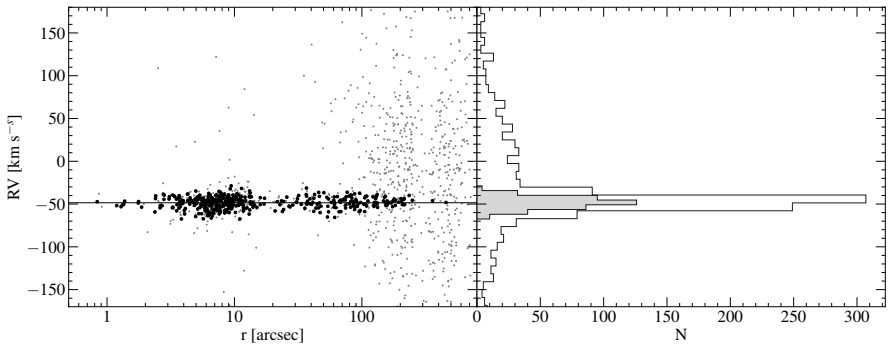

Figure 5.6: *Left panel:* RVs of the final catalog as a function of the distance from the cluster center. The black circles show the sub-sample of stars used for the determination of $V_{\rm sys}$ (solid line), while the gray dots mark the excluded targets. *Right panel:* the open histogram is the number distribution of the entire RV sample, while the gray histogram refers to the sample used to determine $V_{\rm sys}$ (black dots in the left panel).

5.5.3 Systemic rotation

In previous kinematics analyses no clear signals of rotation have been detected in the external regions of NGC 6569 (e.g., Sollima et al., 2019; Vasiliev & Baumgardt, 2021). However, the large sample of RVs data presented here offers the opportunity to push the search for rotation further, also including the central region of the cluster. To this purpose, we used the method already adopted in the previous Chapters 3 and 4, see Section 3.4.3 and 4.3.4.3, respectively, for a complete description of the procedure (see also, Lane et al., 2009; Bellazzini et al., 2012; Lanzoni et al., 2013; Ferraro et al., 2018a; Lanzoni et al., 2018a; Lanzoni et al., 2018b).

As mentioned in the case of NGC 6440 (see Section 4.3.4.3), a meaningful application of this method requires a uniform distribution of the RV measures in the plane of the sky. Thus, we are forced to avoid some strongly under-sampled regions and limit the analysis to the innermost 5″, where the combination of the MUSE and SINFONI targets offers a reasonably symmetric coverage (see Figure 5.3), and the annular region between 15″ and 150″, which is sampled by FLAMES and KMOS data.

The maximum signal of rotation in these regions has been detected at $40'' < r < 90''$. This is shown in the diagnostic diagrams plotted in Figure 5.7, which indicate a maximum amplitude of $\sim (1.9 \pm 0.3)$ km s^{-1}, a position angle of the rotation axis $PA_0 = (91 \pm 3)°$, and a p-value of the KS test p =0.0016, indicating that the difference between cumulative RV distributions of the two sub-samples on either side of the rotation axis is significant at $\sim 2.4\sigma$. However, the number of stars observed in this region is admittedly small (67), and additional spectroscopic observations are needed to solidly confirm the presence of systemic rotation in this GC.

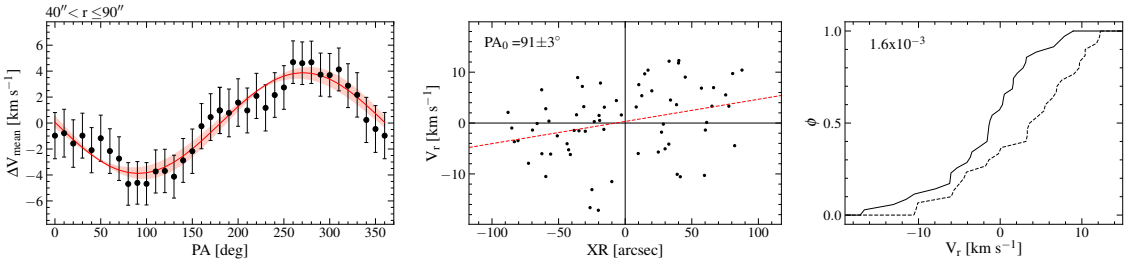

Figure 5.7: Diagnostic diagrams of the most significant rotation signal detected in NGC 6569 in the annular region $40'' < r < 90''$ from the cluster center. The *left panel* shows the difference between the mean RV on each side of a line passing through the center with a given PA as a function of PA itself (see Section 3.4.3 and 4.3.4.3 for more details about the method). The continuous line is the sine function that best fits the observed patterns. The *central panel* shows the distribution of the velocities referred to V_{sys} (V_r), as a function of the projected distances from the rotation axis (XR) in arcseconds. The value of PA_0 is labeled. The red dashed line is the least square fit to the data. The *right panel* shows the cumulative V_r distributions for the stars with XR< 0 (solid line) and for those with XR> 0 (dotted line). The KS probability that the two sub-samples are extracted from the same parent distribution is labeled.

5.5.4 Velocity dispersion profile

As discussed in previous Chapters, the measure of the observed RV dispersion at different radial distances from the center corresponds to the second velocity moment profile $\sigma_{II}(r)$, which is linked to the VD profile $\sigma_P(r)$ through the relation 3.1. Since the evidence of rotation in NGC 6569 is highly uncertain (see previous Section 5.5.3), we assume that the rotation contribution is negligible and $\sigma_P^2(r) = \sigma_{II}^2(r)$.

Hence, to determine the VD profile of the cluster, we used the sample of RVs selected with the criteria described in Section 5.5.1 (only member stars, with S/N> 15 and RV error < 5 km s^{-1}). This has been divided into concentric radial bins with increasing distance from the center, ensuring both a proper radial sampling and a statistically sufficient number of targets (at least 25) in each bin. After a $3\sigma-$clipping procedure used to exclude the obvious outliers, we then determined the VD value in each bin by following the Maximum-Likelihood method described in Walker et al. (2006, see also Martin et al., 2007; Sollima et al. 2009). The velocity dispersion uncertainties are estimated adopting the procedure described in Pryor & Meylan (1993b). The results are shown in Figure 5.8 (blue circles) and listed in also 5.2. As it is apparent, the VD decreases from a central value of approximately 6.5 km s^{-1}, down to 3.7 km s^{-1} in the bin centered at $\sim 200''$. For the sake of comparison, in the figure we also report the profile published[‡] in Baumgardt & Hilker (2018, white squares). Their two innermost points are consistent with our measures, but they are limited at $r > 30''$ and therefore do not properly characterize the central portion of the VD profile. The outermost measure from these authors largely exceeds the dispersion velocity obtained here, probably because of residual field contamination.

Table 5.2: Velocity dispersion profile of NGC 6569.

r_i [arcsec]	r_e [arcsec]	r_m [arcsec]	N	σ_P km s^{-1}	ϵ_{σ_P} km s^{-1}
0.01	7.00	4.80	122	6.40	0.51
7.00	15.00	9.58	131	6.60	0.50
15.00	70.00	41.56	65	6.00	0.64
70.00	150.00	98.72	50	5.40	0.61
150.00	550.00	202.63	26	3.70	0.64

NOTE– The table lists: the internal and external radius of each radial bin (r_i and r_e, respectively), the average distance from the center of the stars within the bin (r_m), the number of stars in the bin (N), the measured velocity dispersion and its uncertainty in the bin (σ_P and ϵ_{σ_P}, respectively).

5.6 Star density profile

The HST data set described in Saracino et al. (2019) offers the ideal angular resolution for determining the innermost portion ($r < 120''$) of the projected density

[‡]Note that the comparison has been done with published values; however the online repository is repeatedly revised, and some updated values are in better agreement with our determinations.

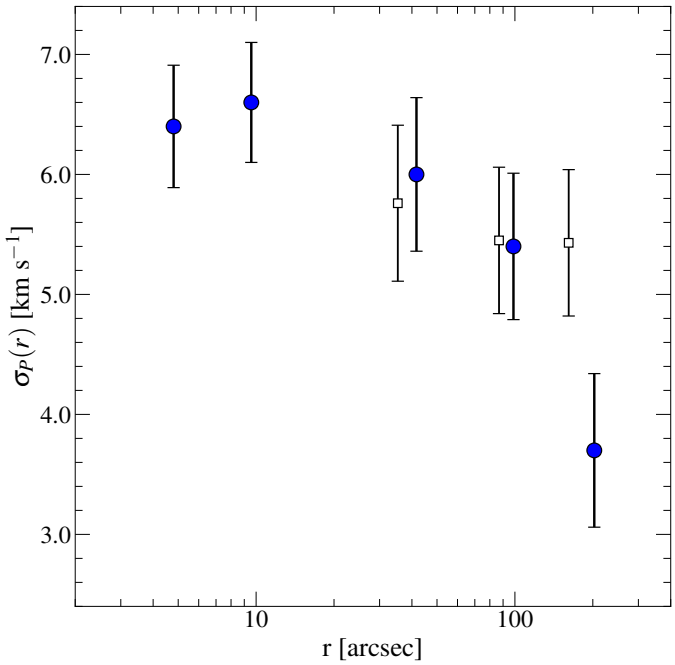

Figure 5.8: Velocity dispersion (second velocity moment) profile of NGC 6569 (blue circles) obtained from the measured individual RVs. For the sake of comparison, the white squares correspond to the profile published in Baumgardt & Hilker (2018).

profile of NGC 6569 from resolved star counts. To cover the entire extension of the system, we complemented this data set with the Gaia EDR3 catalog out to 1200″ from the cluster center. To ensure comparable levels of photometric completeness in the two data sets, and sufficiently large statistics in each bin, we adopted two different magnitude cuts for the sample selection: $m_{F814W} < 20.5$ for the HST/GeMS data set, and $G < 18$ for the Gaia one.

According to the standard procedure adopted also in Chapter 4 and used in several previous work (see, e.g. Lanzoni et al., 2010, 2019; Miocchi et al., 2013), we divided the sample into 20 concentric annuli centered on the C_{grav} and split each annulus into an appropriate number of sectors (usually four). We estimated the star surface density in each sector as the ratio between the number of stars within the sector and the area of the sector itself. The stellar density in each annulus is then obtained as the average of the sectors densities, while their standard deviation is adopted as corresponding uncertainty. Owing to the different magnitude cuts adopted for the sample selections, the external portion of the profile (from Gaia data) has been finally shifted until it matched the last point of the HST/GeMS profile. The projected density profile thus obtained is shown in Figure 5.9 (open circles), where the radius associated to each annulus is the midpoint of the radial bin. The plateau at $r > 200''$ is due to the (dominant) contribution of the Galactic field, which has an essentially constant density at the small scales surveyed here.

Its value has been estimated as the averaging density of the six outermost points (dashed line in Figure 5.9), and it has been subtracted from the observed profile. The results are shown as blue circles in Figure 5.9. As apparent, after the background subtraction, the outermost portion of the profile significantly decreases with respect to the observed one, which demonstrates that an accurate determination of the field level is essential to properly constrain the true density distribution of the system. This has the typical shape observed for most GCs, i.e., an inner flat core followed by a steady decreasing trend (Figure 5.9).

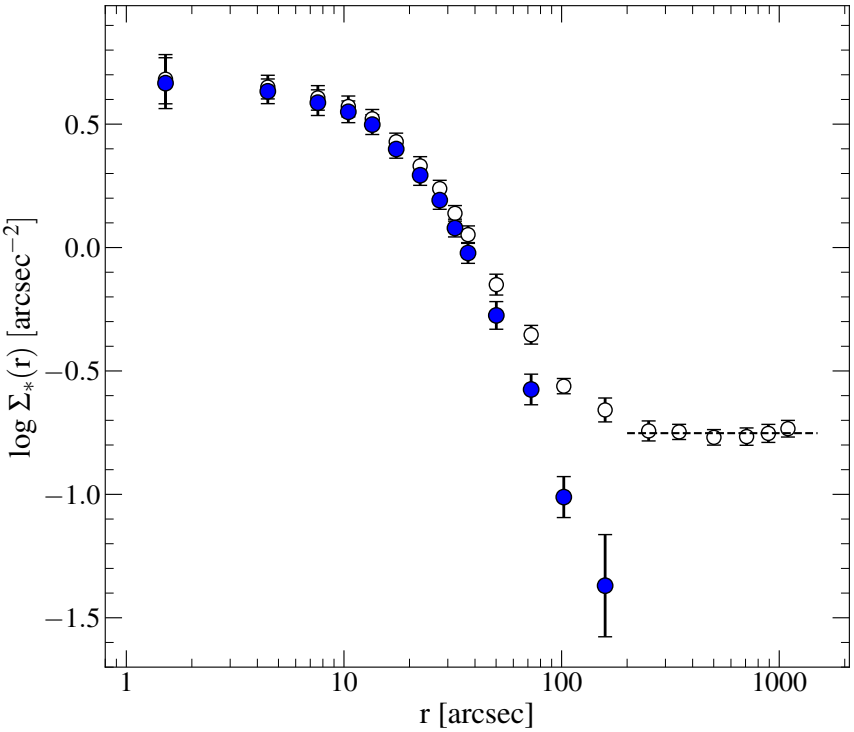

Figure 5.9: Observed density profile of NGC 6569 obtained from resolved star counts (open circles). The 6 outermost points (with $r > 200''$) define a sort of plateau and have been used to measure the density level of the background (dashed line). The blue circles show the cluster density profile obtained after subtraction of the field contribution.

5.7 Discussion and Conclusions

The star density and VD profiles presented in Sections 5.6 and 5.5.4, respectively, have been obtained by using samples of stars with approximately the same mass. In addition, although no definitive conclusions on the possible existence of systemic rotation can be drawn at the moment, the results discussed in Section 5.5.3 suggest that the rotational velocity (if any) is negligible in this system. Hence, we determined

the structural and kinematic parameters of NGC 6569 by simultaneously fitting the density and VD profiles with single-mass, spherical, isotropic and non-rotating King models (King, 1966, see also Chapter 1, Section 1.1.1). To determine the best-fit King model to both the profiles we adopted a Markov Chain Monte Carlo (MCMC) approach, by means of the emcee algorithm (Foreman-Mackey et al., 2013). We assumed uniform priors on the parameters of the fit, obtaining the posterior probability distribution functions (PDFs) for the characteristic parameters of the King models and for the central VD, σ_0. For each parameter, the PDF median has been adopted as best-fit value, while the 16-th and 84-th percentiles of the posterior PDF have been used to estimate the 1σ uncertainty.

The resulting best-fit King model is shown overplotted to the observed density and VD profiles in Figure 5.10 (red lines), where the residuals between the model and the observations are also shown in the bottom panels. A very good agreement is apparent, thus indicating that both the structure (as it is often the case for GGCs) and the internal kinematics of NGC 6569 are well consistent with the King model expectations. The best-fit model is characterized by $W_0 = 6.75$ (which corresponds to $c = 1.46$) and a core radius $r_c = 19.9''$, corresponding to ~ 1 pc at the distance of the cluster ($d = 10.1$ kpc; Saracino et al., 2019). The half-mass and tidal radii are, respectively, $r_h = 72.5''$ and $r_t = 589.7''$, while the effective radius (i.e., the radial distance at which the projected density, or the surface brightness, halves the central value) is $r_{\rm eff} = 54.1''$. For the central velocity dispersion we obtained $\sigma_0 = 6.7 \pm 0.3$ km s $^{-1}$. The best-fit values and the uncertainties of each parameter are listed in Table 5.3.

Comparing our estimates with the results obtained from the surface brightness profile by McLaughlin & van der Marel (2005, which are also the values quoted in Harris 1996, 2010 edition), we find consistent values within the uncertainties: in fact, after conversion from parsec to arcseconds using the cluster distance provided in that paper ($d = 10.7$ kpc), these authors quote: $W_0 = 6.20 \pm 0.2$, $c = 1.31 \pm 0.05$, $r_c = 21''$, $r_{\rm eff} = 48''$, and $r_t = 461''$. Within the errors, our values are in agreement also with those of Baumgardt & Hilker (2018, $r_c = 20.74''$ and $r_h = 78.86''$, converted into arcseconds using the cluster distance quoted in their paper: $d = 12.0$ kpc). We remark, however, that this comparison is neither obvious nor rigorous, because Baumgardt & Hilker (2018) derive these quantities from N-body simulations instead of fitting the observations with King models. As for the estimate of σ_0, our value is lower than that quoted in Baumgardt & Hilker (2018, $\sigma_0 \sim 7.5$ km s^{-1}). This discrepancy is likely due to the fact that the VD profile used in that work is poorly constrained (see Figure 5.8, and also Figure E12 in Baumgardt & Hilker 2018).

Under the (well-motivated) assumption of a King model structure and by adopting the obtained value of σ_0, we estimated the total mass of the cluster as $M = 166.5\ r_0\mu/\beta$ (Majewski et al., 2003), where r_0 is the King radius, μ is a

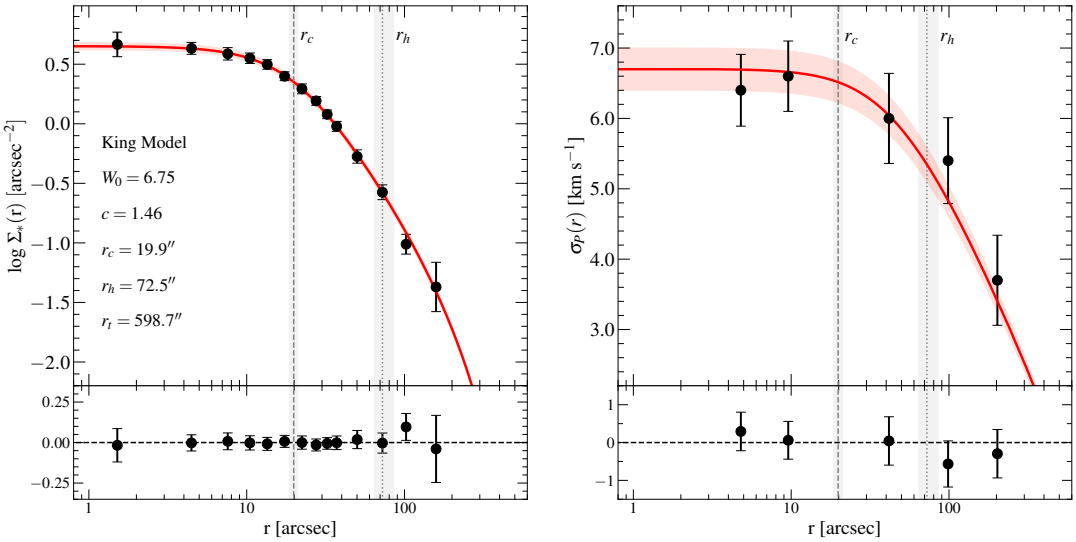

Figure 5.10: Best-fit King model (as derived in Section 5.7; red solid lines) overplotted to the star density profile (left panel) and the VD profile (right panel) of NGC 6569. The best-fit values of the central dimensionless potential (W_0), concentration parameter (c), and core, half-mass and tidal radii (r_c, r_h and r_t, respectively) are labeled in the left panel, where the dashed and dotted lines mark r_c and r_h , respectively. The shaded regions show the associated uncertainties. The bottom panels show the residuals between the model and the observations. The red shaded region in the right panel marks the 1σ confidence level on the estimate of the central velocity dispersion (see Section 5.7).

scaling parameter depending on the King concentration c (Djorgovski, 1993), and $\beta = 1/\sigma_0^2$ (Richstone & Tremaine, 1986). The uncertainty has been estimated as the dispersion of the mass values resulting from 1000 Monte Carlo simulations, run by adopting appropriate normal distributions for c, r_0 and σ_0 (see Chapter 3, Section 3.4.7 for more details). The resulting total mass is $M = 1.72^{+0.20}_{-0.18} \times 10^5 M_\odot$. This is lower than the value obtained by Baumgardt & Hilker (2018, $3.02 \pm 0.36 \times 10^5$ $M_\odot$) from N-body simulations, presumably due to the different VD profile used as constraint, other than the different assumptions and methods adopted in the two works (for instance, Baumgardt & Hilker, 2018 adopt a 20% larger distance of the cluster than assumed here, and they compare the observations with a library of N-body simulations). Finally, by adopting the structural parameters determined here, the total mass and the cluster distance of Saracino et al. (2019), we estimated the central and half-mass relaxation times ($t_{\rm rc}$ and $t_{\rm rh}$) from equation (10) and equation (11) of Djorgovski (1993), respectively. To estimate the central relaxation time (in years), we used:

$$t_{\rm rc} = \frac{0.834 \times 10^7}{\ln(0.4N)} \frac{\rho_{0,M}^{1/2} r_c^3}{m}, \tag{5.2}$$

where N is the total number of stars, $\rho_{0,M}$ is the central mass density, and m is the

average stellar mass. For the half-mass relaxation time (in years), we adopted:

$$t_{\rm rh} = \frac{2.055 \times 10^6}{\ln(0.4N)} \frac{M^{1/2} r_h^3}{m}. \tag{5.3}$$

We found $\log(t_{\rm rc}) = 8.3$ and $\log(t_{\rm rh}) = 9.2$, which are roughly consistent with the values quoted in the Harris (1996, 2010 edition, 8.38 and 9.05, respectively) catalog, consistently with the fact that also the differences in terms of structural parameters and cluster distance are small. These values suggest that NGC 6569 is in an intermediate stage of its dynamical evolution, although dedicated investigations of this issue (see, e.g., Ferraro et al., 2018c and Bhat et al., 2022, 2023; Cadelano et al., 2020b) are needed to properly confirm it.

Table 5.3: Summary of the main parameters used and obtained for the GGC NGC 6569.

Parameter	Estimated value	Reference
Cluster center	$\alpha_{\rm J2000} = 18^{\rm h}13^{\rm m}38.70^{\rm s}$ $\delta_{\rm J2000} = -31°49'37.13''$	this work
Metallicity	$[{\rm Fe/H}] = -0.79$	Valenti et al. (2011)
	$[\alpha/{\rm Fe}] = +0.4$	Valenti et al. (2011)
Cluster distance	$d = 10.1 \pm 0.2$ kpc	Saracino et al. (2019)
Dimensionless central potential	$W_0 = 6.75 \pm 0.4$	this work
Concentration parameter	$c = 1.46^{+0.12}_{-0.11}$	this work
Core radius	$r_c = 19.9'' \pm 1.2 = 0.97$ pc	this work
Three-dimensional half-mass radius	$r_{\rm h} = 72.5''^{+12.9}_{-7.9} = 3.55$ pc	this work
Effective radius	$r_{\rm eff} = 54.1''^{+9.3}_{-5.7} = 2.65$ pc	this work
Tidal radius	$r_t = 589.7''^{+167.9}_{-109.3} = 28.88$ pc	this work
Systemic velocity	$V_{sys} = -48.5 \pm 0.3$ km s^{-1}	this work
Central velocity dispersion	$\sigma_0 = 6.7 \pm 0.3$ km s^{-1}	this work
Absolute Proper Motions	$\mu_\alpha cos\delta = -4.125$ mas yr^{-1} $\mu_\delta = -7.315$ mas yr^{-1}	Vasiliev & Baumgardt (2021)
Total Mass	$M = 1.72^{+0.20}_{-0.18} \times 10^5 M_\odot$	this work
Central relaxation time	$\log(t_{\rm rc}) = 8.3$ [in yr]	this work
Half-mass relaxation time	$\log(t_{\rm rh}) = 9.2$ [in yr]	this work

Chapter 6

Discussion and Conclusions

In this thesis we presented a thorough and comprehensive investigation of the kinematic properties of three GGCs. Such a study is of paramount importance for a full understanding of the dynamical evolution and formation mechanisms of these systems, and to address some fundamental issues of the present-day astrophysics, such as the existence of the mysterious IMBHs.
As largely discussed, the detailed characterization of the kinematic features in GGCs (aimed at addressing the existence of unusual trends in the VD profile, the presence and the extent of rotation and anisotropy, etc.) combined with complementary information on their structural properties and their exotic stellar population, could provide valuable insights into the complex evolutionary history of collisional stellar systems.

In this context, this thesis project takes advantage of the exceptional database provided by the ongoing ESO-VLT MIKiS survey. The basic strategy driving the survey is to exploit the capabilities of the current generation of ESO-VLT spectrographs to derive the LOS velocity from resolved individual stars located over the entire radial extension of the clusters, from the high-density innermost core to the outermost regions. This multi-instrument approach is allowing us to properly construct the entire LOS velocity dispersion profile and the rotation curve of a large sample of GGCs. The initial strategy of the MIKiS survey involved the use of three specific spectrographs, SINFONI, KMOS, and FLAMES, to sample the inner, intermediate and external regions of GCs, respectively. In this thesis work, this scheme has been further strengthened by the complementary use of the spectrograph MUSE/NFM, which has been recently implemented into the MIKiS survey through an additional, still ongoing large program (PI: Ferraro). This has substantially improved the sampling of the cluster cores. In fact, thanks to the highly efficient AO facility, MUSE/NFM provides very high spatial resolution, allowing to resolve the stars even in the overcrowded innermost regions of GCs at optical wavelengths, thus also sampling the Calcium Triplet that is a prominent spectral feature well suitable to properly measure LOS velocities (SINFONI, instead, works in the near-IR band, where these measures are obtained from molecular bands). Indeed, by providing samples of hundreds of spectra even in the innermost arcseconds of high-density

clusters, the unique performances of MUSE/NFM have made the kinematic exploration of GC cores one of the main goals of this thesis.

THE OBSERVED SAMPLE - In this thesis work, we have investigated three GGCs: NGC 1904, NGC 6440 and NGC 6569. These clusters have similar high central densities, while they are located in different environments: two are in the Galactic bulge (NGC 6440 and NGC 6569) and one in the halo (NGC 1904). Our multi-instrumental approach allowed us to acquire spectra of resolved stars from the very crowded regions, where we reach sub-arcsecond spatial resolution, to the outskirt (at several arcmin from the cluster center), obtaining huge final samples of RV measures: $\sim$ 1700 RVs of individual stars have been measured in NGC 1904, $\sim$ 1800 in NGC 6440, and a sample of $\sim$ 1300 in NGC 6569. Notably, thanks to the MUSE/NFM performances, we were able to acquire up to a few hundreds of resolved star spectra within the innermost 5″ from the center (see Figure 6.1).

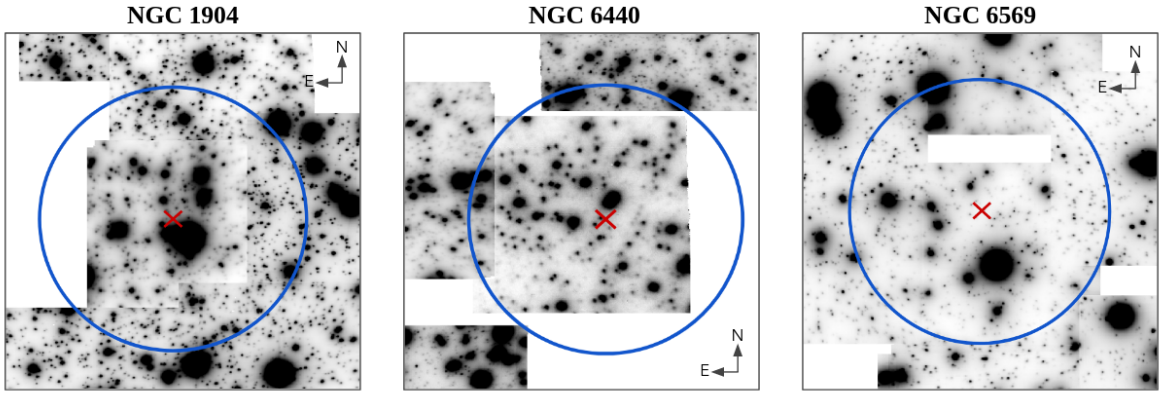

Figure 6.1: Reconstructed *I*-band images of MUSE/NFM pointings in the core of NGC 1904 (left panel), NGC 6440 (central panel) and NGC 6569 (right panel). In each panel, the blue circle is centered on the cluster center (red cross) and has a radius of 5″.

VELOCITY DISPERSION PROFILES - By using only the cluster member stars, we determined the entire VD profile of each of the three clusters, exploring for the first time the kinematics of the inner core. The resulting profiles are shown in Figure 6.2, and confirm the characteristic behavior usually observed in GCs, with a constant inner plateau and a declining trend at larger distances from the center. For the sake of comparison, in the same figure we also report the profiles available in the literature for the investigated clusters.
In particular, in the case of NGC 1904, our profile (black circles in the left-hand panel, see also Table 3.3 and Table 3.6) agrees with that obtained by Scarpa et al. (2011, empty squares) from individual RVs at large distance, while the profile derived in the core region by Lützgendorf et al. (2013, empty triangles) from the line broadening of integrated-light spectra shows values significantly larger than our measures,

with an increasing central trend up to a value of ~ 8 km s^{-1}, which was interpreted as the signature of a 3000 $M_{\odot}$ IMBH. In this specific case, the proper sampling of the core obtained in this work allowed us to refute the hypothesis of the presence of a massive central IMBH in NGC 1904. From our analysis, we can exclude an IMBH more massive than 10^3 $M_{\odot}$, i.e. massive enough to imprint detectable perturbations in the VD profile at the radial distance probed here. As discussed in Chapter 3, Section 3.4.5, we derived the central velocity dispersion of NGC 1904 finding $\sigma_0 = 5.9 \pm 0.3$ km s^{-1}. This value is quite in agreement with the measure quoted by Harris (1996, 2010 edition, $\sigma_0 = 5.3$ km s^{-1}) and Baumgardt & Hilker (2018, $\sigma_0 = 6.5$ km s^{-1}), although the latter has been determined from the simultaneous fit to the projected density distribution and the central VD profile determined in Lützgendorf et al. (2013).
In the case of NGC 6440, our profile (black circles in the central panel of Figure 6.2, see Table 4.4), obviously samples a much inner region compared to that published by Baumgardt & Hilker (2018, empty triangles), while in the common region, we find overall good agreement between the two profiles, with not very significant difference in the case of the two outermost points. Our estimate of the central velocity dispersion ($\sigma_0 = 12.0 \pm 0.4$ km s $^{-1}$) is smaller compared to that quoted in Baumgardt & Hilker (2018, 15.8 km s $^{-1}$), likely due both to the fact that our profile samples more efficiently the core region, allowing us to properly characterize the shape of the VD profile, and to the different methods used to estimate σ_0, since Baumgardt & Hilker (2018) adopt N-body simulations to determine this quantity.
Also in the case of NGC 6569, for comparison purposes, in Figure 6.2 (right panel) we overplotted the profile by Baumgardt & Hilker (2018, empty triangles) to that obtained in our study (black circles). We find that the two innermost points of the Baumgardt & Hilker (2018) profile are consistent within the errors with our measures, while their outermost point has a larger value than that measured in this work, which could be due to an effect of residual field star contamination. Also in this case, the value of σ_0 quoted in Baumgardt & Hilker (2018, 7.5 km s $^{-1}$) is larger than our estimation $\sigma_0 = 6.7 \pm 0.3$ km s $^{-1}$, presumably for the same reasons discussed above for NGC 6440.

NEW STAR DENSITY PROFILES - In the cases of NGC 6440 and NGC 6569 no appropriate star density profiles were available in the literature at the beginning of this work. Therefore, by using high-quality photometric data sets, we also constructed star count density profiles in order to re-determine the structural properties of both clusters. In addition, adopting the same data sets we performed a new determination of the gravitational center of NGC 6440 and NGC 6569. We prefer to adopt star counts, instead of the surface brightness profile, to avoid possible biases due to the sparse presence of bright stars, which can locally alter the

luminosity distribution. The stars density profiles obtained for the two clusters are shown in Figure 6.3 (black circles), where the overplotted red curves represent the best-fit King model profiles as derived in Chapter 4 and Chapter 5 for NGC 6440 and NGC 6569, respectively. The values of the structural parameters are summarized in Table 4.6 for NGC 6440 and Table 5.3 for NGC 6569.
We verified that the King models that best-fit the density distributions are also able to properly reproduce the observed VD profiles, finding successful results in each cluster (see the red lines in Figure 6.2).

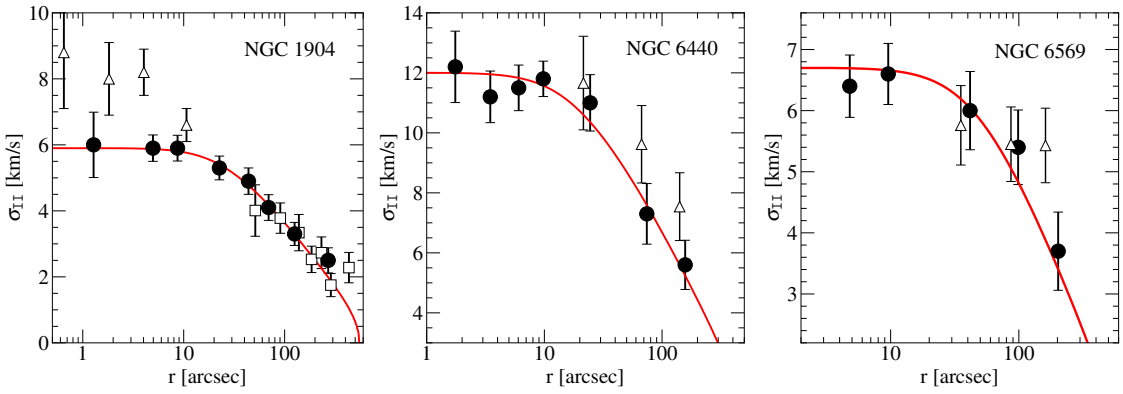

Figure 6.2: VD profiles of NGC 1904 (left panel), NGC 6440 (central panel), and NGC 6569 (right panel) obtained in this thesis work (black circles). The empty squares and triangles in the left panel show the VD profile derived for NGC 1904 in Scarpa et al. (2011) and Lützgendorf et al. (2013), respectively. The empty triangles in the central and right panels mark the profiles quoted by Baumgardt & Hilker (2018) for NGC 6440 and NGC 6569, respectively. The red curve in each panel represents the King model that best fits the observed density distribution of the cluster as obtained in this thesis for NGC 6440 and NGC 6569 (see Figure 6.3 and Chapter 4 and 5, respectively), and derived in Miocchi et al. (2013) for NGC 1904.

INTERNAL ROTATION - We have also investigated the presence of LOS rotation in each analyzed cluster. Following the procedures described in Chapter 3 (Section 3.4.3 and 3.4.4), we found a clear rotation pattern in NGC 1904, and derived the well-defined rotation curve shown in the top panel of Figure 6.4. This rotation profile is nicely described by the analytical model represented in equation 3.2 and introduced in Lynden-Bell (1967, red curve in the figure) to describe the equilibrium rotational profile emerging at the end of the violent relaxation phase. It shows a rotation peak of ~ 1.5 km s^{-1} at $\sim 70''$ from the cluster center (corresponding to about 1.5 half-mass radius, with $r_{\rm h} = 56.7''$ by Miocchi et al. 2013).
In the case of NGC 6569, a signal of rotation was detected only between $40'' - 90''$ from the center with a position angle of the rotation axis PA$= (91 \pm 3)^\circ$ and a maximum amplitude of ~ 1.9 km s^{-1}. The signature of rotation is evident in the diagnostic plots shown in the bottom panels of Figure 6.4 and obtained as described in Chapter 5. Interestingly, in both NGC 1904 and NGC 6569, the rotation peak is

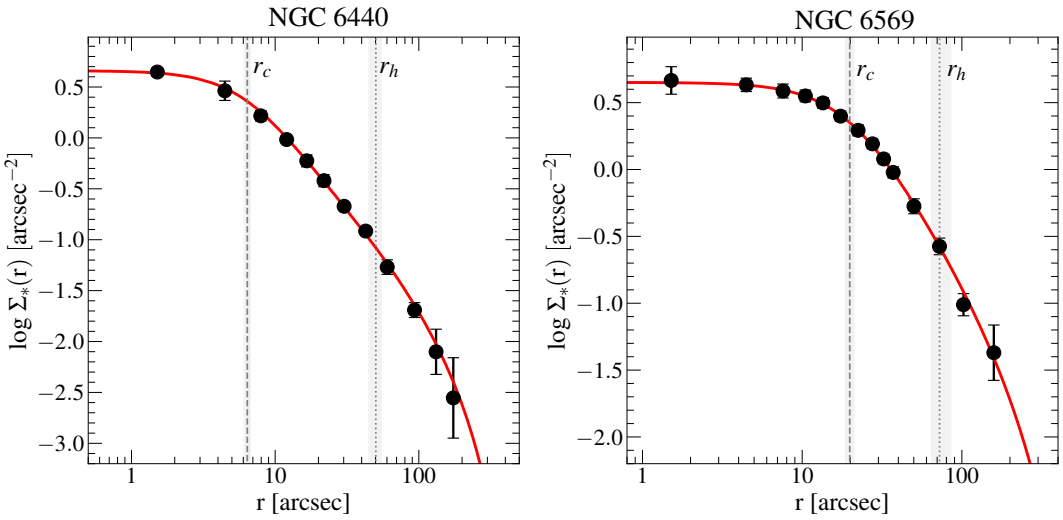

Figure 6.3: Star density profiles of NGC 6440 (left panel) and NGC 6569 (right panel) obtained in Chapter 4 and Chapter 5 of this thesis, respectively. The corresponding best-fit King models are overplotted (red curves). In both panels, the dashed and dotted lines mark the core radius (r_c) and the half-mass radius (r_h) of the cluster, respectively, while the shaded regions show the associated uncertainties.

located between 1-2 half-mass radii as predicted by theoretical studies (e.g., Ernst et al., 2007; Hong et al., 2013; Tiongco et al., 2017).

More intriguing is the case of NGC 6440, where we detected a significant core rotation, with average PA $\sim 132°$, and a maximum amplitude of ~ 3.4 km s^{-1} (corresponding to $V_{\rm rot}^{\rm peak}/\sigma_0 \sim 0.3$) between $3''$ and $5''$ from the center (see the central panels of Figure 6.4; see also Chapter 4, Section 4.3.4.3 for more details). While no evidence of rotation has been found in the outer regions ($r > 50''$), unfortunately, our data set provides a non-uniform and poor sampling between $5''$ and $50''$ from the center, thus preventing the exploration of the rotation structure beyond the core region. Such a central rotation peak is a rare feature in GCs, with only two similar cases known to date in the literature (NGC 6362, Dalessandro et al., 2021a, and M15, van den Bosch et al. 2006; Usher et al. 2021). However, M15 is a post-CC GC and the observed peculiar rotation patterns can be due to recent physical events like gravothermal oscillations (see Usher et al., 2021). On the other hand, results of N-body simulations (Tiongco et al., 2017) show that a very inner rotation peak ($r < r_h$) is expected only in very dynamically evolved systems that lost a significant amount of their mass and angular momentum due to both two-body relaxation effects and interaction with the host galaxy potential. This simulations predict that in rotating star clusters the rotation peak is expected to be located between 1-2$\times r_h$ during the first phases of the cluster evolution, and then gradually moves inward in very advanced dynamical stages.

According to this scenario, NGC 6440 is likely to be more dynamically evolved than NGC 1904 and NGC 6569. This is also in agreement with their estima-

tion of the half-mass relaxation time: for NGC 6440, $\log(t_{rh}\ \mathrm{yr}^{-1}) = 9.0$ as derived in Chapter 4, while Baumgardt & Hilker 2018 find $\log(t_{rh}\ \mathrm{yr}^{-1}) = 8.63$; for NGC 1904 $\log(t_{rh}\ \mathrm{yr}^{-1}) = 9.10$ from Baumgardt & Hilker 2018, and for NGC 6569 $\log(t_{rh}\ \mathrm{yr}^{-1}) = 9.2$ as obtained in Chapter 5. However, these conclusions are valid only if the value that we measured at $3'' < r < 5''$ is the actual peak and the rotation does not increase at larger distances. Therefore, determining the real extension of the rotational structure and derive the exact shape of the rotation curve in NGC 6440 is a crucial point to understand the current dynamical state and the formation mechanism of the system. To this aim, it would be interesting to complement our MUSE data with additional MUSE/WFM observations by uniformly sampling the still unexplored radial region between $5'' < r < 50''$ form the center.

THE COMPREHENSIVE CASE OF NGC 1904 - To complete the kinematic study, we investigate also the rotation in the plane of the sky. Unfortunately, PM analysis was possible only for the GC NGC 1904, since no reliable internal PM measurements are currently available for NGC 6440 and NGC 6569, because Gaia's capabilities are limited in the direction of the Galactic bulge.
For NGC 1904 we analyzed PMs from the Gaia EDR3 data set (see Chapter 3, Section 3.4.6), detecting a signal of rotation also in the plane of the sky with a maximum amplitude of ~ -2.0 km s^{-1} at $\sim 80''$ ($\sim 1.5 \times r_h$) from the cluster center, in agreement with the values obtained in the LOS direction. Moreover, the study has shown that NGC 1904 is characterized by an isotropic velocity distribution, which indicates that the system has lost most of the anisotropy developed during its early evolution (see, Tiongco et al., 2016b), suggesting again an advanced dynamical stage for the cluster.
We then used a sub-sample of 130 stars for which we have the three velocity components (LOS velocity and PMs) to double-check our results by reconstructing the three-dimensional kinematic structure of the cluster. By following the procedure described, e.g., in Sollima et al. (2019), we have confirmed the presence of a rotation pattern with an amplitude consistent with the value previously determined, and we estimated an inclination angle of the rotation axis with respect to the LOS of 37°.
As last step, we compared the observed rotation curves in the plane of the sky and in the LOS direction with the results obtained from N-body simulations of a rotating star cluster (Tiongco et al., 2017, see Chapter 3, Figure 3.20). The comparison has shown overall good agreement with advanced dynamical phases for NGC 1904. This finding is also consistent with the dynamical stage estimated from the radial distribution of blue straggler stars (see Lanzoni et al., 2016; Ferraro et al., 2020).
The comprehensive study performed on NGC 1904 is a clear example of how the synergy between the investigation of the structural and kinematic properties, and the use of theoretical models is essential to increasingly improve our understanding

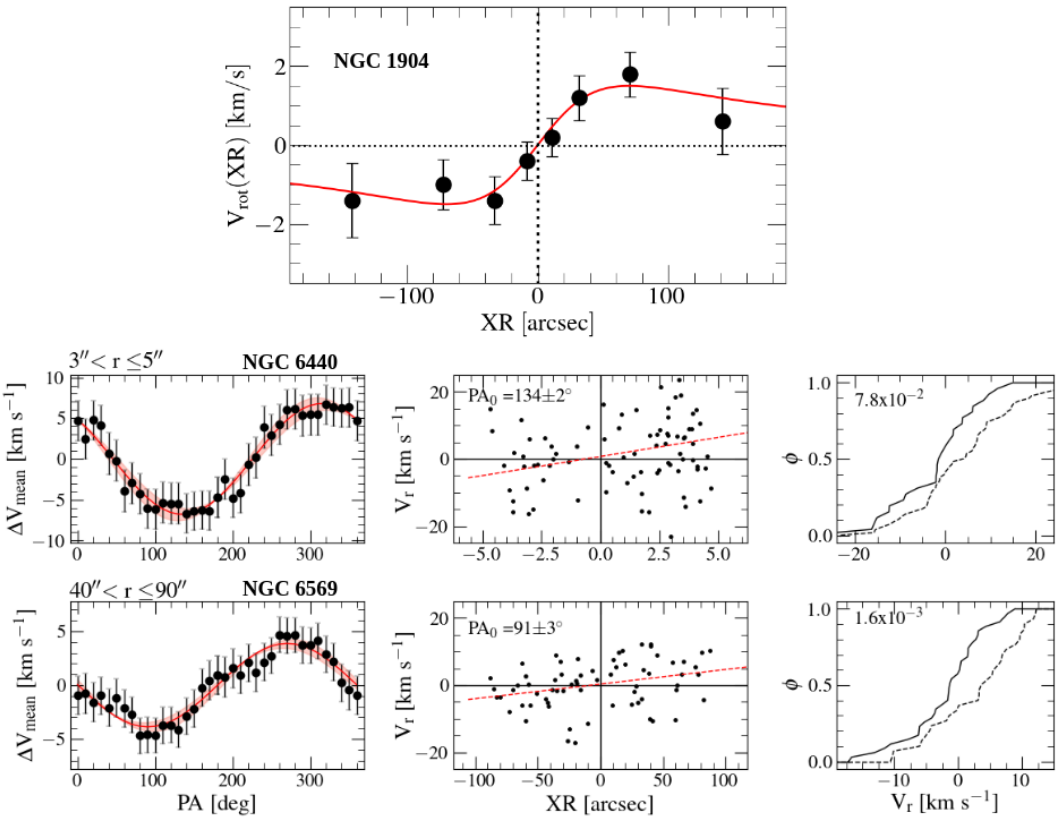

Figure 6.4: *top panel:* rotation curve of NGC 1904. The red line is the analytical model presented in Lynden-Bell (1967) and shown in equation (3.2), with A_{peak} = 1.5 km s^{-1} and XR$_{peak}$ = 70″. *Middle panels*: diagnostic diagrams of the rotation signature detected in NGC 6440 between 3″-5″ (see Chapter 4, Section 4.3.4.3). The left panel shows the difference between the mean RV on each side of a line passing through the center with a given PA, as a function of PA itself. The red line is the sine function that best fits the observed patterns and the shaded region marks the confidence level at 3σ. The central panel shows the velocity distribution as as a function of the projected distances from the rotation axis (XR) having the labelled position angle (PA$_0$). The red dashed lines are the least square fits the data. The panel on the right represent the cumulative velocity distributions for the stars with XR< 0 (solid line) and for those with XR> 0 (dotted line). The Kolmogorov-Smirnov probability that the two distributions are extracted from the same parent family is also labelled. *Bottom panels:* as in the central panels but for the GC NGC 6569 considering the radial bin 40″-90″.

of the formation processes and the dynamical evolution of old stellar systems.

In conclusion, this thesis contributed to demonstrate that GGCs are much more complex stellar systems than long thought, and that a punctual knowledge of their structural and kinematic properties is a precious piece to add to the puzzle of their intricate dynamical evolution and formation.

Future perspectives

The results presented in this thesis offer a first overview of the potentiality of the approach proposed in the VLT-ESO MIKiS survey in the exploration of the internal kinematics of GCs. The VD profiles obtained for NGC 1904, NGC 6440 and NGC 6569 have clearly demonstrated that an adequate characterization in terms of LOS velocities of individual stars is currently possible even in the core of high-density clusters. In fact, in this thesis work, we have presented some of the very first kinematic characterizations of GGC cores by using accurate LOS velocity measurements from spectra of individual resolved stars.
In addition, integrating LOS velocity with PM measurements, ensured by Gaia in the outer regions and by HST in the innermost regions of the clusters, provides a comprehensive three-dimensional study of the internal kinematics of these dense stellar systems. Another key step is the comparison of the observational findings with updated theoretical models based on Monte Carlo and N-body simulations, which include an extensive range of parameters, initial conditions, and complex stellar physical processes. This will offer increasingly realistic representations of the dynamical evolution of these systems. In this respect, the case of NGC 1904 represents a sort of reference case, by clearly demonstrating the importance of a complete three-dimensional kinematic characterization of stellar systems, which allows not only a proper determination of the actual extent of the cluster internal rotation, but also to constrain the dynamical phase of the system. Therefore, this approach will be now extended to other clusters observed in the MIKiS survey, thus providing the community with a panoramic view of the internal kinematics of star clusters with different structure and dynamical age.
Of course, further major improvements will also be achieved thanks to the new generation of telescopes. For example, the IF spectrograph ERIS at ESO-VLT by combining sub-arcsecond spatial resolution and high spectral resolution (R$\sim$10,000), is the perfect facility for an important contribution to the exploration of GC kinematic properties. On the other hand, the impressive performance of the *James Webb Space Telescope* (JWST) observations will certainly mark a turning point for the characterization of the structural properties and the population of stellar exotica even in the highest-density GCs. Last but not least, the next generation of telescopes, as MAVIS at ESO-VLT and MICADO at the awaited ESO *Extremely Large Telescope* (ELT), will mark a breakthrough in the exploration of crowded fields, including the internal kinematics of GCs, thanks to the expected very high accuracy of stellar PM measurements in crowded regions (see, e.g, Fiorentino et al., 2020; Monty et al., 2021).

Appendix A

Validation of the MUSE data

In the presented work, we used MUSE IFU spectroscopy to measure the RV from the spaxels illuminated by individual, resolved stars in highly crowded GC cores. Before deriving the radial velocity (RV), we validated the data by verifying that the the S/N and the spectral line measurability of the MUSE/NFM spactra were in agreement with the expectations. Then we started to test the accuracy of the RV measurements. Doing this, we noticed that RV estimates from the spectrum of different spaxels illuminated by the same star can provide values differing by up to 10 km s^{-1}. An example is shown in Figure A.1, where the RV map and distribution obtained for the same star are plotted. We found analogous results for stars with different magnitudes and regardless of their position in the field of view.

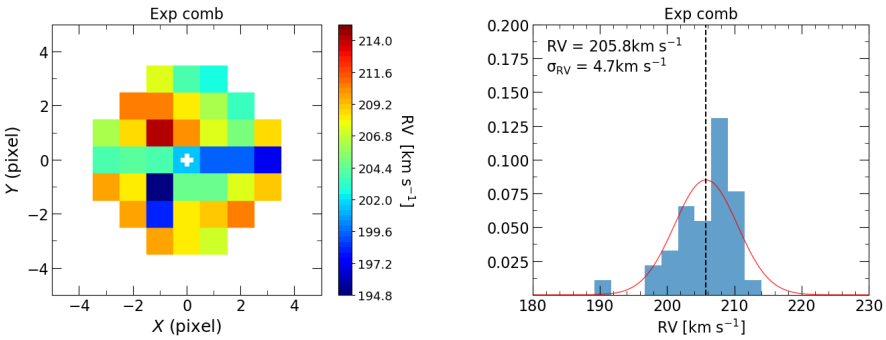

Figure A.1: Radial velocity (RV) map and distribution obtained from the analysis of a combined datacube for one of the stars observed in NGC 1904 with MUSE/NFM. The stellar centroid is marked with the white cross. Although all the spaxels are illuminated by the same individual source, they provide RV values that can differ by ~ 10 km s^{-1}.

To understand the origin of this effect and evaluate its impact on the final results, we performed the analysis using the datacubes of the individual exposures separately, also switching off the telluric correction option in the pipeline. This surprisingly revealed the presence of a spurious gradient in the RV distribution with respect to the stellar centroid, as clearly shown in Figure A.2, where the maps and histograms of the RV values obtained from the three single exposures of the same star shown in Figure A.1 are plotted. The detected pattern clearly follows the change of direction of the instrument, which has been rotated each time by 90° , from exposure Exp#1

(top panel), to Exp#2 (middle panel), to Exp#3 (bottom panel).

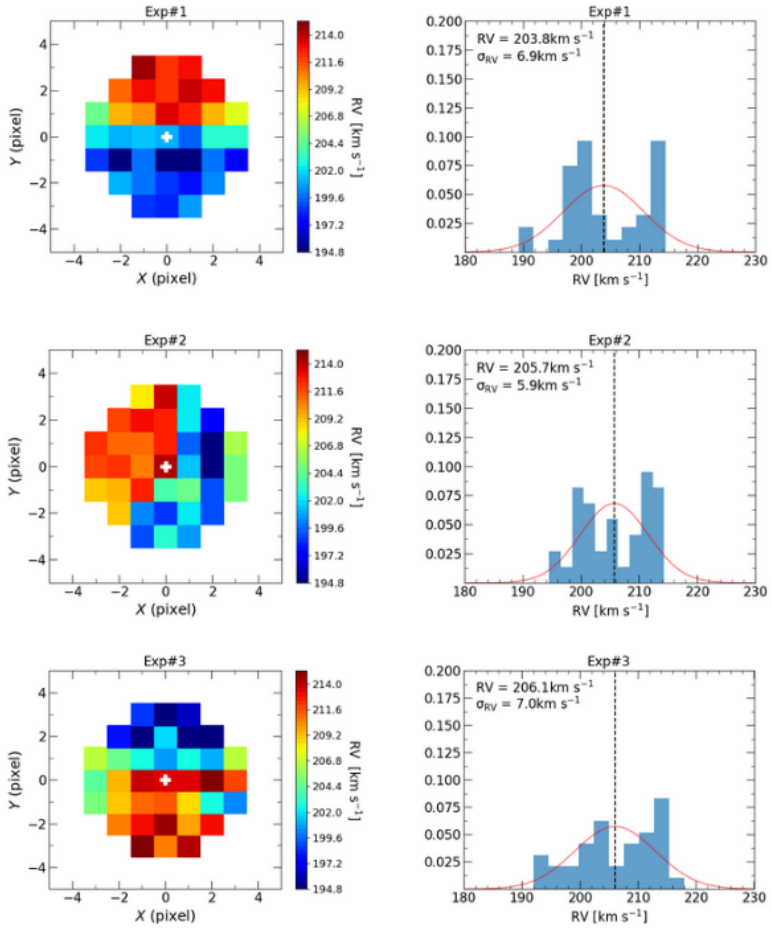

Figure A.2: Map and distribution of the RV values measured for the same star shown in Figure A.1, but as obtained from the analysis of the three different exposures (Exp#1, Exp#2, Exp#3 in the top, middle and bottom panels, respectively. A spurious RV pattern is dearly apparent in each single datacube.

We analyzed the problem thoroughly and searched for a solution, finding that we could correct the gradient by estimating the "velocity offset" of each spaxel in each exposure using the telluric lines (in particular the Fraunhofer A band at ~ 7600 Å). This is illustrated in Figure A.3, showing the RV map and distribution obtained from the telluric lines (top panel) and those of the RV after applying this correction (bottom panel) for the Exp#1 of the same star as in Figure A.2. The applied correction is able to remove the RV pattern and provides a much more uniform distribution of the RV values measured in the different spaxels illuminated by the same star.

Then we performed a very detailed comparisons between the results obtained from the combined spectra (from rotated exposures) and those from individual exposure (corrected with telluric lines), also evaluating possible dependencies on the

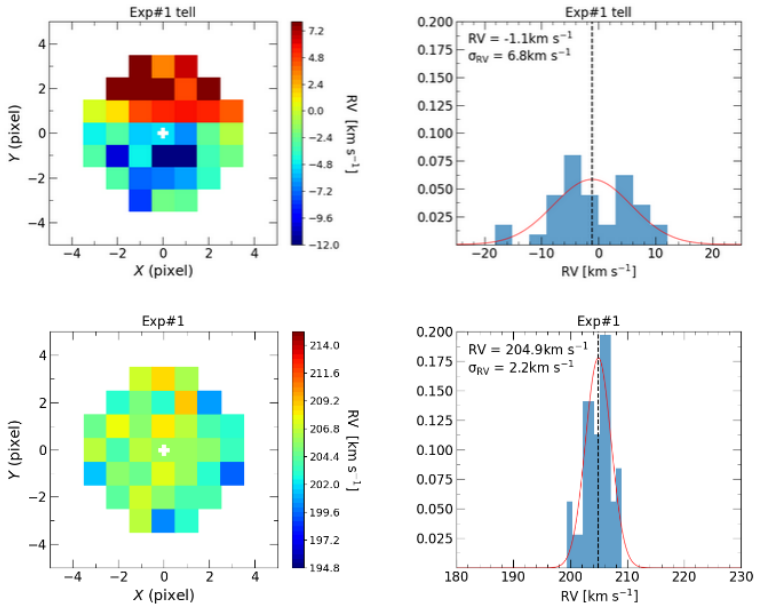

Figure A.3: *Left panel:* RV map and distribution obtained from the telluric lines measured in the exposure Exp#1 of the same shown in Figure A.2 (top panel). *Right panel:* RV map and distribution from Exp#1 obtained after applying the telluric correction.

S/N ratio, the stellar crowding, the star magnitude, etc. Our findings indicates that RVs measured using the 5 spaxels drawing a cross centered on the source (i.e., the centroid spaxel of the target and the 4 adjacent ones along the X and Y directions) in the spectrum obtained from the combination of three exposures rotated by 90° can reasonably cancel out the offsets. The obtained RVs are consistent with those obtained from individual exposures corrected via the telluric lines. In spite of being quite time-expensive, this effort, clearly has represented a key step for the proper analysis of these data. Indeed, we find that rotations among different exposures is important not only *to reject cosmics and get a more uniform combined data set in terms of noise properties* as quoted in the manual, but also to cancel out any spurious RV pattern.

Bibliography

Aarseth, S. J., & Heggie, D. C. 1998, MNRAS, 297, 794-806

Alonso-García, J., Minniti, D., Catelan, M., et al. 2017, ApJ, 849, L13

Anderson, J., & King, I. R. 2006, PSFs, Photometry, and Astronomy for the ACS/WFC, Instrument Science Report ACS 2006-01, 34 pages

Anderson, J., & van der Marel, R. P. 2010, ApJ, 710, 1032-1062

Armandroff, T. E., & Zinn, R. 1988, AJ, 96, 92

Arsenault, R., Madec, P. Y., Hubin, N., et al. 2008, in Society of Photo-Optical Instrumentation Engineers (SPIE) Conference Series, Vol. 7015, Adaptive Optics Systems, ed. N. Hubin, C. E. Max, & P. L. Wizinowich, 701524

Bacon, R., Accardo, M., Adjali, L., et al. 2010, in Ground-based and Airborne Instrumentation for Astronomy III, ed. I. S. McLean, S. K. Ramsay, & H. Takami, Vol. 7735, International Society for Optics and Photonics (SPIE), 131 – 139

Bahcall, J. N., & Wolf, R. A. 1976, ApJ, 209, 214-232

Bailyn, C. D. 1995, ARA&A, 33, 133-162

Barbuy, B., Chiappini, C., & Gerhard, O. 2018, ARA&A, 56, 223-276

Barnard, E. E., Frost, E. B., & Calvert, M. R. 1927, A Photographic Atlas of Selected Regions of the Milky Way

Baumgardt, H., & Hilker, M. 2018, Monthly Notices of the Royal Astronomical Society, 478, 1520–1557

Baumgardt, H., Hilker, M., Sollima, A., & Bellini, A. 2019, MNRAS, 482, 5138-5155

Baumgardt, H., & Makino, J. 2003, MNRAS, 340, 227-246

Baumgardt, H., Makino, J., & Hut, P. 2005, ApJ, 620, 238-243

Baumgardt, H., & Vasiliev, E. 2021, MNRAS, 505, 5957-5977

Bellazzini, M., Dalessandro, E., Sollima, A., & Ibata, R. 2012, MNRAS, 423, 844-855

Bellini, A., Anderson, J., & Bedin, L. R. 2011, PASP, 123, 622

Bellini, A., Bianchini, P., Varri, A. L., et al. 2017, ApJ, 844, 167

Bellini, A., Piotto, G., Bedin, L. R., et al. 2009, A&A, 493, 959-978

Bellini, A., Anderson, J., van der Marel, R. P., et al. 2014, ApJ, 797, 115

Bellini, A., Vesperini, E., Piotto, G., et al. 2015, ApJ, 810, L13

Bellini, A., Libralato, M., Bedin, L. R., et al. 2018, ApJ, 853, 86

Bhat, B., Lanzoni, B., Ferraro, F. R., & Vesperini, E. 2022, ApJ, 926, 118

—. 2023, arXiv e-prints, , arXiv:2301.07706

Bianchini, P., Sills, A., & Miholics, M. 2017, MNRAS, 471, 1181-1191

Bianchini, P., van der Marel, R. P., del Pino, A., et al. 2018, MNRAS, 481, 2125-2139

Bianchini, P., Varri, A. L., Bertin, G., & Zocchi, A. 2013, ApJ, 772, 67

Bica, E., Bonatto, C., Barbuy, B., & Ortolani, S. 2006, A&A, 450, 105-115

Bica, E., Ortolani, S., & Barbuy, B. 2016, Publ. Astron. Soc. Australia, 33, e028

Binney, J., & Mamon, G. A. 1982, MNRAS, 200, 361-375

Binney, J., & Tremaine, S. 1987, Galactic dynamics

Boberg, O. M., Vesperini, E., Friel, E. D., Tiongco, M. A., & Varri, A. L. 2017, ApJ, 841, 114

Breen, P. G., & Heggie, D. C. 2012a, MNRAS, 420, 309-319

—. 2012b, MNRAS, 425, 2493-2500

Bressan, A., Marigo, P., Girardi, L., et al. 2012, MNRAS, 427, 127-145

Cadelano, M., Chen, J., Pallanca, C., et al. 2020a, ApJ, 905, 63

Cadelano, M., Dalessandro, E., Webb, J. J., et al. 2020b, MNRAS, 499, 2390-2400

Cadelano, M., Pallanca, C., Ferraro, F. R., et al. 2017, ApJ, 844, 53

Cadelano, M., Ransom, S. M., Freire, P. C. C., et al. 2018, ApJ, 855, 125

Calzetti, D., de Marchi, G., Paresce, F., & Shara, M. 1993, ApJ, 402, L1

Cardelli, J. A., Clayton, G. C., & Mathis, J. S. 1989, ApJ, 345, 245

Carretta, E., Bragaglia, A., Gratton, R., & Lucatello, S. 2009a, A&A, 505, 139-155

Carretta, E., Bragaglia, A., Gratton, R. G., et al. 2009b, A&A, 505, 117-138

Casagrande, L., & VandenBerg, D. A. 2014, MNRAS, 444, 392-419

Chaboyer, B., Demarque, P., Kernan, P. J., & Krauss, L. M. 1998, ApJ, 494, 96-110

Chandrasekhar, S. 1969a, ApJ, 157, 1419

—. 1969b, ApJ, 157, 1419

Chen, C. W., & Chen, W. P. 2010, ApJ, 721, 1790-1819

Cote, P., Welch, D. L., Fischer, P., & Gebhardt, K. 1995, ApJ, 454, 788

Dalessandro, E., Miocchi, P., Carraro, G., Jílková, L., & Moitinho, A. 2015, MNRAS, 449, 1811-1818

Dalessandro, E., Raso, S., Kamann, S., et al. 2021a, MNRAS, 506, 813-823

Dalessandro, E., Salaris, M., Ferraro, F. R., Mucciarelli, A., & Cassisi, S. 2013, MNRAS, 430, 459-471

Dalessandro, E., Varri, A. L., Tiongco, M., et al. 2021b, The Astrophysical Journal,

909, 90

Dalessandro, E., Crociati, C., Cignoni, M., et al. 2022, ApJ, 940, 170

Djorgovski, S. 1993, in Astronomical Society of the Pacific Conference Series, Vol. 50, Structure and Dynamics of Globular Clusters, ed. S. G. Djorgovski & G. Meylan, 373

Djorgovski, S., & King, I. R. 1984, ApJ, 277, L49-L52

D'Orazi, V., Gratton, R. G., Angelou, G. C., et al. 2015, MNRAS, 449, 4038-4047

Dotter, A., Chaboyer, B., Jevremović, D., et al. 2008, ApJS, 178, 89-101

Dubath, P., Meylan, G., & Mayor, M. 1997, A&A, 324, 505-522

Ebisuzaki, T., Makino, J., Tsuru, T. G., et al. 2001, ApJ, 562, L19-L22

Eisenhauer, F., Abuter, R., Bickert, K., et al. 2003, in Society of Photo-Optical Instrumentation Engineers (SPIE) Conference Series, Vol. 4841, Instrument Design and Performance for Optical/Infrared Ground-based Telescopes, ed. M. Iye & A. F. M. Moorwood, 1548–1561

Ernst, A., Glaschke, P., Fiestas, J., Just, A., & Spurzem, R. 2007, MNRAS, 377, 465-479

Fabricius, C., Luri, X., Arenou, F., et al. 2021, Astronomy & Astrophysics, 649, A5

Fabricius, M. H., Noyola, E., Rukdee, S., et al. 2014, ApJ, 787, L26

Feldmeier, A., Neumayer, N., Seth, A., et al. 2014, A&A, 570, A2

Ferraro, F. R., Clementini, G., Fusi Pecci, F., Sortino, R., & Buonanno, R. 1992, MNRAS, 256, 391-403

Ferraro, F. R., Lanzoni, B., & Dalessandro, E. 2020, Rendiconti Lincei. Scienze Fisiche e Naturali, 31, 19

Ferraro, F. R., Lanzoni, B., Dalessandro, E., et al. 2019, Nature Astronomy, 3, 1149-1155

Ferraro, F. R., Lapenna, E., Mucciarelli, A., et al. 2016, ApJ, 816, 70

Ferraro, F. R., Messineo, M., Fusi Pecci, F., et al. 1999b, AJ, 118, 1738-1758

Ferraro, F. R., Montegriffo, P., Origlia, L., & Fusi Pecci, F. 2000, AJ, 119, 1282-1295

Ferraro, F. R., Pallanca, C., Lanzoni, B., et al. 2015, ApJ, 807, L1

Ferraro, F. R., Paltrinieri, B., Rood, R. T., & Dorman, B. 1999a, ApJ, 522, 983-990

Ferraro, F. R., Sills, A., Rood, R. T., Paltrinieri, B., & Buonanno, R. 2003, ApJ, 588, 464-477

Ferraro, F. R., Paltrinieri, B., Fusi Pecci, F., et al. 1997, A&A, 324, 915-928

Ferraro, F. R., Beccari, G., Dalessandro, E., et al. 2009, Nature, 462, 1028-1031

Ferraro, F. R., Lanzoni, B., Dalessandro, E., et al. 2012, Nature, 492, 393-395

Ferraro, F. R., Lanzoni, B., Raso, S., et al. 2018a, ApJ, 860, 36

Ferraro, F. R., Mucciarelli, A., Lanzoni, B., et al. 2018b, ApJ, 860, 50

Ferraro, F. R., Mucciarelli, A., Lanzoni, B., et al. 2018c, The Messenger, 172, 18-23

Ferraro, F. R., Pallanca, C., Lanzoni, B., et al. 2021, Nature Astronomy, 5, 311-318

Fétick, R. J. L., Fusco, T., Neichel, B., et al. 2019, A&A, 628, A99

Fiestas, J., Spurzem, R., & Kim, E. 2006, MNRAS, 373, 677-686

Fiorentino, G., Bellazzini, M., Spera, M., et al. 2020, MNRAS, 494, 4413-4425

Foreman-Mackey, D., Hogg, D. W., Lang, D., & Goodman, J. 2013, PASP, 125, 306

Freudling, W., Romaniello, M., Bramich, D. M., et al. 2013, A&A, 559, A96

Frogel, J. A., Stephens, A., Ramírez, S., & DePoy, D. L. 2001, AJ, 122, 1896-1915

Fusi Pecci, F., Ferraro, F. R., Crocker, D. A., Rood, R. T., & Buonanno, R. 1990, A&A, 238, 95

Gaia Collaboration, Prusti, T., de Bruijne, J. H. J., et al. 2016a, A&A, 595, A1

Gaia Collaboration, Brown, A. G. A., Vallenari, A., et al. 2016b, A&A, 595, A2

Gaia Collaboration, Helmi, A., van Leeuwen, F., et al. 2018, A&A, 616, A12

Gaia Collaboration, Brown, A. G. A., Vallenari, A., et al. 2021, A&A, 649, A1

Gieles, M., Heggie, D. C., & Zhao, H. 2011, MNRAS, 413, 2509-2524

Gieles, M., & Zocchi, A. 2015, MNRAS, 454, 576-592

Giersz, M., Heggie, D. C., Hurley, J. R., & Hypki, A. 2013, MNRAS, 431, 2184-2199

Giersz, M., Leigh, N., Hypki, A., Lützgendorf, N., & Askar, A. 2015, MNRAS, 454, 3150-3165

Gott, Richard J., I. 1973, ApJ, 186, 481-500

Göttgens, F., Kamann, S., Baumgardt, H., et al. 2021, MNRAS, 507, 4788-4803

Gratton, R., Sneden, C., & Carretta, E. 2004, ARA&A, 42, 385-440

Gratton, R. G., Carretta, E., & Bragaglia, A. 2012, A&ARv, 20, 50

Gratton, R. G., Fusi Pecci, F., Carretta, E., et al. 1997, ApJ, 491, 749-771

Gustafsson, B., Edvardsson, B., Eriksson, K., et al. 2008, A&A, 486, 951-970

Harris, W. E. 1996, 2010 edition, AJ, 112, 1487

Hénault-Brunet, V., Gieles, M., Agertz, O., & Read, J. I. 2015, MNRAS, 450, 1164-1198

Hénault-Brunet, V., Gieles, M., Evans, C. J., et al. 2012, A&A, 545, L1

Hénault-Brunet, V., Gieles, M., Evans, C. J., et al. 2012, A&A, 545, L1

Hénon, M. 1961, Annales d'Astrophysique, 24, 369

—. 1964, Annales d'Astrophysique, 27, 83

Hong, J., Kim, E., Lee, H. M., & Spurzem, R. 2013, MNRAS, 430, 2960-2972

Husser, T.-O., Kamann, S., Dreizler, S., et al. 2016, A&A, 588, A148

Ibata, R., Bellazzini, M., Chapman, S. C., et al. 2009, ApJ, 699, L169-L173

Ibata, R., Malhan, K., Martin, N., et al. 2021, ApJ, 914, 123

Ibata, R. A., Bellazzini, M., Malhan, K., Martin, N., & Bianchini, P. 2019, Nature Astronomy, 3, 667-672

Jindal, A., Webb, J. J., & Bovy, J. 2019, MNRAS, 487, 3693-3701

Johnson, C. I., Rich, R. M., Caldwell, N., et al. 2018, AJ, 155, 71

Johnson, C. I., Rich, R. M., Simion, I. T., et al. 2022, MNRAS, 515, 1469-1491

Kacharov, N., Bianchini, P., Koch, A., et al. 2014, A&A, 567, A69

Kains, N., Bramich, D. M., Sahu, K. C., & Calamida, A. 2016, MNRAS, 460, 2025-2035

Kamann, S., Wisotzki, L., & Roth, M. M. 2013, A&A, 549, A71

Kamann, S., Husser, T. O., Brinchmann, J., et al. 2016, A&A, 588, A149

Kamann, S., Husser, T. O., Dreizler, S., et al. 2018a, MNRAS, 473, 5591-5616

Kamann, S., Bastian, N., Husser, T.-O., et al. 2018b, Monthly Notices of the Royal Astronomical Society, 480, 1689–1695

Kamann, S., Dalessandro, E., Bastian, N., et al. 2020, MNRAS, 492, 966-977

Kerber, L. O., Libralato, M., Souza, S. O., et al. 2019, MNRAS, 484, 5530-5550

Kim, E., Yoon, I., Lee, H. M., & Spurzem, R. 2008, MNRAS, 383, 2-10

King, I. R. 1966, AJ, 71, 64

Kraft, R. P. 1994, PASP, 106, 553

Kuchinski, L. E., & Frogel, J. A. 1995, AJ, 110, 2844

Kurucz, R. L. 2005, Memorie della Societa Astronomica Italiana Supplementi, 8, 14

Lane, R. R., Kiss, L. L., Lewis, G. F., et al. 2009, MNRAS, 400, 917-923

—. 2010, MNRAS, 406, 2732-2742

Lanzoni, B., Dalessandro, E., Ferraro, F. R., et al. 2007a, ApJ, 668, L139-L142

Lanzoni, B., Ferraro, F. R., Alessandrini, E., et al. 2016, ApJ, 833, L29

Lanzoni, B., Sanna, N., Ferraro, F. R., et al. 2007b, The Astrophysical Journal, 663, 1040–1048

Lanzoni, B., Ferraro, F. R., Dalessandro, E., et al. 2010, ApJ, 717, 653-657

Lanzoni, B., Mucciarelli, A., Origlia, L., et al. 2013, ApJ, 769, 107

Lanzoni, B., Ferraro, F. R., Mucciarelli, A., et al. 2018a, ApJ, 861, 16

Lanzoni, B., Ferraro, F. R., Mucciarelli, A., et al. 2018b, ApJ, 865, 11

Lanzoni, B., Ferraro, F. R., Dalessandro, E., et al. 2019, ApJ, 887, 176

Lapenna, E., Origlia, L., Mucciarelli, A., et al. 2015, ApJ, 798, 23

Leanza, S., Pallanca, C., Ferraro, F. R., et al. 2022, ApJ, 929, 186

—. 2023, ApJ, 944, 162

Leibundgut, B., Bacon, R., Bian, F., et al. 2019, The Messenger, 176, 16-19

Libralato, M., Bellini, A., van der Marel, R. P., et al. 2018, ApJ, 861, 99

Libralato, M., Bellini, A., Vesperini, E., et al. 2022, ApJ, 934, 150

Lin, D., Strader, J., Romanowsky, A. J., et al. 2020, ApJ, 892, L25

Lindegren, L., Klioner, S. A., Hernández, J., et al. 2021, A&A, 649, A2

Lugger, P. M., Cohn, H. N., & Grindlay, J. E. 1995, ApJ, 439, 191

Lützgendorf, N., Kissler-Patig, M., Noyola, E., et al. 2011, A&A, 533, A36

Lützgendorf, N., Kissler-Patig, M., Gebhardt, K., et al. 2013, A&A, 552, A49

Lynden-Bell, D. 1962, MNRAS, 124, 279

—. 1967, MNRAS, 136, 101

Lynden-Bell, D., & Wood, R. 1968, MNRAS, 138, 495

Mackey, A. D., Costa, G. S. D., Ferguson, A. M. N., & Yong, D. 2012, The Astrophysical Journal, 762, 65

Mackey, A. D., Da Costa, G. S., Ferguson, A. M. N., & Yong, D. 2013, ApJ, 762, 65

Madau, P., & Rees, M. J. 2001, ApJ, 551, L27-L30

Madrid, J. P., Leigh, N. W. C., Hurley, J. R., & Giersz, M. 2017, MNRAS, 470, 1729-1737

Magorrian, J., Tremaine, S., Richstone, D., et al. 1998, AJ, 115, 2285-2305

Majewski, S. R., Skrutskie, M. F., Weinberg, M. D., & Ostheimer, J. C. 2003, ApJ, 599, 1082-1115

Mapelli, M. 2017, MNRAS, 467, 3255-3267

Mapelli, M., Colpi, M., Possenti, A., & Sigurdsson, S. 2005, Monthly Notices of the Royal Astronomical Society, 364, 1315-1326

Marchetti, T., Johnson, C. I., Joyce, M., et al. 2022, A&A, 664, A124

Marconi, A., & Hunt, L. K. 2003, ApJ, 589, L21-L24

Marín-Franch, A., Aparicio, A., Piotto, G., et al. 2009, ApJ, 694, 1498-1516

Marino, A. F., Milone, A. P., Renzini, A., et al. 2019, MNRAS, 487, 3815-3844

Martin, N. F., Ibata, R. A., Chapman, S. C., Irwin, M., & Lewis, G. F. 2007, Monthly Notices of the Royal Astronomical Society, 380, 281–300

Massari, D., Mucciarelli, A., Ferraro, F. R., et al. 2014, ApJ, 795, 22

Mauro, F., Moni Bidin, C., Cohen, R., et al. 2012, ApJ, 761, L29

McCall, M. L. 2004, AJ, 128, 2144-2169

McLaughlin, D. E., & van der Marel, R. P. 2005, ApJS, 161, 304-360

Meylan, G., & Heggie, D. C. 1997, A&ARv, 8, 1-143

Milone, A. P., Piotto, G., Renzini, A., et al. 2017, MNRAS, 464, 3636-3656

Minniti, D. 1995, A&A, 303, 468

Miocchi, P. 2007, MNRAS, 381, 103-116

Miocchi, P., Lanzoni, B., Ferraro, F. R., et al. 2013, ApJ, 774, 151

Montegriffo, P., Ferraro, F. R., Fusi Pecci, F., & Origlia, L. 1995, MNRAS, 276, 739-752

Monty, S., Rigaut, F., McDermid, R., et al. 2021, MNRAS, 507, 2192-2207

Muñoz, C., Villanova, S., Geisler, D., et al. 2017, A&A, 605, A12

Nataf, D. M., Gould, A. P., Pinsonneault, M. H., & Udalski, A. 2013b, ApJ, 766, 77

Nataf, D. M., Gould, A., Fouqué, P., et al. 2013a, ApJ, 769, 88

Ness, M., Freeman, K., Athanassoula, E., et al. 2013, MNRAS, 430, 836-857

Nguyen, D. D., Seth, A. C., Neumayer, N., et al. 2018, ApJ, 858, 118

Noyola, E., & Gebhardt, K. 2006, AJ, 132, 447-466

Noyola, E., Gebhardt, K., & Bergmann, M. 2008, The Astrophysical Journal, 676, 1008

Oliveira, R. A. P., Souza, S. O., Kerber, L. O., et al. 2020, ApJ, 891, 37

Origlia, L., Ferraro, F. R., Fabbri, S., et al. 2014, A&A, 564, A136

Origlia, L., Ferraro, F. R., Fusi Pecci, F., & Oliva, E. 1997, A&A, 321, 859-866

Origlia, L., Massari, D., Rich, R. M., et al. 2013, ApJ, 779, L5

Origlia, L., Valenti, E., & Rich, R. M. 2008, MNRAS, 388, 1419-1425

Origlia, L., Rich, R. M., Ferraro, F. R., et al. 2011, ApJ, 726, L20

Ortolani, S., Barbuy, B., & Bica, E. 1994, A&AS, 108, 653-659

Ortolani, S., Bica, E., & Barbuy, B. 2001, A&A, 374, 564-569

Pallanca, C., Beccari, G., Ferraro, F. R., et al. 2017, ApJ, 845, 4

Pallanca, C., Dalessandro, E., Ferraro, F. R., Lanzoni, B., & Beccari, G. 2013, ApJ, 773, 122

Pallanca, C., Ferraro, F. R., Lanzoni, B., et al. 2019, ApJ, 882, 159

Pallanca, C., Dalessandro, E., Ferraro, F. R., et al. 2010, ApJ, 725, 1165-1169

Pallanca, C., Lanzoni, B., Ferraro, F. R., et al. 2021a, ApJ, 913, 137

Pallanca, C., Ferraro, F. R., Lanzoni, B., et al. 2021b, ApJ, 917, 92

Pallanca, C., Leanza, S., Ferraro, F. R., et al. 2023, arXiv e-prints, , arXiv:2304.09472

Pancino, E., Bellazzini, M., Giuffrida, G., & Marinoni, S. 2017, MNRAS, 467, 412-

427

Pasquini, L., Avila, G., Blecha, A., et al. 2002, The Messenger, 110, 1-9

Piotto, G., Bedin, L. R., Anderson, J., et al. 2007, ApJ, 661, L53-L56

Pooley, D., Lewin, W. H. G., Anderson, S. F., et al. 2003, ApJ, 591, L131-L134

Popowski, P. 2000, ApJ, 528, L9-L12

Portegies Zwart, S. F., Baumgardt, H., Hut, P., Makino, J., & McMillan, S. L. W. 2004, Nature, 428, 724-726

Pryor, C., & Meylan, G. 1993a, in Astronomical Society of the Pacific Conference Series, Vol. 50, Structure and Dynamics of Globular Clusters, ed. S. G. Djorgovski & G. Meylan, 357

Pryor, C., & Meylan, G. 1993b, in Astronomical Society of the Pacific Conference Series, Vol. 50, Structure and Dynamics of Globular Clusters, ed. S. G. Djorgovski & G. Meylan, 357

Ransom, S. M., Hessels, J. W. T., Stairs, I. H., et al. 2005, Science, 307, 892-896

Raso, S., Ferraro, F. R., Dalessandro, E., et al. 2017, ApJ, 839, 64

Reines, A. E., & Volonteri, M. 2015, ApJ, 813, 82

Richer, H. B., Heyl, J., Anderson, J., et al. 2013, ApJ, 771, L15

Richstone, D. O., & Tremaine, S. 1986, AJ, 92, 72-74

Riello, M., Cassisi, S., Piotto, G., et al. 2003, A&A, 410, 553-563

Riello, M., De Angeli, F., Evans, D. W., et al. 2021, A&A, 649, A3

Salinas, R., Jílková, L., Carraro, G., Catelan, M., & Amigo, P. 2012, MNRAS, 421, 960-970

Santos, João F. C., J., Maia, F. F. S., Dias, B., et al. 2020, MNRAS, 498, 205-222

Saracino, S., Dalessandro, E., Ferraro, F. R., et al. 2015, ApJ, 806, 152

—. 2016, ApJ, 832, 48

—. 2019, ApJ, 874, 86

Sbordone, L., Bonifacio, P., Castelli, F., & Kurucz, R. L. 2004, ATLAS and SYNTHE under Linux

Scarpa, R., Marconi, G., Carraro, G., Falomo, R., & Villanova, S. 2011, A&A, 525, A148

Sharples, R., Bender, R., Agudo Berbel, A., et al. 2013, The Messenger, 151, 21-23

Skrutskie, M. F., Cutri, R. M., Stiening, R., et al. 2006, AJ, 131, 1163-1183

Sollima, A., Baumgardt, H., & Hilker, M. 2019, MNRAS, 485, 1460-1476

Sollima, A., Bellazzini, M., Smart, R. L., et al. 2009, Monthly Notices of the Royal Astronomical Society, 396, 2183-2193

Sollima, A., Bellazzini, M., Smart, R. L., et al. 2009, MNRAS, 396, 2183-2193

Spitzer, L. 1987, Dynamical evolution of globular clusters (Princeton University Press)

Stetson, P. B. 1987, Publications of the Astronomical Society of the Pacific, 99, 191

Stetson, P. B. 1994, PASP, 106, 250

Stetson, P. B., Pancino, E., Zocchi, A., Sanna, N., & Monelli, M. 2019, Monthly Notices of the Royal Astronomical Society, 485, 3042-3063

Strader, J., Chomiuk, L., Maccarone, T. J., et al. 2012, ApJ, 750, L27

Ströbele, S., La Penna, P., Arsenault, R., et al. 2012, in Society of Photo-Optical Instrumentation Engineers (SPIE) Conference Series, Vol. 8447, Adaptive Optics Systems III, ed. B. L. Ellerbroek, E. Marchetti, & J.-P. Véran, 844737

Takahashi, K., & Portegies Zwart, S. F. 2000, ApJ, 535, 759-775

Tanaka, T., & Haiman, Z. 2009, The Astrophysical Journal, 696, 1798–1822

Tiongco, M. A., Vesperini, E., & Varri, A. L. 2016a, MNRAS, 455, 3693-3701

—. 2016b, MNRAS, 461, 402-411

Tiongco, M. A., Vesperini, E., & Varri, A. L. 2017, MNRAS, 469, 683-692

Tiongco, M. A., Vesperini, E., & Varri, A. L. 2018, MNRAS, 475, L86-L90

Tonry, J., & Davis, M. 1979a, AJ, 84, 1511-1525

—. 1979b, AJ, 84, 1511-1525

Tremou, E., Strader, J., Chomiuk, L., et al. 2018, The Astrophysical Journal, 862, 16

Udalski, A. 2003, ApJ, 590, 284-290

Ulvestad, J. S., Greene, J. E., & Ho, L. C. 2007, ApJ, 661, L151-L154

Usher, C., Kamann, S., Gieles, M., et al. 2021, Monthly Notices of the Royal Astronomical Society, 503, 1680–1687

Valenti, E., Ferraro, F. R., & Origlia, L. 2004, MNRAS, 351, 1204-1214

—. 2004b, MNRAS, 354, 815-820

—. 2007, AJ, 133, 1287-1301

—. 2010, MNRAS, 402, 1729-1739

Valenti, E., Origlia, L., & Ferraro, F. R. 2005, MNRAS, 361, 272-282

Valenti, E., Origlia, L., & Rich, R. M. 2011, MNRAS, 414, 2690-2695

van de Ven, G., van den Bosch, R. C. E., Verolme, E. K., & de Zeeuw, P. T. 2005, Astronomy & Astrophysics, 445, 513–543

van den Bergh, S. 2008, AJ, 135, 1731-1737

van den Bosch, R., de Zeeuw, T., Gebhardt, K., Noyola, E., & van de Ven, G. 2006, The Astrophysical Journal, 641, 852–861

van Leeuwen, F., Le Poole, R. S., Reijns, R. A., Freeman, K. C., & de Zeeuw, P. T.

2000, A&A, 360, 472-498

Varri, A. L., & Bertin, G. 2012, A&A, 540, A94

Vasiliev, E., & Baumgardt, H. 2021, MNRAS, 505, 5978-6002

Vesperini, E., & Heggie, D. C. 1997, MNRAS, 289, 898-920

Vesperini, E., McMillan, S. L. W., D'Antona, F., & D'Ercole, A. 2013, MNRAS, 429, 1913-1921

Vesperini, E., Varri, A. L., McMillan, S. L. W., & Zepf, S. E. 2014, MNRAS, 443, L79-L83

Vitral, E., Kremer, K., Libralato, M., Mamon, G. A., & Bellini, A. 2022, MNRAS, 514, 806-825

Walker, M. G., Mateo, M., Olszewski, E. W., et al. 2006, AJ, 131, 2114-2139

Watkins, L. L., van der Marel, R. P., Bellini, A., & Anderson, J. 2015, ApJ, 803, 29

Weilbacher, P. M., Palsa, R., Streicher, O., et al. 2020, The Data Processing Pipeline for the MUSE Instrument

Wilson, C. P. 1975, AJ, 80, 175-187

Zoccali, M., Cassisi, S., Piotto, G., Bono, G., & Salaris, M. 1999, ApJ, 518, L49-L52

Zoccali, M., & Valenti, E. 2016, Publ. Astron. Soc. Australia, 33, e025

Zocchi, A., Gieles, M., & Hénault-Brunet, V. 2017, MNRAS, 468, 4429-4440